

# UNIVERSITY OF CINCINNATI

Date: March 17, 2005

I, Soujanya Marisarla,

hereby submit this work as part of the requirements for the degree of:

Master of Science,

in:

Mechanical Engineering,

It is entitled:

Structural Analysis of an Equivalent Box-Wing Representation of  
Sensorcraft Joined-Wing Configuration for High-Altitude, Long-Endurance  
(HALE) Aircraft

This work and its defense approved by:

Chair: Dr. Urmila Ghia (Professor, MINE)

Dr. Karman Ghia (Professor, ASE&EM)

Dr. Kumar Vemaganti (Asst. Professor, MINE)

**STRUCTURAL ANALYSIS OF AN EQUIVALENT BOX-WING  
REPRESENTATION OF SENSORCRAFT JOINED-WING  
CONFIGURATION FOR  
HIGH-ALTITUDE, LONG-ENDURANCE (HALE) AIRCRAFT**

A thesis submitted to the  
Division of Research and Advanced Studies  
of the University of Cincinnati

in partial fulfillment of the  
requirements for the degree of

**MASTER OF SCIENCE**  
in the Department of  
Mechanical, Industrial and Nuclear Engineering  
of the College of Engineering

March 2005

by

Soujanya Marisarla

B.Tech., Jawaharlal Nehru Technological University,  
Hyderabad, India (2000)

## **ABSTRACT**

The current research focuses on studying the modal response of a joined wing aircraft based on the Sensorcraft configuration. Sensorcraft, a class of High-Altitude, Long-Endurance (HALE) aircraft, is an Unmanned Air Vehicle (UAV), and is being studied by the AFRL for applications involving telecommunication relay, environmental sensing and military reconnaissance. The Sensorcraft is designed to operate at high altitudes (60,000 ft) with low speed and for long durations of time (60 to 80 hours). At these operating conditions, the density, and hence, the Reynolds number, is low. These conditions require the Sensorcraft to operate with high lift and low drag with high-aspect ratio wings. Moreover, the vehicle must be lightweight and strong, and offer high aerodynamic performance and efficiency. The AFRL has identified a diamond shape joined wing configuration for Sensorcraft due to the primary structural advantage of strength as each wing braces the other against lift loads.

The University of Cincinnati (UC), along with its partners, AFRL and Ohio State University are working together to study the complete nonlinear aeroelastic behavior of the joined-wing model.

At UC, four different structural modeling approaches were adopted for analysis. The current research focuses on the analysis of an in-house Sensorcraft joined wing model developed by the AFRL. This model is an equivalent representation of the actual 3-D joined wing model. The wing is idealized as a box structure consisting of shells, rods, beams, shear panels and concentrated masses. This box wing structure has the advantage of being computationally inexpensive over the full 3-D model, and has been optimized to minimize the deflections of the antennae equipment in the control surface of

the wing. The fluid loads applied on the box-wing structure are obtained from a concurrent aerodynamic analysis for different mach numbers and angles of attack performed at UC.

A modal representation is obtained for different operating boundary conditions as the first step in the overall aeroelastic analysis of the joined wing. AFRL has obtained the modal representation for the Sensorcraft model using NASTRAN, and as part of the DAGSI project requirement, the structural analyses at UC are performed using ANSYS. The results are compared with those from NASTRAN and the correctness of the methodology is verified.

Prior to the NASTRAN box-wing model translation into ANSYS, a number of validation tests are performed to test the consistency between the functionalities of the ANSYS elements and NASTRAN elements. Once the results of the validation test cases are found to be satisfactory, the actual analysis of the joined wing is performed for clamped, rigid and symmetry boundary conditions at the wing roots. The frequencies were found to be different between the two codes for each of these boundary conditions. In order to trace the issue causing the differences in the results, a number of simpler joined wing models are analyzed. Finally, the problem is traced down to differences in the formulation between the constraint equations in ANSYS and RBE1 elements in NASTRAN.

Due to the assumption of small deflections, linear static analysis is performed and considered sufficient for predicting the displacement response. However, a nonlinear analysis is also performed to validate the assumptions of linearity that have been used in the modeling of the wing. The tip deflection from linear is estimated to be 5.3 % of the

span of the wing. For higher angles of attack, the pressure difference between the upper and lower surfaces of the wing is higher, and consequently the lift forces are greater in magnitude. This could cause larger deformation in the main wing that could potentially lead to buckling of the aft wing. Hence, an eigenvalue buckling analysis is performed which show that the wing is stable and not prone to buckling for the loads employed for the linear static analysis. A procedure is also established to determine the structural response under time varying aerodynamic loads from the CFD analysis. This analysis serves as a starting point for future complete aeroelastic analysis of the joined wing.

## **ACKNOWLEDGEMENTS**

I would like to express my sincere gratitude to my advisor and mentor Dr. U. Ghia, for her constant guidance and encouragement at every stage of this project. I am thankful for her help and suggestions in my thesis work.

Thanks are also due to Dr. K.N. Ghia for his useful suggestions and help throughout my Masters study. I am also thankful to Dr. Kumar Vemaganti for agreeing to be on the committee in short notice and for his thoughtful and meaningful suggestions.

I would also like to thank Drs. Larry Huttzell, Greg Reich and Phil Beran of AFRL, for providing me with Sensorcraft Inhouse Joined Wing Model and the information necessary for my research. I would also like to thank Mr. Rob Ogden of the AsE&EM Department, Mr. Larry Schartman of the MINE Department, David Webb and the rest of the staff at the Office of College Computing at UC for their software and hardware support. I also acknowledge my colleagues in the Joined wing project, Vijay Narayanan, Rangarajan Sivaji, and Valentina Kalayanova, for many a useful discussion regarding the load transfer process. The rest of the CFDRL deserve a warm share of my thanks for their friendship and help at different times in various ways.

Lastly, I would like to thank my family members for their constant support throughout the course of this research.

## TABLE OF CONTENTS

<b>ABSTRACT</b> .....	<b>3</b>
<b>ACKNOWLEDGEMENTS</b> .....	<b>6</b>
<b>LIST OF FIGURES</b> .....	<b>10</b>
<b>NOMENCLATURE</b> .....	<b>11</b>
<b>CHAPTER 1 Introduction</b> .....	<b>14</b>
1.1. Background .....	14
1.2. Literature Review .....	17
1.3. Scope of the Present Work .....	26
<b>CHAPTER 2 Mathematical Formulation</b> .....	<b>28</b>
2.1. Introduction .....	28
2.2. Principle Of Virtual Work .....	28
2.3. Equilibrium Equation .....	30
2.4. Stress And Strain Measures .....	31
2.4.1. Cauchy Stress Tensor .....	31
2.4.2. Second Piola-Kirchoff Stress Tensor .....	32
2.4.2.1 Second Piola-Kirchoff Stress Increment .....	32
2.4.3. Green-Lagrange Strain Tensor .....	32
2.4.3.1 Green Strain Increment .....	33
2.5. Incremental Constitutive Law .....	35
2.6. Incremental Equilibrium Equation .....	36
2.7. Discretized Finite Element Form .....	37
<b>CHAPTER 3 Finite Element Modeling and Analysis of Sensorcraft</b>	
<b>Box-Wing Model</b> .....	<b>44</b>
3.1. General Principles of Aircraft Wing Design .....	44

3.2. Sensorcraft Joined Wing Design.....	46
3.3. Finite Element Model Description.....	47
3.4. Material Properties.....	50
3.5. Validation Tests .....	50
3.5.1. Modal Analysis of beam modeled with shear panels.....	51
3.5.2. Modal Analysis of beam modeled with shell elements .....	51
3.5.3. Modal Analysis of fuselage modeled with beam elements.....	52
3.5.4. Linear Static Analysis of a 2-D truss modeled with rods .....	53
3.6. NASTRAN FE Model Translation into ANSYS.....	53
3.7. Structural Analyses of Sensorcraft Box-Wing Model .....	54
3.7.1. Modal Analysis .....	54
3.7.1.1 Symmetric Case .....	54
3.7.1.2 Clamped Case .....	55
3.7.1.3 Rigidly Clamped Case .....	55
3.7.2. Linear Static Analysis.....	56
3.7.3. Linear Buckling Analysis .....	56
3.7.4. Dynamic Analysis.....	57
<b>CHAPTER 4 RESULTS AND DISCUSSION.....</b>	<b>58</b>
4.1. Validation Test Cases .....	58
4.1.1. Modal Analysis of Beam Modeled with Shear Panels.....	58
4.1.2. Modal Analysis of Beam Modeled with Shells .....	59
4.1.3. Modal Analysis of Fuselage modeled with beam elements.....	60
4.1.4. Static Analysis of a Truss .....	61
4.2. Box-Wing Modal Analysis .....	63
4.2.1. Clamped Boundary Condition .....	63
4.2.2. Rigidly-Clamped Boundary Condition.....	69
4.2.3. Symmetry Boundary Condition .....	71
4.3. Linear static Analysis.....	73
4.4. Linear Buckling Analysis .....	76
4.5. Dynamic Analysis.....	77

<b>CHAPTER 5 Summary and Future Work .....</b>	<b>79</b>
5.1. Conclusion .....	79
5.2. Future Work .....	81
<b>REFERENCES .....</b>	<b>82</b>

## **LIST OF FIGURES**

## NOMENCLATURE

$C_0, C_1, C_2, C_3, \dots,$	=	Equilibrium positions of a body
$\Delta t$	=	Time increment
${}^{t+\Delta t} \tau_{ij}$	=	Cartesian components of the Cauchy stress tensor
$\delta_{t+\Delta t} e_{ij}$	=	Strain tensor corresponding to virtual displacements
$\delta u_i$	=	Virtual displacement vector components imposed on configuration at time $t + \Delta t$
${}^{t+\Delta t} x_i$	=	Cartesian coordinates of material point at time $t + \Delta t$
${}^{t+\Delta t} V$	=	Volume at time $t + \Delta t$
${}^{t+\Delta t} f_i^B$	=	Components of externally applied forces per unit volume at time $t + \Delta t$
${}^{t+\Delta t} f_i^S$	=	Components of externally applied surface tractions per unit surface area at time $t + \Delta t$
${}^{t+\Delta t} S_f$	=	Surface at time $t + \Delta t$ on which external tractions are applied
$\delta u_i^S$	=	$\delta u_i$ evaluated on the surface ${}^{t+\Delta t} S_f$ .
${}^{t+\Delta t} {}_0 S_{ij}$	=	Second Piola-Kirchoff stress tensor at $C_2$ configuration
${}^t {}_0 S_{ij}$	=	Second Piola-Kirchoff stress tensor at $C_1$ configuration
${}^{t+\Delta t} {}_0 \tau_{ij}$	=	Cauchy stress tensor at $C_1$ configuration
${}^0 \rho$	=	Mass density of the material at $C_0$ configuration
${}^{t+\Delta t} \rho$	=	Mass density of the material at $C_2$ configuration
${}^0 S_{ij}$	=	Kirchoff stress increment tensor
${}^{t+\Delta t} {}_0 \epsilon_{ij}$	=	Green-Lagrange strain tensor of the body at $C_2$ configuration
${}^t {}_0 \epsilon_{ij}$	=	Green-Lagrange strain tensor of the body at $C_1$ configuration

${}_0 \boldsymbol{\varepsilon}_{ij}$	=	Green strain increment tensor
${}_0 \mathbf{e}_{ij}$	=	Linear component of Green strain increment tensor
${}_0 \boldsymbol{\eta}_{ij}$	=	Nonlinear component of Green strain increment tensor
${}_0 \mathbf{C}_{ijrs}$	=	Incremental constitutive tensor w.r.t $C_0$ configuration
$\lambda, \mu$	=	Lamé constants
$\nu$	=	Poisson's ratio
$\delta_{ij}$	=	Kronecker delta
$m$	=	Superscript denoting element $m$
$\mathbf{u}^{(m)}$	=	Displacements within an element $m$
$\mathbf{N}^{(m)}$	=	Shape-function (displacement interpolation) matrix dependent on the element type and order
$\hat{\mathbf{U}}$	=	Vector of the three global displacement components $U_i, V_i,$ and $W_i$ at all nodal dof
$\mathbf{B}^{(m)}$	=	Strain-displacement matrix for element $m$
${}_0^t \hat{\mathbf{S}}$	=	Second Piola-Kirchoff stress vector for each element
$\mathbf{M}$	=	Time independent mass matrix
${}_0^t \mathbf{K}_L$	=	Linear stiffness matrix
${}_0^t \mathbf{K}_{NL}$	=	Nonlinear stiffness matrix
${}^{t+\Delta t} \mathbf{R}$	=	Externally applied load vector at $t + \Delta t$
${}_0^t \mathbf{F}$	=	Nodal force vector equivalent to elements stresses at $t$
$\mathbf{K}$	=	Stiffness matrix of the entire element assemblage
$\mathbf{R}$	=	Load vector
$\mathbf{R}_B$	=	Element body force vector
$\mathbf{R}_S$	=	Surface force vector
$\mathbf{R}_I$	=	Initial stress vector
$\mathbf{R}_C$	=	Nodal concentrated load vector
$\dot{\mathbf{U}}$	=	Nodal point velocity vector
$\kappa$	=	Damping property parameter

$C$  = Damping matrix of the structure  
 $\omega_1$  = Fundamental vibration frequency

# CHAPTER 1 Introduction

## 1.1. Background

The Air Force Research Laboratory (AFRL) is pursuing a program which blends a wide spectrum of emerging technologies to produce an Unmanned Air Vehicle (UAV) with revolutionary intelligence, surveillance, and reconnaissance (ISR) capabilities. Technological breakthroughs in aeronautics, electronics, materials, and propulsion have led to the development of the latest generation of UAVs. These airborne reconnaissance aircraft have been configured and optimized, with multiple advanced sensing modalities, sustaining an enduring presence. Extremely long endurance, combined with omnidirectional sensing, enables a virtual presence which allows vantage point flexibility/optimization necessary for continuous and detailed air and ground target detection, identification, and tracking. This unique combination of advanced sensors and sustained presence facilitates continuous and rapid reaction to the dynamic combat operational requirements confronting current and evolving military operations.

The Air Vehicles Directorate, in coordination with the Sensors and Propulsion Directorates, identified Sensorcraft, a current generation High-Altitude Long Endurance (HALE) aircraft, as the subject of study based on an initial Simulation Based Research & Development technology assessment process. Sensorcraft, an Intelligence-Surveillance-Reconnaissance (ISR) UAV designed around its sensing capabilities, is an essential element in the mix of platforms that is envisaged to meet the Air Force needs of the 21st century. Sensorcraft is envisioned as the air breather component of a fully integrated ISR enterprise that cohesively integrates space, air, and ground components of the total ISR apparatus.

Several aircraft and propulsion candidate designs and configurations were considered to determine the best trade-off between long endurance, altitude, engine efficiency, and power generation. Factors that drive the aircraft design include the advanced sensor payload and radio frequency (RF) aperture requirements necessary for enhancing the sensing capabilities. One of the most innovative aspects of this program is the integration of the large antenna apertures required for lower frequency operations into the structural components of the Sensorcraft to provide foliage-penetration radar capability.

Advanced air-vehicle technologies featuring new design approaches enabled the embedding of the radar antenna into the actual load-bearing structure, achieving a new level of electrical-structural integration. Additionally, the aerodynamic efficiency of the wing design for high-altitude, long-endurance operation involves design and validation to reach efficiency improvements exceeding 10% over conventional designs through lift/drag (L/D) optimization. This is most significant since such L/D improvements could increase mission duration by several hours. The combined impact of these air-vehicle technologies is expected to lower the operational and support costs, while dramatically improving vehicle efficiency, resulting in a 25-50% reduction in gross vehicle take-off weight (GVTOW). Vehicle weight reduction has a profound impact on lowering the acquisition cost of the platform.

Lastly, technological improvements in engine materials and aerodynamic design are expected to improve engine performance, and reduce specific fuel consumption by up to 35%. Specifically, this 35% fuel efficiency improvement reduces the GVTOW by 50% to meet the mission duration for Sensorcraft.

The primary design driver<sup>1</sup> for the Sensorcraft configuration was the 360° coverage requirement for both the X-band and very high frequency (VHF) radar. The X-band radar required a large area for its antenna array (30 ft long x 1.5 ft high), which created the need for thick airfoil sections. In addition, the X-band antenna was extremely sensitive to structural deflections due to aerodynamic loads. The VHF radar required a 100 ft long antenna in each quadrant of the configuration, thus driving the span of the wing to exceed this length. The team conceptualized a Joined-Wing configuration with a 240 ft wingspan, a National Advisory Committee for Aeronautics 4421 airfoil section, and creative control surface layout, to accommodate the antenna requirements and still fulfill the mission needs.

The joined-wing design is an innovative concept, which incorporates two wings that form a truss arrangement with conformal antennae integrated into the wing structure. The forward wing is swept back with a positive dihedral angle, and joined with an aft wing, which is swept forward. The wings connect in a diamond pattern when viewed from the front and from above. This diamond shape allows the sensorcraft to have a 360° view of its environment in the azimuthal plane, thus allowing fewer potential targets to go undetected.

The University of Cincinnati (UC), the AFRL and the Ohio State University (OSU) have teamed up to study the aeroelastic behavior of the conceptual joined wing model by performing a comprehensive computational fluid dynamics (CFD) and structural analyses.

## 1.2. Literature Review

This section discusses relevant joined-wing structural research accomplished by various researchers in the past. Review of the advantages gained with joined-wing configuration and issues encountered as a result of past and current research are highlighted in this section.

Joined-wing design was first proposed by Julian Wolkovitch in 1976<sup>3</sup>. The basic idea of this design was that the forward swept aft wing connects with the trailing edge of the front wing. This configuration creates a diamond shape when viewing the aircraft from a front or top-down perspective. Subsequent joined-wing work done by Wolkovitch<sup>4,5</sup> compared the performance of a joined wing to a conventional wing on a transport aircraft. His studies claimed several advantages of joined wings over conventional single wings, namely low induced drag, high trimmed maximum coefficient of lift, lower parasitic drag and good stability and control.

Wolkovitch observed that the out-of-plane lift component acting on the wing structure bends the wing about an axis that is tilted forward which results in a downward pitching moment on the front wing, inducing a twist which is not the case with conventional aircraft. This twisting motion is an important consideration for antenna arrays that conform to the surface of the wing because it adds another element of wing deformation besides the typical bending motion. In order to compensate for the tilted bending axis, Wolkovitch recommended an optimal wing-box structure for the joined wing where the structural material is concentrated at the upper leading edge and lower trailing edge. In addition, Wolkovitch claimed a potential weight advantage if the internal joined-wing structure represents this optimum skin thickness taper.

Sensorcraft mission requirements include ability to remain aloft for 7 days which drives fuel requirement much higher than conventional aircraft. Fuel volume comparison studies by Wolkovitch showed the joined wing potentially contained 150 % of the fuel available in a single wing, allowing it greater endurance and range performance.

Samuels<sup>6</sup> continued on Wolkovitch's work, focusing on validating the potential weight savings of a joined-wing over a conventional wing. Two joined-wing designs were compared to a Boeing 727 design and were found to be lighter than the conventional wing. Samuels work did not take into consideration nonlinear behavior due to large deformations typically seen in such wings.

Shyu and Miura<sup>7</sup> of NASA Ames Research Center performed comprehensive structural analyses of several joined-wing configurations. Wolkovitch compared their results with those independently obtained by Samuels and Hajela<sup>8</sup> and observed that the joined wing typically weighs 65-78 % of the weight of the aerodynamically equivalent cantilever wing-plus-tail when both systems are aerodynamically equivalent. That is, both the systems had the same gross projected areas (GPA), equal taper ratios, equal magnitudes of sweep angles, and equal ratios of front to rear lifting-surface projected areas. The total design air loads and the structural properties were also the same for the two systems. Wolkovitch concluded that the joined wing leads to large weight savings when various geometric parameters of the joined wing such as sweep, dihedral angle, taper ratio, and the joint location (as a fraction of the span) are properly chosen. Also the leading edge and trailing edge spars should occupy the airfoil section between 5 and 75 % chord leading to an optimized internal wing structure. It was suggested that for an overall optimum design the joint should be located at 60 to 100% of the span. In

addition, it was observed that for a given span, GPA, and maximum lift, with constant sweep and dihedral angles, an inter-wing joint located inboard provides a lighter wing system than joining the wings at their tips, even though the tip-jointed configuration enjoys some aerodynamic advantages. A feasibility study of building a joined-wing research airplane by Wolkovitch<sup>9</sup> provides useful initial data on performance at low cost for a wide range of joined wing configurations.

Smith, Cliff, and Kroo<sup>10</sup>, in conjunction with NASA Ames Research Center, designed a flight demonstrator aircraft with joined wing structure. Their objectives were to demonstrate good handling characteristics and validate the existing joined wing design methods. Their JW-1 design, a modified NASA AD-1 aircraft, was based on the idea that the joined-wing aircraft would be most beneficial as a medium-range transport due to the potential weight savings offered by this type of configuration. A one-sixth scale wind tunnel model of the JW-1 design was built and tested in the NASA Ames 12-ft wind tunnel. Wind-tunnel-test data were used to assess performance, stability, and control, and to confirm that the relatively simple design tools used for the JW-1 are suitable for designing joined wings.

Eight different joint configurations were investigated in a study performed using the JW-1 in 1990, by Lin, Jhou, and Stearman<sup>11</sup>, to determine the amount of influence that the type of joint has on the strength and stiffness of a joined wing. Different types of joints such as ball joints, pin joints, universal joints, link joints, and rigid joints were considered to study the influence of the joint on the distribution of stress and aeroelastic stability. It was observed that the rigid joint reduces the bending moment in the front wing and also satisfies all of the other criteria of the minimum strain energy, most

uniform strain energy density, and minimum level of joint reaction. Nonlinearities were not considered in the study and only linear modeling was employed under cruise flight conditions, but the study did ascertain that the fixed joint configuration is most likely the best overall choice for a joined-wing aircraft.

In other journal articles, Gallman and Kroo<sup>12,13,14,15</sup>, evaluated the weight optimization method and the fully stressed design (FSD) method to compare the direct operating cost of a conventional wing with a joined-wing design. It was determined that using a fully stressed design based on non-linear analysis produces adequate results with much less computational time than a weight optimization method. They also observed that adding a buckling criterion to the design caused the joined-wing to have a higher direct operating cost than the conventional aircraft.

Livne<sup>16</sup> presented an extensive survey of papers in the area of aeroelastic and aeroservoelastic analysis and design of joined-wing configurations. The author pointed out that possible interactions on surveillance joined-wing aircraft between antennas built into the composite lifting surfaces and the structure itself should be studied. Such interactions may involve effects on stiffness, damping and inertia of the integrated, multipurpose structure, as well as effects of antenna power consumption and heating. The key recommendation in this work is that the joined wing configuration which is a slender beam structure should be modeled as a nonlinear structure to capture the effect of large deformations. In addition, the author also recommended multidisciplinary design approach to effectively study aerodynamics and structures simultaneously.

Active Aeroelastic Wing technology<sup>17</sup> was utilized by G. Reich<sup>18</sup> et. al. which minimized deformation in the embedded antennae. Six control surfaces were

concurrently used, to minimize wing deformation and trim the aircraft for 1-g level flight. This constitutes a novel approach to minimize the deformation of structurally integrated antennas<sup>19,20</sup>. The antennas are strictly modeled as non-structural masses placed in the front and aft wings and are not load-bearing members of the structure, and therefore, the stiffness properties of the antennas are not incorporated into the design. Their research also points out that while most outboard and inboard, trailing edge control surfaces on the front wing appear to be the most effective for trimming the aircraft, all three leading edge surfaces appeared to be impractical trim devices. The results of this study show that the Active Aeroelastic Wing technology is a feasible concept for minimizing the wing deflection, and thereby minimizing the antenna deformation. This will help to keep the degradation of the antenna performance to a minimum. The current thesis is based on Reich et al. model.

Blair<sup>21,22</sup> et al. used a FSD model of a joined wing in their work and created a design process that generates reliable weight estimations of joined-wing aircraft. They wanted a design that simultaneously satisfies the range requirements, equilibrium in lift and pitching moment, and stress in static aeroelastic equilibrium. The structural and aerodynamic interface, and non-linear trim were automated using the Adaptive Modeling Language (AML) to link ASTROS, NASTRAN and PanAir into a common design environment called the Air Vehicles Technology Integration Environment (AVTIE). MSC.NASTRAN is used to investigate buckling in the wing and analyze the geometric nonlinearity of the model. The authors concluded that geometric nonlinearity is an important design consideration for a joined-wing aircraft and should be included in future

models. An effort is currently underway to incorporate this nonlinearity into the design procedure.

Today, many companies and organizations are continuing Wolkovitch's work to make the joined-wing configuration a flying reality. Lockheed Martin is working to incorporate the joined-wing design on the next generation tanker, designated as the New Strategic Aircraft, which carries more fuel and has a two-boom system, thereby allowing the Air Force to refuel more planes with fewer tankers. A radio-scaled model has flown eleven successful flights, validating Lockheed Martin's choice of the joined-wing configuration. Other companies are looking to validate the joined wing as well. NASA Langley (LaRC), in conjunction with the Boeing Military Airplane Company is working to verify Boeing's joined-wing design. Wind tunnel tests have been performed in the LaRC 16-foot transonic tunnel at Mach 0.32 to 0.9. The Boeing configuration is proposed to replace the Navy's E-2C Hawkeye.

The AFRL directorates, in partnership with the UC, and the OSU are vigorously pursuing HALE Sensorcraft joined-wing model with capabilities such as longer mission duration of seven days at high altitudes of about 60000 feet to replace the current generation Global Hawk aircraft. Complete nonlinear aeroelastic behavior of the Sensorcraft joined wing model is analyzed in order to realize this multidisciplinary concept. The aerodynamics of the Sensorcraft joined-wing configuration was effectively studied by performing CFD analysis using COBALT<sup>23</sup>. The structural response of the joined-wing is determined using four different structural modeling approaches. While the researchers at AFRL have employed ASTROS, NASTRAN and PanAir for analyzing the joined-wing model, the team at UC has used ANSYS and COBALT to perform its

analysis on joined wings. The results are then compared to ensure the correctness of the procedure.

In the first approach by Marisarla<sup>24</sup> et al, the joined-wing is modeled as a solid wing structure in order to understand its behavior using simple techniques and to ensure the correct usage of the ANSYS software. Solid tetrahedral elements are used to model the wing in ANSYS transforming it to behave like a solid wing whereas in reality a wing is a hollow shell reinforced with ribs, spars and stringers. It is assumed that the necessary stiffness is provided by the solid elements without the need for modeling complex internal reinforcements. Figure 5 shows the CAD model of the joined wing and Fig. 6 shows the finite-element mesh. The material is assumed to be an alloy of Aluminum typically used in aircraft structures (Ti-6Al-4V). Uniformly distributed pressure loads are applied on the lower surface of the wing, and the wing roots are clamped. Linear static and nonlinear static analyses are performed on this model to obtain the deflections and stresses. It is however, important to note that the pressure distribution is assumed to be uniform on the wing skin, whereas in reality it is non-uniform. Also the structural response of the joined-wing can be obtained accurately only if the wing is modeled with reinforcements instead of a solid. The solid model is thus unrealistic and over-weight.

The second approach<sup>25</sup> focuses on 1-D approximation of the actual 3-D model. The focus of this approach was to establish a procedure to perform a loosely-coupled fluid-structure analysis rather than high fidelity modeling. Beam elements are used to model the structure with the elastic axis coinciding with the aerodynamic axis of the joined-wing model. Integrated pressure loads from CFD analysis are applied to the model and a linear static analysis is performed. Resulting deformations are utilized to

obtain the actual 3-D deformed geometry using Euler-Bernoulli beam theory assumptions and other geometric considerations. The deflections are then transferred back to the 3-D model in order to recompute the aerodynamic loads. The complex webbing in the joint area where the two airfoil sections from the main and the aft wing meet creates complications in the deflection transfer process. The major drawback observed in this approach is lack of stress distribution information on the wing skin as it is a 1-D model. It is not possible to check if the failure criteria imposed on the stress distribution on the wing has been met or not.

The third model<sup>26</sup> analyzed is a reinforced shell wing which is an attempt to approach to a realistic model of the wing. The surface mesh for the structure is the same as the grid used for CFD analysis facilitating an easy load transfer process wherein the pressure loads obtained from the CFD analysis are applied to the structure directly without the need for including load interpolation routines. Ribs, spars and stringers are incorporated under the skin of the wing. The major drawback of this model is the poor element quality of the surface skin elements. Very high aspect ratios and poor element shapes are found in sizeable proportions in the model. Also, the dimensions, thicknesses and the placement of the reinforcements are arbitrary and no standard aircraft design methodology or sizing procedures are adopted. Linear and nonlinear analyses are performed by applying the fluid loads directly, without load averaging calculations or load interpolation techniques. Linear analysis exhibited a wrinkling effect on the wing surface, i.e., buckling of the skin in regions where there are no reinforcements. A nonlinear structural analysis is very sensitive to the quality of elements used, and hence the nonlinear analysis failed to progress. With the insights attained from the previous

effort another model was built but this time not considering the CFD grid same as the structural mesh. The structure is meshed with shell elements only and averaged fluid loads are applied. Linear and nonlinear analyses are performed by subjecting the structure to a range of uniformly distributed pressure loads that are normally encountered during flight conditions. The main drawback of this model is that it does not include the stringers which provide stiffening to the wing, and the ribs and spars are modeled with shell elements instead of shear panel elements. The placement and the number of the ribs and spars and their geometric properties are again arbitrary. Although fraught with drawbacks, this approach provided valuable insight, emphasizing the need for good mesh quality and, incorporating standard sizing procedures and design principles in building a wing. Currently, an effort to accomplish building a structural model for the joined wing adopting design optimization principles is ongoing in UC.

The fourth model analyzed is a computationally inexpensive, Sensorcraft box-wing model developed by Reich et al. at the AFRL which is an equivalent representation of the actual joined wing structural model. This is a fully detailed finite element model of a hollow, optimized, twin-fuselage, and twin-tail structure. This model is built using the Active Aeroelastic Wing technology. Ribs and spars are modeled as shear panel elements, and the wing skin is modeled as constant strain membranes. The stringers are incorporated in the model to provide stiffening to the entire wing structure. Provision is made to account for placement and mass of the fuel, signal processing equipment as well as VHF antennae.

AFRL used ASTROS and NASTRAN to analyze the model and designated UC to carry out the translation of the NASTRAN model into ANSYS for subsequent analyses.

A modal representation has been obtained for this model and the resulting natural frequencies and mode shapes from ANSYS have been compared with the corresponding modal analysis results generated using NASTRAN by the AFRL. This model is built by AFRL with the assumption of small deflections and hence can be considered a linear model. Nonlinear analysis is performed to validate this assumption. Due to the difference in the shape, and the grid resolution of the box-wing model compared to its corresponding aerodynamic model, the procedure for load transfer between the non-matching discrete fluid and the box-wing structure interfaces is complicated. Hence, averaged pressure loads obtained from the aerodynamic analysis are applied on the wing for linear and nonlinear analysis. Linear buckling analysis is performed by retaining the prestress effects from a linear analysis and buckling eigenvalues are determined providing buckling load factors information for future complete dynamic analyses.

### **1.3. Scope of the Present Work**

The overall objective is to study the complete nonlinear aeroelastic behavior of the joined-wing configuration by coupling the flow solver and the structural solver within the framework of a Multi Disciplinary Computing Environment (MDICE) along with a grid generator. The current work focuses on translating the NASTRAN Sensorcraft box-wing model into ANSYS and analyzing its structural response. Test cases are performed for various elements in ANSYS to compare their functionality with the corresponding elements in NASTRAN. Modal representation for various boundary conditions is obtained. Due to the assumption of small deflections, linear static analysis is performed and considered sufficient for predicting the structural response. Nonlinear analysis is performed to validate this assumption. Buckling load factors are determined by

performing linear buckling analysis of the model. A procedure is also established to determine the structural response under time varying aerodynamic loads from the CFD analysis.

## **CHAPTER 2     Mathematical Formulation**

### **2.1. Introduction**

A consistent continuum-mechanics based approach<sup>27</sup> should be employed to develop the governing finite-element equations when considering a complex problem. The standard formulation for the finite element solution of solids is the displacement method and is based on the principle of virtual work (also called principle of virtual displacements). Displacement method consists of idealizing the complete structure as an assemblage of individual structural elements. The solution of equilibrium equations of the assemblage of elements yields the element displacements which are then used to calculate element stresses.

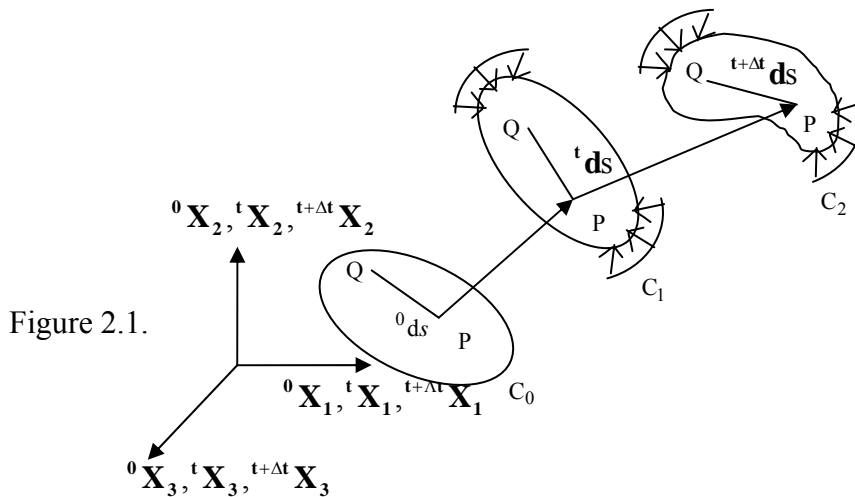
The objective of this chapter is to present the governing continuum-mechanics equations for a displacement-based finite element solution. In the following discussion, the principle of virtual work is defined and applied to a general elasticity problem. It is then used as the basis for formulating the governing continuum-mechanics equations. The discussion will progress with the definitions of suitable stress and strain measures adopted for formulation of governing equations taking nonlinearities into account. The governing finite element equations are then derived for a complex structure with nonlinearities such as large displacements and rotations, large strains and nonlinear stress-strain relationships.

### **2.2. Principle Of Virtual Work**

The principle of virtual work takes into account body motions resulting from large displacements and rotations, large strains and nonlinear stress-strain relationship. It

states that the total internal virtual work is equal to the total external virtual work for any compatible virtual displacements imposed on the body in its state of equilibrium.

Lagrangian (or material) formulation of the problem is adopted in the analysis by following the motion of all particles of the body, from the original to the final configuration of the body. The subsequent discussion mainly concerns with establishing equilibrium equations using the principle of virtual work in the Lagrangian incremental analysis approach. The motion of a general body in a stationary Cartesian coordinate system is considered. The equilibrium of the body is established by employing an incremental formulation by defining a time variable to conveniently describe the loading and the motion of the body. The aim is to evaluate the equilibrium positions of the body denoted as  $C_0, C_1, C_2, C_3, \dots$ , etc at the discrete time instants  $0, \Delta t, 2\Delta t, 3\Delta t, \dots$ , where  $\Delta t$  is an increment in time. The solutions for the static and kinematic variables for all time steps from time 0 to time  $t$ , inclusive, are assumed to have been obtained. The solution process derived in this chapter will outline the steps required for advancing the solution from time instant  $t$  to the next time instant  $t + \Delta t$ .



### 2.3. Equilibrium Equation

The equilibrium of the body in this discussion utilizes the Lagrangian incremental approach based on the principle of virtual work. It is expressed in the tensor form at time instant  $t + \Delta t$  as follows:

$$\int_{t+\Delta t V} \tau_{ij} \delta_{t+\Delta t} e_{ij} d^{t+\Delta t} V = {}^{t+\Delta t} \mathfrak{R}, \quad (2.1)$$

where

${}^{t+\Delta t} \tau_{ij}$  = Cartesian components of the Cauchy stress tensor

$\delta_{t+\Delta t} e_{ij}$  = strain tensor corresponding to virtual displacements

$\delta u_i$  = virtual displacement vector components imposed on configuration at time  $t + \Delta t$

${}^{t+\Delta t} x_i$  = Cartesian coordinated of material point at time  $t + \Delta t$

${}^{t+\Delta t} V$  = volume at time  $t + \Delta t$

and

$${}^{t+\Delta t} \mathfrak{R} = \int_{t+\Delta t V} {}^{t+\Delta t} f_i^B \delta u_i d^{t+\Delta t} V + \int_{t+\Delta t S_f} {}^{t+\Delta t} f_i^S \delta u_i^S d^{t+\Delta t} S, \quad (2.2)$$

where

${}^{t+\Delta t} f_i^B$  = components of externally applied forces per unit volume at time  $t + \Delta t$

${}^{t+\Delta t} f_i^S$  = components of externally applied surface tractions per unit surface area at time  $t + \Delta t$

${}^{t+\Delta t} S_f$  = surface at time  $t + \Delta t$  on which external tractions are applied

$\delta u_i^S = \delta u_i$  evaluated on the surface  ${}^{t+\Delta t} S_f$ .

Equation (2.1) is expressed above at time instant  $t + \Delta t$ . Since the configuration at time is unknown, Eq. (2.1) needs to be restated in terms of known configuration  $C_0$ .

Hence, appropriate stress and strain measures and constitutive relations which are defined with respect to the known configuration  $C_0$  should be adopted in Eq. (2.1). For this purpose, the following section discusses the stresses and strains which refer to the known initial undeformed configuration  $C_0$ .

## **2.4. Stress And Strain Measures**

As stated earlier, problems due to changes in the configuration of a body subjected to displacements can be resolved by using appropriate strain and stress measures and constitutive relations. Specifically, Eq. 2.1 can be expressed in terms of measures of stress and strain referred to a known configuration.

Energetically conjugate stress and strain measures are used to conserve the strain energy of the body. Cauchy stresses are energetically conjugate to actual strains, and since 2<sup>nd</sup> Piola-Kirchoff stresses and Green-Lagrange strains are an energetically conjugate pair, the former can be replaced by the latter. The following section will define and mathematically express the 2<sup>nd</sup> Piola-Kirchoff stress and the Green-Lagrangian strain, and then replace Cauchy stress and actual strain quantities in Eq. (2.1). The mathematical formulations of the stress-strain pairs are presented in greater detail in most standard finite element text books.

### **2.4.1. Cauchy Stress Tensor**

The Cauchy stress tensor, also known as the Euler stress tensor, is a natural physical concept. It is always expressed with respect to the configuration in which the stresses occur. In an incremental formulation described previously, the configuration of the body changes continuously and hence the strains are referred to the initial configuration of the body. It is therefore necessary to define the stresses with respect to

the same undeformed configuration which is not possible with Cauchy stress tensor. This can be facilitated with the usage of Second Piola-Kirchoff Stress tensor in place of the Cauchy stress tensor defined in the subsequent subsection.

### 2.4.2. Second Piola-Kirchoff Stress Tensor

The second Piola-Kirchoff stress tensor is measured in the deformed body, but referred to the reference configuration. The 2<sup>nd</sup> P-K stress tensors at  $C_2$  and  $C_1$  configurations are denoted by  ${}^{t+\Delta t}{}_0S_{ij}$  and  ${}_0^tS_{ij}$ , respectively.

The Cauchy stress tensor  ${}^{t+\Delta t}{}_0\tau_{ij}$  can be related to the 2<sup>nd</sup> P-K stress tensor  ${}^{t+\Delta t}{}_0S_{ij}$  as follows:

$${}^{t+\Delta t}{}_0S_{ij} = \frac{{}_0\rho}{{}^{t+\Delta t}\rho} \frac{\partial^0 X_i}{\partial {}^{t+\Delta t} X_m} \frac{\partial^0 X_j}{\partial {}^{t+\Delta t} X_n} {}^{t+\Delta t}\tau_{mn} = \frac{{}_0\rho}{{}^{t+\Delta t}\rho} \left[ {}^{t+\Delta t}{}_0X_{i,m} {}^{t+\Delta t}{}_0X_{j,n} {}^{t+\Delta t}\tau_{mn} \right], \quad (2.3)$$

$${}^{t+\Delta t}\tau_{ij} = \frac{{}^{t+\Delta t}\rho}{{}_0\rho} \frac{\partial {}^{t+\Delta t} X_i}{\partial^0 X_m} \frac{\partial {}^{t+\Delta t} X_j}{\partial^0 X_n} {}^{t+\Delta t}{}_0S_{mn} = \frac{{}^{t+\Delta t}\rho}{{}_0\rho} \left[ {}^{t+\Delta t}{}_0X_{i,m} {}^{t+\Delta t}{}_0X_{j,n} {}^{t+\Delta t}{}_0S_{mn} \right], \quad (2.4)$$

where  ${}_0\rho$  and  ${}^{t+\Delta t}\rho$  represent the mass densities of the material at  $C_0$  and  $C_2$ , respectively.

#### 2.4.2.1 Second Piola-Kirchoff Stress Increment

In an incremental analysis, the 2<sup>nd</sup> P-K stress tensor at  $C_2$  can be decomposed as

$${}^{t+\Delta t}{}_0S_{ij} = {}_0^tS_{ij} + {}_0S_{ij}, \quad (2.5)$$

where  ${}_0S_{ij}$  is referred to as the Kirchoff stress increment tensor.

### 2.4.3. Green-Lagrange Strain Tensor

The Green-Lagrange strain tensor is an appropriate strain tensor extremely useful in formulating the governing continuum equations including all nonlinearities such as large deformations. The internal virtual work must be expressed in terms of an integral

over a known volume. In addition, the strain measure adopted should be incrementally decomposable into linear, nonlinear, and incremental terms. Green-Lagrange strain tensor derivatives are defined with respect to the initial, known coordinates of the material particles. Also, it is a complete strain tensor, in the sense that higher-order terms are not neglected. The Green-Lagrange strain tensors  ${}^{t+\Delta t}{}_0\boldsymbol{\varepsilon}_{ij}$  and  ${}^t{}_0\boldsymbol{\varepsilon}_{ij}$  of the body at the  $C_2$  and  $C_1$  configurations, respectively, can be defined in terms of the displacement components with respect to the  $C_0$  configuration by the following formulas.

$$\begin{aligned} {}^{t+\Delta t}{}_0\boldsymbol{\varepsilon}_{ij} &= \frac{1}{2} \left[ \frac{\partial^{t+\Delta t}\mathbf{u}_i}{\partial^0x_j} + \frac{\partial^{t+\Delta t}\mathbf{u}_j}{\partial^0x_i} + \frac{\partial^{t+\Delta t}\mathbf{u}_k}{\partial^0x_i} \frac{\partial^{t+\Delta t}\mathbf{u}_k}{\partial^0x_j} \right] \\ &= \frac{1}{2} \left[ {}^{t+\Delta t}{}_0u_{i,j} + {}^{t+\Delta t}{}_0u_{j,i} + {}^{t+\Delta t}{}_0u_{k,i} {}^{t+\Delta t}{}_0u_{k,j} \right], \end{aligned} \quad (2.6)$$

$$\begin{aligned} {}^t{}_0\boldsymbol{\varepsilon}_{ij} &= \frac{1}{2} \left[ \frac{\partial^t\mathbf{u}_i}{\partial^0x_j} + \frac{\partial^t\mathbf{u}_j}{\partial^0x_i} + \frac{\partial^t\mathbf{u}_k}{\partial^0x_i} \frac{\partial^t\mathbf{u}_k}{\partial^0x_j} \right] \\ &= \frac{1}{2} \left[ {}^t{}_0u_{i,j} + {}^t{}_0u_{j,i} + {}^t{}_0u_{k,i} {}^t{}_0u_{k,j} \right], \end{aligned} \quad (2.7)$$

where it is noted that the symmetry of the tensor holds, i.e.,

$${}^{t+\Delta t}{}_0\boldsymbol{\varepsilon}_{ij} = {}^{t+\Delta t}{}_0\boldsymbol{\varepsilon}_{ji}, \quad (2.8)$$

and

$${}^t{}_0\boldsymbol{\varepsilon}_{ij} = {}^t{}_0\boldsymbol{\varepsilon}_{ji}. \quad (2.9)$$

### 2.4.3.1 Green Strain Increment

In an incremental formulation, the difference between the strains  ${}^{t+\Delta t}{}_0\boldsymbol{\varepsilon}_{ij}$  and  ${}^t{}_0\boldsymbol{\varepsilon}_{ij}$  at time  $t$  and  $t + \Delta t$  is defined as the Green strain increment tensor  ${}_0\boldsymbol{\varepsilon}_{ij}$ :

$${}_0\boldsymbol{\varepsilon}_{ij} = {}^{t+\Delta t}{}_0\boldsymbol{\varepsilon}_{ij} - {}^t{}_0\boldsymbol{\varepsilon}_{ij}. \quad (2.10)$$

By substituting Eqs. (2.6), and (2.7) into Eq. (2.10), we can write

$${}_0\varepsilon_{ij} = {}_0e_{ij} - {}_0\eta_{ij}, \quad (2.11)$$

where  ${}_0e_{ij}$  are the linear components:

$$\begin{aligned} {}_0e_{ij} &= \frac{1}{2} \left[ \frac{\partial u_i}{\partial^0 x_j} + \frac{\partial u_j}{\partial^0 x_i} + \frac{\partial^t u_k}{\partial^0 x_i} \frac{\partial u_k}{\partial^0 x_j} + \frac{\partial u_k}{\partial^0 x_i} \frac{\partial^t u_k}{\partial^0 x_j} \right] \\ &= \frac{1}{2} [{}_0u_{i,j} + {}_0^t u_{j,i} + {}_0^t u_{k,i} {}_0u_{k,j} + {}_0u_{k,i} {}_0^t u_{k,j}], \end{aligned} \quad (2.12)$$

and  ${}_0\eta_{ij}$  are the nonlinear components:

$${}_0\eta_{ij} = \frac{1}{2} \frac{\partial u_k}{\partial^0 x_i} \frac{\partial u_k}{\partial^0 x_j} = \frac{1}{2} [{}_0u_{k,i} {}_0u_{k,j}]. \quad (2.13)$$

Now that the relations between  ${}^{t+\Delta t}\tau_{ij}$  and  ${}^{t+\Delta t}{}_0S_{ij}$  are established, the reference configuration of the virtual work equation Eq. (2.16) can be restated in terms of the known configuration  $C_0$ :

$$\int_{{}^{t+\Delta t}V} {}^{t+\Delta t}\tau_{ij} \delta_{{}^{t+\Delta t}} e_{ij} d{}^{t+\Delta t}V = \int_{{}^0V} {}^{t+\Delta t}{}_0S_{ij} \delta_{{}^{t+\Delta t}} \varepsilon_{ij} d^0V, \quad (2.14)$$

$$\therefore \int_{{}^0V} {}^{t+\Delta t}{}_0S_{ij} \delta_{{}^{t+\Delta t}} \varepsilon_{ij} d^0V = {}^{t+\Delta t}\mathfrak{R} \quad (2.15)$$

The virtual work equation is by itself a nonlinear equation of equilibrium for the body under consideration. Though the reference has been changed from the current configuration  $C_2$  to the initial configuration  $C_0$ , the equation remains an exact statement of equilibrium for the structure under consideration. It can be used as a valid basis for deriving the incremental nonlinear equations in the total Lagrangian formulation. On substitution of Eqs. (2.11), and (2.13) in Eq. (2.15), we obtain

$$\int_{^0V} {}^0S_{ij} \delta_0 \varepsilon_{ij} d^0V + \int_{^0V} {}^tS_{ij} \delta_0 \eta_{ij} d^0V = {}^{t+\Delta t}{}^0\mathfrak{R} - {}^t{}^0\mathfrak{R} \quad (2.16)$$

where  ${}^t{}^0\mathfrak{R}$  is defined as

$${}^t{}^0\mathfrak{R} = \int_{^0V} {}^tS_{ij} \delta_0 e_{ij} d^0V. \quad (2.17)$$

## 2.5. Incremental Constitutive Law

For total Lagrangian formulation, the constitutive law can be expressed in terms of the Kirchoff stress increment tensor  ${}^0S_{ij}$ , the Green strain increment tensor  ${}^0\varepsilon_{ij}$  as incremental constitutive law:

$${}^0S_{ij} = {}^0C_{ijrs} \varepsilon_{rs}, \quad (2.18)$$

where  ${}^0C_{ijrs}$  denotes the incremental constitutive tensor with respect to the C0 configuration and us given as

$${}^0C_{ijrs} = \lambda \delta_{ij} \delta_{rs} + \mu (\delta_{ir} \delta_{js} + \delta_{is} \delta_{jr}). \quad (2.19)$$

Also,  $\lambda$  and  $\mu$  are Lamé constants and can be expressed as

$$\lambda = \frac{Ev}{(1+\nu)(1-2\nu)}, \quad \mu = \frac{E}{2(1+\nu)}, \quad (2.19a)$$

where  $\nu$  = Poisson's ratio,

and Kronecker delta  $\delta_{ij} = \begin{cases} 0; & i \neq j \\ 1; & i = j \end{cases}$ .

Equation (2.16) can now be written as

$$\int_{^0V} {}^0C_{ijrs} \varepsilon_{rs} \delta_0 \varepsilon_{ij} d^0V + \int_{^0V} {}^tS_{ij} \delta_0 \eta_{ij} d^0V = {}^{t+\Delta t}{}^0\mathfrak{R} - {}^t{}^0\mathfrak{R}. \quad (2.20)$$

Equations (2.16) and (2.20) cannot be solved directly, since they are nonlinear in displacement increments  $u_i$ . An incremental formulation of the equilibrium equations leading to an approximate solution is presented in the following section.

## 2.6. Incremental Equilibrium Equation

If the strain increments can be considered small within each incremental step, approximate solutions can be obtained by making the following assumption:

$$\delta_0 \epsilon_{ij} = \delta_0 e_{ij} \quad (2.21)$$

Accordingly, Eq. (2.20) reduces to

$$\int_{0V} C_{ijkl} e_{kl} \delta_0 e_{ij} d^0V + \int_{0V} S_{ij} \delta_0 \eta_{ij} d^0V = {}^{t+\Delta t} \mathfrak{R} - {}^t \mathfrak{R} \quad (2.22)$$

where

$${}^{t+\Delta t} \mathfrak{R} = \int_{0V} {}^{t+\Delta t} f_i^B \delta u_i d^0V + \int_{0S_r} {}^{t+\Delta t} f_i^S \delta u_i^S d^0S \quad (2.23)$$

Equation (2.22) is the linearized version of the Eq. (2.20) of the motion of the body from C1 to C2 with reference to the axes at the initial undeformed configuration C0.

The assumed loading, (i.e., body forces and surface tractions) is deformation-independent and limited to certain loading types such as concentrated loading that does not change its direction as a function of deformation.

The external virtual work is now assumed as deformation-dependent and sufficiently small load (time) step is considered. Using the loading intensity corresponding to time  $t + \Delta t$ , and integrating over volume and area last, the external virtual work due to body forces  $f_i^B$  and surface tractions  $f_i^S$  can be approximated as:

$$\int_{t+\Delta t}^{} \mathbf{f}_i^B \delta \mathbf{u}_i \, d^{t+\Delta t} \mathbf{V} = \int_{t+\Delta t}^{} \mathbf{f}_i^B \delta \mathbf{u}_i \, d^{t+\Delta t} \mathbf{V} \quad (2.24)$$

$$\int_{t+\Delta t}^{} \mathbf{f}_i^S \delta \mathbf{u}_i^S \, d^{t+\Delta t} \mathbf{S} = \int_{t+\Delta t}^{} \mathbf{f}_i^S \delta \mathbf{u}_i^S \, d^{t+\Delta t} \mathbf{S} \quad (2.25)$$

An important loading condition that must be included with Eq. (2.22) is the inertia force loading in dynamic analyses. Hence, the mass effects are taken into consideration, and mathematically represented as:

$$\int_{t+\Delta t}^{} \rho \, {}^{t+\Delta t} \ddot{\mathbf{u}}_i \delta \mathbf{u}_i \, d^{t+\Delta t} \mathbf{V} = \int_0^{} \rho \, {}^{t+\Delta t} \ddot{\mathbf{u}}_i \delta \mathbf{u}_i \, d^0 \mathbf{V} \quad (2.26)$$

The final form of the incremental equilibrium equation with inertia effects is as follows:

$$\int_0^{} \rho \, {}^{t+\Delta t} \ddot{\mathbf{u}}_i \delta \mathbf{u}_i \, d^0 \mathbf{V} + \int_0^{} \mathbf{C}_{ijkl} \, \delta_0 \mathbf{e}_{kl} \delta_0 \mathbf{e}_{ij} \, d^0 \mathbf{V} + \int_0^{} \mathbf{S}_{ij} \delta_0 \eta_{ij} \, d^0 \mathbf{V} = {}^{t+\Delta t} \mathfrak{R} - {}^t \mathfrak{R} \quad (2.27)$$

The following section discusses the procedure of discretizing the governing equations of the continuum derived above using the finite element method.

## 2.7. Discretized Finite Element Form

The finite element equations are now derived in this section by approximating the body as an assemblage of discrete finite elements interconnected at nodal points on the element boundaries. The finite element equations for linear static, linear dynamic, modal, and nonlinear static problems are derived in the following sections.

It is assumed that the displacements within each element are a function of the displacements at the  $n$  finite element nodal points, i.e., the nodal d.o.f. For an element  $m$ ,

$$\mathbf{u}^{(m)} = \mathbf{N}^{(m)} \hat{\mathbf{U}}, \quad (2.27)$$

where

$N^{(m)}$  = the shape-function (displacement interpolation) matrix which is dependent on the element type and order

$m$  = superscript denoting element  $m$

$\hat{U}$  = vector of the three global displacement components  $U_i$ ,  $V_i$ , and  $W_i$  at all nodal dof

The corresponding element strain matrix can be also expressed as

$$\varepsilon^{(m)} = B^{(m)} \hat{U}, \quad (2.28)$$

where  $B^{(m)}$  is the strain-displacement matrix whose row entries are obtained by appropriately differentiating and combining the rows of matrix  $N^{(m)}$ . Substituting Eq. (2.27) and (2.28) in the final incremental equation leads to effective assemblage process of all element matrices into the governing structure matrices presented subsequently.

For case of a nonlinear analysis, the incremental formulation of the continuum equations derived in the previous section is used to arrive at the discretized finite element form.

$$\int_{0V} \rho \, {}^{t+\Delta t} \ddot{u}_i \delta u_i d^0V + \int_{0V} C_{ijkl} e_{kl} \delta_0 e_{ij} d^0V + \int_{0V} {}^t S_{ij} \delta_0 \eta_{ij} d^0V = {}^{t+\Delta t} \mathfrak{R} - {}^t \mathfrak{R}, \quad (2.22)$$

$$\text{where } {}^{t+\Delta t} \mathfrak{R} = \int_{0V} {}^{t+\Delta t} f_i^B \delta u_i d^0V + \int_{0S_f} {}^{t+\Delta t} f_i^S \delta u_i^S d^0S.$$

Use of Eqs. (2.27) and (2.28) in the Eq. (2.22) leads to the discretized nonlinear finite element form is as follows:

$$\begin{aligned} & \left( \int_{0V} \rho N^T N d^0V \right) {}^{t+\Delta t} \ddot{\mathbf{u}} + \left[ \left( \int_{0V} {}^t B_{L0}^T C_0^t B_L d^0V \right) + \left( \int_{0V} {}^t B_{NL0}^T {}^t S_0^t B_{NL} d^0V \right) \right] \hat{\mathbf{u}} \\ & = \int_{0V} N^T {}^{t+\Delta t} \mathbf{f}^B d^0V + \int_0 N^{ST} {}^{t+\Delta t} \mathbf{f}^S d^0S - \int_{0V} {}^t B_{L0}^T \hat{\mathbf{S}} d^0V, \end{aligned} \quad (2.29)$$

where  ${}^t \hat{\mathbf{S}}$  is the 2nd Piola-Kirchoff stress vector, which will be defined for each element.

In the Eq. (2.29) the inertia forces are taken into consideration along with nonlinearities.

Denoting the time independent mass matrix as  $M$ , Eq. (2.47) can be written in a compact form as follows,

$$M {}^{t+\Delta t}\ddot{U} + \left( {}^t_0K_L + {}^t_0K_{NL} \right) U = {}^{t+\Delta t}R - {}^t_0F, \quad (2.30)$$

where

$${}^t_0K_L = \left( \int_{{}^t_0V} {}^t_0B_L^T C_0^t B_L d^0V \right) = \text{linear stiffness matrix,}$$

$${}^t_0K_{NL} = \left( \int_{{}^t_0V} {}^t_0B_{NL}^T {}^t_0S_0^t B_{NL} d^0V \right) = \text{nonlinear stiffness matrix,}$$

$${}^{t+\Delta t}R = \int_{{}^t_0V} N^T {}^{t+\Delta t}f^B d^0V + \int_{{}^t_0V} N^{S^T} {}^{t+\Delta t}f^S d^0S. = \text{externally applied load vector at } t + \Delta t,$$

$${}^t_0F = \int_{{}^t_0V} {}^t_0B_L^T \hat{S} d^0V = \text{nodal force vector equivalent to the elements stresses at time } t.$$

$$M {}^{t+\Delta t}\ddot{U} = \left( \int_{{}^t_0V} \rho N^T N d^0V \right) {}^{t+\Delta t}\ddot{u} = \text{mass matrix due to inertia effects.}$$

Equation (2.30) is the finite element equation for geometrically nonlinear problem with inertia effects. The solution to such an equation should be approached iteratively. An incremental solution procedure such as the Newton-Raphson technique is widely used for obtaining nonlinear solutions.

For a linear static problem free of inertia effects, the nonlinear stiffness matrix terms drop out due to the assumption of small displacements, and the final discretized equation is simplified to be:

$$KU = R, \quad (2.31)$$

where the load vector  $R = R_B + R_S - R_I + R_C$ .

The matrix  $K$  is the stiffness matrix of the entire element assemblage denoted by

$$K = \int_V B^T C B dV. \quad (2.32)$$

The load vector  $R$  includes the effect of the element body forces,

$$R_B = \int_V N^T f^B dV, \quad (2.33)$$

the effect of the surface forces,

$$R_S = \int N^{ST} f^S dS, \quad (2.34)$$

the effect of the initial stresses,

$$R_I = \int_V B^T \tau^I dV, \quad (2.35)$$

and the nodal concentrated loads  $R_C$ .

The above matrix equation is a system of simultaneous algebraic equations to be solved for nodal d.o.f. Equation (2.31) is a statement of static equilibrium of the element assemblage at any specific point in time where the applied forces and hence the displacements do not vary with time or vary slow enough to neglect the dynamic effect.

In the static case, loads are assumed to be constant or slowly varying with respect to time and do not change significantly during the time taken for the displacement or stress perturbation to reach the most distant point in the body. For a quasistatic problem the effects of inertia can be neglected, when the frequency of excitation applied to the structure is less than one-third of the structure's lowest natural frequency. The equation  $KU = R$  is sufficiently accurate, even though the loads vary slowly with time.

Inertia has significant effect in structural dynamics problems in case of higher excitation frequencies. In such cases, inertia effects can be accounted by incorporating the mass in the equations governing the dynamic response. The effects of structural

damping should also be taken into account in structural dynamics problems where applicable.

The dissipated energy during vibration in actually measured dynamic responses of structures is accounted by introducing velocity-dependent damping forces as additional contributions to the body forces,

$$R_B = \int_V N^T [f^B - \rho N \ddot{U} - \kappa N \dot{U}] dV , \quad (2.36)$$

where the vector  $f^B$  no longer includes inertia and velocity-dependent damping forces,  $\dot{U}$  is a vector of the nodal point velocities and  $\kappa$  is the damping property parameter. The equilibrium equations in this case are,

$$M\ddot{U} + C\dot{U} + KU = R , \quad (2.37)$$

where  $C$  is the damping matrix of the structure;

$$C = \int_V \kappa N^T N dV . \quad (2.38)$$

The usual first step in performing a dynamic analysis is determining the natural frequencies and mode shapes of the structure with damping neglected. These results characterize the basic dynamic behavior of the structure and are an indication of how the structure will respond to dynamic loading and provide enough information to make design decisions. If a natural frequency of the structure is close to an excitation frequency, then severe vibration of the structure resulting in resonance could occur. This condition is called resonance and to avoid resonance, the natural frequencies of the structure must be altered by making design changes. The solution for undamped natural frequencies and mode shapes is called real eigenvalue analysis or normal modes analysis. Decisions regarding subsequent dynamic analyses (i.e., transient response, frequency response, response spectrum analysis, etc.) can be based on the results of a natural

frequency analysis. The important modes can be evaluated and used to select the appropriate time or frequency step for integrating the equations of motion.

For a freely vibrating structure with no external excitation, Eq. (2.37) reduces to

$$M\ddot{U} + KU = 0 \quad (2.39)$$

Such a structure undergoes harmonic motion in which each d.o.f moves in phase with all other d.o.f. The solution to such a problem has a simple, real, periodic form

$$U = \Phi \sin \omega t \quad , \quad (2.40)$$

and

$$\ddot{U} = -\omega^2 \Phi \sin \omega t \quad . \quad (2.41)$$

Applying Eq. 2.31 and Eq. 2.32 in Eq. 2.30, we get

$$(K - \omega^2 M)\Phi = 0 \quad . \quad (2.42)$$

Equation 2.35 is valid only for certain values of  $\omega$  for which the determinant of the matrix in parenthesis is zero.

$$\det|K - \omega^2 M| = 0 \quad . \quad (2.43)$$

For a determinant of order  $n$  (with matrices of size  $n \times n$ ), in general  $n$  real roots exist. These give the natural angular frequencies of the system and the problem is referred to as an eigenvalue problem. The lowest nonzero  $\omega_1$  is called the fundamental vibration frequency.

The mathematical formulation of the equation and its finite element discretized form for a complex structure with nonlinearities such as large displacements and rotations, large strains and nonlinear stress-strain relationships is presented in this chapter. Finite element formulations for linear, nonlinear, dynamic and modal analyses

are presented in detail. Finite element modeling and analyses of Sensorcraft Joined-wing model are discussed in Chapter 3.

## **CHAPTER 3      Finite Element Modeling and Analysis of Sensorcraft Box-Wing Model**

This chapter discusses the general principles in aircraft wings construction, the background of the current work, the description of the box-wing finite element model, validation tests conducted to verify the accuracy of translation of the box-wing model from NASTRAN to ANSYS, loads and boundary conditions used for modal, linear, nonlinear, eigenvalue buckling and dynamic structural analyses performed on the wing.

### **3.1. General Principles of Aircraft Wing Design**

An aircraft structure's basic functions are transmission and resistance of the applied loads, providing an aerodynamic shape, sustaining the environmental conditions encountered in the flight. These requirements result in thin shell structures whose outer surface is usually supported by longitudinal stiffening members (rods or stringers) and transverse frames to enable resistance to bending, compressive and torsional loads without buckling. Such structures are termed as semi-monocoque structures as compared to monocoque structures which rely entirely on their skins for their capacity to resist loads.

A typical aircraft wing constitutes an arrangement of ribs, spars, stiffener rods and encompassing outer wing skin. A brief discussion of the wing structural components is presented here.

The primary function of the ribs is to maintain the shape of the wing cross-section for all load conditions. Ribs also act with the wing skin in resisting the distributed aerodynamic pressure loads and distribute the concentrated loads due to wing stores and

undercarriage to the structure. The dimensions of the ribs are governed by their span-wise location and the loads required to be supported. For instance, at the sections closer to the wing root, the requirement is to absorb and transmit large concentrated loads such as those from the undercarriage, engine thrust and fuselage attachment point reactions, thus necessitating thicker and sturdier ribs.

Wing skin forms an impermeable surface for supporting the aerodynamic pressure distribution and results in lift of the wing. Also, the wing skin transmits the aerodynamic forces to the ribs, spars and stiffener rods by plate and membrane action. Resistance to shear and torsional loads is supplied by shear stresses developed in the skin and spars, while axial and bending loads are resisted by the combined action of the skin and the stiffener rods.

The role of the stiffener rods also known as stringers is to reinforce the wing and help in reducing the weight penalty. Good resistance to shear loads and tensile loads can be obtained by adopting a thin wing skin, but this advantage is offset by danger of buckling under comparatively low compressive loads. Increasing the wing thickness poses the consequence of weight penalty. The stiffener rods attached to the skin and ribs provide the necessary stabilizing action by increasing resistance to the buckling and failing stresses. As mentioned previously, the combined action of skin and stiffener rods resists the axial and bending loads.

The spars exert similar stabilizing influence on the wing skin in a similar manner to the stiffener rods. The primary function of the spar webs is to develop shear stresses to resist shear and torsional loads. Along with the wing skin the spars stabilize the spar

flanges or caps which are capable of supporting large compressive loads due axial and bending effects.

In the construction of aircrafts, the wing ribs and spars are reinforced with stiffener rods. These elastic sheets stiffened with rods are idealized by lumping the normal stress-resisting properties into stiffener rods and the shear-resisting properties of the sheet into shear panels. Hence the spars and ribs are modeled with shear panel elements which resist the action of tangential forces and not the normal forces.

In some aircraft, the larger compartments of the wings are used as fuel tanks. The current generation of aircrafts favors all-metal construction and cantilever wing configurations. The design of a particular depends upon many factors for example, size, weight, use of the aircraft, desired landing speed, and desired rate of climb.

### **3.2. Sensorcraft Joined Wing Design**

The current study is based on a wing design model which represents a significant departure from traditional aircraft design philosophy. A conceptual design study is hence necessary in order to identify the current and future technologies required for a sensorcraft vehicle to perform the unmanned aerial vehicle (UAV) intelligence, surveillance and reconnaissance (ISR) mission. The mission requirements include 3000-n mile radius combined with a 40-h loiter period, which represents a 150% increase in mission radius and 67% increase in time on station compared to the Global Hawk.

The joined wing design with dual, offset fuselages configuration meets the requirement of 360-degree radar coverage. The vehicle conceptual design created is aimed to meet all the UAV ISR requirements as well as sensor requirements. Reich et al

researched on Sensorcraft air vehicle which is designed around the antennas, and all of the performance requirements were driven by antenna requirements.

Reich's Sensorcraft model incorporates both vhf (a long wire) and X-band (flat phased-array panels) antennas. The vhf antenna operates at a sufficiently low frequency to be unaffected by deformations, on the other hand, the deformation of the X-band antenna is potentially great enough to significantly reduce its performance. The motivation for their study is the deformation of the X-band panels that are attached to the wing box. This wing-box model termed as the Sensorcraft In-house Model is an equivalent representation of the Joined wing configuration.

Active-Aeroelastic-Wing (AAW) concept was employed which demonstrated performance benefits from multiple control surfaces and in particular the reduction of antenna deformations in a joined-wing sensorcraft configuration, for antenna performance improvements. The trim optimization study carried out using ASTROS code resulted in minimization of the structural elastic deformations at structural nodes corresponding to the antennas. Huttshell et al from AFRL translated the ASTROS model into NASTRAN and carried out modal analysis for three boundary conditions.

The current research focuses on the translation of Reich's box-wing model from NASTRAN to ANSYS, as part of the AFRL -DAGSI proposed tasks for UC in the Joined wing project.

### **3.3. Finite Element Model Description**

The Sensorcraft box-wing model was developed for multi-control surface trim optimization, based on the AFRL/VA In-House Technical Assessment of a vehicle to meet the UAV/ISR mission requirements.

The finite element model of the box-wing, shown in Fig. X, is a half-span model of the dual-fuselage, joined-wing sensorcraft vehicle. The box-wing model is an “equivalent” representation of the complete wing.

The span of this symmetric thin-walled box-wing model is 122.86 ft and the chord is 3.35 ft. The top and bottom wing skin panels are designed on a per panel basis, where each panel is constrained by two spars and two ribs. Wing skins are considerably thicker at the joint and at the roots to accommodate high stress concentrations. Similarly, the spars at the roots of the wing and at the joint region are thicker compared to those in other regions.

The wing skin on the main and the aft wing-boxes is modeled with CQUAD4 membrane elements in NASTRAN and SHELL63 elements in ANSYS. The wing skin at the joint region is modeled with triangular membrane elements. The default options for SHELL63 element includes both bending and membrane actions. Hence the key options need to be set in order for the element to act as a membrane in ANSYS. The minimum gauge thickness of the wing skin is 0.00313 ft. The skins of both main and aft wings from the root out to the fuselage are optimized to have larger than the minimum gauge thickness (0.00781 ft.) in order to resist the stresses generated at the constrained roots.

The shear panel elements serve as the wing spars and ribs in the box-wing model; CSHEAR is the shear panel element in NASTRAN and SHELL28 is the corresponding element in ANSYS. The SHELL28 element in ANSYS has both shear panel and twist panel options and for the present study, the shear panel option was selected. The minimum gauge thickness of the spars and webs is 0.00104 ft except for the spars and

ribs located from the wing roots to the fuselage which are designed to have larger than minimum gauge thickness of 0.0026 ft.

The stiffener rods (stringers) which reinforce the box-wing are modeled with rod elements. CROD element in NASTRAN is translated as tension-compression LINK8 element in ANSYS.

The fuselage and the tail are modeled at about 30 feet from the centerline of the aircraft. The symmetry of the aircraft permits modeling only half-span of the total aircraft. The off-center fuselage is represented by beam elements with large cross-sectional area of 0.3913 ft<sup>2</sup>. The beam elements represented by CBAR in NASTRAN are translated as BEAM4 elements in ANSYS. The rear fuselage is connected to the aft wing with a vertical tail structure modeled with beam elements with cross-sectional area of 0.2997 ft<sup>2</sup>. The elements used to model the tail structure in NASTRAN and ANSYS are same as that of the fuselage elements.

The antennas are modeled as nonstructural masses along the main and aft wings themselves, as the antennas are not assumed to contribute significant stiffness to the spars on which they are mounted. The avionics and sensor electronics, landing gear, engines, and fuel are also accounted by nonstructural mass elements. According to Reich et al., the physical placement of these items is based on stability and control c.g. calculations made by the technology assessment team. The CONM2 mass elements in NASTRAN are translated into MASS21 elements in ANSYS with six degrees of freedom. The value of the masses which account for the account for the signal processing equipment, VHF antennae, X-Band, fuel, etc. are specified.

The corresponding aerodynamic model for the box-wing model is a two-dimensional panel model. A high-fidelity full 3-D aerodynamic model is analyzed at UC and as such the low-fidelity 2-d aerodynamic panel model is not studied at UC for the Joined wing project. The nodes shown on the leading and trailing edges of the box-wing model are non-structural and are included only to transfer aerodynamic loads from the aerodynamic analysis to the structural analysis. The load transfer is done using rigid body elements (RBE1) that do not add stiffness to the finite element model. Constraint equations (CE) are adopted in ANSYS to account for the RBE1s in the NASTRAN model.

### **3.4. Material Properties**

The wing material adopted for analysis is generic aircraft type aluminum with Young's Modulus  $144e07 \text{ lbf/ft}^2$ , Poisson's ratio 0.28 and density  $5.37 \text{ slug/ft}^3$ . This material has excellent mechanical properties such as high strength and lightweight, and is ideal for Sensorcraft airframe construction.

### **3.5. Validation Tests**

A number of validation tests which have direct bearing on the problem at hand are conducted using NASTRAN and ANSYS codes. These exercises led not only to a more complete understanding of working and features of the codes but also helped in bringing to light the differences and commonalities between the two codes. The NASTRAN model of the box-wing obtained from AFRL essentially consists of nonstructural masses, membranes, shear panels, stiffener rods, beams and rigid body elements for the purpose of performing modal analysis. The validation tests conducted in both the codes

specifically target these elements for achieving the present goal of finding differences if any between both codes.

### **3.5.1. Modal Analysis of beam modeled with shear panels**

The present validation test is adopted from the text book ‘Formulas for natural frequency and mode shape’ in order to verify the functionality of the shear panel elements in NASTRAN and ANSYS codes. A thin-walled uniform beam with square cross-section is modeled with SHELL 28 elements in ANSYS and CSHEAR elements in NASTRAN respectively. The length, width and thickness dimensions are assumed to be 30 m, 10 m and 0.01 m respectively. The material properties include Young’s Modulus of 200 GPa, Poisson’s ratio of 0.27 and density of 7860 Kg/m<sup>3</sup>. The beam is clamped at the base and is allowed to freely vibrate. The flexural deformations are eliminated by coupling the X and Y degrees of nodes with the same z-coordinate. Modal analysis performed on the model with Block Lanczos extraction and the first five modes of vibration are obtained from NASTRAN and ANSYS. It is observed that the frequencies obtained from NASTRAN and ANSYS match closely.

### **3.5.2. Modal Analysis of beam modeled with shell elements**

A hollow beam of span length 65 ft, width 3.35 ft and thickness 1.5 ft is modeled in ANSYS with SHELL63 elements. A corresponding model is built in NASTRAN with CSHEAR elements. The cross-sectional area of the shell is 0.00781 sq.ft. Material properties of the beam include Young’s Modulus 144E07 lbf/sq.ft., density 5.37 slug/cu.ft., and a Poisson’s ratio of 0.28. The beam is cantilevered by constraining the four nodes of one end all degrees of freedom. The entire model is rotationally constrained. Block Lanczos extraction method is adopted for extracting the first five

modes for comparison of the results from the two codes. It is observed that the natural frequencies match closely between the two codes.

### 3.5.3. Modal Analysis of fuselage modeled with beam elements

The test cantilever beam has the same length and cross sectional properties as the box-wing fuselage beam elements. The longitudinal axis of the beam coincides with the global x-axis. The geometric properties of the beam are summarized in Table 4.2. In the actual joined wing, one end of the fuselage is connected to a trailing edge point of the front wing by RBE1 elements, and the other end is connected to the vertical tail. For this test case, the tail section is ignored, and one end of the beam is clamped, while the other end is free.

The fuselage and tail section of the box-wing are modeled with 20 CBAR elements in NASTRAN. The corresponding ANSYS model used BEAM4 elements. The material chosen has the following properties: Young's Modulus  $144E7$  lbf/ft<sup>2</sup>, Poisson's ratio 0.28 and density 5.37 slug/cu.ft. The cross-sectional area of the beam is assumed to be 0.3913 ft<sup>2</sup>. Modal analysis is performed with Block Lanczos Extraction method using both codes and the first five mode shapes are extracted.

**Table 4.2. Geometric Properties of Cantilever Beam Model**

<b>Property</b>	<b>Value</b>
<b>Length</b>	50 ft
<b>Cross Sectional Area</b>	0.3913 ft <sup>2</sup>
<b>Moment of Inertia <math>I_{YY}=I_{ZZ}</math></b>	1.7485 ft <sup>4</sup>
<b>Mass per unit length</b>	2.952 lb/ft

#### **3.5.4. Linear Static Analysis of a 2-D truss modeled with rods**

The stiffener rods, also cited as stringers in the aircraft terminology form the reinforcements for the wing skin, ribs and spars. These rods encompass the normal stress-resisting properties of the wing. CRODS were used to represent the tension-compression rods with three degrees of freedom at each node in NASTRAN and LINK8 elements in ANSYS. Geometric properties include rod area of cross section of 4 sq. inch. The material assumed for this case has the Young's Modulus 30E6 lbf/in<sup>2</sup>, and Poisson's ratio 0.3. Clamped boundary conditions are applied for nodes 1 and 2 and the loading consists of a force of 1000 lbf acting on node 4. The resultant displacements match satisfactorily between NASTRAN and ANSYS.

#### **3.6. NASTRAN FE Model Translation into ANSYS**

The NASTRAN finite element model of the box-wing is translated into ANSYS as part of the AFRL -DAGSI proposed tasks for UC. NASTRAN modal analysis results for three cases, namely, Symmetric Case, Clamped Case, Rigidly Clamped Case (Larry Huttshell, AFRL: Private Communication) are used to verify the corresponding modal analysis results obtained from the translated ANSYS box-wing model. Differences were observed in the natural frequencies obtained from NASTRAN and ANSYS codes.

The validation tests conducted helped in determining the accuracy of the translation of various NASTRAN elements into corresponding ANSYS elements. The membranes, shear panels, stiffener rods and the fuselage beams were found to be accurately modeled in ANSYS giving identical results with their NASTRAN counterparts.

### **3.7. Structural Analyses of Sensorcraft Box-Wing Model**

The structural behavior of the box-wing model is evaluated by performing modal, linear, eigenvalue buckling and dynamic analyses in ANSYS discussed subsequently. It should be noted that the rotational degrees of freedom are arrested throughout the model in all these analyses. The results from the following structural analyses are presented and discussed in Chapter 4.

#### **3.7.1. Modal Analysis**

Modal analysis is performed to determine the natural frequencies and mode shapes of the box-wing model. The wing subjected to unsteady aerodynamic loads may be prone to failure due to resonance if its natural frequency coincides with the frequency of the loading. Modal analysis serves as a precursor to future comprehensive dynamic analysis on the joined-wing model.

Modal analysis is performed on the box-wing model for three different cases of boundary conditions.

##### **3.7.1.1 Symmetric Case**

The Sensorcraft is modeled as twin-fuselage aircraft, where the fuselage is not located at the roots of the main and aft wings but is offset by 30 feet from the plane of symmetry as shown in Fig. 8. For this case, symmetry boundary conditions are enforced along the centerline by disallowing y-displacement. The wing roots are constrained in all degrees of freedom except plunging and pitching degrees of freedom in the Z-direction translation ( $U_Z$ ) and Y-direction rotation ( $\theta_Y$ ). Block-Lanczos algorithm is used for extracting the first five modes. The first two modes obtained are rigid body modes and the rest are flexible modes.

### **3.7.1.2 Clamped Case**

For the modal analysis case with clamped boundary conditions, the main and aft wing roots are constrained in all degrees of freedom except the Z-direction translation ( $U_z$ ). The analysis is performed using Block Lanczos extraction method to extract the first five modes. The modal results from NASTRAN and ANSYS codes are compared.

### **3.7.1.3 Rigidly Clamped Case**

For the modal analysis case with rigidly clamped boundary conditions, the aft wing roots are constrained in all degrees of freedom and the main wing roots are constrained in all degrees of freedom except the Z-direction translation ( $U_z$ ). The first five mode shapes and frequencies are extracted using the Block Lanczos extraction method and the results are compared with the corresponding NASTRAN analysis results.

Modal analysis results from NASTRAN and ANSYS differ and the cause of differences was determined due to differences in the RBE1 and CE functionalities in NASTRAN and ANSYS codes respectively. In the NASTRAN model, rigid body elements (RBE1) are used to define and model the rigid connections from leading-edge and trailing-edge end points to the structural wing box in order to interpolate and transfer the loads and deflections between the structural model and the aerodynamic model. RBE1 elements are also utilized in the NASTRAN model to connect the fuselage to the main wing.

To understand the exact nature of the differences in the results the box-wing model was run with the following variations in both NASTRAN and ANSYS. The results comparison from these analyses and the key observations are presented in the Chapter 4.

### **3.7.2. Linear Static Analysis**

Following the modal analyses for clamped, rigid and symmetry boundary conditions, a linear static analysis is performed to study the response of the wing in terms of deflections and stresses. Even though linear static analysis was not one of the requirements of the AFRL, the analysis is still performed to understand the behavior of the structure under static pressure loading. For this analysis, the aerodynamic loads from the CFD analysis corresponding to the case Mach = 0.4,  $\alpha = 0^\circ$ , and altitude = 60,000 feet are considered. The integrated value of the discrete pressure loads on the upper and lower surfaces of the wing is divided by the surface of the wing and applied as pressure loads on the upper and lower surfaces of the wing. The upper surface of the wing is subjected to a pressure load of 104 lbf/in<sup>2</sup> and on the lower surface, a pressure load of 125 lbf/in<sup>2</sup> is applied. The main and aft wing roots clamped in all degrees of freedom form the boundary conditions for this analysis.

The same loading and boundary conditions as in the case of linear static analysis are adopted to perform nonlinear static analysis on the box-wing model in order to test the small-deformation theory the model is based on. Effect due to geometric nonlinearity is accounted by turning on the large deformation option in ANSYS. The results from the linear and nonlinear static analysis are discussed in next chapter.

### **3.7.3. Linear Buckling Analysis**

Linear (eigenvalue) buckling analysis is performed in order to calculate the eigenvalues and buckling mode shapes of the structure. The buckling eigenvalues represent buckling load factors which are useful in calculating the critical buckling loads.

It is valuable to know the critical buckling loads for a slender structure like the joined wing and especially when the aft wing is highly prone to buckling. At high loads, the large deformations of the main wing could put the aft wing in compression and cause it to buckle. A load factor of less than unity means that the structure is highly prone to buckling. Eigenvalue buckling analysis in ANSYS consists of first performing the linear static analysis essentially adopting the exact conditions as in the previous section but additionally activating the pre-stress effects, and subsequently performing the eigenvalue buckling analysis.

#### **3.7.4. Dynamic Analysis**

Time history data of integrated forces obtained from the flow analysis is applied as uniform distribution of loading over the upper and lower surfaces of the box wing model. The response of the wing under the action of time varying aerodynamic loading from CFD analysis for  $M = 0.4$ ,  $\alpha = 12^\circ$  and altitude 60,000 is studied. The box-wing model is constrained in all rotational degrees of freedom through out the model. In addition the wings are clamped at the roots.

The results from the above finite element analyses conducted on the box-wing model are discussed in the next chapter.

## CHAPTER 4 RESULTS AND DISCUSSION

This chapter discusses the results obtained for the structural analysis of the box-wing model. Several validation tests are also performed, to check the compatibility between the NASTRAN and ANSYS elements that constitute the joined-wing model.

These test cases include:

1. Modal analysis of transverse shear beam using shear panels,
2. Modal analysis of beam using shell elements,
3. Modal analysis of fuselage using beam elements,
4. Static analysis of truss using rods.

Following the analyses of the validation cases, the NASTRAN box-wing model is translated into ANSYS, and its structural response is determined by performing modal analysis using clamped, rigid and symmetry boundary conditions. Also, linear static, linear buckling and dynamic analyses are performed to study the response of the wing under static and dynamic loading conditions. Results from these various analyses are presented in the subsequent sections.

### 4.1. Validation Test Cases

#### 4.1.1. Modal Analysis of Beam Modeled with Shear Panels

To maintain flexural rigidity, the nodes at every section of the beam are coupled in x and y directions. This coupling of the nodes ensures that the cross section remains rigid when the beam undergoes deformation. The frequencies obtained using NASTRAN for the modal analysis of the beam modeled with shear panels, are listed in Table 4.1. The Block Lanczos method is used to extract the first five modes. Due to the square

cross section of the beam, the frequencies are repeated, one in the x-direction and the other in the y-direction. The longitudinal axis of the beam coincides with the global z-axis. The mode shapes are shown in Figs. 9 through 18. The first two modes represent the first bending mode of the beam in the x- and y-directions, respectively. The third and fourth modes are again repeated, and show the second bending of the beam in the x- and y-directions. The fifth mode shows the third bending mode of the beam in the x-direction. The modal analysis was also conducted using ANSYS, and the frequencies and mode shapes are in exact agreement with those projected by NASTRAN, as seen in Table 4.1. This confirms that the functional behavior of shear panel elements in NASTRAN and ANSYS is the same.

**Table 4.1. Comparison of Frequencies for Modal Analysis of Beam Modeled with Shear Panels using NASTRAN and ANSYS**

Mode	Frequencies (HZ)		% Error
	NASTRAN	ANSYS	
1	18.621	18.621	0
2	18.621	18.621	0
3	55.146	55.146	0
4	55.146	55.146	0
5	89.552	89.552	0

#### 4.1.2. Modal Analysis of Beam Modeled with Shells

For this case, the shear panel elements are replaced with shell elements in the beam model described in the previous section. Again, the Block Lanczos method is used

to extract the first five modes. The mode shapes are shown in Figs. 19 through 28. The frequencies and the mode shapes obtained from NASTRAN and ANSYS match well, thus verifying that SHELL63 elements in ANSYS are compatible with the CQUAD4 elements in NASTRAN. The first and second modes show the first normal and in-plane bending of the beam. Bending occurs in both the in-plane and normal directions due to coupling effect of the nodes at every section in the x- and y-directions. The nodes are coupled to keep the cross section rigid. Similarly, modes 3 and 4 represent the second bending of the beam in the normal and in-plane directions. Mode 5 is combination of the third bending of the beam in the normal and in-plane directions. Mild torsion is also observed for this case.

**Table 4.2. Comparison of Frequencies for Modal Analysis of Beam Modeled with Shell Elements using NASTRAN and ANSYS**

Mode	Frequencies (HZ)		% Error
	NASTRAN	ANSYS	
1	1.1364	1.1364	0
2	1.5457	1.5457	0
3	7.1222	7.1222	0
4	9.6867	9.6867	0
5	20.476	20.476	0

#### 4.1.3. Modal Analysis of Fuselage modeled with beam elements

Table 4.3 shows the first five frequencies obtained using NASTRAN and ANSYS, and the mode shapes of the fuselage beam are shown in Figs. 29 through 38.

The fuselage is analyzed with a mesh identical to the actual joined-wing fuselage mesh (8 beam elements) and modal analysis results obtained using NASTRAN and ANSYS are found to be different. The fuselage model is made finer than the actual joined-wing fuselage to ensure that the results are converged and mesh independent in both the codes. The frequencies and the mode shapes obtained from both the codes are found to be identical as seen in Table 4.3. Two pairs of repeated roots are obtained, with the first pair corresponding to the first bending mode and the second pair representing the second bending mode. The fifth mode represents the elongation of the beam along the longitudinal axis. The differences in the results for the joined-wing model could be attributed to the differences in the accuracy of modeling in NASTRAN and ANSYS.

**Table 4.3. Comparison of Frequencies for Modal Analysis of Fuselage Modeled with Beam Elements using NASTRAN and ANSYS**

Mode	Frequencies (Hz)		% Error
	NASTRAN	ANSYS	
1	4.991	4.991	0
2	4.991	4.991	0
3	31.19	31.19	0
4	31.19	31.19	0
5	52.78	52.78	0

#### 4.1.4. Static Analysis of a Truss

For the simple truss structure shown in Fig. 39, node 4 is subjected to a vertical force of 1000 lbf. The rods are the main stiffening members in the wing, and it is critical

that LINK8 elements of ANSYS and the CROD elements of NASTRAN give identical results. This test is a simple yet satisfactory means of examining the consistency between the two elements. Nodal displacements are obtained from the linear static analysis of the truss using NASTRAN and ANSYS as shown in Figs. 40 and 41, and results are shown in Table 4.4.

Since this is a 2-D problem in the x-y plane, the translational displacements in the z-direction are zero. Also, as the rotational d.o.f. are constrained throughout the model, the rotations about x-, y- and z-axes are also zero. Nodes 1 and 2, which are constrained in all d.o.f., have zero displacements. There is a small variation in the U<sub>x</sub> values for node 3, but the deviation is only 0.4 %. All the displacements obtained using the two codes match well.

**Table 4.4 Comparison of Nodal Displacements from Linear Static Analysis of a Truss Modeled with Rod elements using NASTRAN and ANSYS**

<b>NODE</b>		<b>U<sub>x</sub></b>	<b>U<sub>y</sub></b>	<b>U<sub>z</sub></b>	<b>R<sub>x</sub></b>	<b>R<sub>y</sub></b>	<b>R<sub>z</sub></b>
<b>1</b>	<b>NASTRAN</b>	0	0	0	0	0	0
	<b>ANSYS</b>	0	0	0	0	0	0
<b>2</b>	<b>NASTRAN</b>	0	0	0	0	0	0
	<b>ANSYS</b>	0	0	0	0	0	0
<b>3</b>	<b>NASTRAN</b>	1.243E-02	-1.285E-01	0	0	0	0
	<b>ANSYS</b>	1.248E-02	-1.285E-01			0	0
<b>4</b>	<b>NASTRAN</b>	-1.252E-02	-1.290E-01	0	0	0	0
	<b>ANSYS</b>	-1.252E-02	-1.290E-01	0	0	0	0

All the constituting elements in the ANSYS model have been tested and compared with the corresponding elements in NASTRAN, and the results are found to

agree. The actual analysis of the joined wing model is then performed, and the results are discussed in the following sections.

## **4.2. Box-Wing Modal Analysis**

For the modal analysis of the box wing, the NASTRAN model translated into ANSYS is analyzed for clamped, rigid, and symmetry boundary conditions, as discussed in Chapter 3, and the results are compared with the corresponding NASTRAN model for each boundary condition.

### **4.2.1. Clamped Boundary Condition**

For the case of clamped boundary condition, the main and aft wing roots are constrained in all degrees of freedom except z-translation. Grid point 2 on the main wing is constrained in all d.o.f. The analysis is performed using the Block Lanczos method to extract the first five free-vibration modes shown in Figs. 42 through 51. Table 4.5 lists the frequencies obtained using NASTRAN and ANSYS. The frequencies from the ANSYS analysis differ from the NASTRAN results by approximately 1% – 13%. Even though the mode shapes look similar, the eigenvectors are actually different, as shown by the values of the contour legends. The first mode shows the first bending of the main and the aft wings. Since the translational d.o.f. of the aft wing root are free, the displacement of the root can be either in the +z-direction or in the -z-direction, as shown by Figs, 41 and 42, respectively. The second mode represents second bending of the main and aft wings, while the third and fourth modes include the third and fourth bending of the aft wing in a plane normal to the wing, and the first bending of the main wing in a plane parallel to the wing. The fifth mode is characterized by torsion near the root of the main

wing. Also, the main wing experiences second bending about a plane normal to plane of the wing, as shown in Fig. 51.

**Table 4.5. Comparison of Frequencies for Modal Analysis with Clamped BC with RBEs and with Fuselage using NASTRAN and ANSYS**

Mode	Frequencies (Hz)		% Error
	NASTRAN	ANSYS	
1	0.6288	0.65405	3.9
2	1.2183	1.0817	12.6
3	2.8504	2.8953	1.5
4	3.8006	3.5164	8.1
5	5.4751	6.0775	9.9

Since all the elements comprising the ANSYS model (except constraint equations (CE) that are mathematical equations) were successfully tested prior to this analysis for consistency with the corresponding NASTRAN elements, the variations in the results suggest that the error could be due to differences in formulation between the constraint equations and the rigid body elements.

To investigate this problem further, a simplified joined wing is chosen where the RBE1 elements and the fuselage elements are removed from the NASTRAN model. Similarly, in the ANSYS model, the constraint equations are deleted along with the fuselage elements. Now, the ANSYS and the NASTRAN models contain only shells,

shear panels, rods and mass elements. A modal analysis is now performed on this simplified model, and the frequencies of the ANSYS model, listed in Table 4.6, match exactly with the NASTRAN model frequencies. Also, the mode shapes and the eigenvectors match between the two models, as shown in Figs, 52 through 61. The first and second modes show the first and second bending of the main and aft wings. The third mode represents the third bending of the aft wing, and the first bending of the main wing in the plane of the wing. The fourth mode includes second bending of the main wing, while the fifth mode includes in-plane bending of portions of the main and aft wing prior to the joint.

This simplified model analysis rules out possibilities of inconsistencies between the NASTRAN and ANSYS shells, shear panels, rods and concentrated mass elements. Following the analysis of this simplified model, the RBE1 elements were included to this simplified model in NASTRAN. Similarly, the constraint equations were included in the ANSYS model. The fuselage beam elements are still excluded from the NASTRAN and ANSYS models. The first 5 frequencies extracted are listed in Table 4.7, and match the NASTRAN results exactly. Comparison of the results presented in Tables 4.6 and 4.7 shows that the addition of the RBE1 elements has no influence on the frequencies, eigenvectors and mode shapes of the structure, as shown in Figs 62 through 71. The removal of the fuselage causes lower natural frequencies with an increase in the amplitude of vibrations and a reduction in the stiffness of the structure, compared to the results obtained in the case including the fuselage.

In order to check if the fuselage elements are responsible for the differences in the results, the RBE1 elements and the constraint equations were deleted from the

NASTRAN and ANSYS models, and the fuselage beam elements were added to the simplified model. Both the ANSYS and the NASTRAN models now have shells, shear panels, rods, fuselage beams, and concentrated masses. From Table 4.8 and Figs. 72 through 81, it is clear that the frequencies and the eigenvectors agree well with the NASTRAN results. At best, the minor difference in the results can be attributed to difference in the accuracy of modeling in the NASTRAN and ANSYS codes.

**Table 4.6. Comparison of Frequencies for Modal Analysis with Clamped BC without RBEs and without Fuselage using NASTRAN and ANSYS**

Mode	Frequencies (Hz)		% Error
	NASTRAN	ANSYS	
1	0.3154	0.3154	0
2	0.9681	0.9681	0
3	2.1069	2.1069	0
4	3.5759	3.5759	0
5	4.2019	4.2019	0

The first 4 mode shapes obtained using NASTRAN and ANSYS appear to be different, the sign of the eigenvectors is opposite, but the magnitude is the same. The first two modes depict the first and second bending modes of the aft wing, and the first bending mode of the main wing. The third mode and fourth modes represent the first in-plane bending of the main wing, while the fifth mode is characterized by torsion near the intersection of the aft wing and tail, while the main wing experiences second bending.

It is evident that the results match when the models are analyzed without constraint equations or without fuselage or without both.

**Table 4.7. Comparison of Frequencies for Modal Analysis with Clamped BC with RBEs and without Fuselage using NASTRAN and ANSYS**

Mode	Frequencies (Hz)		% Error
	NASTRAN	ANSYS	
1	0.3154	0.3154	0
2	0.9681	0.9681	0
3	2.1069	2.1069	0
4	3.5759	3.5759	0
5	4.2019	4.2019	0

The discrepancy comes in only when the fuselage and the constraint equations are combined. The deviations in the frequencies could be due to differences in the formulation between NASTRAN and ANSYS for constraint equations/RBE1 elements that connect the 2-D shell elements of the main wing with the 3-D solid beam elements of the fuselage. In other words, the anomaly could be at only one grid point, namely grid point 2003, where the 3-D beam elements are connected to the 2-D shell elements by the constraint equations. In the remaining portions of the wing, where the 2-D shell elements are not in contact with the 3-D beam elements, the constraint equations are consistent with the RBE1 elements.

To confirm this, the constraint equations connecting the main wing to the fuselage at node 2003 are removed and replaced with a beam element, as shown in Fig. 68.

**Table 4.8. Comparison of Frequencies for Modal Analysis with Clamped BC without RBEs and with Fuselage using NASTRAN and ANSYS**

Mode	Frequencies (Hz)		% Error
	NASTRAN	ANSYS	
1	0.1665	0.1665	0
2	0.8906	0.8906	0
3	1.6192	1.6187	0.03
4	2.3061	2.3061	0
5	3.2159	3.2199	0.12

Similarly, the RBE1 element in NASTRAN is also deleted, and replaced with a beam element. The constraint equations and the RBE1 elements in the rest of the model are retained. The objective in doing this is to confirm the inconsistency at the point where the constraint equations connect 2-D and 3-D elements in ANSYS. The ANSYS results, listed in Table 4.9, agree well with the NASTRAN results. The small differences in the results are attributed to the linking an additional beam element. The mode shapes look similar, and shown by Figs. 83 through 92, but the difference in the magnitude of the eigenvectors increases for higher modes that are dominated by bending. Nevertheless, the results are much better than the original joined wing case with constraint equations at

node 2003. It is clear that the discrepancy between the ANSYS and the NASTRAN results is due to differences in formulation at the point where the main wing is connected to the fuselage through constraint equations. The following section discusses the results obtained for the rigid boundary condition.

**Table 4.9. Comparison of Frequencies for Modal Analysis with Clamped BC with RBEs and with Extended Fuselage using NASTRAN and ANSYS**

Mode	Frequencies (Hz)		% Error
	NASTRAN	ANSYS	
1	0.6447	0.6447	0
2	1.2386	1.2383	0.02
3	2.8835	2.8848	0.04
4	3.8352	3.8373	0.05
5	5.7621	5.7605	0.02

#### 4.2.2. Rigidly-Clamped Boundary Condition

For the rigidly clamped boundary condition, the analysis is carried out similar to the case of clamped boundary condition. To begin with, the ANSYS model is analyzed with all constraint equations and fuselage beam elements. The NASTRAN model is also analyzed with RBE1 and fuselage elements. Block Lanczos method is used to extract the first five free-vibration mode shapes and frequencies. The results are listed in Table 4.10. and the mode shapes are shown in Figs. 93 through 102. It is observed that the frequencies obtained using NASTRAN and ANSYS codes do not match. The eigenvectors are significantly different for the first two modes. However, the difference

is seen to decrease for higher modes and is least for the fifth mode. The first two modes represent the first and second bending modes of the main and the aft wings, while the third mode includes the first bending mode in the plane of the wing. The fourth mode depicts the second bending mode of the main wing, and a more pronounced in-plane deformation of the main wing. The fifth mode is characterized by torsion of the main wing, and second bending of the aft wing. In order to check if the discrepancy in the results is caused by the constraint equations connecting the fuselage with the main wing, a simplified model is analyzed similar to the clamped boundary condition case. The NASTRAN and ANSYS models are first analyzed without constraint equations/RBE1 elements, and without fuselage. The frequencies and the mode shapes were found to match. The mode shapes are shown in Figs. 103 through 112. Unlike the previous cases, the third mode shows considerable in-plane deformation of both the main and the aft wing sections between the root and the joint. Also, a minor twist is seen in the main wing near the intersection of the fuselage and the main wing. Next, the models are analyzed without fuselage, but with constraint equations and RBE1 elements. Again, no differences in the frequencies and mode shapes were observed for this case too. Following this, the fuselage elements are added to the model, and the modal response was sought. The error in the results is less than 0.1 %. Finally, the constraint equations/RBE1 elements connecting the main wing to the fuselage are removed and replaced with a beam element, as shown in Fig. 68. The constraint equations and the RBE1 elements for the rest of the model are retained. The ANSYS results correspond with the NASTRAN results, and the error is less than 0.1 %. The frequencies for all of the above cases are summarized in Table 4.10 for the rigidly clamped boundary condition.

### 4.2.3. Symmetry Boundary Condition

For the 2-dof lift trim case with symmetry boundary condition, the aft wing root are constrained in  $U_y$ ,  $\theta_x$ ,  $\theta_y$ ,  $\theta_z$ , while nodes 1, 3 and 4 on the main wing root are constrained in  $U_y$ ,  $\theta_x$ ,  $\theta_y$ ,  $\theta_z$ . Grid point 2 on the main wing root is constrained in  $U_x$ ,  $U_y$ ,  $\theta_x$  and  $\theta_z$ . Symmetry boundary conditions are enforced along the centerline by constraining y-displacement. The NASTRAN code implements this boundary conditions using a SUPORT1 entry that references the  $U_z$  (pitching) and  $\theta_y$  (plunging) d.o.f. for rigid-body motion. This free body analysis results in two rigid body modes along the  $U_z$  and  $\theta_y$  directions. In ANSYS however, the rigid body motion is specified through the subspace method which unlike the lanczos method has the option of allowing the user to specify the rigid body d.o.f for the eigenvalue analysis. The results are summarized for the models in Table 4.11. The first five free-vibration modes for the full NASTRAN and ANSYS models with symmetry boundary condition are shown in Figs. 113 through 122. The first two modes obtained are rigid body modes and the rest are flexible modes.

The first rigid body mode shows displacement of the whole wing in the  $z$  direction (plunging), while the second rigid body mode shows  $+z$  translation of the aft wing and the  $-z$  translation of the main wing. In both the rigid body modes, the first fuselage beam element that connects to the main wing through constraint equations has huge deformation. Fig. 109 shows the undeformed fuselage beam element (shown by broken lines) and the deformed beam element.

On the other hand, no severe deformations are seen in the NASTRAN model, observed, and the RBE1 elements provide a rigid connection between the fuselage beam elements and the main wing elements.

**Table 4.10. Summary of Frequencies from Modal Analysis with Rigid BC for all Models using NASTRAN and ANSYS**

Case	Mode	Frequencies (Hz)		% Error
		NASTRAN	ANSYS	
Full Model	1	0.7353	1.0784	31.82
	2	1.832	1.5358	19.29
	3	3.3299	3.1998	4.07
	4	5.4719	5.9837	8.55
	5	7.1573	7.3316	2.38
Without RBEs and without Fuselage	1	0.7972	0.7972	0.00
	2	2.0433	2.0433	0.00
	3	3.0499	3.0499	0.00
	4	4.1511	4.1511	0.00
	5	4.6481	4.6481	0.00
With RBEs and without Fuselage	1	0.7972	0.7972	0.00
	2	2.0433	2.0433	0.00
	3	3.0499	3.0499	0.00
	4	4.1511	4.1511	0.00
	5	4.6481	4.6481	0.00
With Fuselage and without RBEs	1	0.7029	0.7029	0.00
	2	1.1289	1.1289	0.00
	3	2.1243	2.1255	0.06
	4	2.3631	2.3636	0.02
	5	4.0247	4.0248	0.00
Extended Fuselage	1	0.7408	0.7408	0.00
	2	1.8439	1.8426	0.07
	3	3.3997	3.3998	0.00
	4	5.762	5.7603	0.03
	5	7.4257	7.4271	0.02

From this, it is evident that the constraint equations are not producing the desired rigid connection of the fuselage with the main wing. Mode 3 shows the first bending of the main and the aft wings, while modes 4 and 5 are similar and show the second bending of the aft wing, and the first in-plane bending of the main wing.

### **4.3. Linear static Analysis**

Linear static analysis is performed for the case of  $M = 0.4$ ,  $\alpha = 0^\circ$ , and altitude = 60,000 feet. The wing is subjected to a pressure load of  $104 \text{ lbf/in}^2$  on the upper surface and  $125 \text{ lbf/in}^2$  on the lower surface. The main and aft wing roots are clamped in all degrees of freedom.

Figure 109 shows the deflection contours, and the magnitude of the tip deflection is 6.562 ft. The span of the wing is 122.86 ft and the ratio of tip deflection to the span is 5.34 %. Lift is produced due to pressure difference between the pressure and the suction surfaces of the wing. For  $\alpha = 0$ , this pressure difference is small, and consequently the magnitude of the lift is also less. Hence, the tip deflection obtained from linear analysis is also small. This is because the pressure difference between the pressure and the suction surfaces is for the pressure loads corresponding to  $\alpha = 0$ . The inlaid figure in Fig. 123 shows the left view of the deformed structure as against the original undeformed structure. The deflection is minimum near the root and increases towards the free end of the wing behaving like a cantilever beam. Figure 124 shows the plot of deflection versus distance along the span at the leading edge of the main wing. While the deflection is zero at the roots and maximum at the tip, it is seen to vary smoothly along the span for the optimized box-wing structure. An important observation made during this analysis

**Table 4.11. Summary of Frequencies from Modal Analysis with SUPORT1 BC for all Models using NASTRAN and ANSYS**

Case	Mode	Frequencies (Hz)		% Error
		NASTRAN	ANSYS	
Full Model	1	0	0	0.00
	2	0	0	0.00
	3	0.9906	1.3134	-32.59
	4	1.6238	1.5751	3.00
	5	1.7706	2.2107	-24.86
Without RBEs and without Fuselage	1	0	0	0.00
	2	0	0	0.00
	3	0.366	0.3667	-0.19
	4	0.8357	0.8357	0.00
	5	2.0838	2.0841	-0.01
With RBEs and without Fuselage	1	0	0	0.00
	2	0	0	0.00
	3	0.366	0.3667	-0.19
	4	0.8357	0.8357	0.00
	5	2.0838	2.0841	-0.01
With Fuselage and without RBEs	1	0	0	0.00
	2	0	0	0.00
	3	0.3335	0.3337	-0.06
	4	0.5324	0.5326	-0.04
	5	1.64238	1.64238	0.00
Extended Fuselage	1	0	0	0.00
	2	0	0	0.00
	3	1.2731	1.2731	0.00
	4	1.6752	1.6757	-0.03
	5	2.2279	2.2283	-0.02

is that the first fuselage element that connects to the main wing through the constraint equations does not undergo severe deformation like the model with symmetry boundary conditions.

The stress contours, shown in Figs. 125 and 126 indicate that the stress levels are higher near the roots of the main and the aft wing. This stress distribution is similar to that conventional cantilevered structure. The stress is higher near the roots when compared to the tip of the wing; but the maximum stress occurs at the trailing edge of the aft wing midsection. This is because of two reasons. Firstly; the wing skin elements near the wing roots and at the joint are optimized to possess considerably higher thickness than other regions in the wing in order to avoid stress concentration typically seen at the wing roots. Secondly, as the pressure loads applied normal to the wing surface cause the main wing to deflect upwards, the aft wing is subjected to compressive loads leading to high stress concentration in the midsection. The yield stress for this material is in the range of 65 MPa – 221 MPa and the ultimate stress is about 172-269 MPa. The maximum stress obtained is 136.45 MPa which is within the range of the yield stress for this material.

The box-wing finite element model is built with small-deformations assumption in order to analyze this detailed but simple model with minimum computational cost. Hence, a linear analysis is accurate to predict the structural response instead of an expensive nonlinear analysis. In order to verify this assumption, a nonlinear analysis is performed on the model with same load and boundary conditions as in the linear analysis but taking into consideration, large deformation effects. It is observed that results from linear and nonlinear analyses almost match. The tip deflection, shown in Fig. 127, from

nonlinear static analysis is 6.53 ft which is about 5.31% of the main wing span. Also, maximum stress, from Fig. 129, is found at the midsection of the aft wing is about 135.02 MPa almost equal to the maximum stress predicted by the linear analysis. Figure 131 shows the plot of deflection versus distance along the span of the main for nonlinear analysis, and when compared with the plot obtained from linear analysis, is found to be almost identical.

The linear analysis results are used to predict the buckling response of the box-wing model. The following section discusses the results obtained from the eigenvalue buckling analysis.

#### **4.4. Linear Buckling Analysis**

The eigenvalue buckling mode shapes for the clamped boundary condition are shown in Fig. 132 through Fig. 136. The first buckling mode is a first bending mode of the main wing with the eigenvalue 9.536. The second, third and the fourth buckling modes are all characterized by torsion of the main and the aft wings, while the fifth buckling mode is similar to the first. The eigenvalues corresponding to the first five buckling modes for the clamped boundary conditions run ANSYS are summarized in Table 4.12. A load factor of less than one means that the structure is highly prone to buckling. In this case, the lowest eigenvalue is well above one and indicates that the structure is stable. Buckling is caused due to large compressive (axial) forces, but in this case the model is subjected to normal loads which do not induce compressive stresses in the structure. This explains why the buckling load factors for the averaged pressure loads are high, and hence the structure is less prone to buckling.

**Table 4.12. Buckling Load Factors obtained from Eigenvalue Buckling Analysis.**

<b>Mode</b>	<b>Buckling Load Factors</b>
1	9.536
2	13.641
3	13.956
4	16.222
5	20.821

#### **4.5. Dynamic Analysis**

The response of the wing under the action of time varying aerodynamic loading is also studied. The unsteady normal component of the force ( $F_z$ ) is obtained from the CFD analysis for  $M = 0.4$ ,  $\alpha = 12^\circ$  and altitude 60,000. This force component is divided by the surface area of the wing and applied as time varying pressure as shown in Fig. 123. The boundary conditions consist of rotational constraints throughout the model and clamped wing roots. Results are obtained for tip deflection and von Mises stress w.r.t time.

The tip deflection and von Mises stress w.r.t. time are obtained from linear analysis results. Figures. 137 and. 138 show the tip nodal z-displacement and von Mises stress versus time obtained from linear analysis. As expected, the deflection and stress plots follow the same trend as the time history of loads. The results converge to a steady state and the wing does not experience any unstable oscillations. The objective behind doing this analysis is to obtain the response of the structure as a function of time which

will serve as a starting point for future wing flutter analysis. The following chapter summarizes and discusses the key outcomes of this research.

## CHAPTER 5 Summary and Future Work

### 5.1. Conclusion

The NASTRAN box-wing model is translated into ANSYS, and its structural response is determined by performing modal analysis for three different types of boundary conditions. Also, linear static, linear buckling and dynamic analyses are performed to predict the displacements, stresses and buckling behavior. By using ANSYS at UC, the results can be compared with the corresponding NASTRAN modal analysis results obtained at the AFRL and the correctness of the procedure can be verified. The first step in the aeroelastic analysis of the joined wing is to obtain a modal representation of the wing, and this forms the focus of the current research. The box-wing is intended for multi-control surface trim-optimization using ASTROS with ZONA51 and was desired by the AFRL to be translated into ANSYS or FEMSTRESS. As the capabilities of FEMSTRESS has limited availability of element types are very, this work mainly concentrated on translating the box-wing model into ANSYS. The objective of this research is to obtain a correct working model in ANSYS for future aeroelastic simulations of the joined-wing box model.

To translate the model into ANSYS, a careful selection of the right elements is necessary to ensure that the functionality of the original elements is retained in ANSYS. After a thorough review of several different element types available in ANSYS, the elements consistent with those from the NASTRAN were chosen for shells, shear panels, beams, rods, mass and rigid body elements. A number of suitable test cases were performed to check the functionality of the chosen elements, and after the results of the

test cases analyses were confirmed to be satisfactory, the actual analysis of the joined wing model was carried out. The model was translated into ANSYS using Hypermesh software, and the chosen element types were assigned in ANSYS. The translated model was first analyzed for clamped boundary conditions, and the results obtained using the NASTRAN and ANSYS were found to be different. Even though the mode shapes were similar, the frequencies and magnitude of the eigenvectors were different. To locate the cause of differences, a number of simpler joined wing models were analyzed. Finally, the cause was traced to the difference in the coupling of the fuselage with the main wing by the constraint equations in ANSYS. These findings were further strengthened by the results of the symmetric boundary condition case where large and inconsistent deformations were observed on the first fuselage beam element that is connected to the main wing by the constraint equations. A more thorough understanding of the mathematics of the formulations used in the code for constraint equations is necessary in order to resolve this issue.

A linear static analysis is performed for averaged aerodynamic pressure loading, and the tip deflection was found to be 5.34% of the wing span. Also, the maximum stress was found to be within the range of the yield stress of the wing material. This linear static analysis also serves as a starting point for the eigenvalue buckling analysis. The eigenvalues obtained from the buckling analysis serve as the buckling load factors for the applied load, and at critical buckling load, the deformations of the structure may grow unboundedly. The buckling load factors computed from the buckling analysis for the averaged pressure loads were all found to be above zero indicating that the structure is stable and not prone to buckling.

Finally, a dynamic analysis is performed to obtain the displacement and the stress response of the structure as a function of time for time-varying pressure loads obtained from the CFD analysis. The displacements and stresses stabilized to a steady state, and follows the trend of the time-varying pressure loads. The dynamic analysis serves as a starting point for future aeroelastic flutter analysis of the joined wing.

## **5.2. Future Work**

The High-Altitude, Long-Endurance (HALE) joined-wing configuration is highly flexible, undergoing large deformations. The present research is based on a linear model, built with assumptions of small deformations. However, recent studies indicate that a nonlinear analysis which takes into account the effect of geometric nonlinearities can yield more accurate results. The box-wing model built on the assumptions of small deformations needs to be modified in order to study the effect of geometric nonlinearities on this highly flexible structure.

The geometry of the box-wing structural model is different from the 3-D aerodynamic model. Hence, a procedure for accurate load/displacement transfer between the non-matching fluid and the box-wing structure interfaces is required. This will necessitate the integration of the fluid and structural solvers in order to facilitate load/displacement data exchange. Studies indicate MDICE (Multi-Disciplinary Computing Environment) as a likely simulation environment, where fluid dynamics and structural-analysis solvers are integrated, along with a dynamic visualizer of the results. MDICE also has in-built interpolation routines to facilitate load/displacement data exchange between the CFD and structural systems.

## REFERENCES

1. [www.afrlhorizons.com/Briefs/Sept02/VA0207.html](http://www.afrlhorizons.com/Briefs/Sept02/VA0207.html)
2. <http://www.afrlhorizons.com/Briefs/0006/VA9901.html>
3. Wolkovitch, J. "Joined Wing Aircraft," US Patent, 3942747, March 1976.
4. Wolkovitch, J. "Joined Wing Aircraft," US Patent, 4365773 December 1982.
5. Wolkovitch, J. "The Joined Wing: An Overview," Journal of Aircraft, Vol. 23, pp. 161– 178, March 1986.
6. Samuels, M. F., "Structural Weight Comparison of a Joined Wing and a Conventional Wing," Journal of Aircraft, Vol. 19, June 1982, pp. 485-491.
7. Miura, H., Shyu, A., and Wolkovitch, J., "Parametric Weight Evaluation of Joined Wings by Structural Optimization," AIAA Paper 85-0642-CP, April 1985.
8. Hajela, P., Weight Evaluation of Joined Wing, NASA Ames Research Center, Co-Principal Investigator with Prof L.A. Schmit, October 1982.
9. Wolkovitch, J. "Joined Wing Research Airplane Feasibility Study," AIAA Paper 84-2471, 1984.
10. Smith, S.C., Cliff, S.E., Kroo, I., "The Design of a Joined-Wing Demonstrator Aircraft," AIAA Aircraft Design Meeting, Sept. 1987, AIAA-87-2930.
11. Lin, H-H, et al. "Influence of Joint Fixity on the Aeroelastic Characteristics of a Joined Wing Structure." 31 AIAA/ASME/ASCE/AHS/ASC Structures, Structural Dynamics and Materials Conference, Long Beach, CA. 1442–1454. April 1990.
12. Gallman, J.; Kroo, I., "Structural Optimization for Joined-Wing Synthesis", AIAA Journal of Aircraft, Vol. 33 No.1, pp. 214-223, January 1996.
13. Gallman, J.W., Kroo, I., Smith, S.C., "Design Synthesis and Optimization of Joined-Wing Transports," AIAA 90-3197, Sept. 1990.

14. Kroo, I., Gallman, J., Smith, S.C., "Aerodynamic and Structural Studies of Joined Wing Aircraft," *Journal of Aircraft*, Jan. 1991.
15. Gallman, J., Kroo, I., "Preliminary Design Optimization of Joined-Wing Aircraft," *Journal of Aircraft*, Nov. 1993
16. Livne, E. "Aeroelasticity of Joined-Wing Airplane Configurations: Past Work and Future Challenges -A Survey." 42 AIAA/ASME/ASCE/AHS/ASC Structures, Structural Dynamics and Materials Conference, Seattle, WA. AIAA Paper 2001-1370. April 2001.
17. <http://www.aiaa.org/aerospace/Article.cfm?issuetocid=256&ArchiveIssueID=30>
18. Reich, G. W., et al. "Application of Active Aeroelastic Wing Technology to a Joined-Wing Sensorcraft." 43r AIAA/ASME/ASCE/AHS/ASC Structures, Structural Dynamics and Materials Conference, Denver, AIAA 2002-1633, April 2002.
19. Smallwood, B.P., R.A. Canfield, and A.J. Terzuoli, Jr., "Structurally Integrated Antennas on a Joined-Wing Aircraft," Proceedings of the 44th AIAA/ASME/ASCE/AHS Structures, Structural Dynamics, and Materials Conference, no. AIAA-2003-1459, Norfolk VA, April 7-10, 2003.
20. Smallwood, B.P., A.J. Terzuoli, Jr., and R.A. Canfield, "Conformal Antennas on a Joined-Wing Aircraft," Proceedings of the 2003 IEEE/AP-S/URSI International Symposium, n. 736, Columbus OH, June 23-27, 2003.
21. Blair, M. and R. A. Canfield, "A Joined-Wing Aeroelastic Design with Geometric Non-Linearity," CEAS/AIAA/NVvL International Forum on Aeroelasticity and Structural Dynamics (IFASD), Amsterdam, Netherlands, June 4-6, 2003.
22. Canfield, R.A., "A Joined-Wing Aeroelastic Design with Geometric Non-Linearity," NATO Research and Technology Agency Advanced Course on Novel Aircraft Design Concepts for the 21st Century, Instituto Superior Tecnico, Lisbon, Portugal, October 20-22, 2003.
23. Sivaji, R., Master's Thesis, "Aerodynamic Analysis of the Joined-Wing Configuration of a High-Altitude, Long Endurance (HALE) Aircraft", 2004.

24. Marisarla, S., Narayanan, V., Ghia, U. and Ghia, K., "Prediction of Structural Behavior of Joined-Wing Configuration of High-Altitude Long Endurance (HALE) Aircraft," 41st AIAA Aerospace Science Meeting & Exhibit, January, Reno, NV, AIAA 2003-0625.
25. Sivaji, R., Narayanan, V., Marisarla, S., Kaloyanova, V., Ghia, U., and Ghia, K. N., "Aeroelastic Analysis of a Joined-Wing of High Altitude Long Endurance (HALE) Aircraft," presented at the 6th International Nobeyama Workshop, Nobeyama, Japan, April 2003.
26. Narayanan, V., Master's Thesis, "Structural Analysis of Reinforced Shell Wing Model for Joined-Wing Configuration", 2005.
27. Bathe, K. J., Finite Element Procedures, Prentice Hall, 1996.
28. MacNeal-Schwendler Corporation. MSC.NASTRAN Version 68 Reference Manual, 1995.
29. ANSYS 7.1 User's Guide, ANSYS Inc.

**Fig. 1. Sensorcraft Joined-Wing Aircraft**

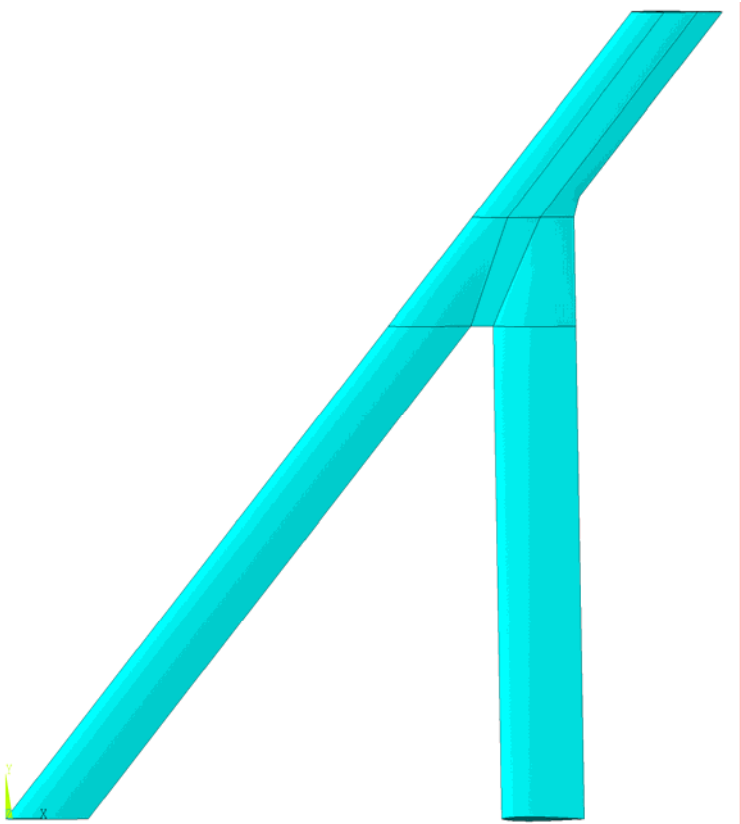


**Fig. 2. CAD Model of Joined-Wing Aircraft**

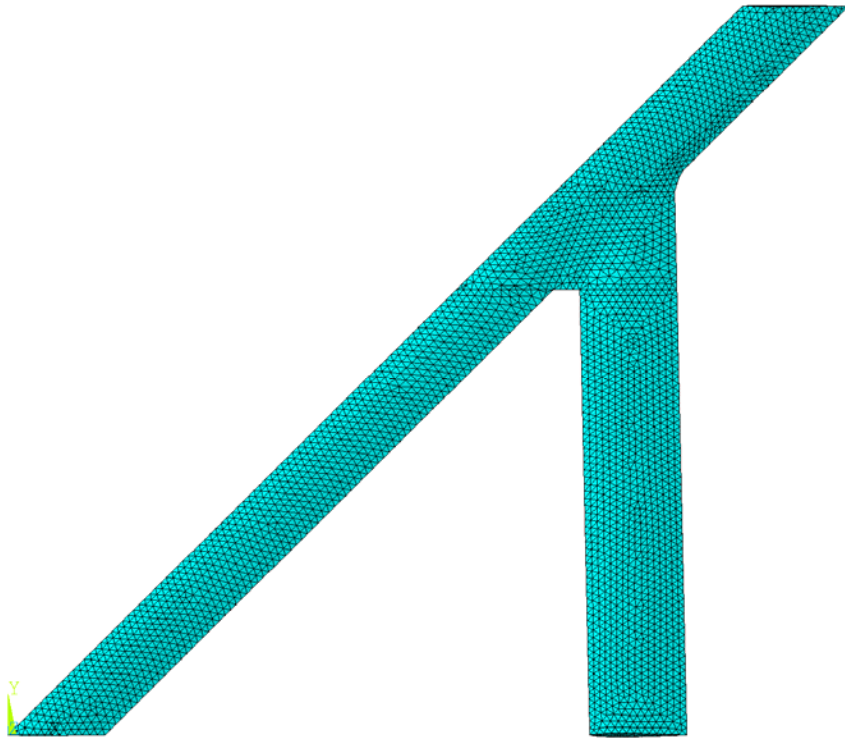


**Fig. 3. Finite Element Mesh Comprising of 10-noded Solid Tetrahedral Elements**

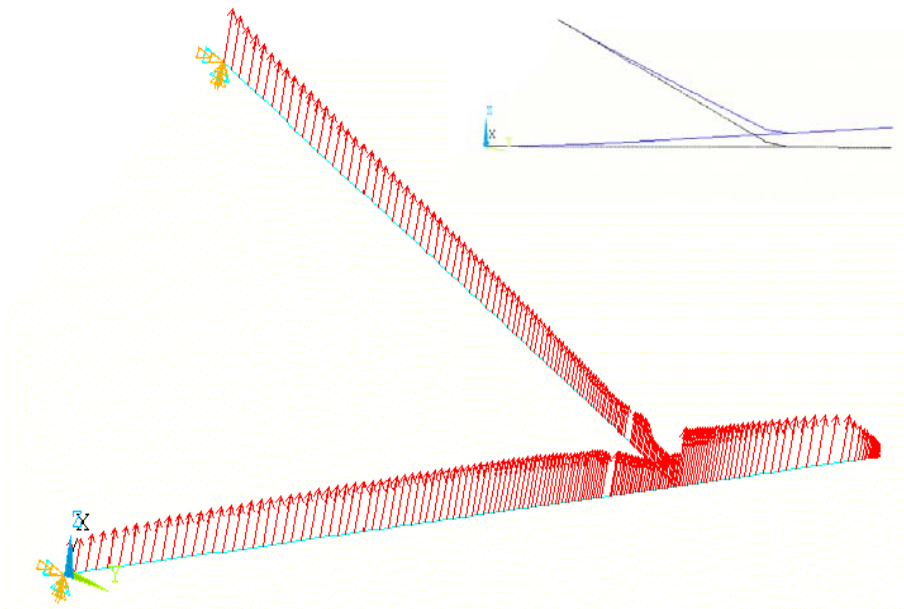


**Fig. 4. Finite 1-D Approximation of Actual 3-D Joined Wing Model**

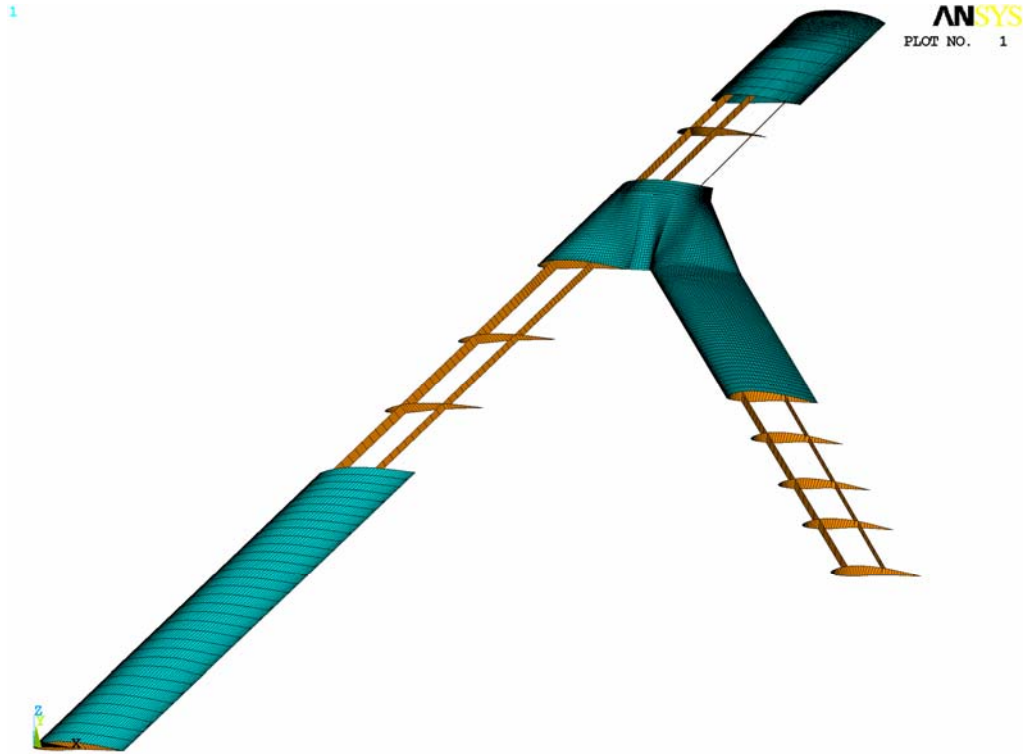


**Fig. 5. Reinforced Shell Wing Model**

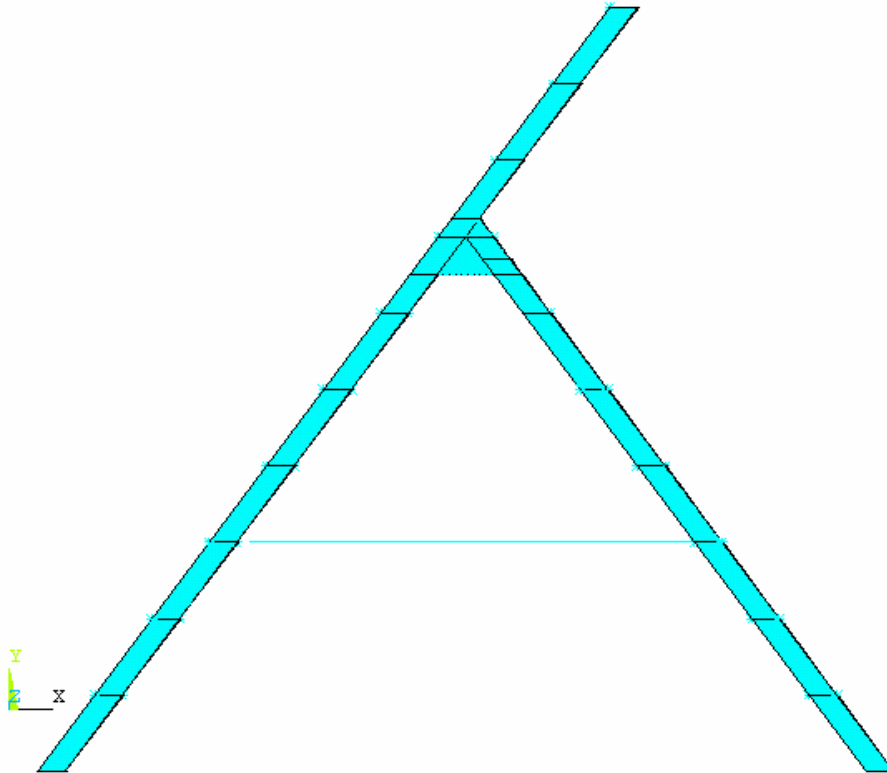


**Fig. 6. Front-View of Box-Wing Finite Element Model**

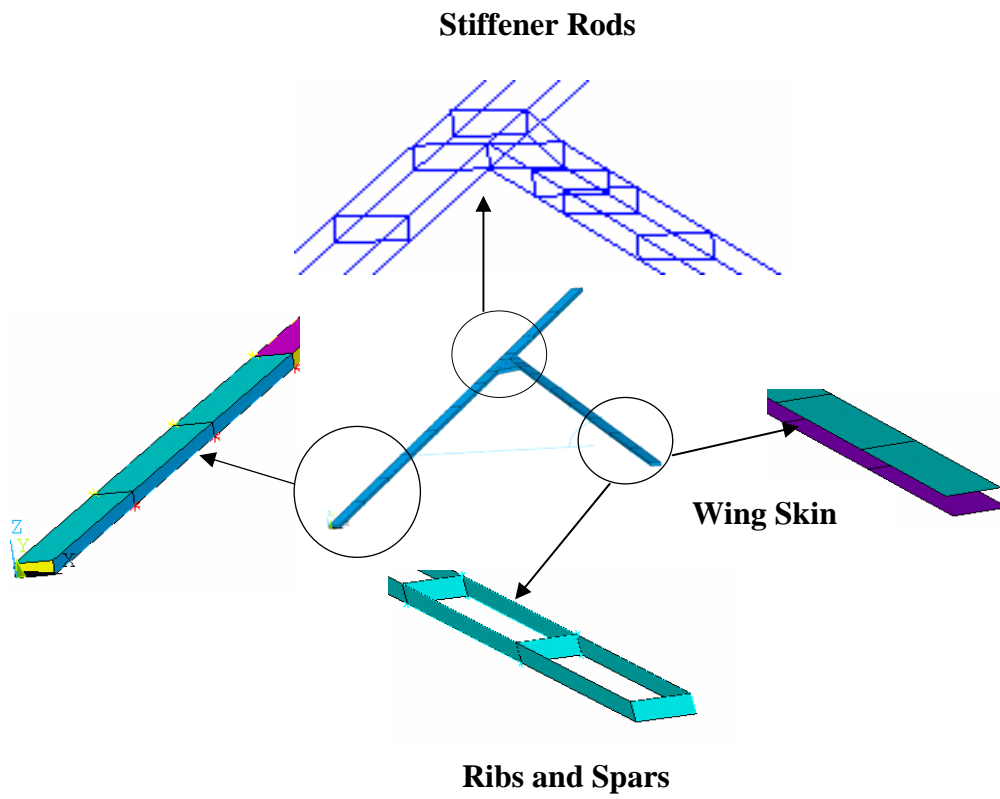


**Fig. 7. Detailed Finite-Element Model of Box Wing**

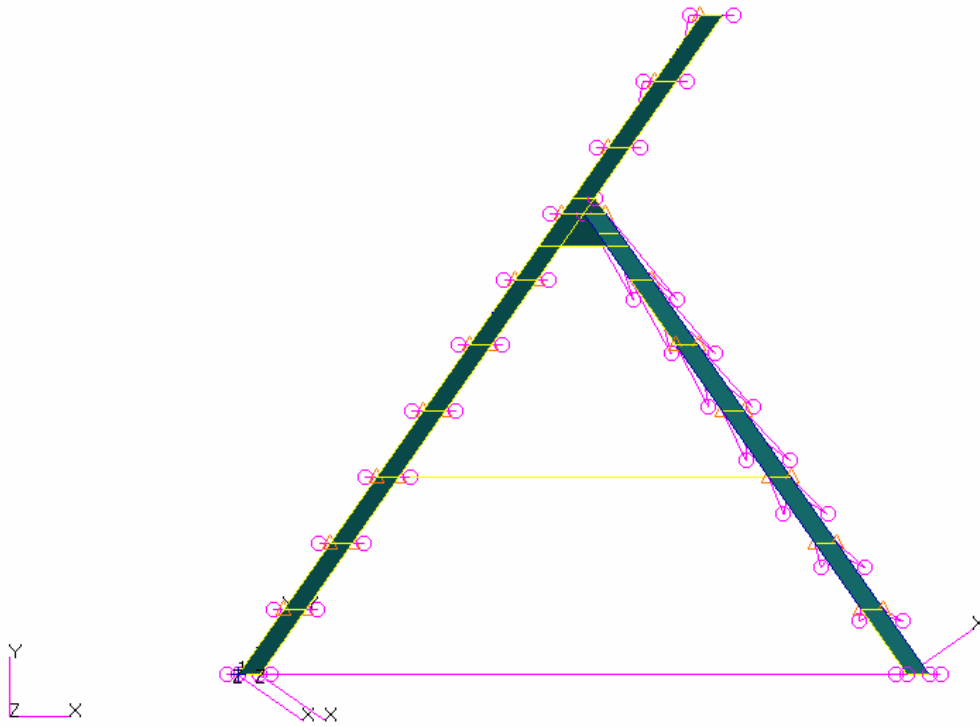


**Fig. 8. AFRL Sencorcraft Box-Wing Finite-Element Model for Clamped BC Case with RBEs in NASTRAN**

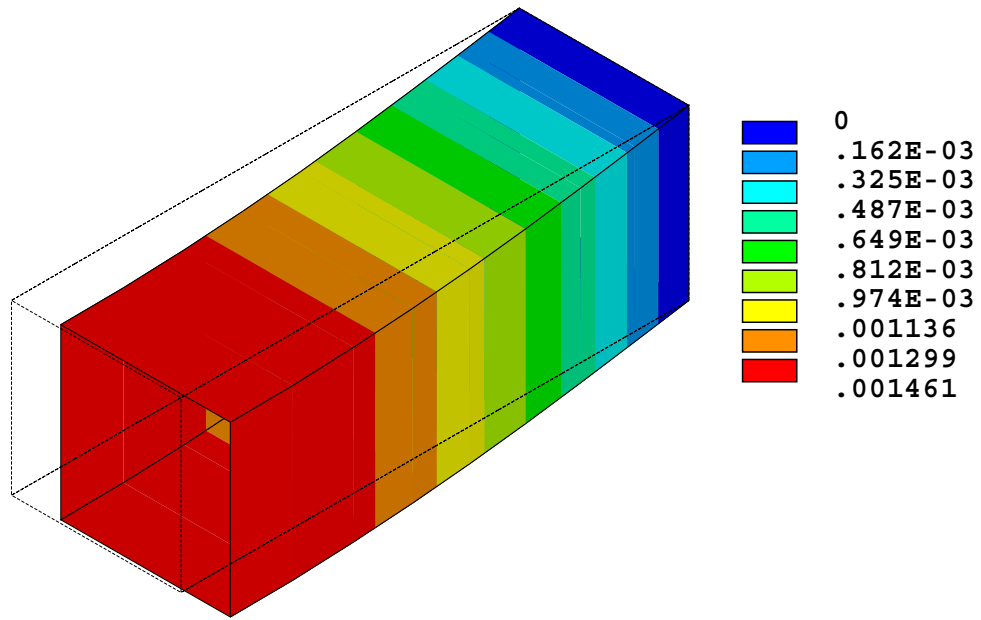


**Fig. 9. Test Case – Modal Analysis of Beam Modeled with Shear Panels, Mode 1, ANSYS, Frequency = 18.621 Hz**

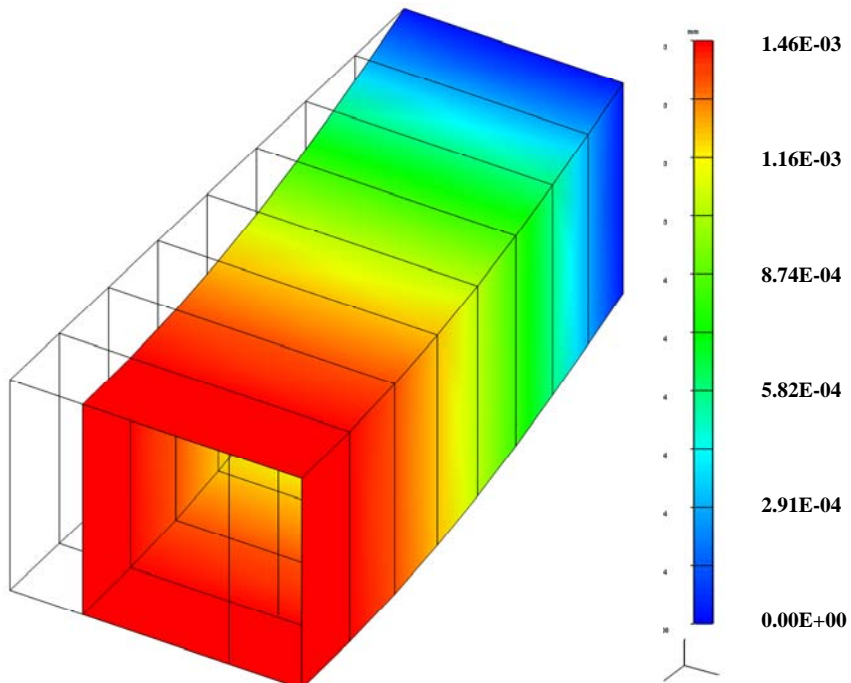


**Fig. 10. Test Case – Modal Analysis of Beam Modeled with Shear Panels, Mode 1, NASTRAN, Frequency = 18.621 Hz**

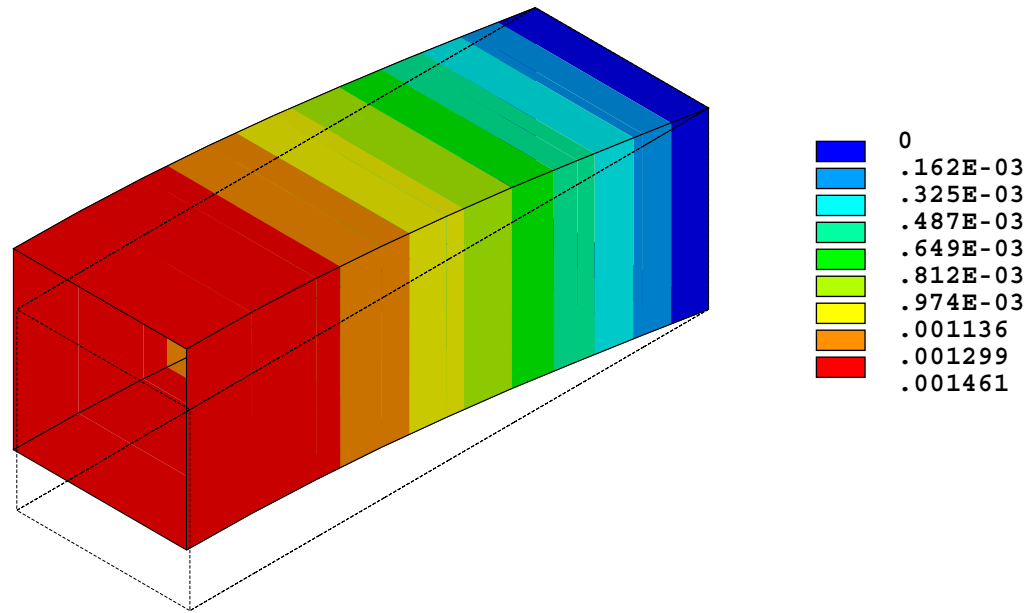


**Fig. 11. Test Case – Modal Analysis of Beam Modeled with Shear Panels, Mode 2, ANSYS, Frequency = 18.621 Hz**

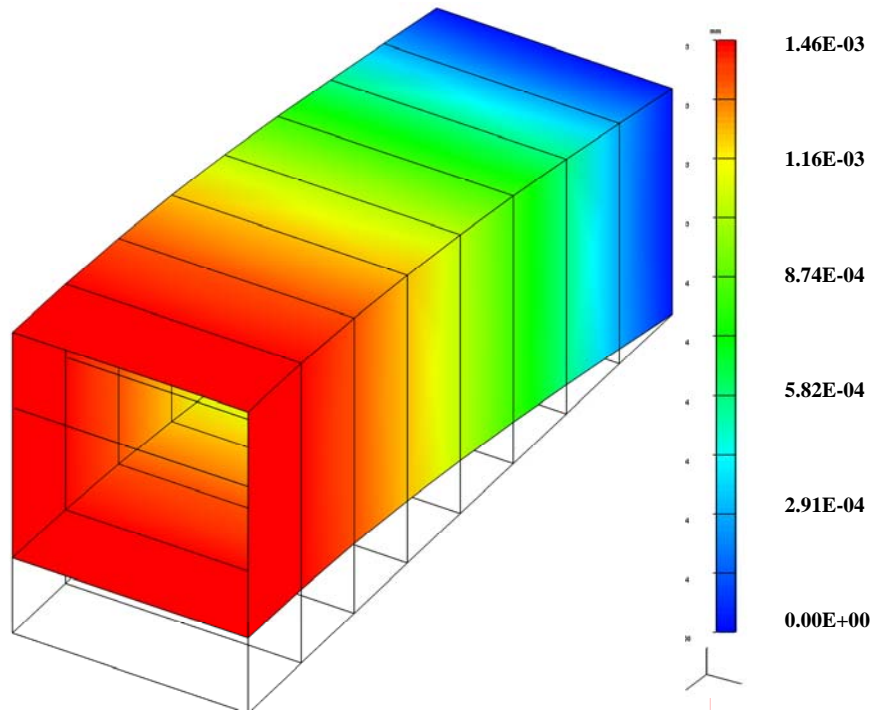


**Fig. 12. Test Case – Modal Analysis of Beam Modeled with Shear Panels, Mode 2, NASTRAN, Frequency = 18.621 Hz**

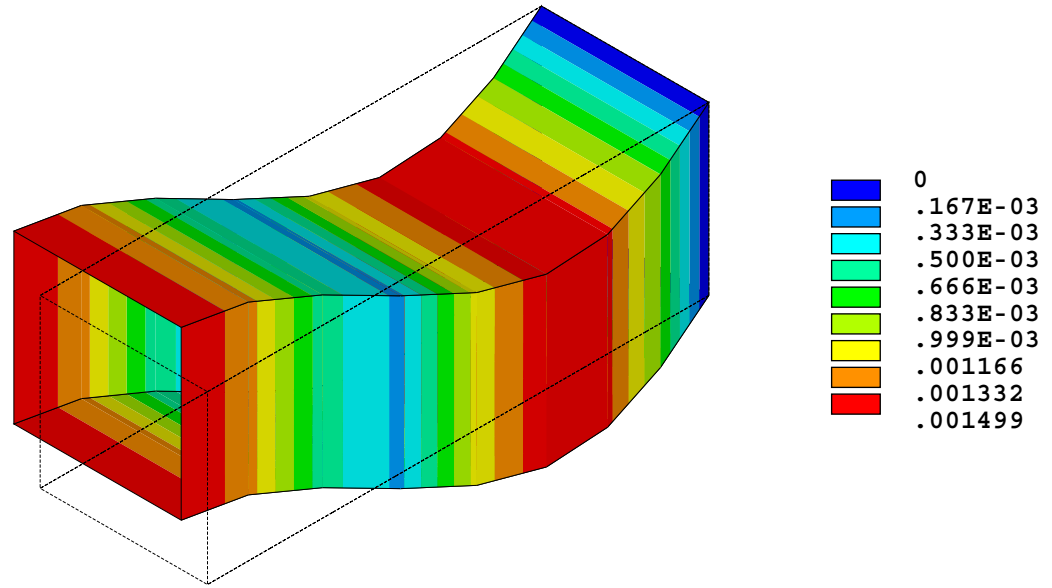


**Fig. 13. Test Case – Modal Analysis of Beam Modeled with Shear Panels, Mode 3, ANSYS, Frequency = 55.146 Hz**

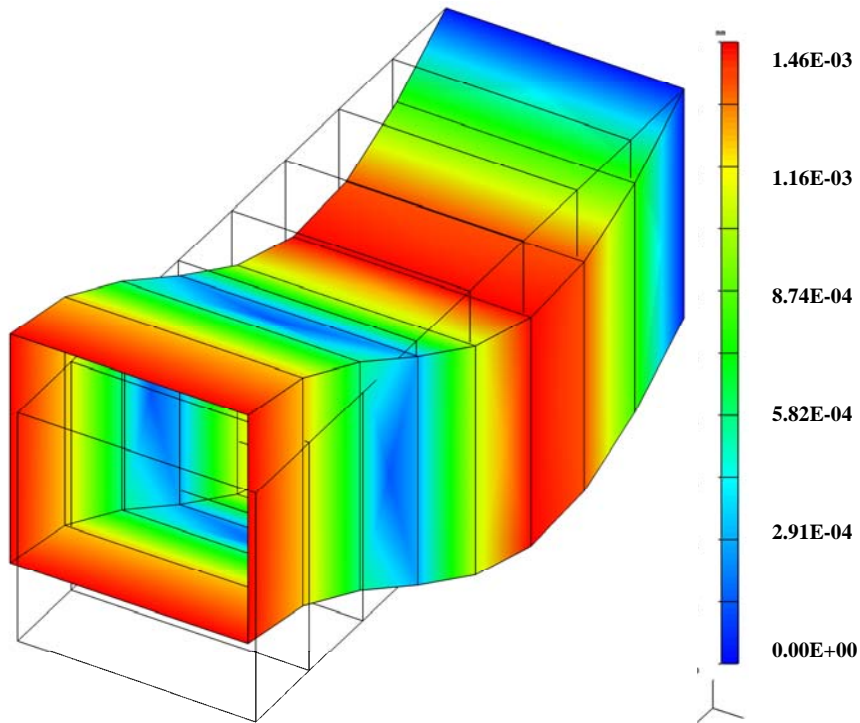


**Fig. 14. Test Case – Modal Analysis of Beam Modeled with Shear Panels, Mode 3, NASTRAN, Frequency = 55.146 Hz**

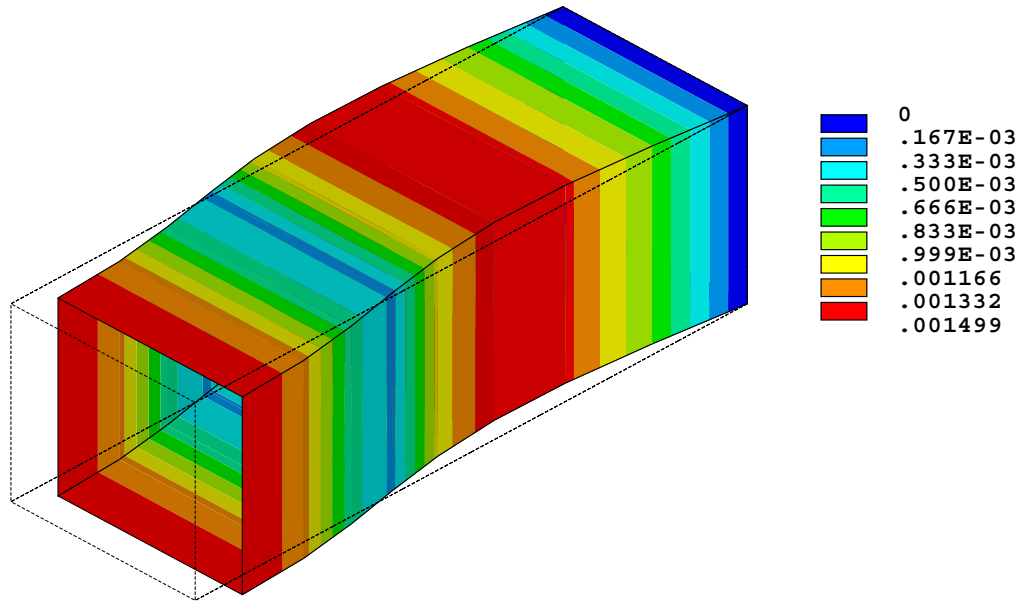


**Fig. 15. Test Case – Modal Analysis of Beam Modeled with Shear Panels, Mode 4, ANSYS,  
Frequency = 55.146 Hz**

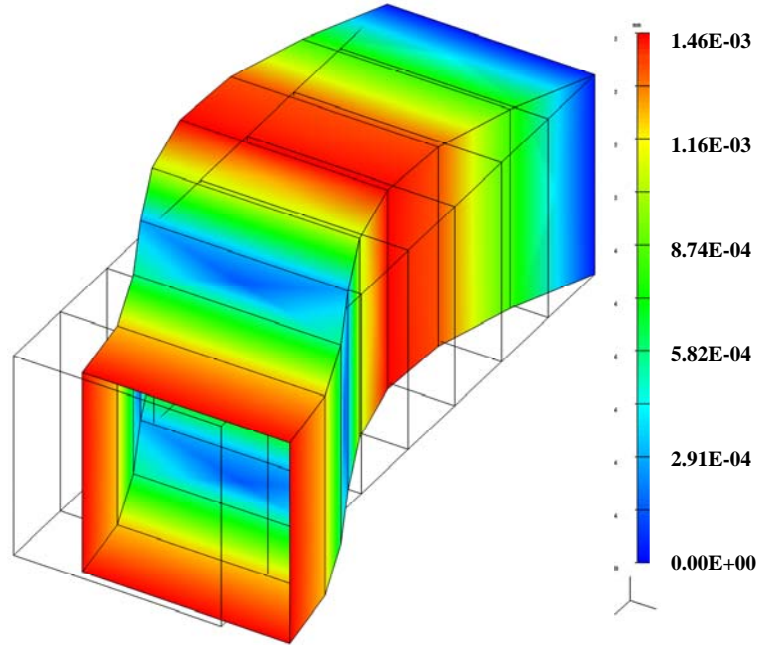


**Fig. 16. Test Case – Modal Analysis of Beam Modeled with Shear Panels, Mode 4, NASTRAN,  
Frequency = 55.146 Hz**

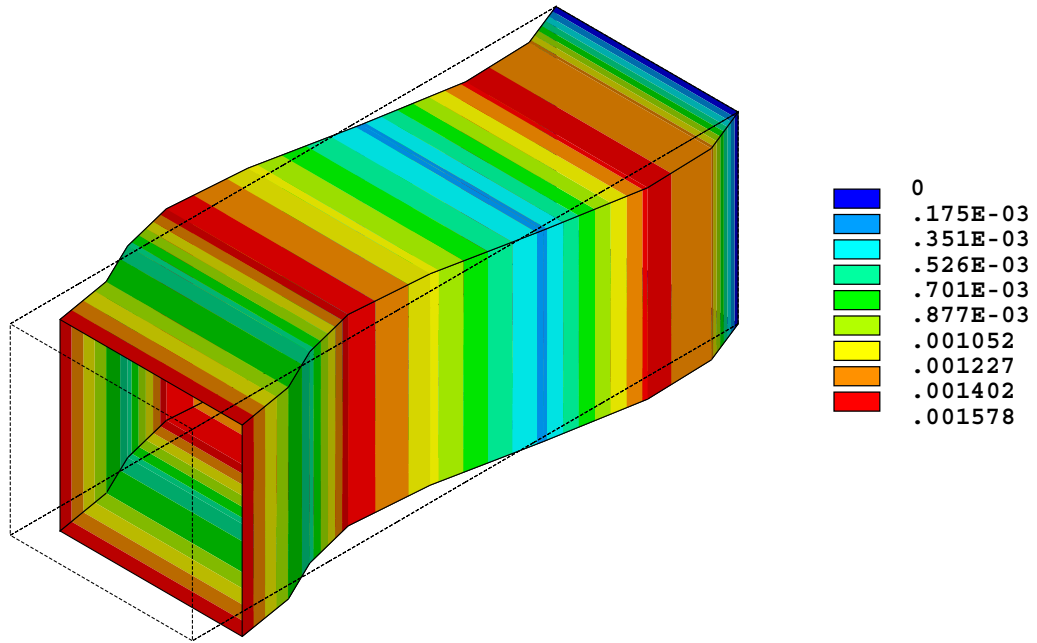


**Fig. 17. Test Case – Modal Analysis of Beam Modeled with Shear Panels, Mode 5, ANSYS, Frequency = 89.552 Hz**

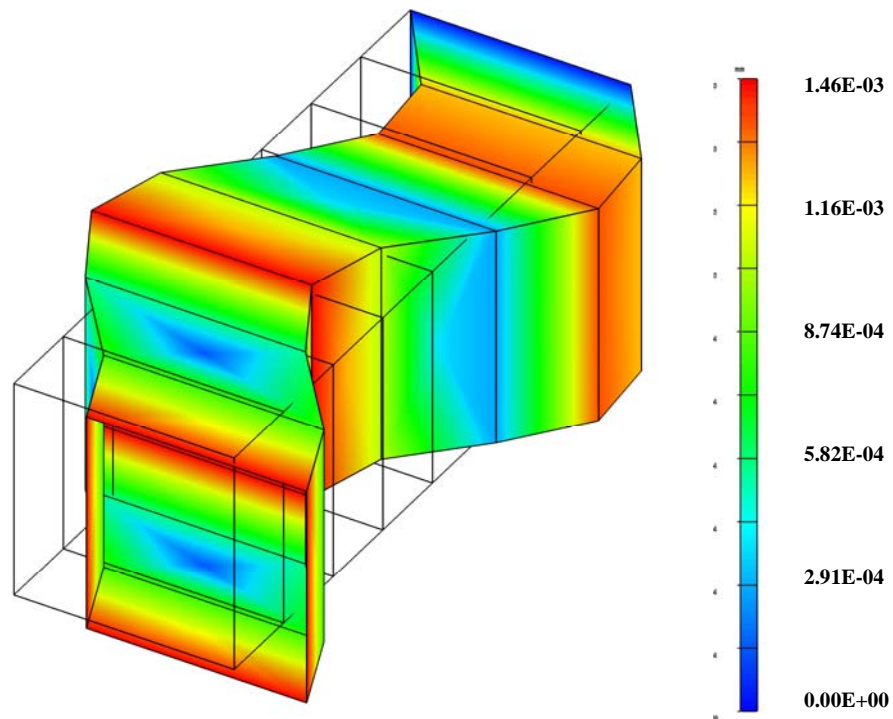


**Fig. 18. Test Case – Modal Analysis of Beam Modeled with Shear Panels, Mode 5, ANSYS, Frequency = 89.552 Hz**

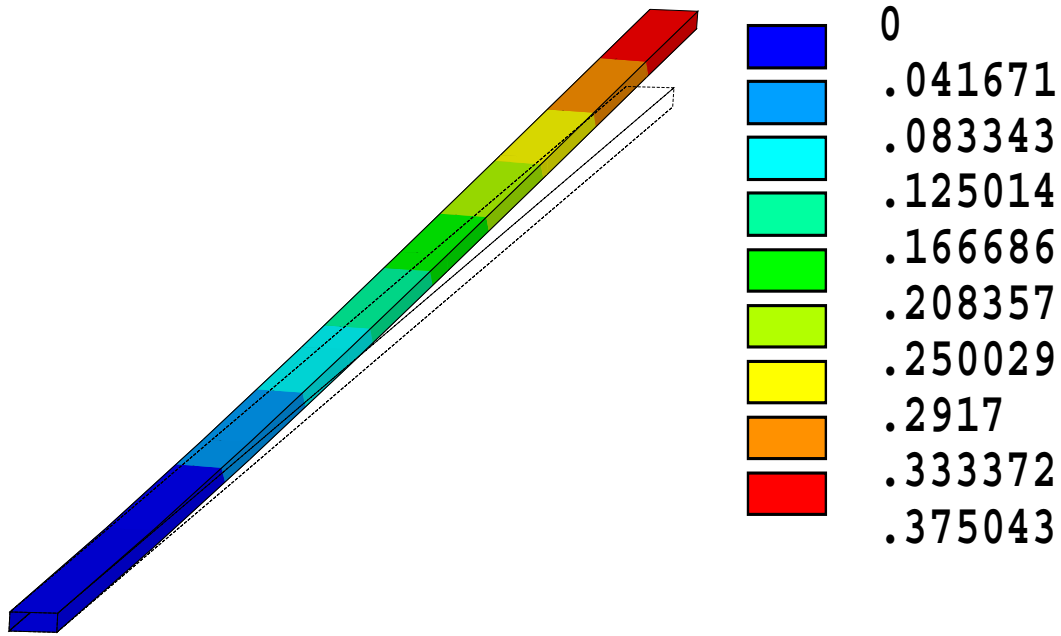


**Fig. 19. Test Case – Modal Analysis of Beam Modeled with Shell Elements, Mode 1, ANSYS,  
Frequency = 1.1364 Hz**

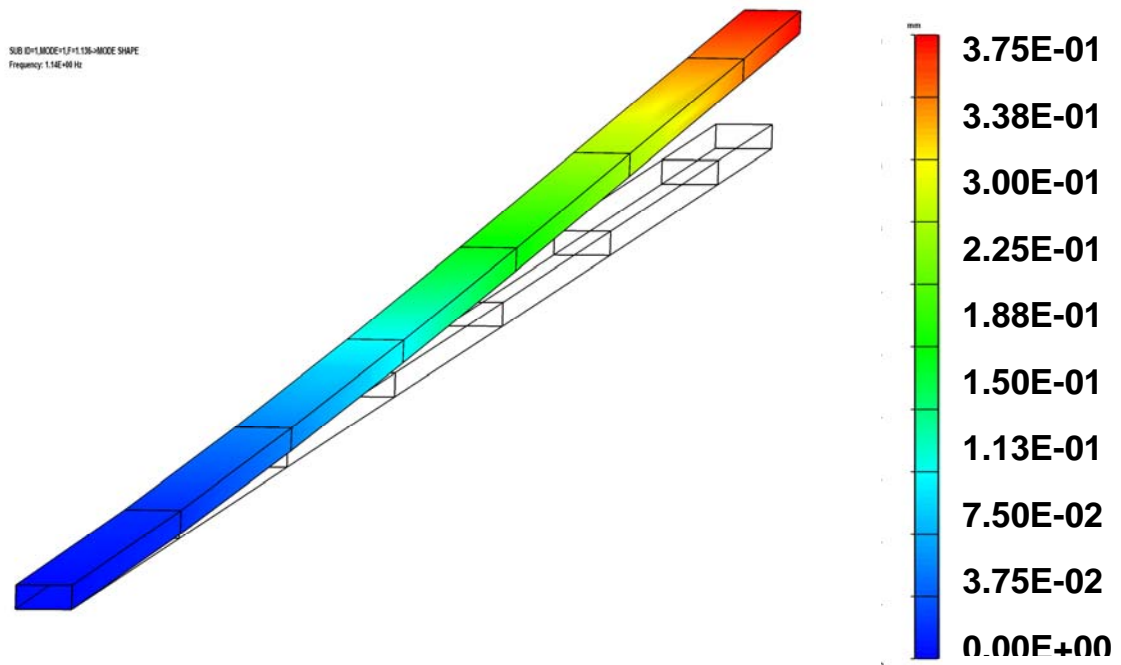


**Fig. 20. Test Case – Modal Analysis of Beam Modeled with Shell Elements, Mode 1, NASTRAN,  
Frequency = 1.1364 Hz**

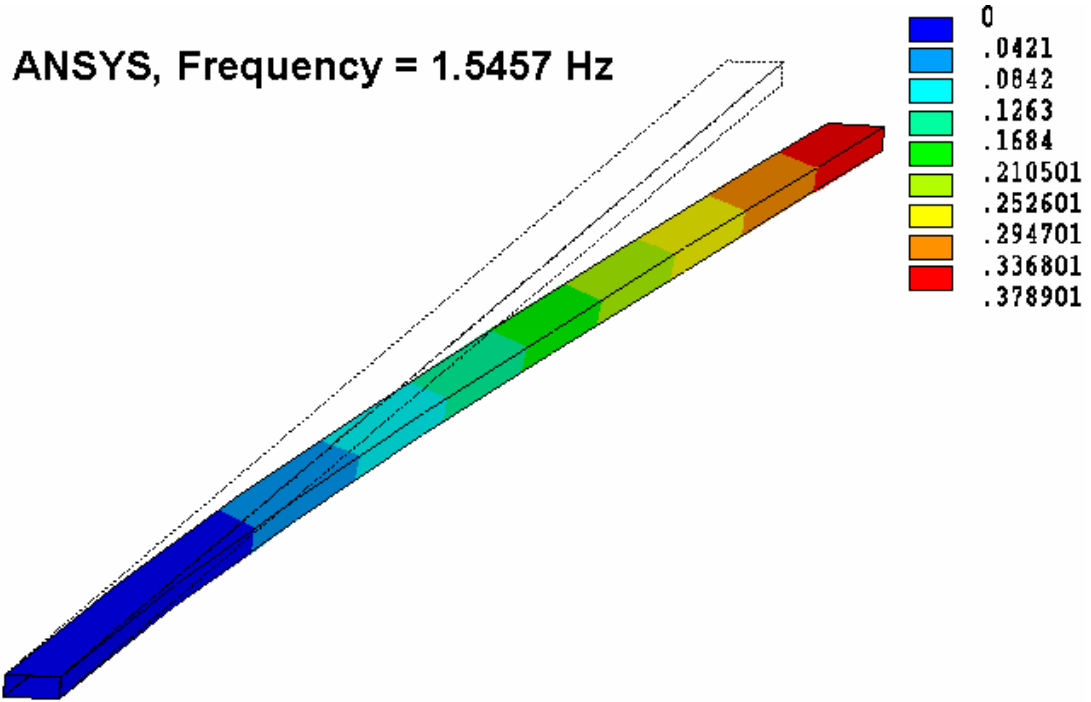


**Fig. 21. Test Case – Modal Analysis of Beam Modeled with Shell Elements, Mode 2, ANSYS,  
Frequency = 1.5457 Hz**

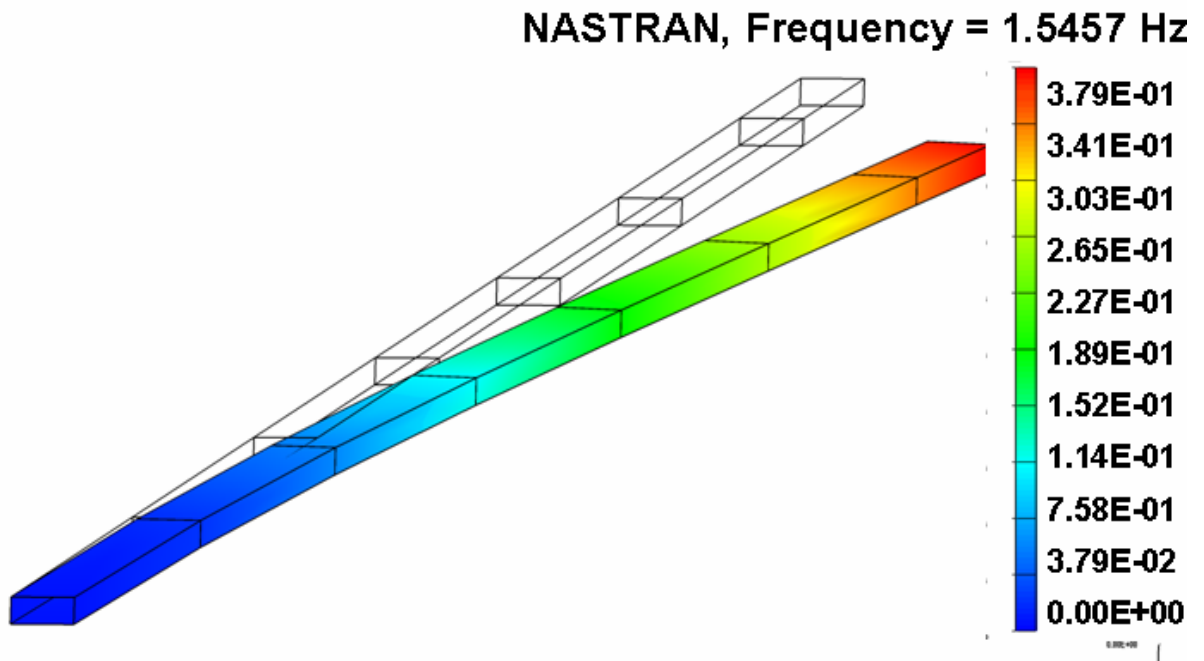


**Fig. 22. Test Case – Modal Analysis of Beam Modeled with Shell Elements, Mode 2, NASTRAN,  
Frequency = 1.5457 Hz**

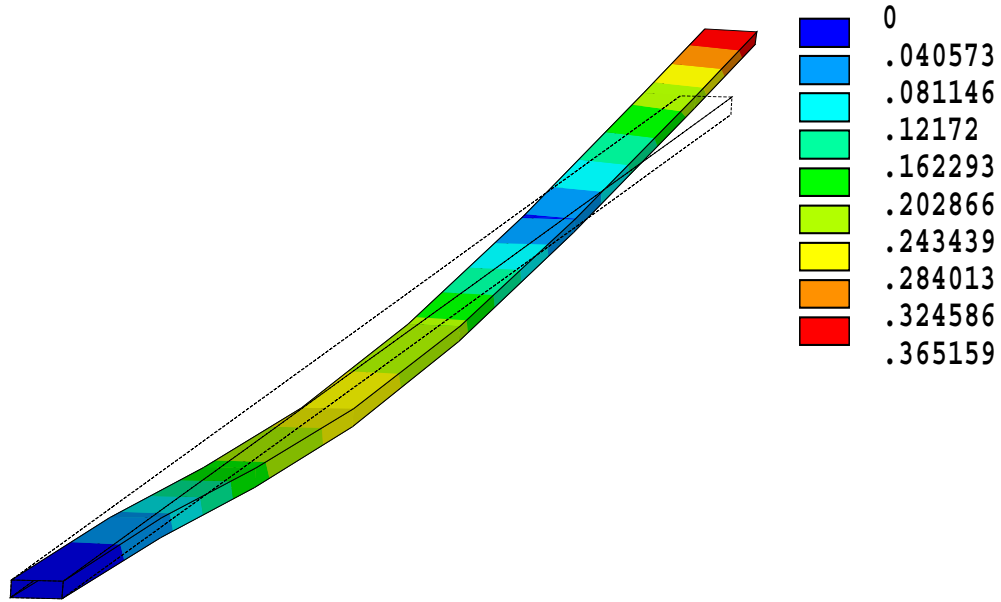


**Fig. 23. Test Case – Modal Analysis of Beam Modeled with Shell Elements, Mode 3, ANSYS, Frequency = 7.1222 Hz**

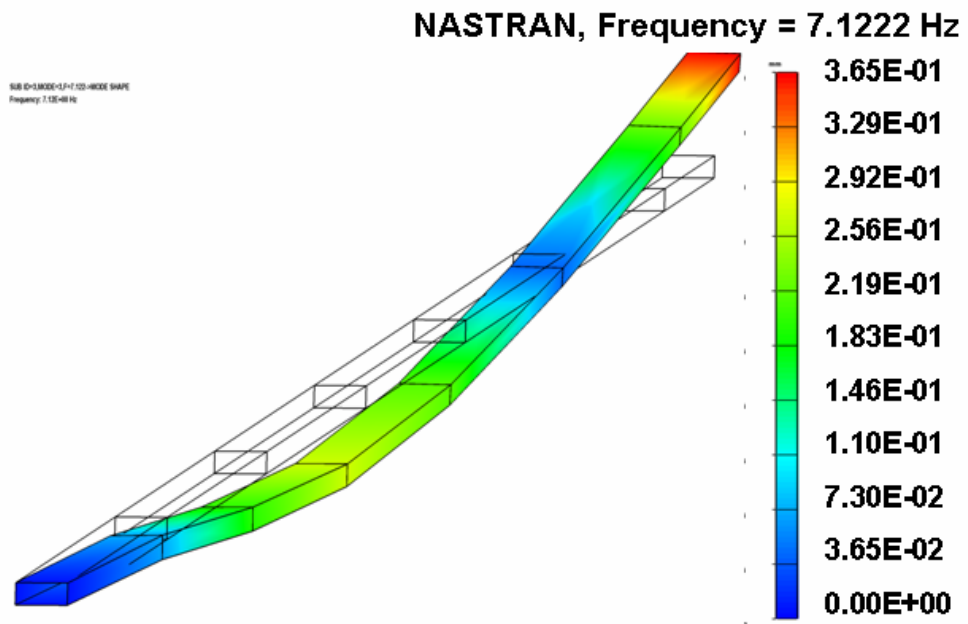


**Fig. 24. Test Case – Modal Analysis of Beam Modeled with Shell Elements, Mode 3, NASTRAN, Frequency = 7.1222 Hz**

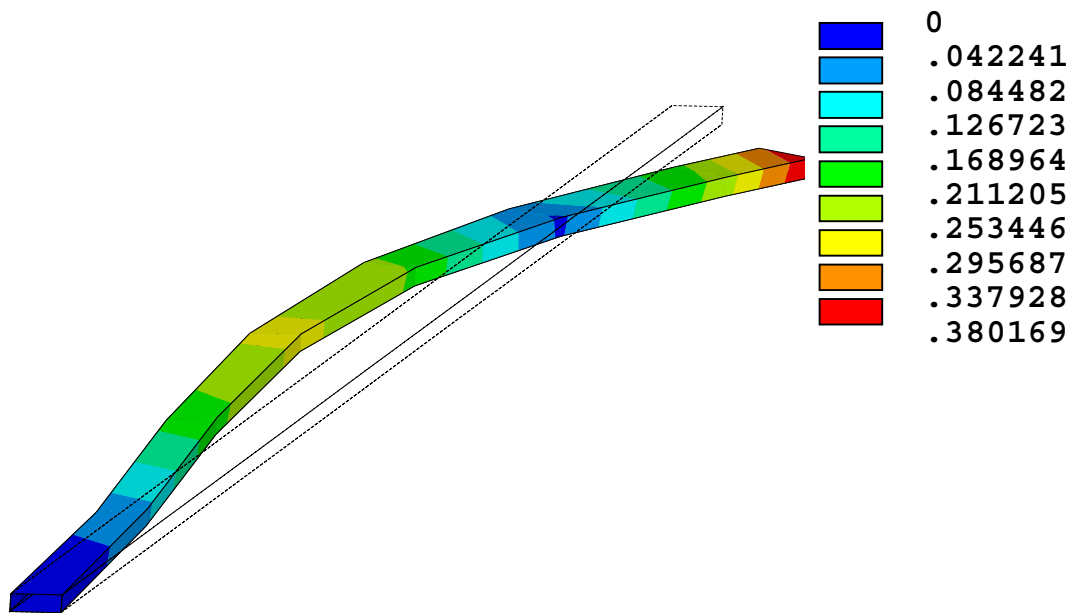


**Fig. 25. Test Case – Modal Analysis of Beam Modeled with Shell Elements, Mode 4, ANSYS,  
 Frequency = 9.6867 Hz**

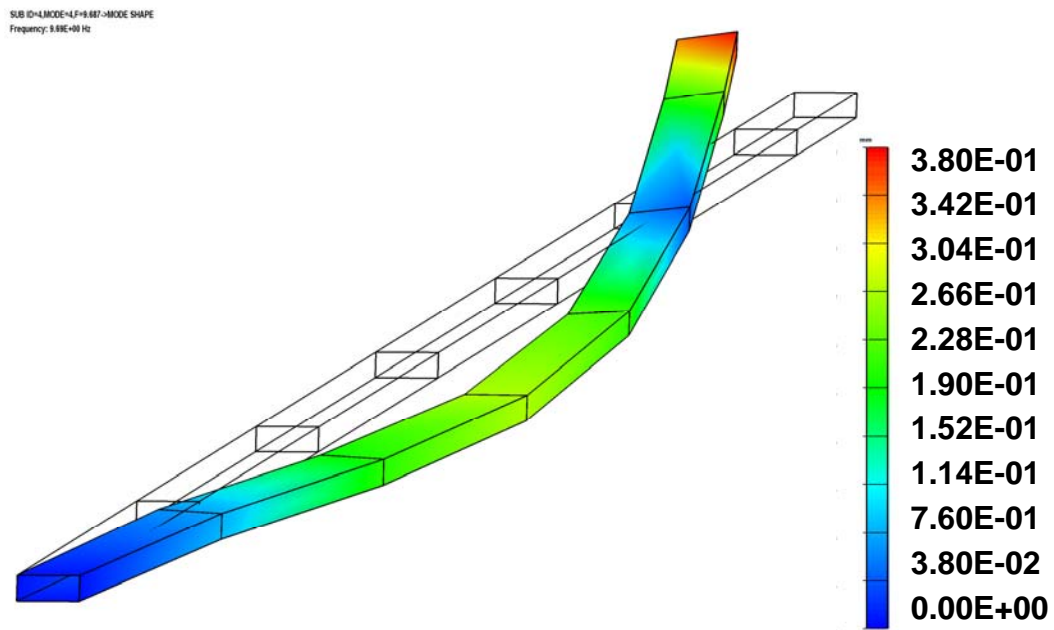


**Fig. 26. Test Case – Modal Analysis of Beam Modeled with Shell Elements, Mode 4, NASTRAN,  
 Frequency = 9.6867 Hz**

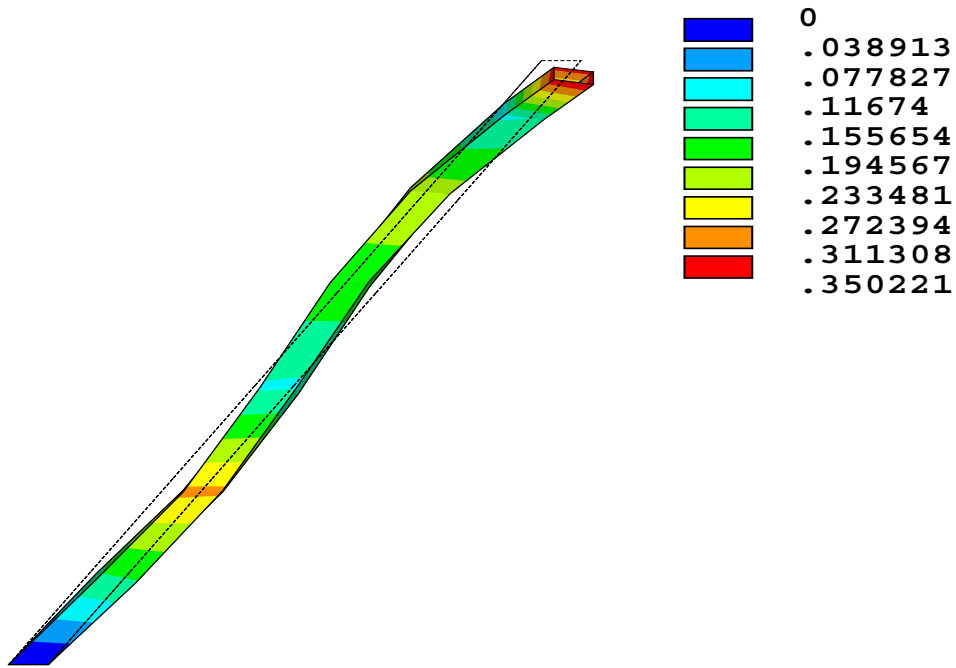


**Fig. 27. Test Case – Modal Analysis of Beam Modeled with Shell Elements, Mode 5, ANSYS,  
Frequency = 20.476 Hz**

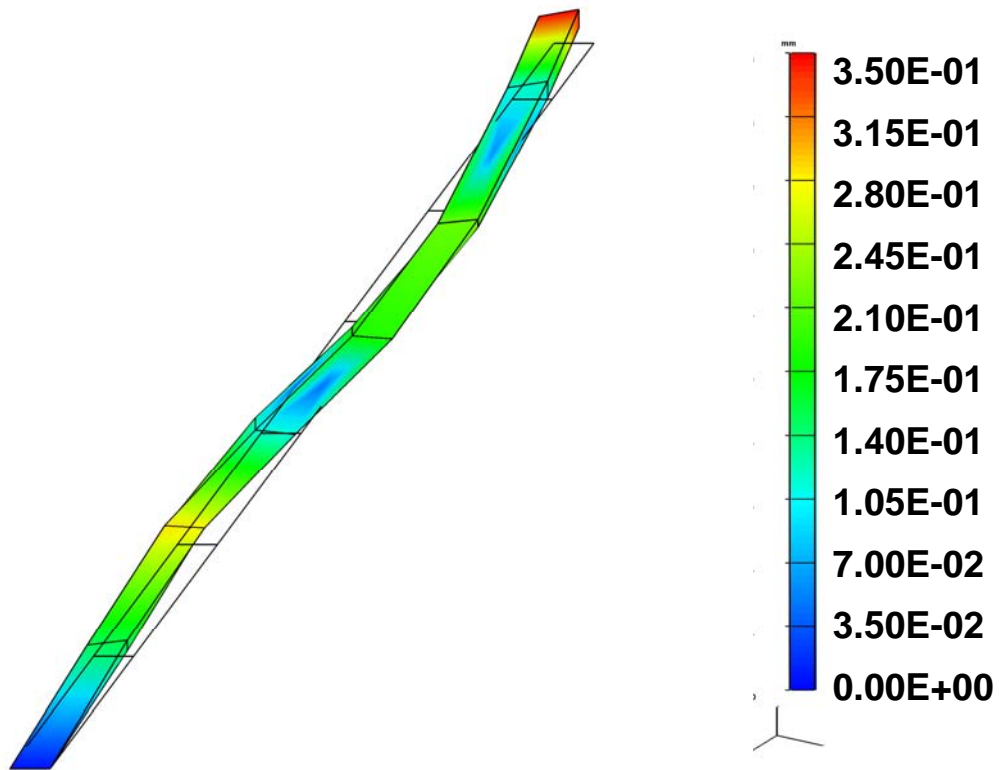


**Fig. 28. Test Case – Modal Analysis of Beam Modeled with Shell Elements, Mode 5, NASTRAN,  
Frequency = 20.476 Hz**

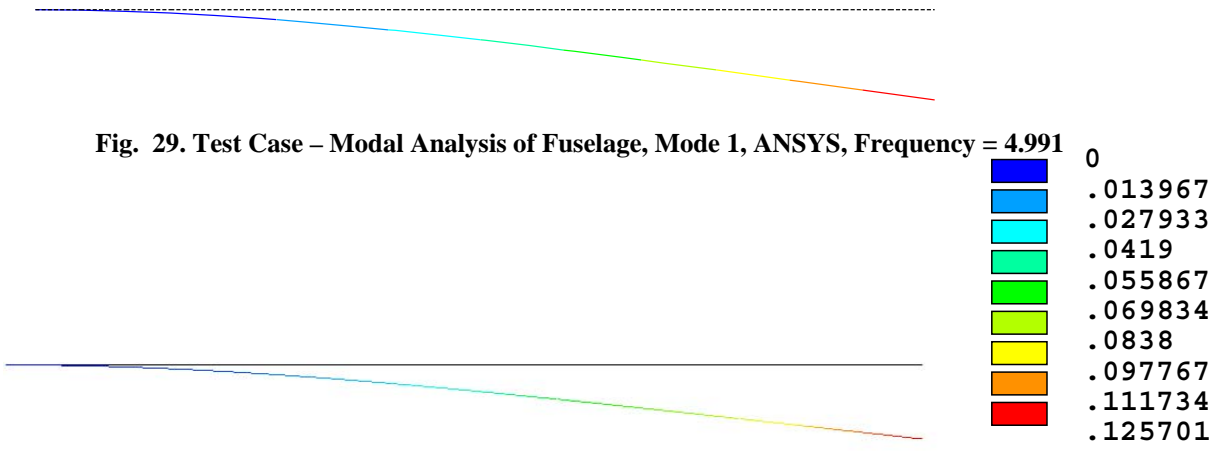


Fig. 30. Test Case – Modal Analysis of Fuselage, Mode 1, NASTRAN, Frequency = 4.991

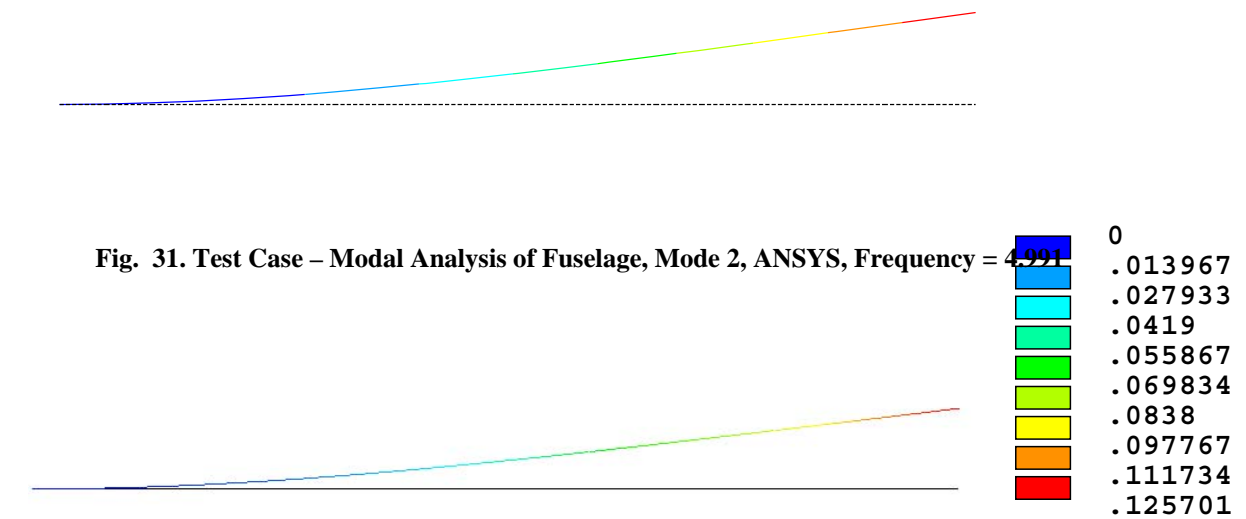


Fig. 32. Test Case – Modal Analysis of Fuselage, Mode 2, NASTRAN, Frequency = 4.991

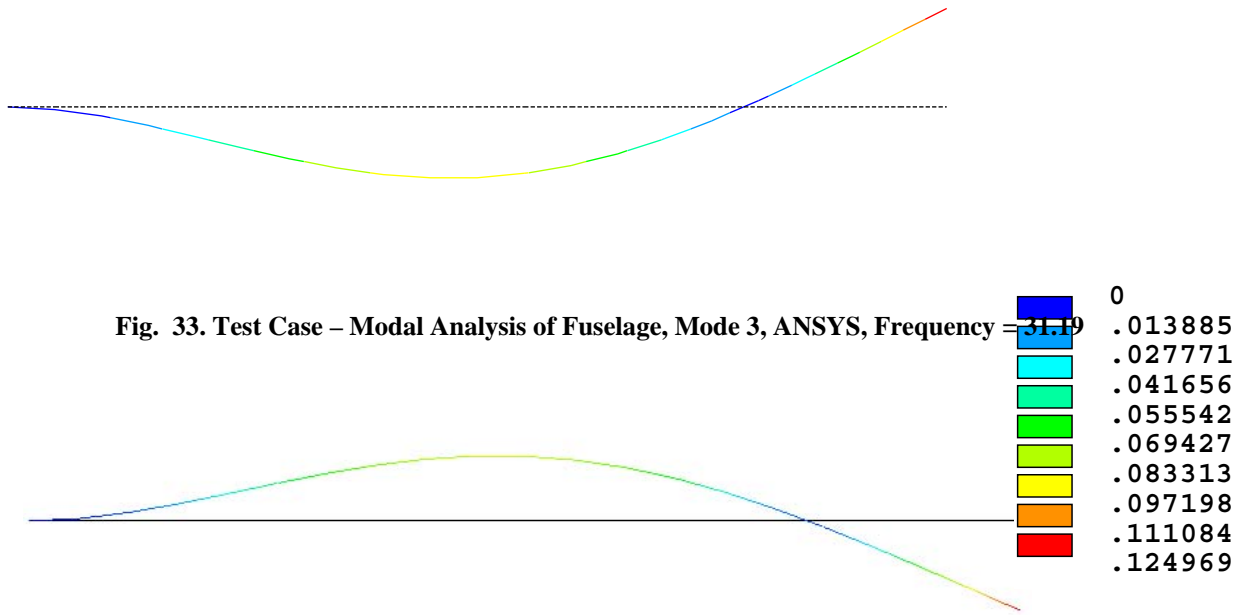


Fig. 34. Test Case – Modal Analysis of Fuselage, Mode 3, NASTRAN, Frequency = 31.19

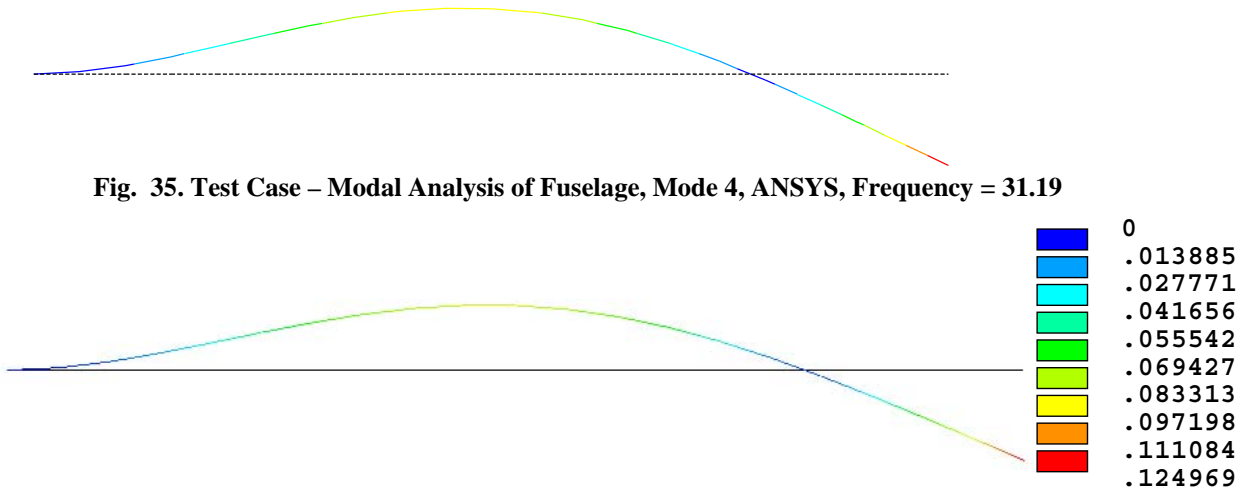


Fig. 36. Test Case – Modal Analysis of Fuselage, Mode 4, NASTRAN, Frequency = 31.19

Fig. 37. Test Case – Modal Analysis of Fuselage, Mode 5, ANSYS, Frequency = 52.78

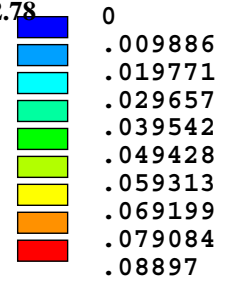


Fig. 38. Test Case – Modal Analysis of Fuselage, Mode 5, NASTRAN, Frequency = 52.78

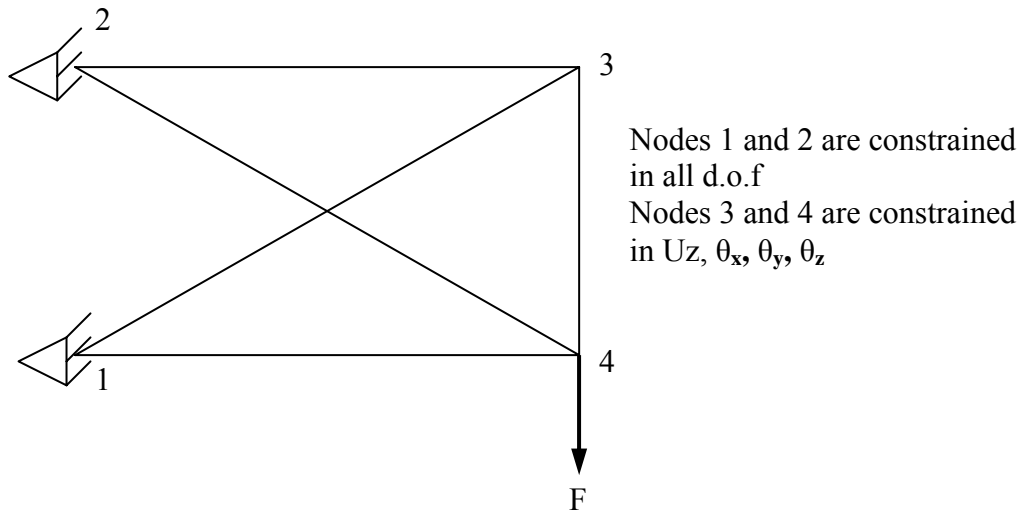
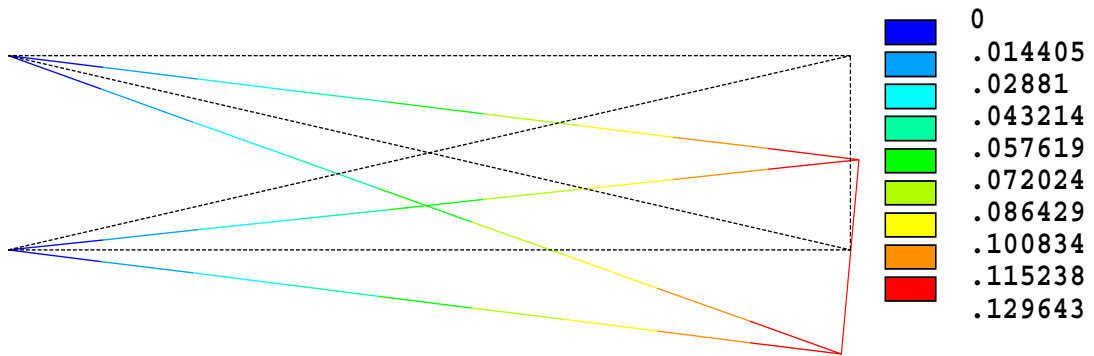
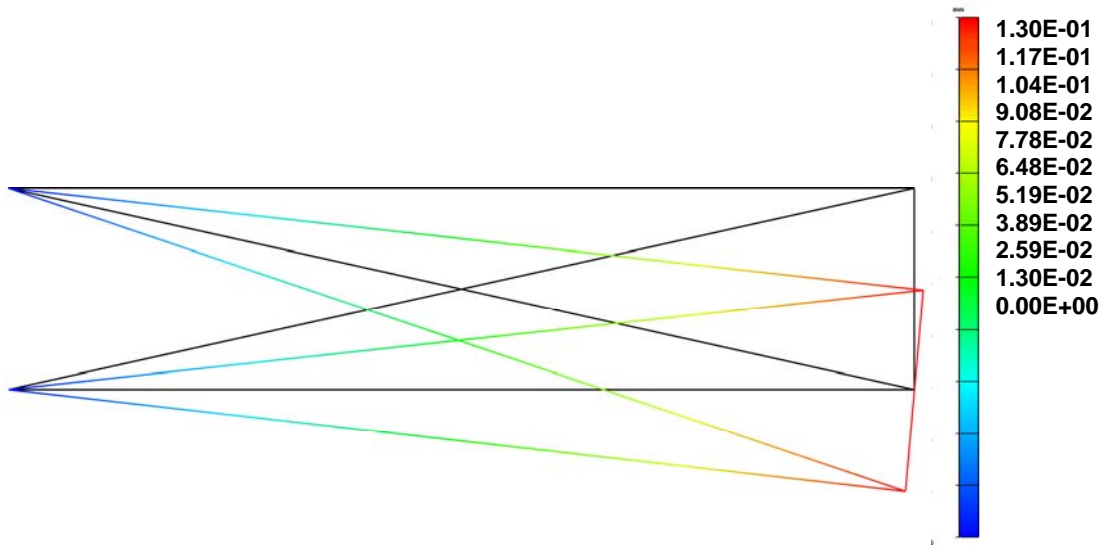


Fig. 39. Test Case – Static Analysis of Truss Modeled with Rods



**Fig. 40. Test Case – Static Analysis of Truss Modeled with Rods in ANSYS-Displacement Contours**



**Fig. 41. Test Case – Static Analysis of Truss Modeled with Rods in NASTRAN-Displacement Contours**

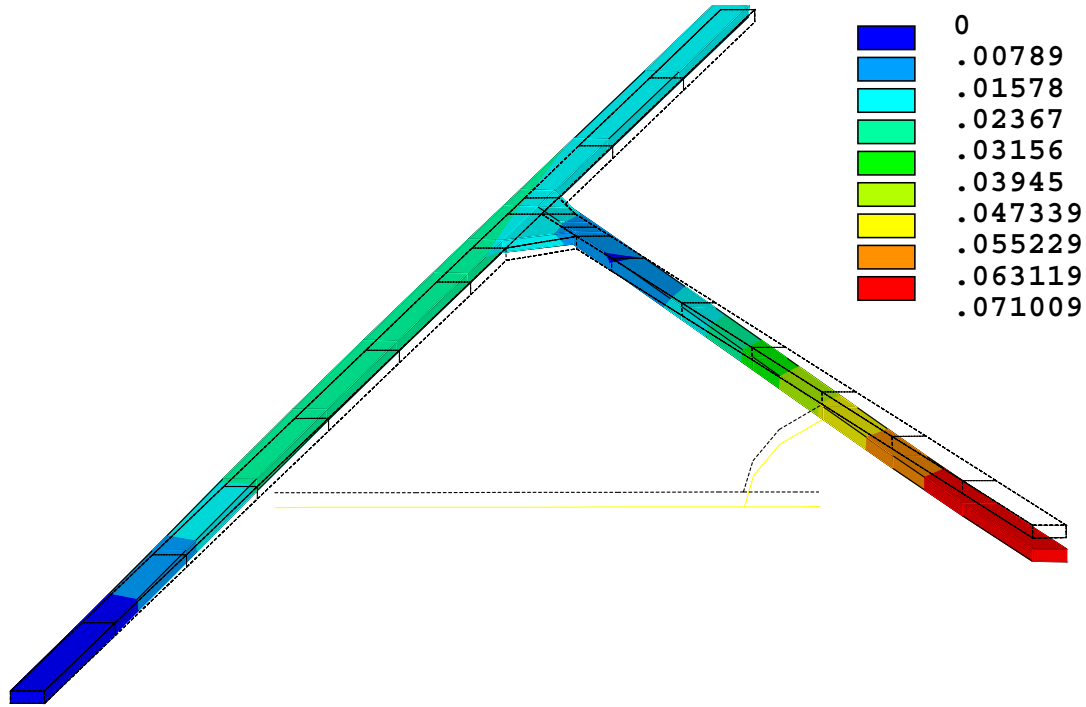


Fig. 42. Mode 1 for Clamped BC with RBEs and Fuselage using ANSYS, Freq. = 0.65405 Hz

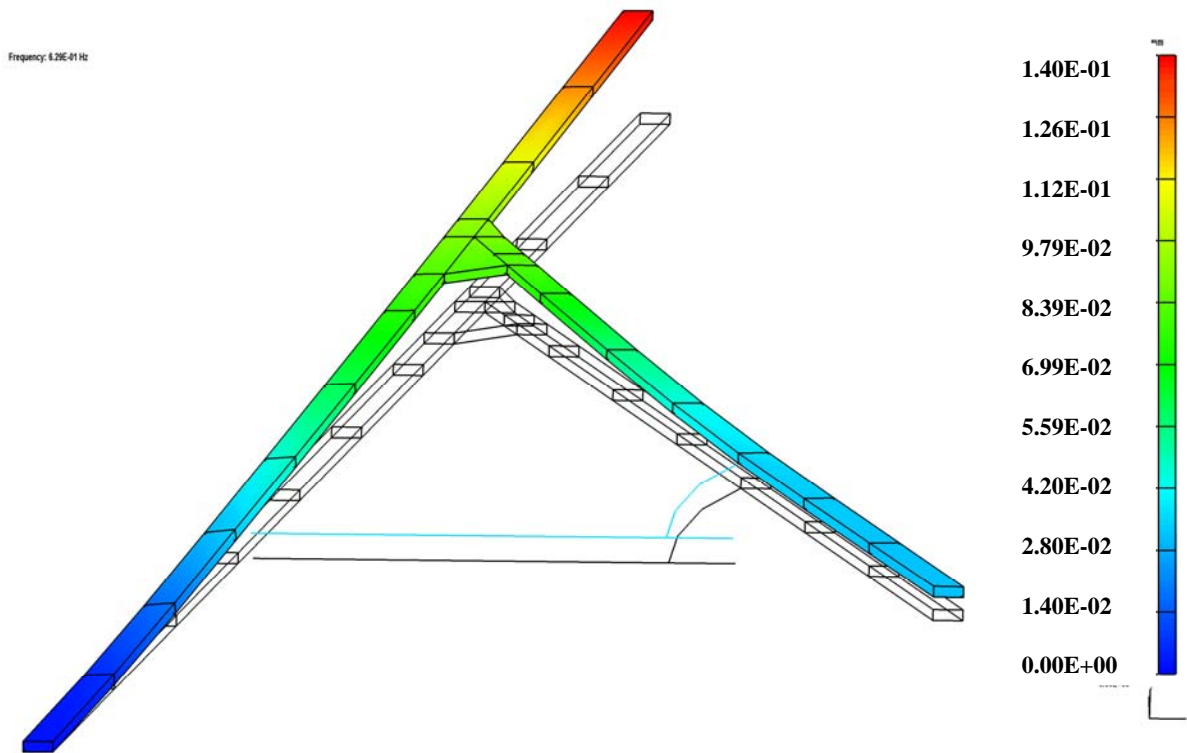


Fig. 43. Mode 1 for Clamped BC with RBEs and Fuselage using NASTRAN, Freq. = 0.6288 Hz

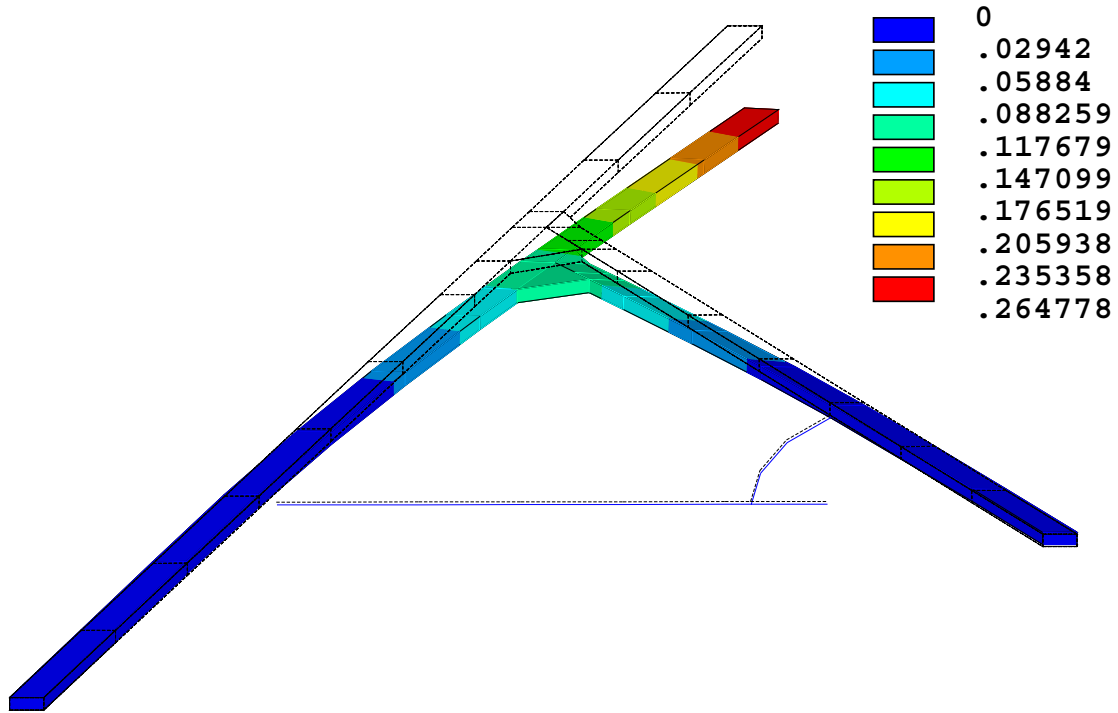


Fig. 44. Mode 2 for Clamped BC with RBEs and Fuselage using ANSYS, Freq. = 1.0817 Hz

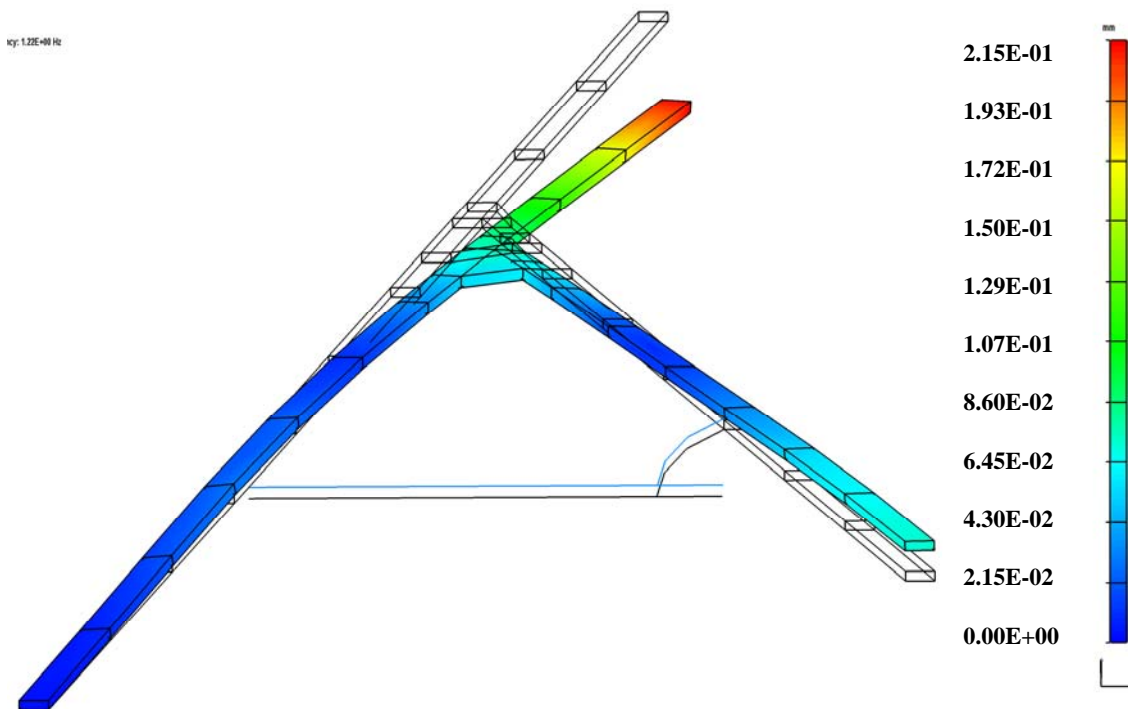


Fig. 45. Mode 2 for Clamped BC with RBEs and Fuselage using NASTRAN, Freq. = 1.2182 Hz

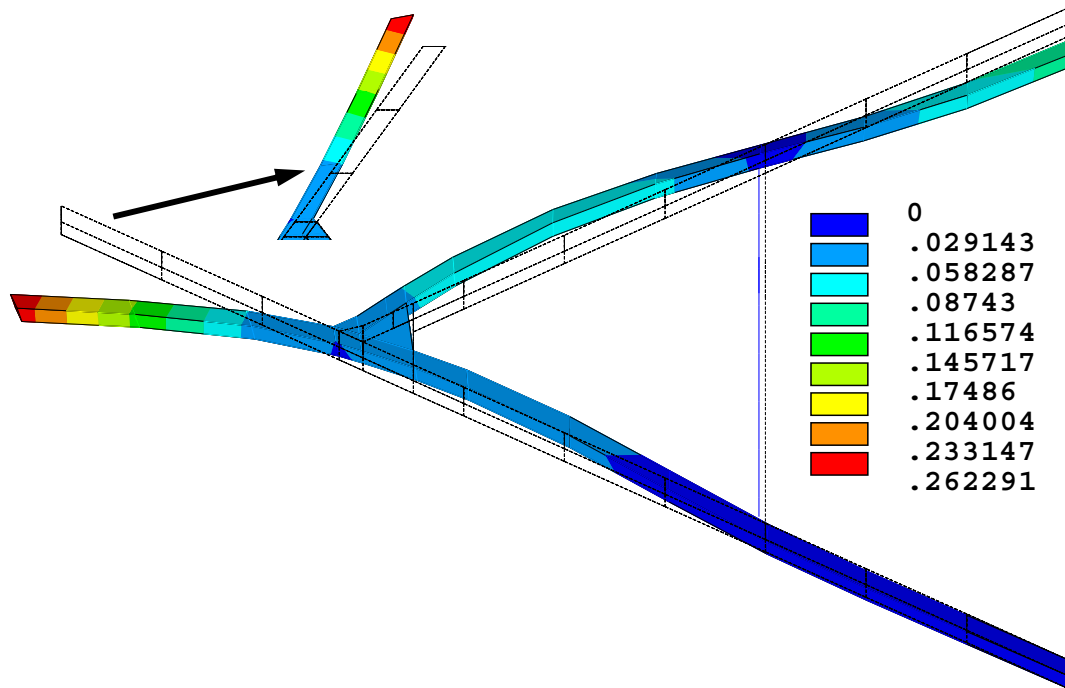


Fig. 46. Mode 3 for Clamped BC with RBEs and Fuselage using ANSYS, Freq. = 2.8953 Hz

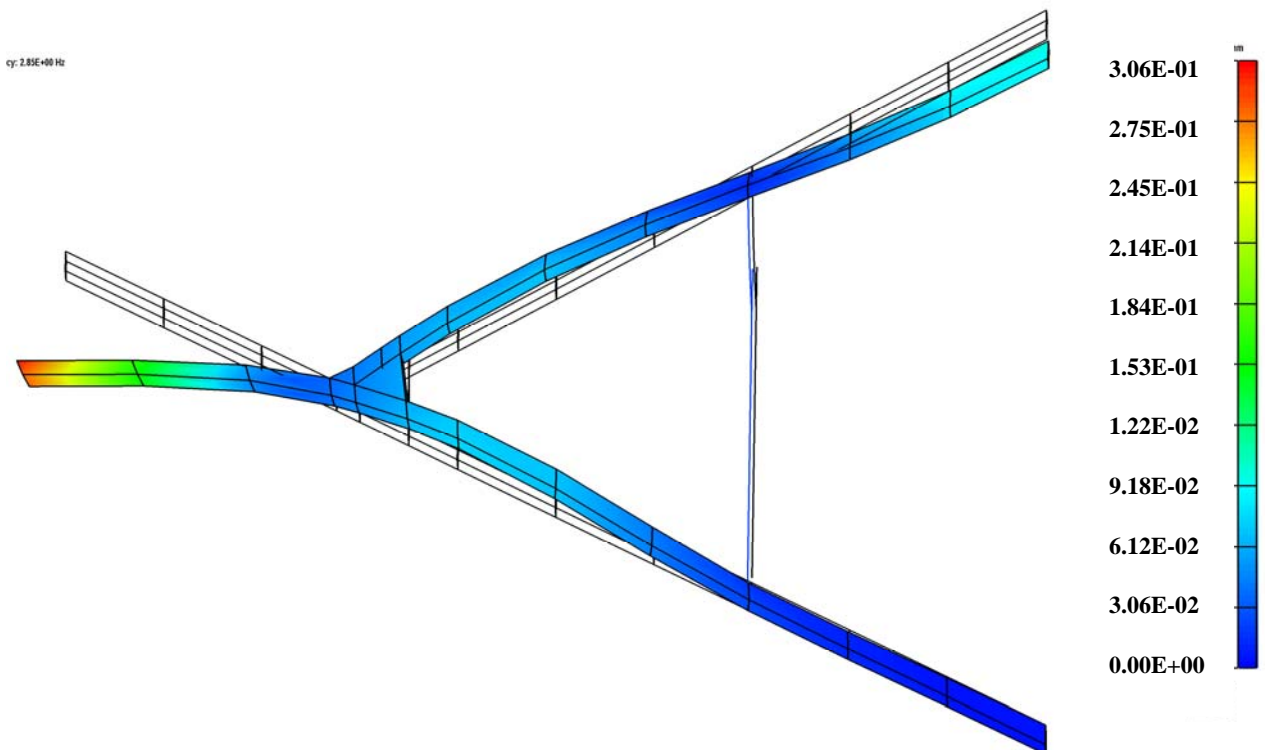


Fig. 47. Mode 3 for Clamped BC with RBEs and Fuselage using NASTRAN, Freq. = 2.8504 Hz

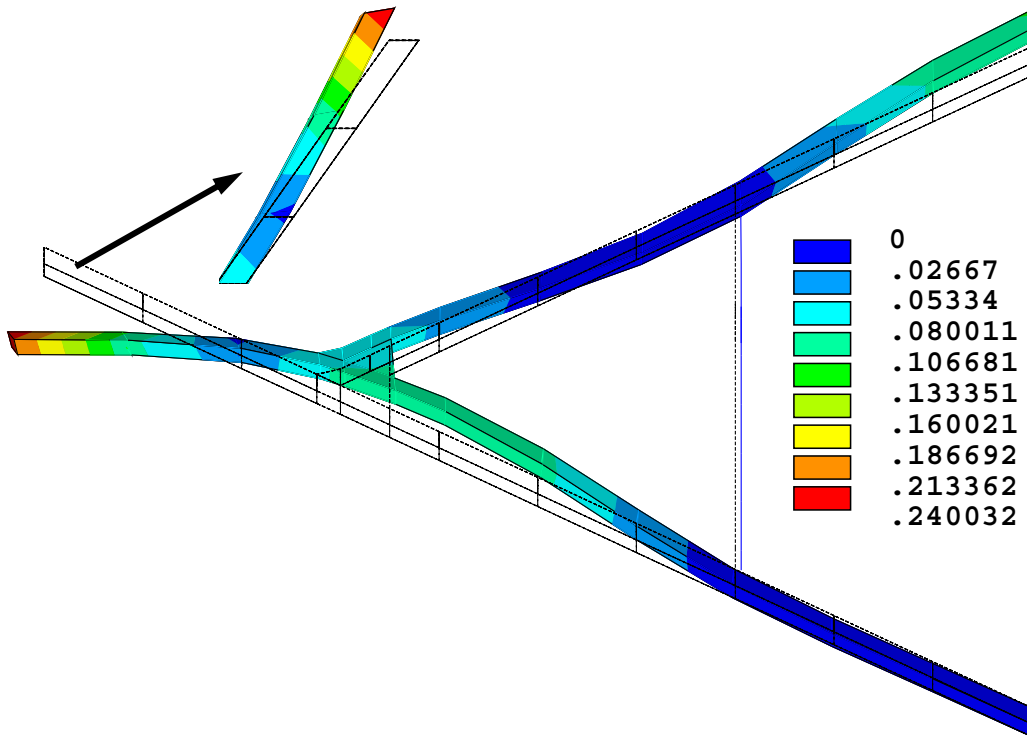


Fig. 48. Mode 4 for Clamped BC with RBEs and Fuselage using ANSYS, Freq. = 3.5164 Hz

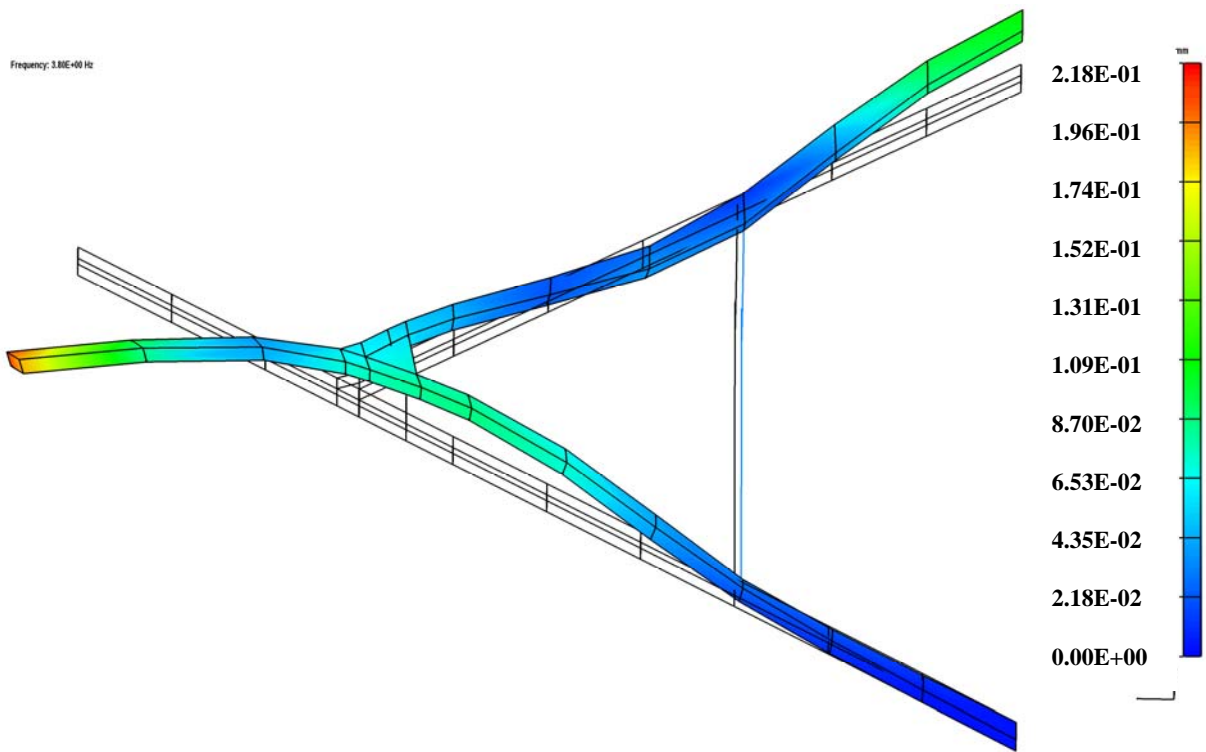


Fig. 49. Mode 4 for Clamped BC with RBEs and Fuselage using NASTRAN, Freq. = 3.8005 Hz

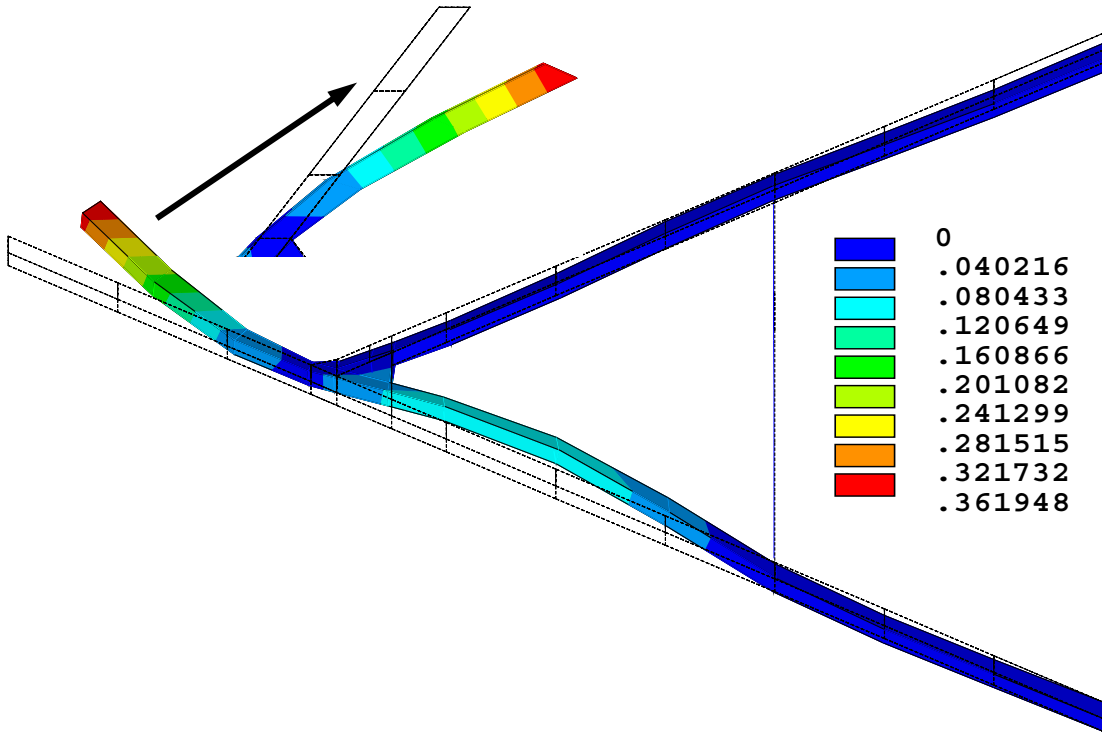


Fig. 50. Mode 5 for Clamped BC with RBEs and Fuselage using ANSYS, Freq. = 6.0775 Hz

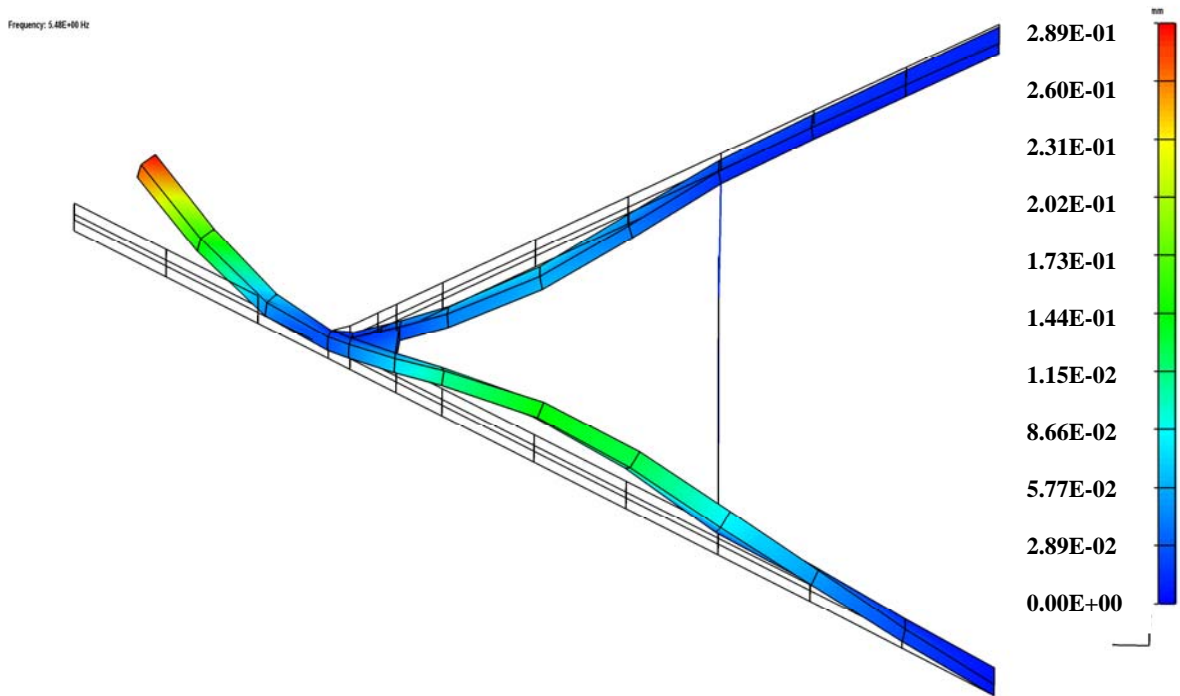


Fig. 51. Mode 5 for Clamped BC with RBEs and Fuselage using NASTRAN, Freq. = 5.4751 Hz

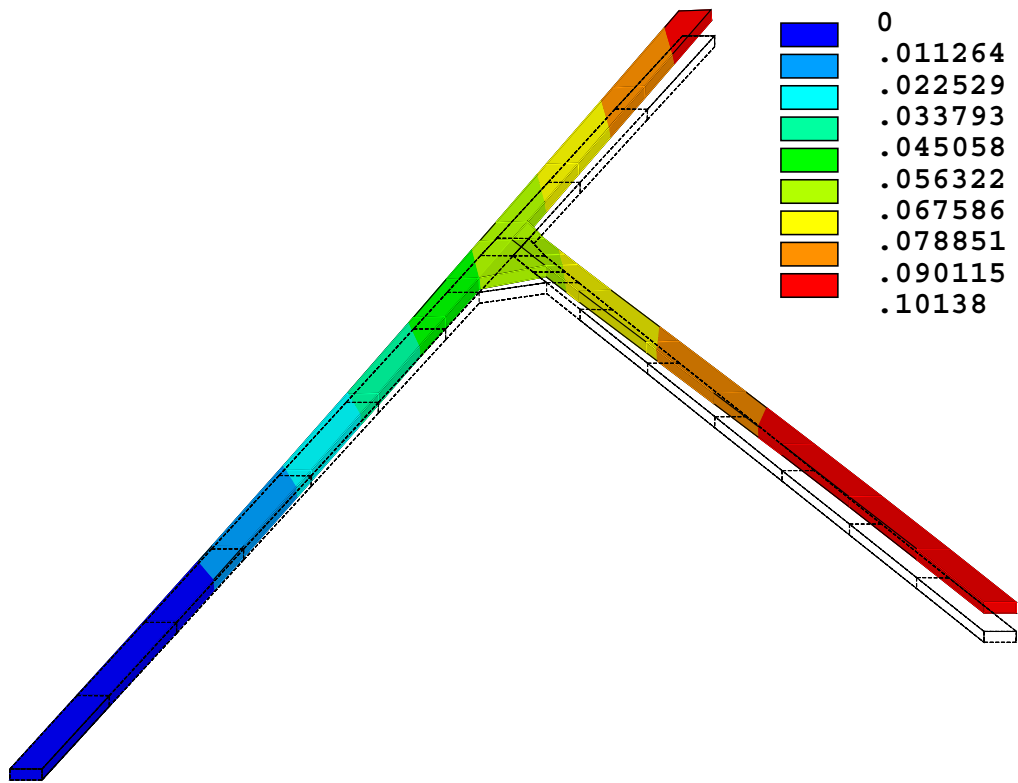


Fig. 52. Mode 1 for Clamped BC without RBEs and Fuselage using ANSYS, Freq. = 0.31542 Hz

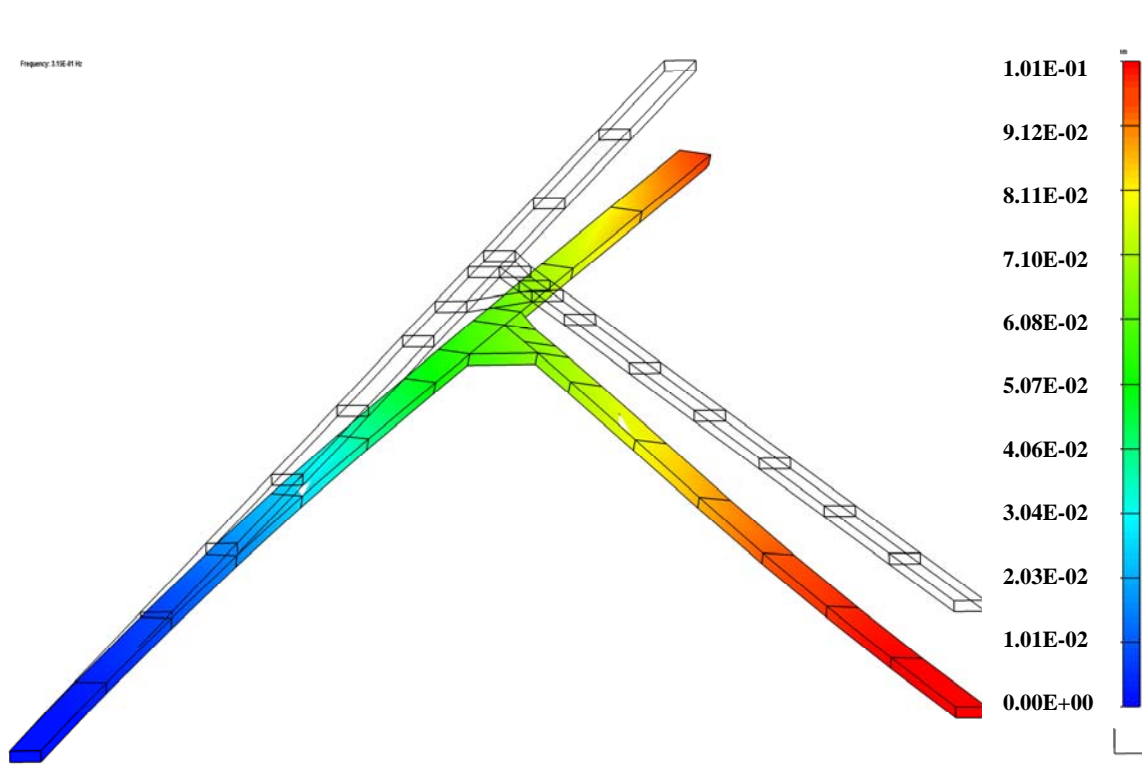


Fig. 53. Mode 1 for Clamped BC without RBEs and Fuselage using NASTRAN, Freq. = 0.31542 Hz

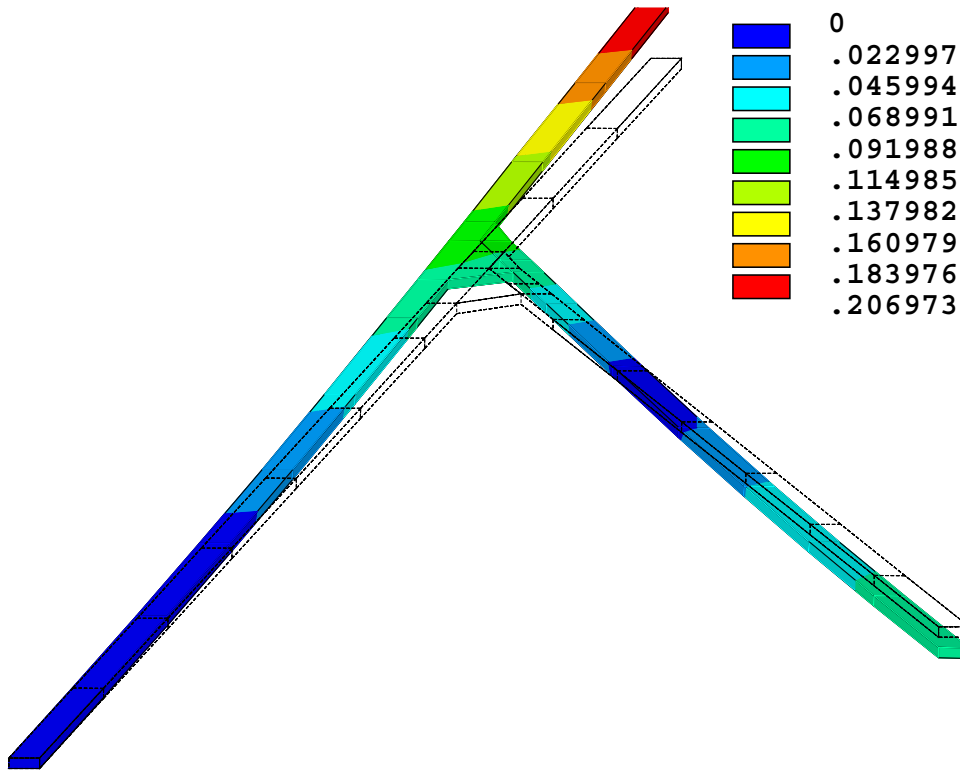


Fig. 54. Mode 2 for Clamped BC without RBEs and Fuselage using ANSYS, Freq. = 0.96808 Hz

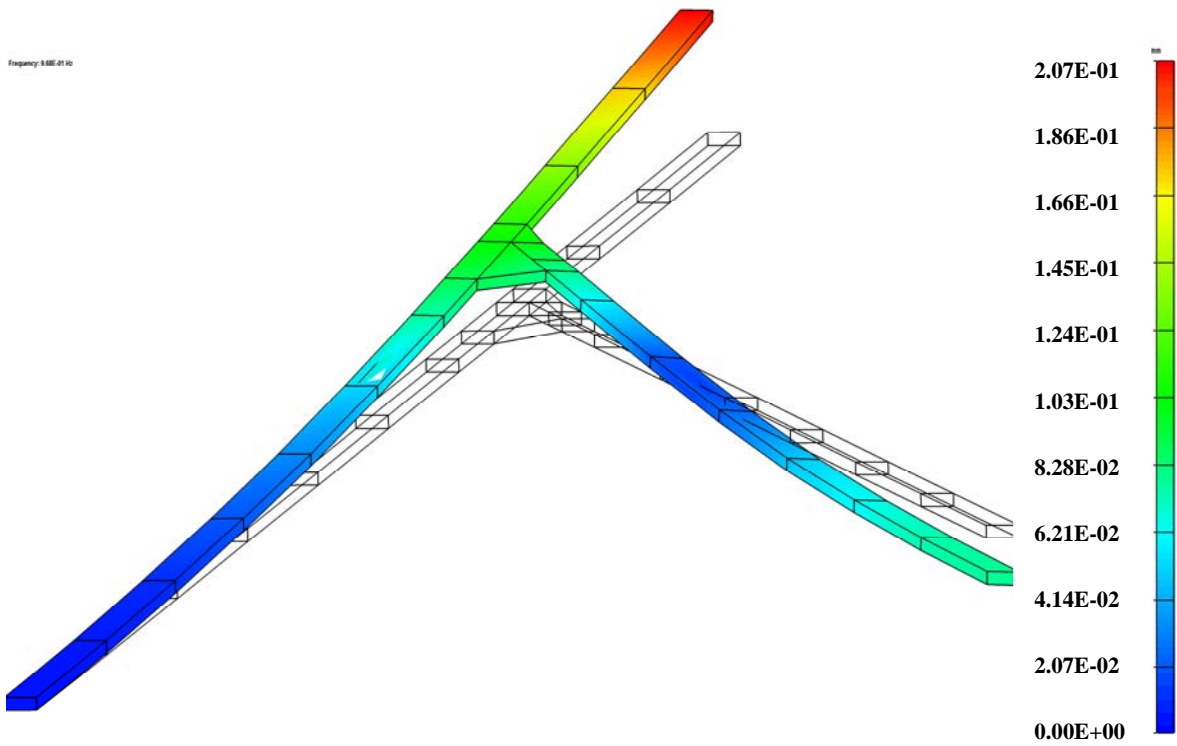


Fig. 55. Mode 2 for Clamped BC without RBEs and Fuselage using NASTRAN, Freq. = 0.96808 Hz

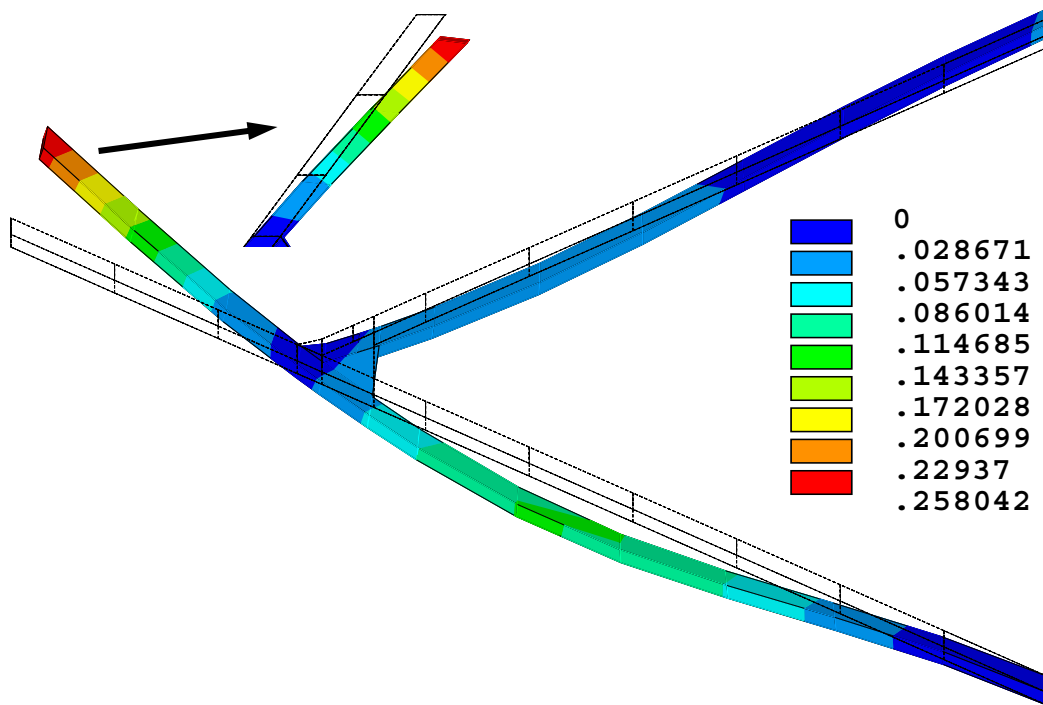


Fig. 56. Mode 3 for Clamped BC without RBEs and Fuselage using ANSYS, Freq. = 2.1069 Hz

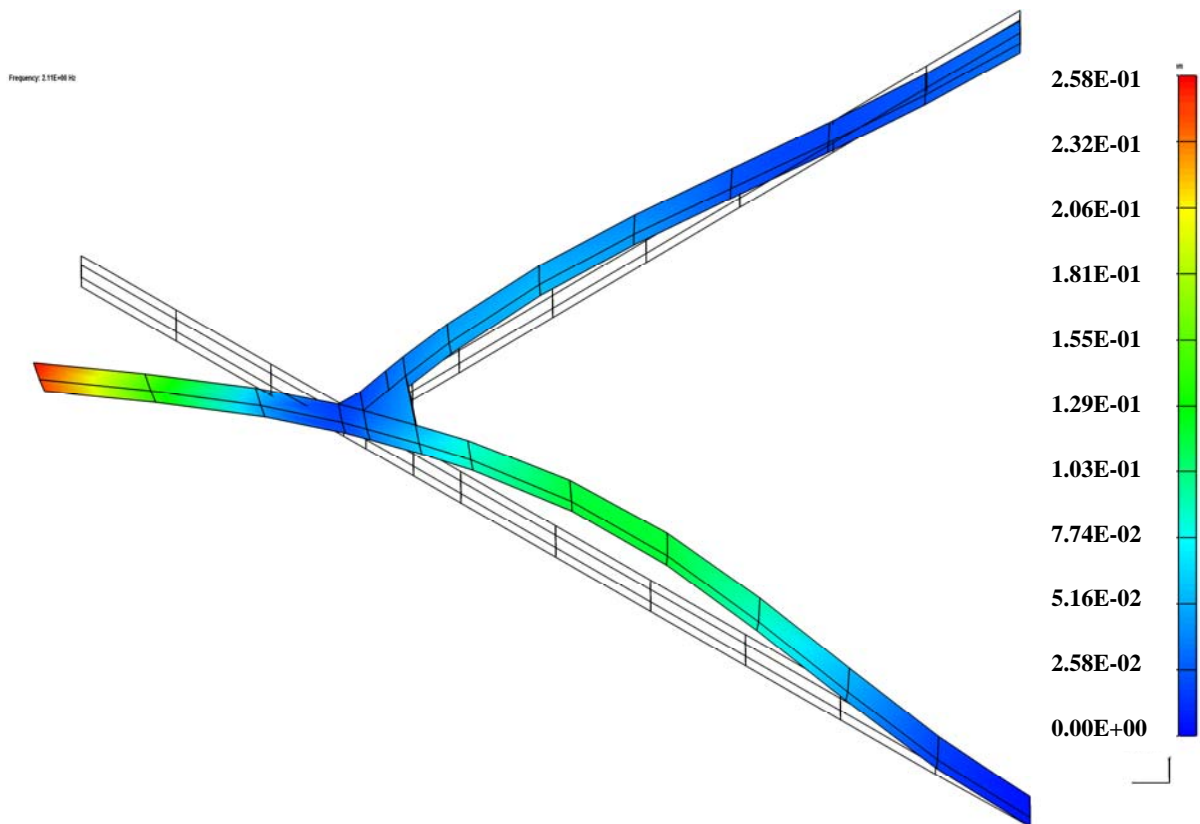


Fig. 57. Mode 3 for Clamped BC without RBEs and Fuselage using NASTRAN, Freq. = 2.1069 Hz

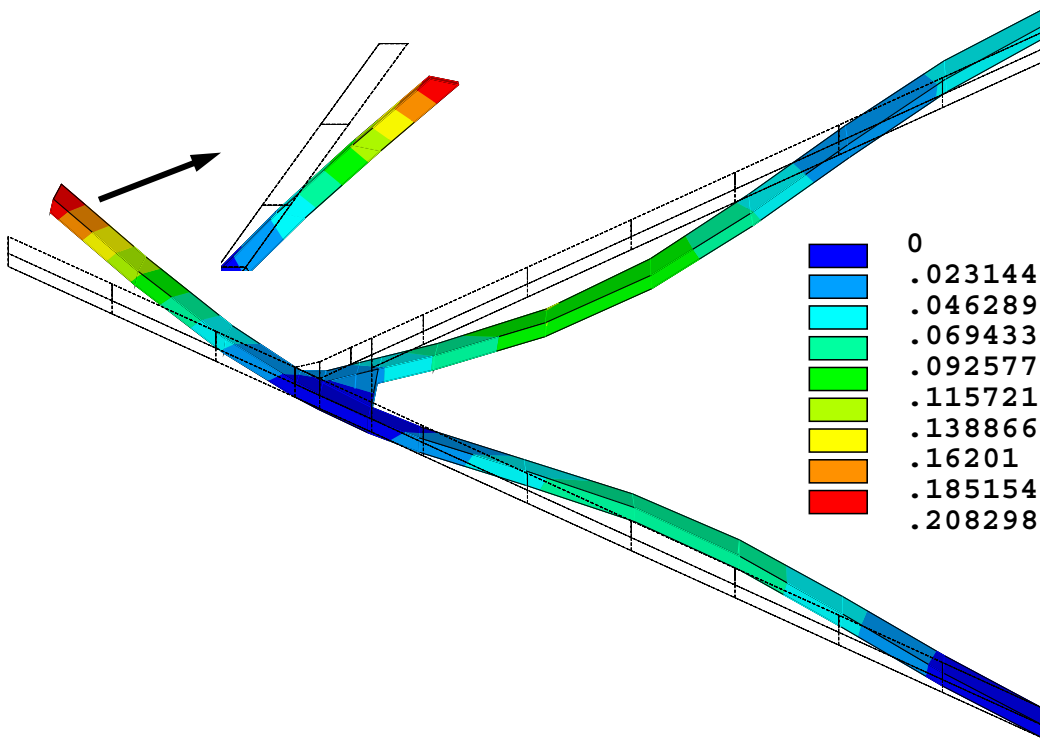


Fig. 58. Mode 4 for Clamped BC without RBEs and Fuselage using ANSYS, Freq. = 3.5759 Hz

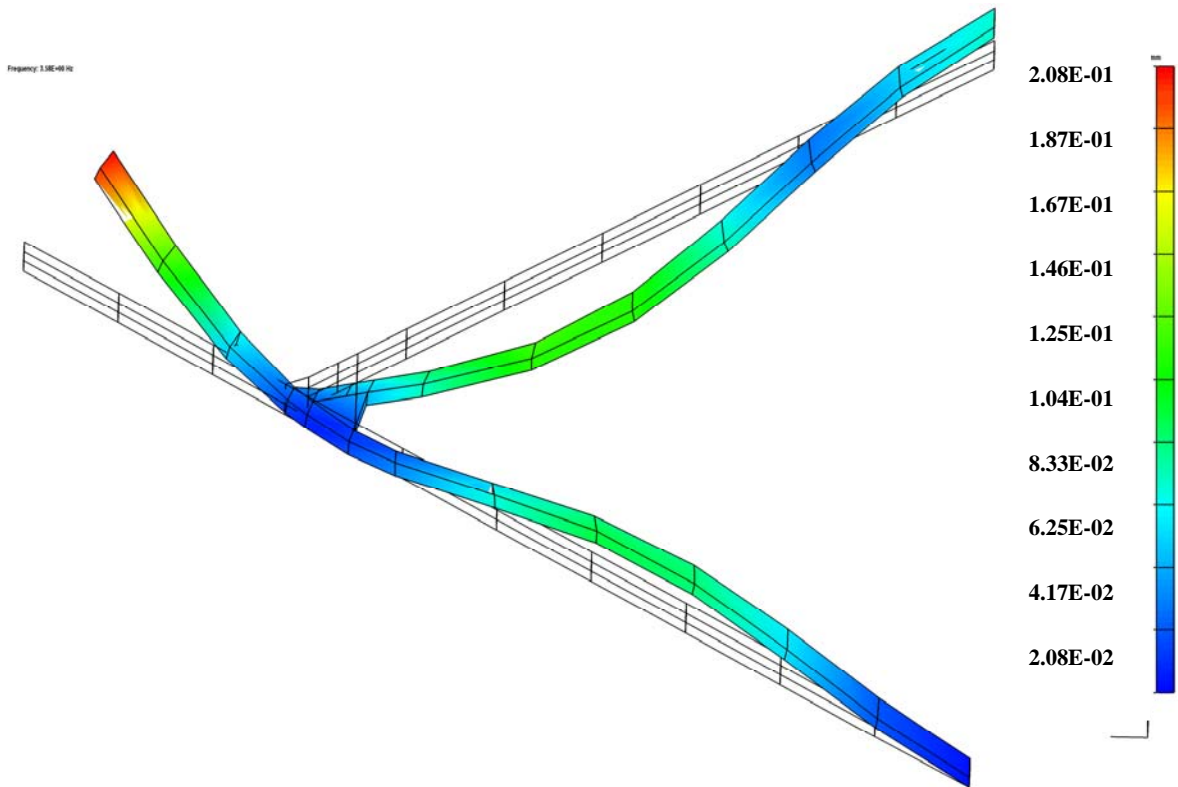


Fig. 59. Mode 4 for Clamped BC without RBEs and Fuselage using NASTRAN, Freq. = 3.5759 Hz

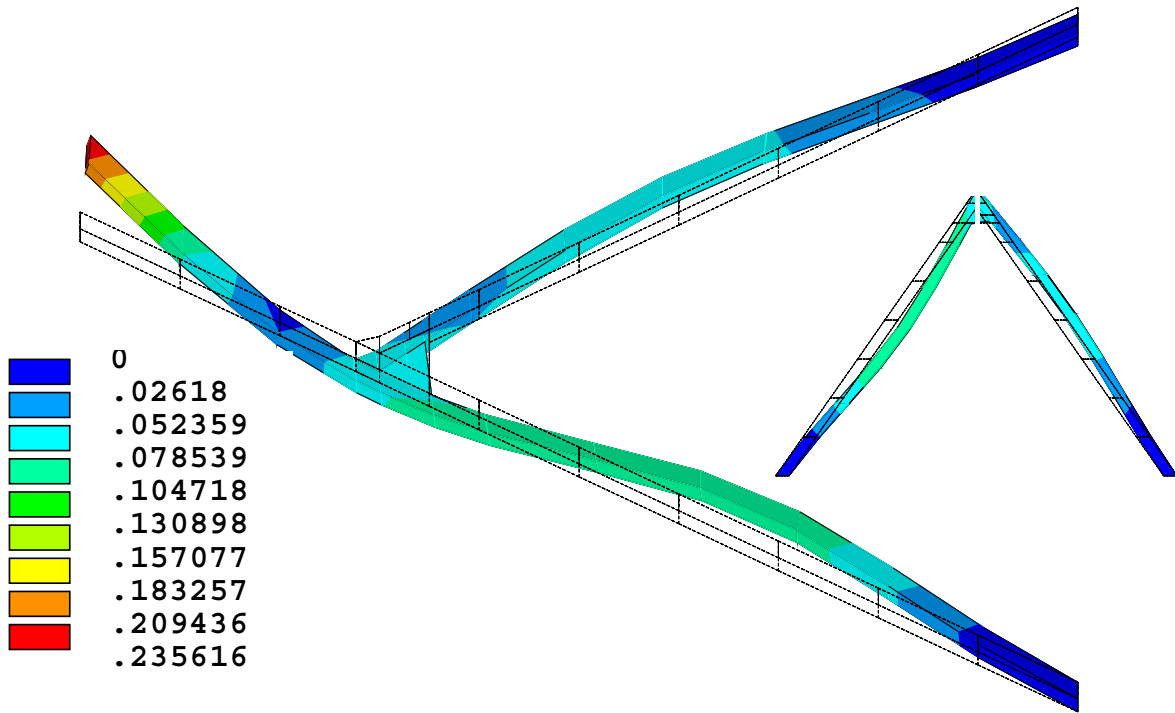


Fig. 60. Mode 5 for Clamped BC without RBEs and Fuselage using ANSYS, Freq. = 4.2019 Hz

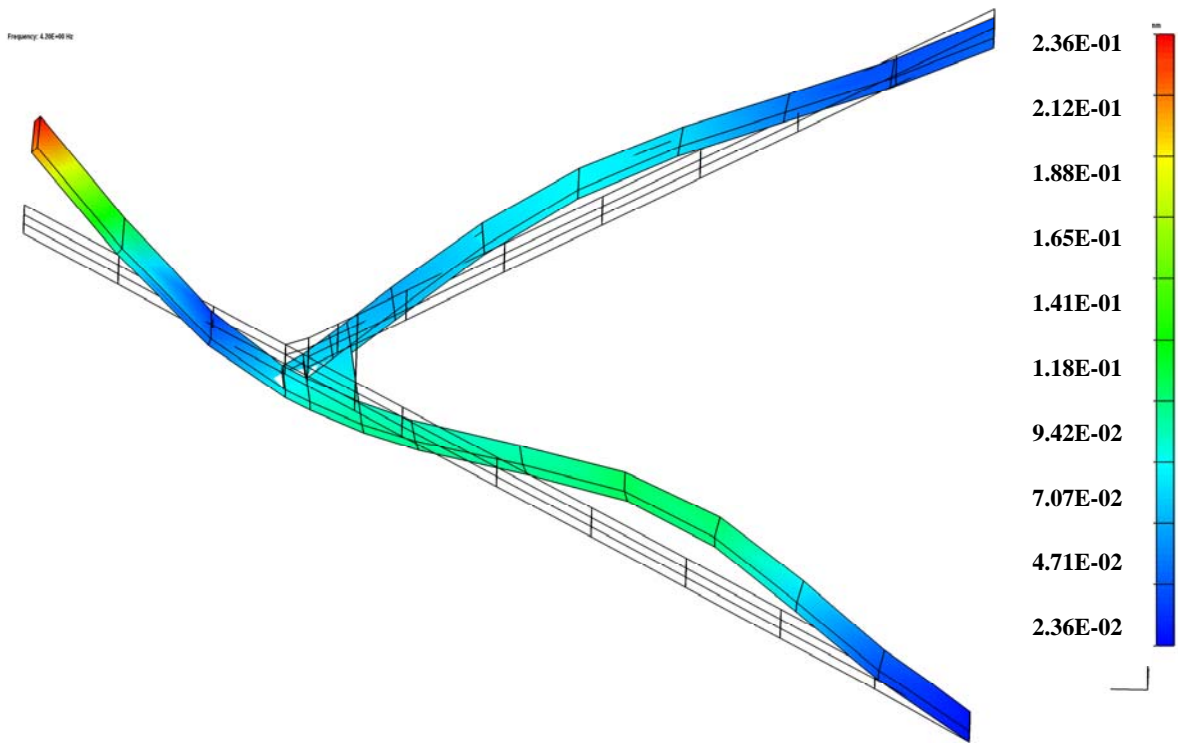


Fig. 61. Mode 5 for Clamped BC without RBEs and Fuselage using NASTRAN, Freq. = 4.2019 Hz

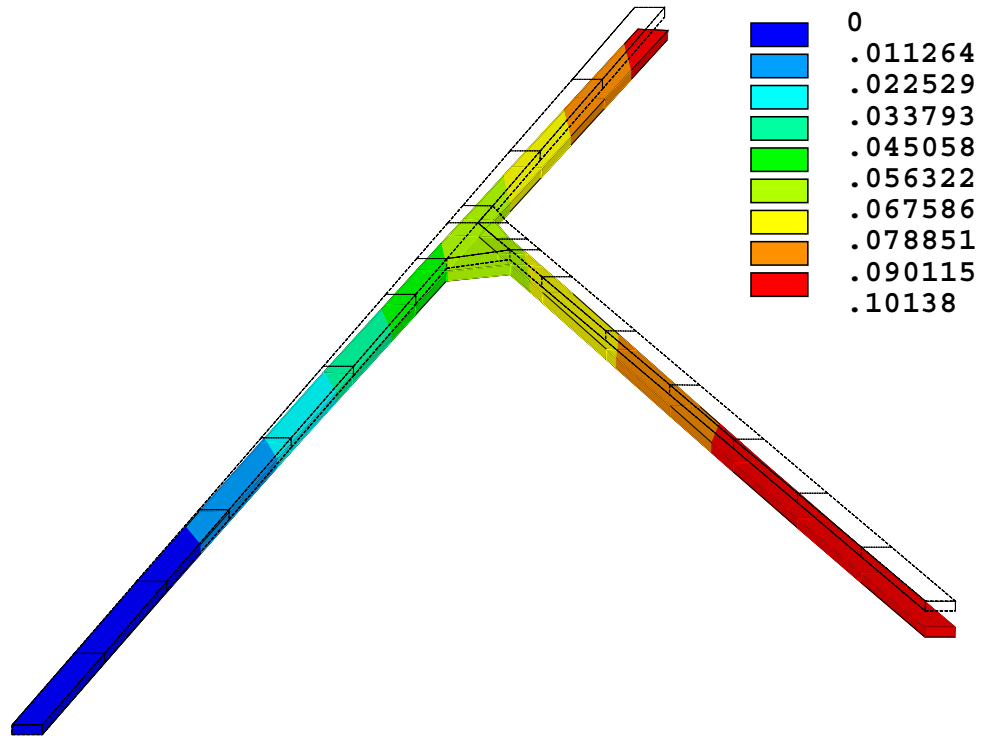


Fig. 62. Mode 1 for Clamped BC with RBEs and without Fuselage using ANSYS, Freq. = 0.3154 Hz

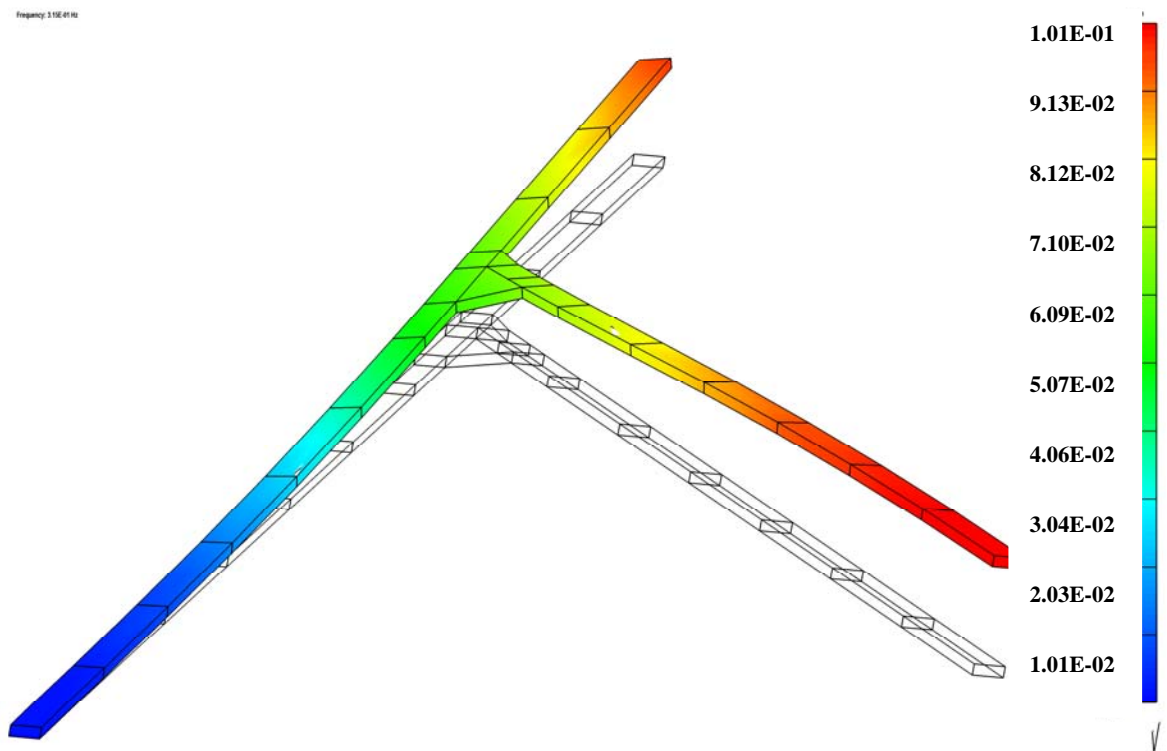


Fig. 63. Mode 1 for Clamped BC with RBEs and without Fuselage using NAST., Freq. = 0.3154 Hz

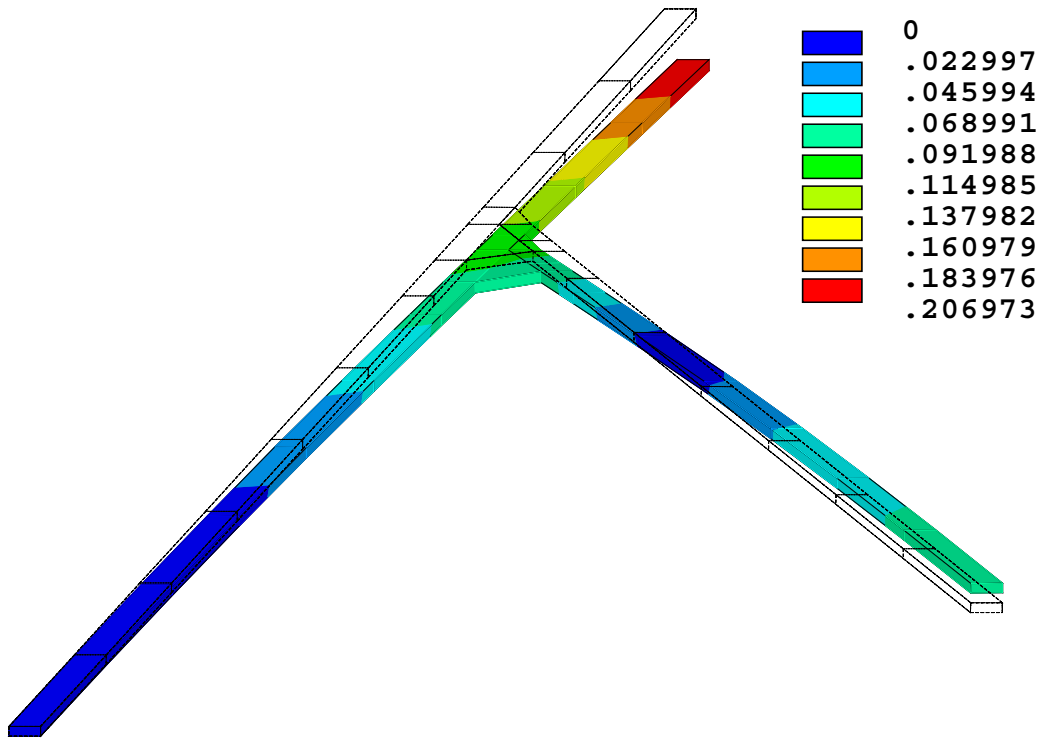


Fig. 64. Mode 2 for Clamped BC with RBEs and without Fuselage using ANSYS, Freq. = 0.9681 Hz

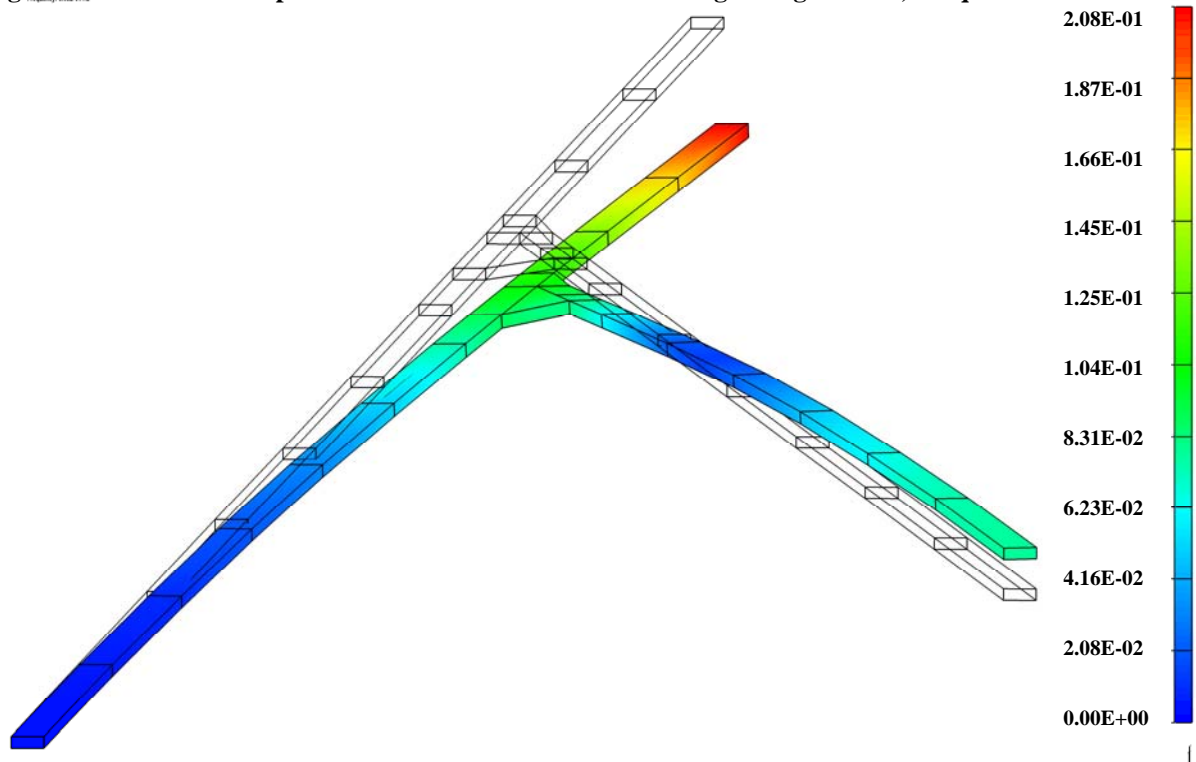


Fig. 65. Mode 2 for Clamped BC with RBEs and without Fuselage using NAST., Freq. = 0.9681 Hz

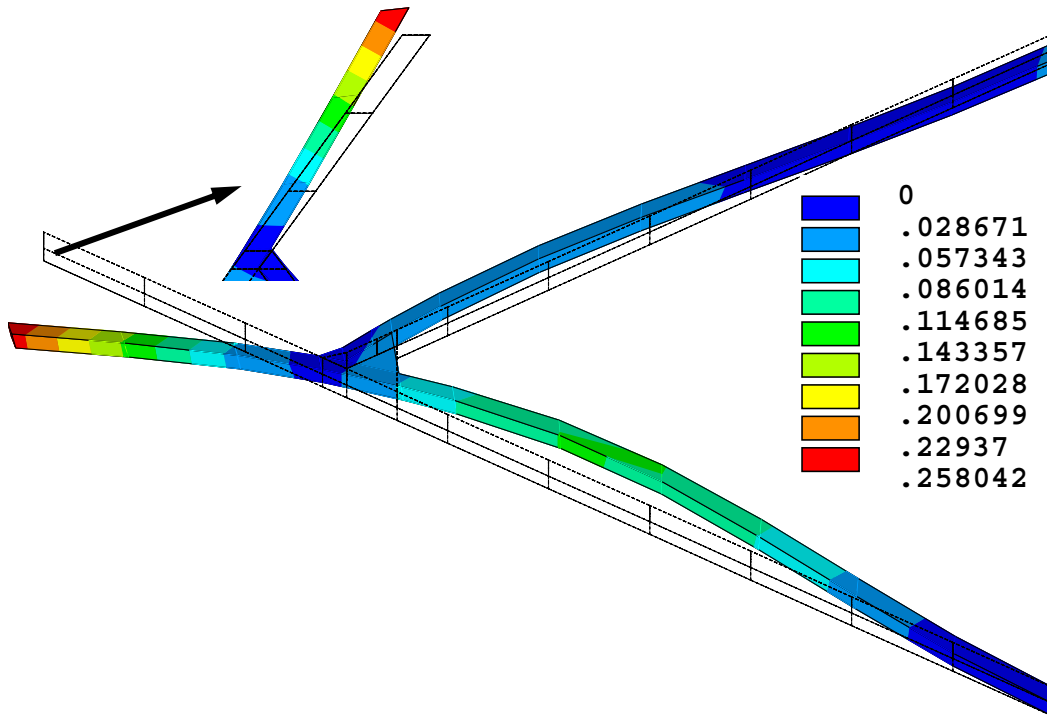


Fig. 66. Mode 3 for Clamped BC with RBEs and without Fuselage using ANSYS, Freq. = 2.1069 Hz

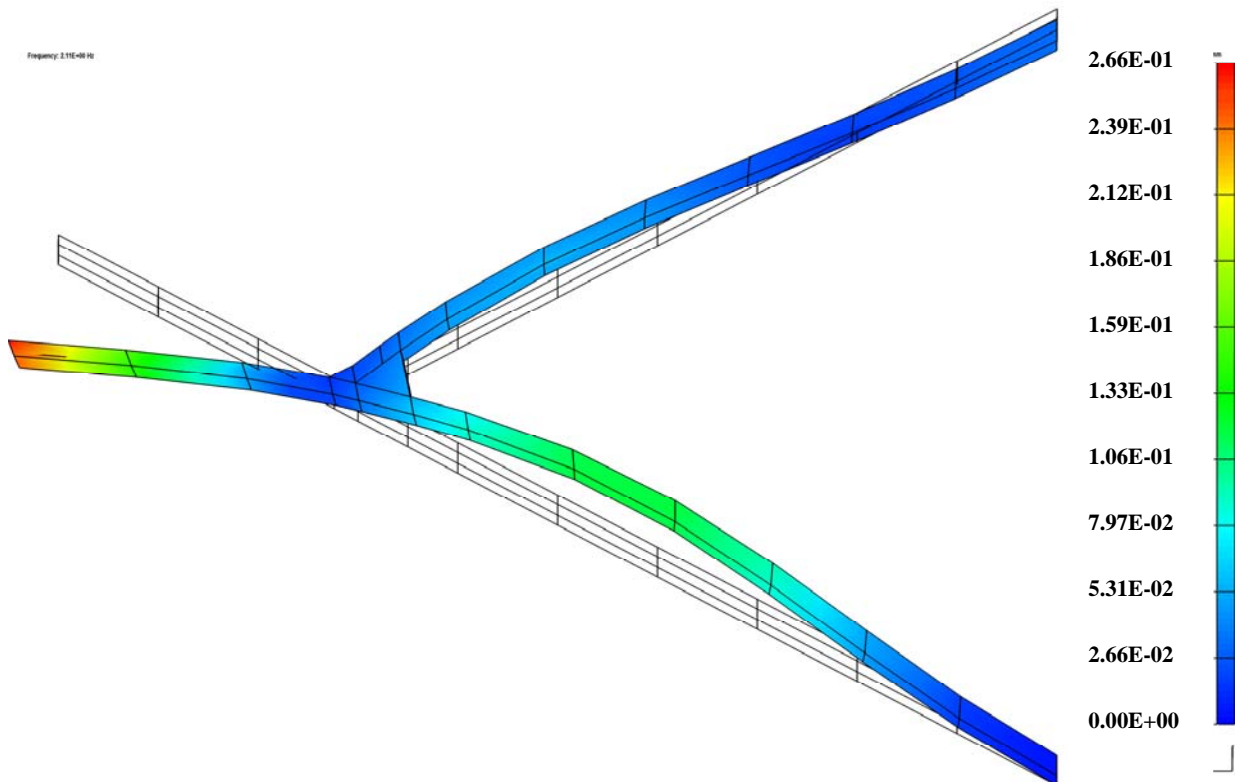


Fig. 67. Mode 3 for Clamped BC with RBEs and without Fuselage using NAST., Freq. = 2.1069 Hz

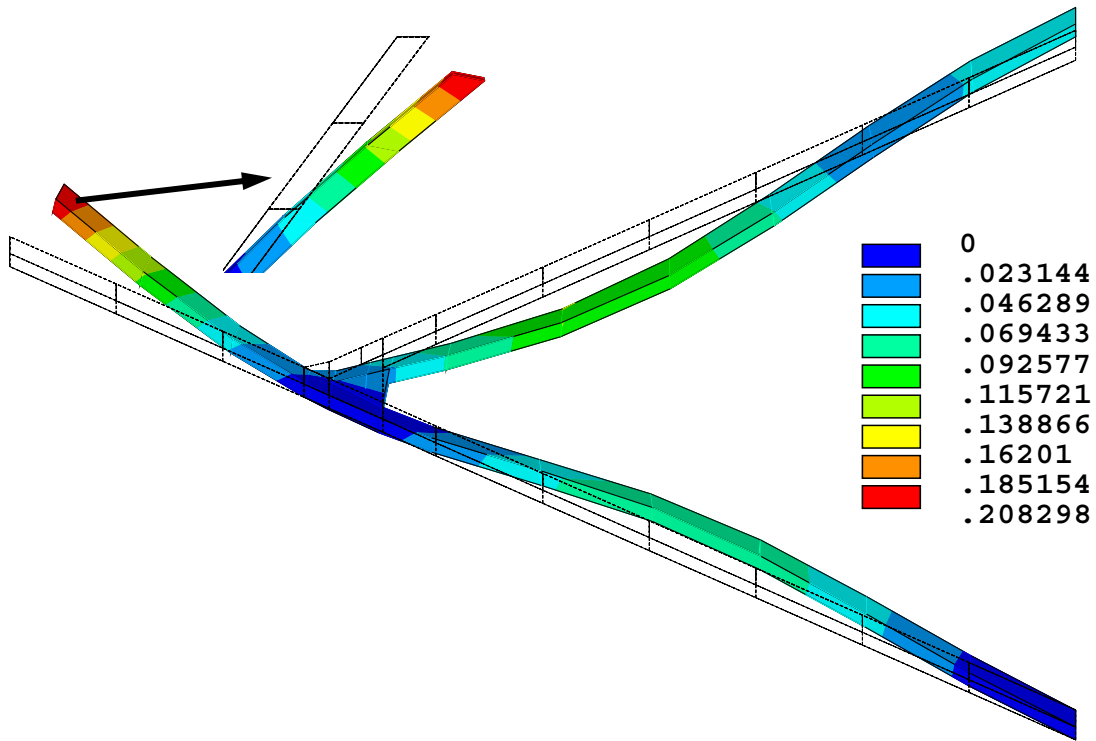


Fig. 68. Mode 4 for Clamped BC with RBEs and without Fuselage using ANSYS, Freq. = 3.5759 Hz

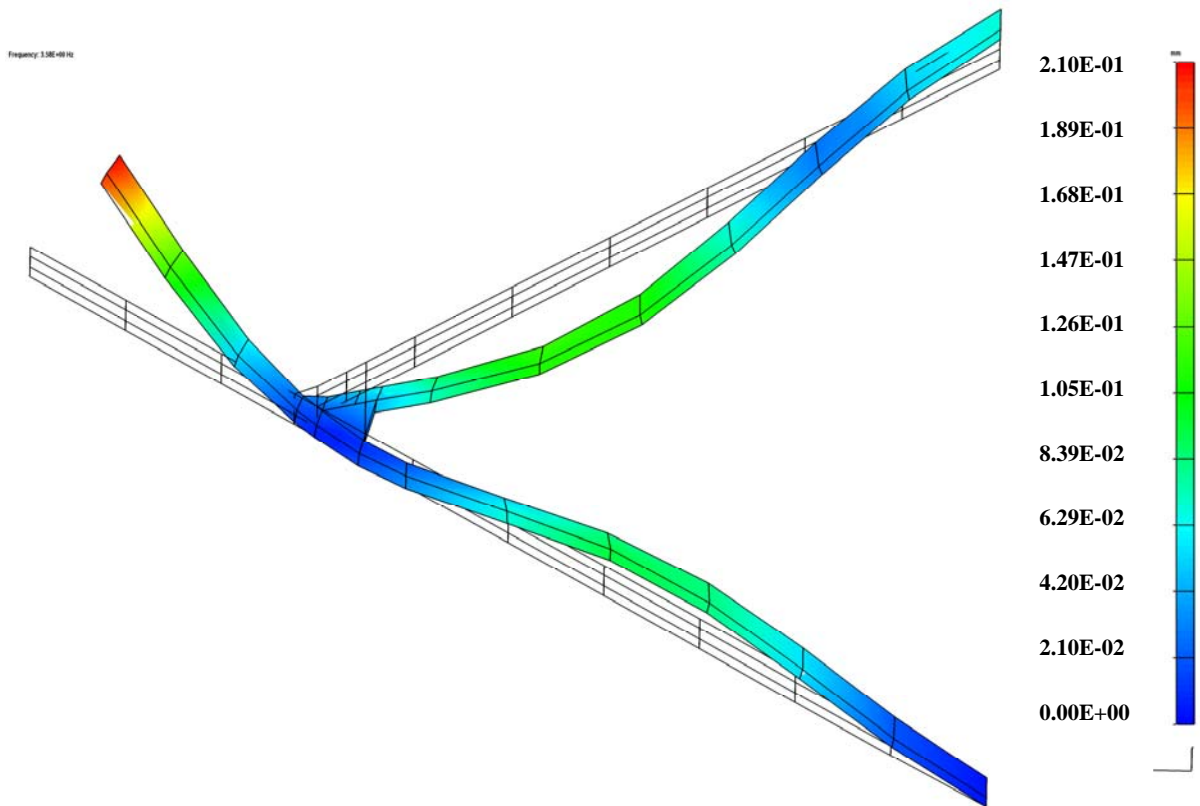


Fig. 69. Mode 4 for Clamped BC with RBEs and without Fuselage using NAST., Freq. = 3.5759 Hz

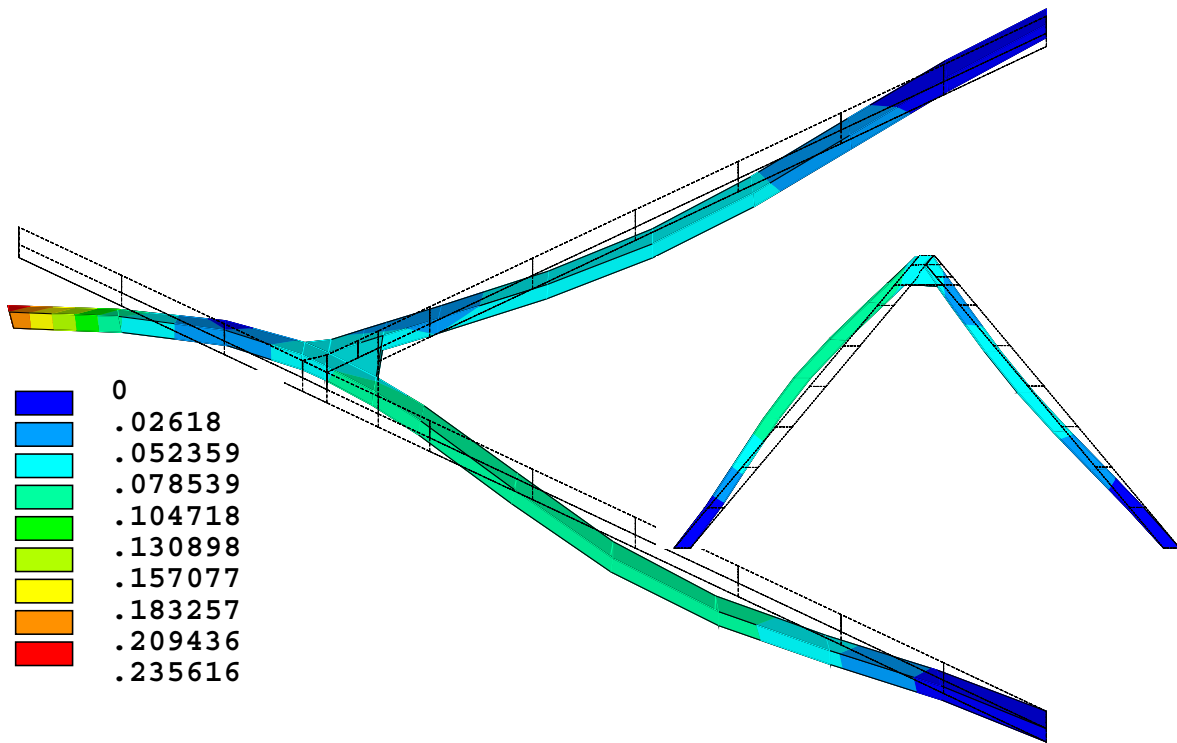


Fig. 70. Mode 5 for Clamped BC with RBEs and without Fuselage using ANSYS, Freq. = 4.2019 Hz

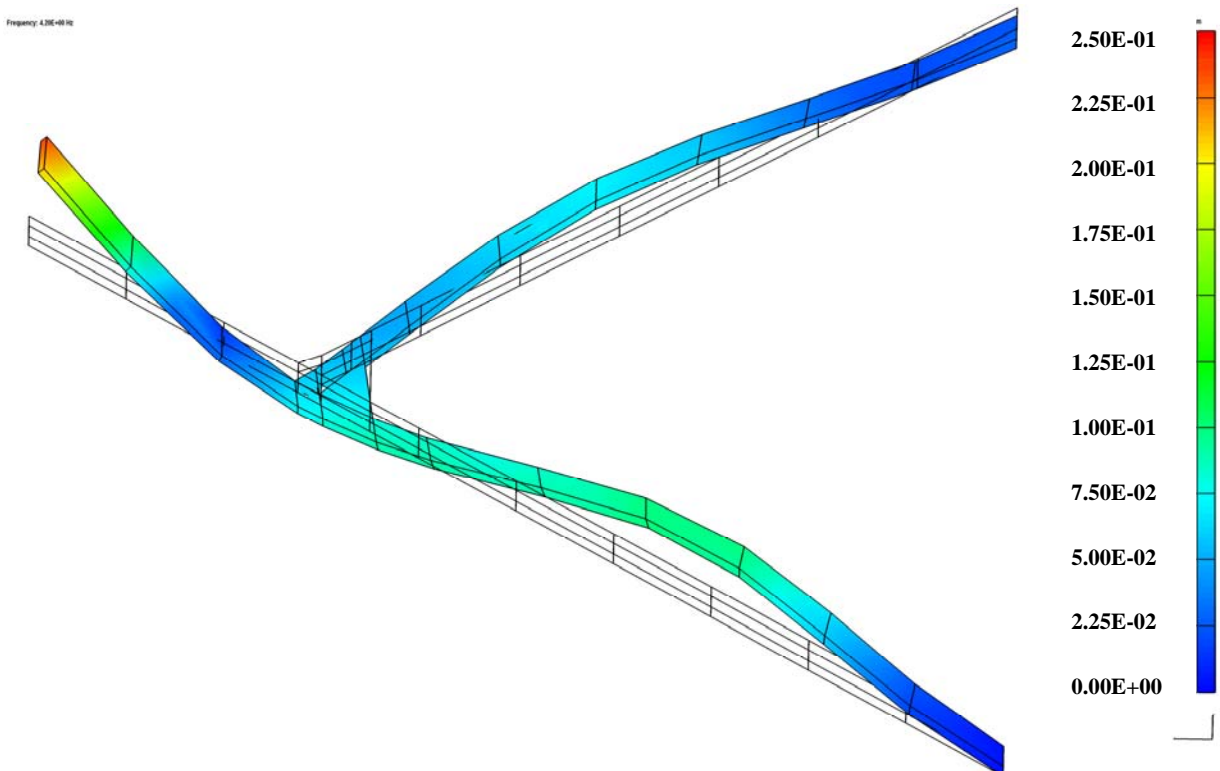


Fig. 71. Mode 5 for Clamped BC with RBEs and without Fuselage using NAST., Freq. = 4.2019 Hz

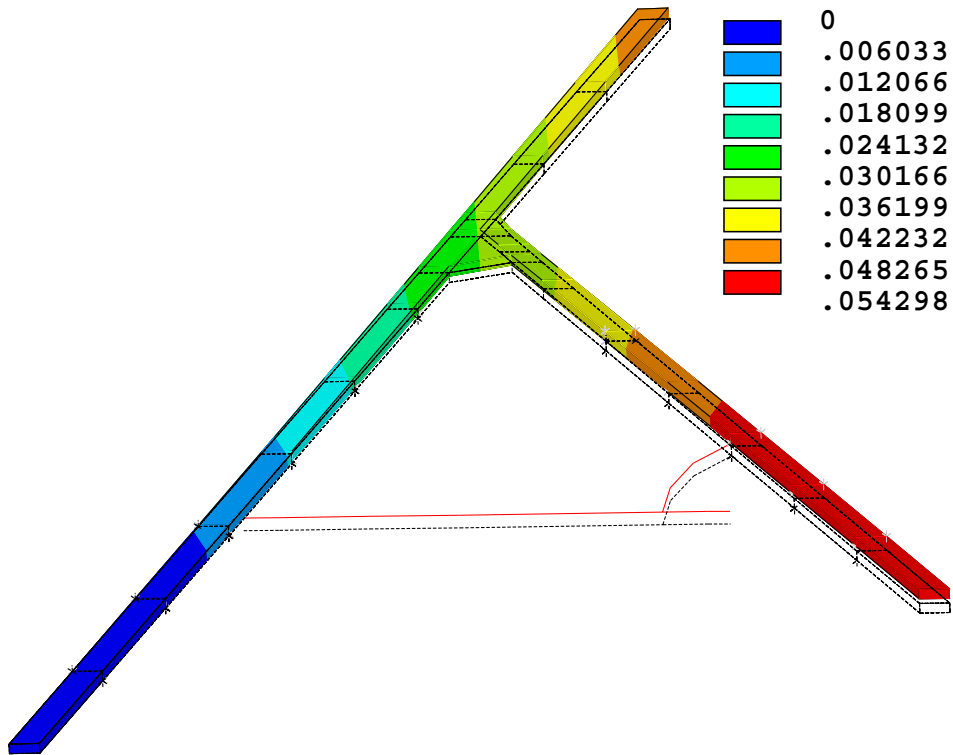


Fig. 72. Mode 1 for Clamped BC without RBEs and with Fuselage using ANSYS, Freq. = 0.1665 Hz

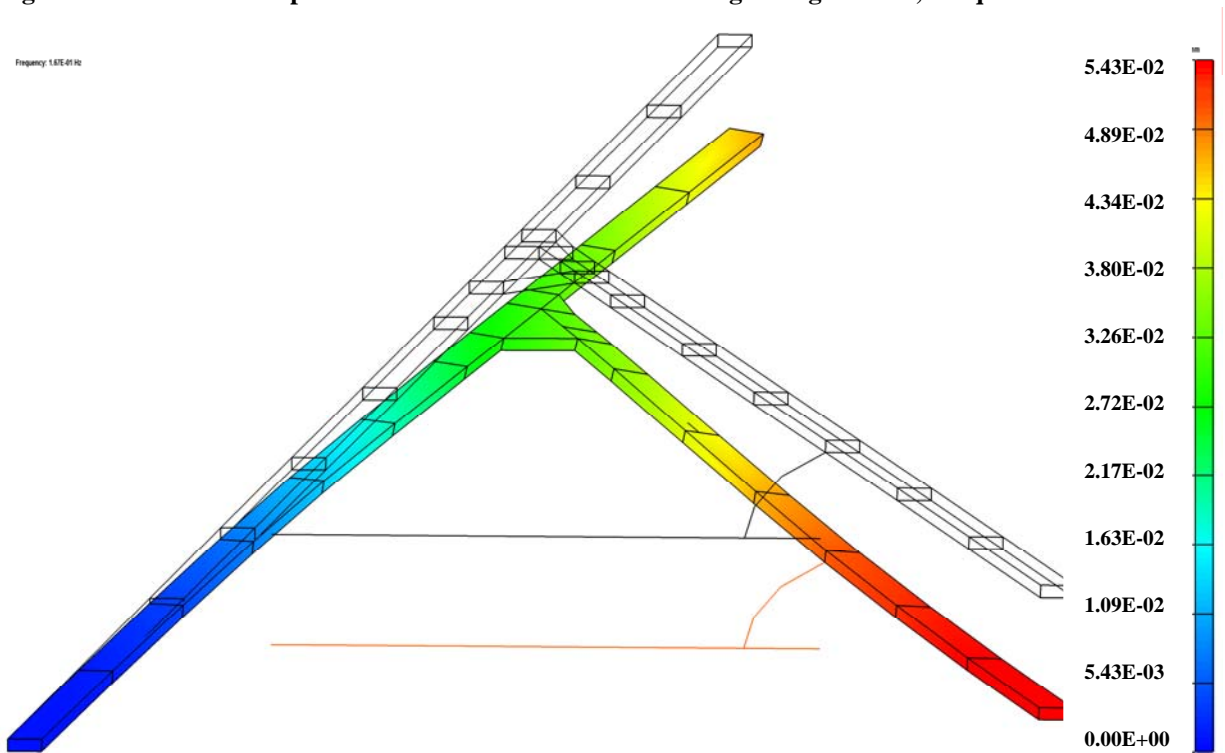


Fig. 73. Mode 1 for Clamped BC without RBEs and with Fuselage using NAST., Freq. = 0.1665 Hz

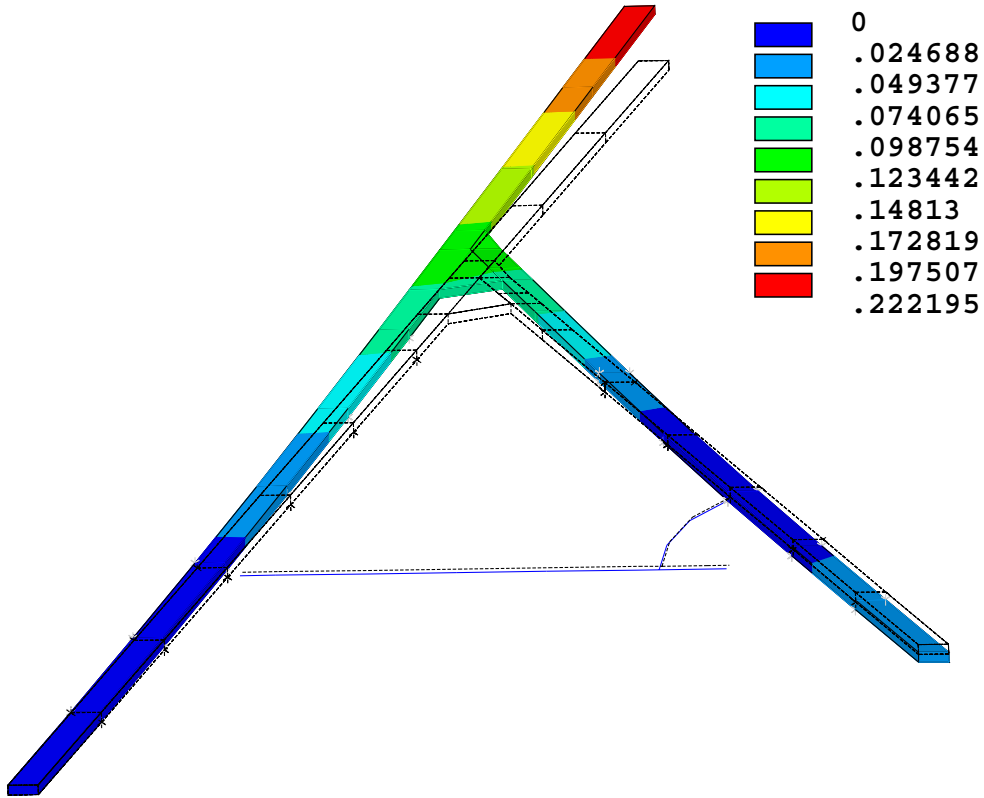


Fig. 74. Mode 2 for Clamped BC without RBEs and with Fuselage using ANSYS, Freq. = 0.8905 Hz

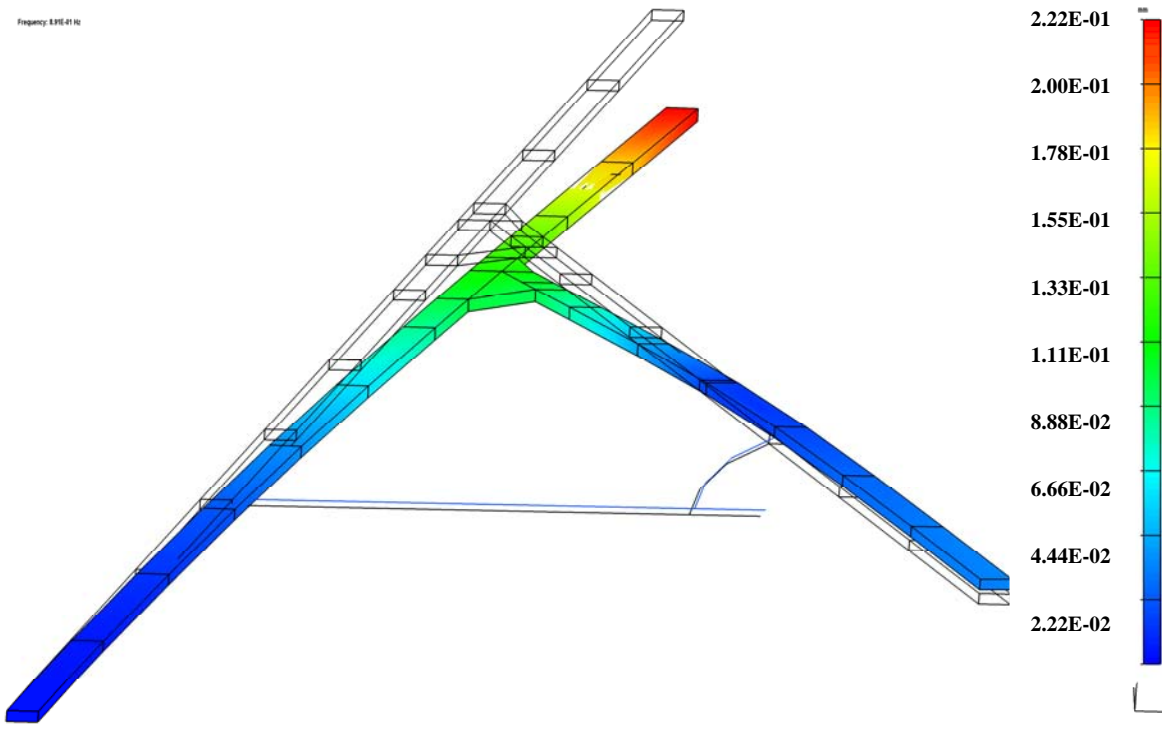


Fig. 75. Mode 2 for Clamped BC without RBEs and with Fuselage using NAST., Freq. = 0.8905 Hz

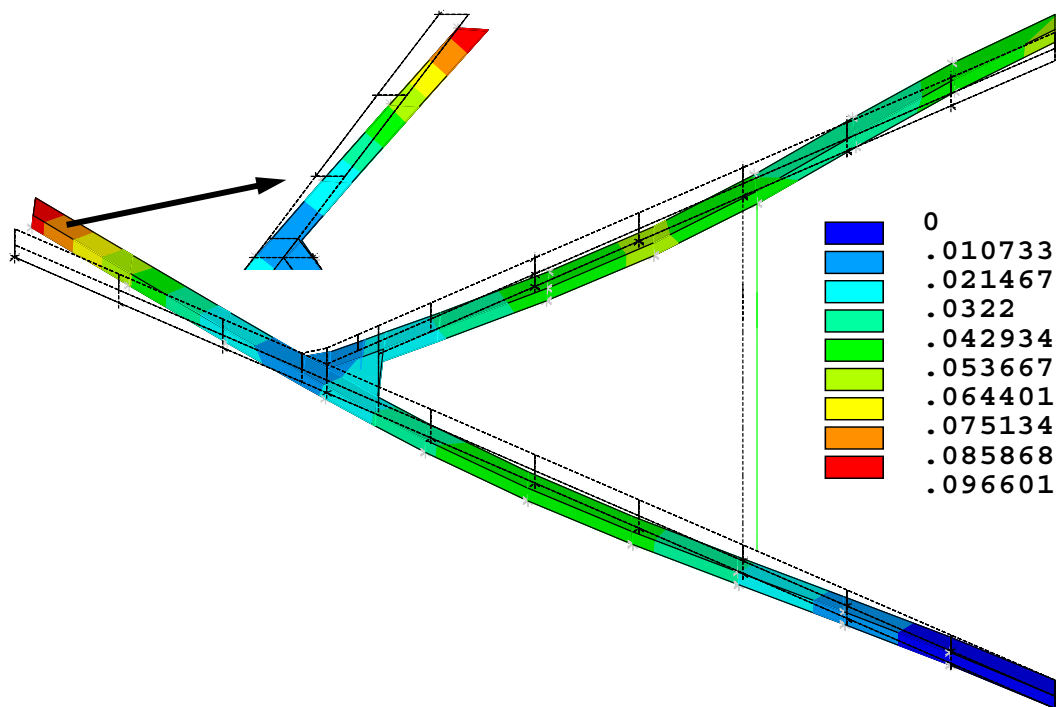


Fig. 76. Mode 3 for Clamped BC without RBEs and with Fuselage using ANSYS, Freq. = 1.6187 Hz

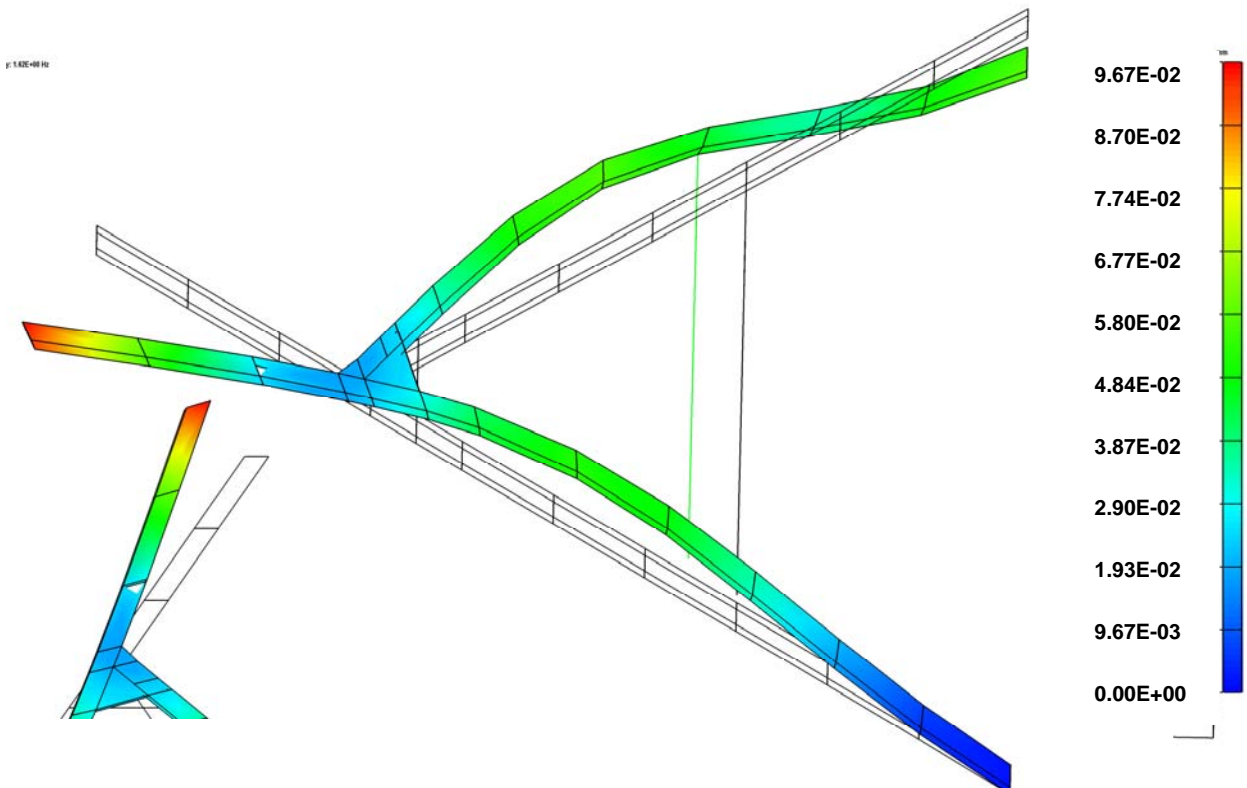


Fig. 77. Mode 3 for Clamped BC without RBEs and with Fuselage using NAST., Freq. = 1.6192 Hz

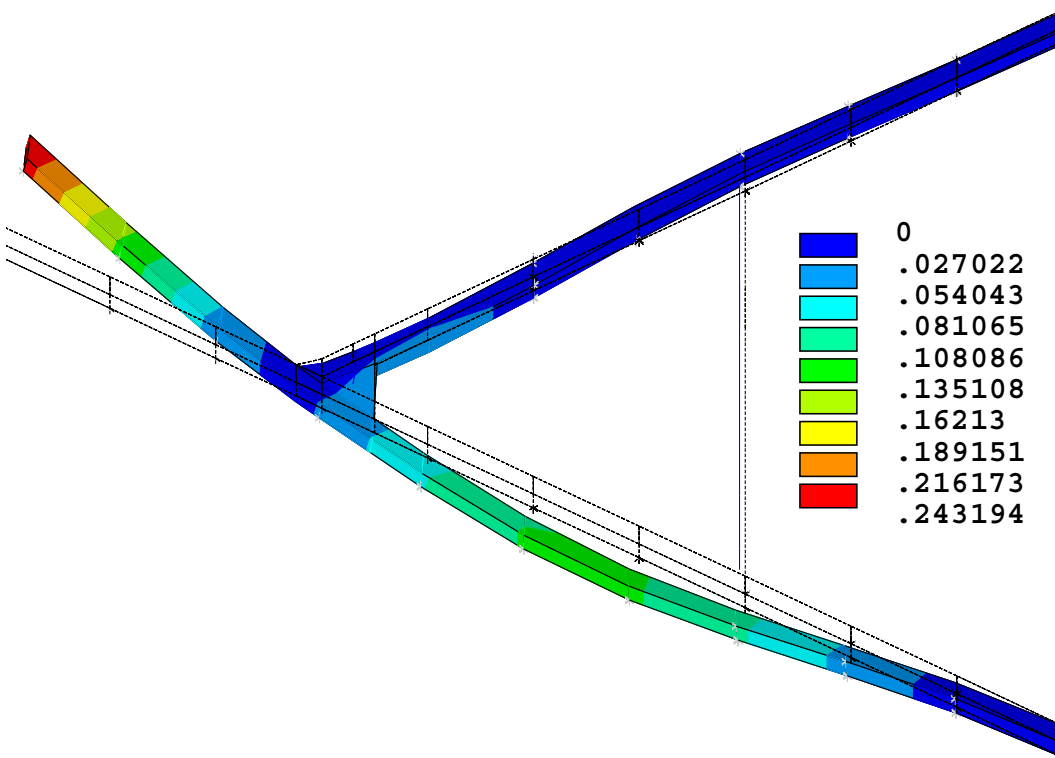


Fig. 78. Mode 4 for Clamped BC without RBEs and with Fuselage using ANSYS, Freq. = 2.3061 Hz

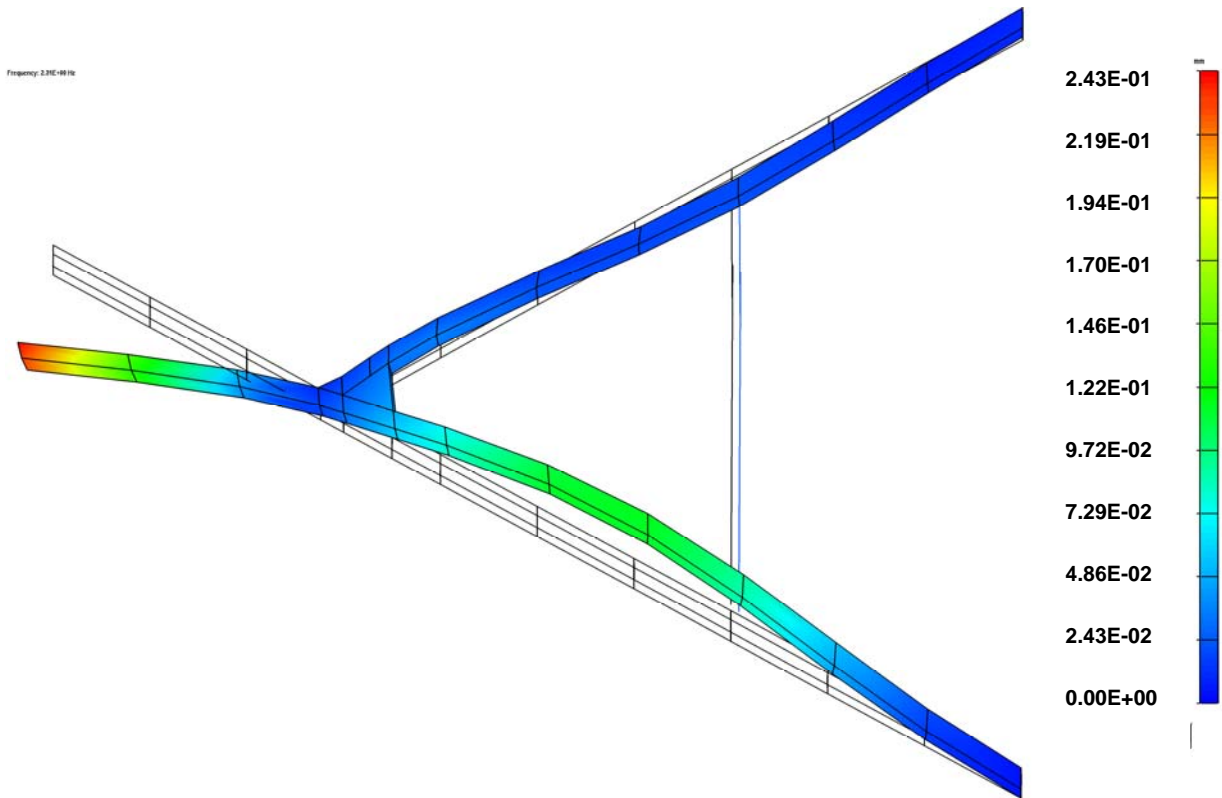


Fig. 79. Mode 4 for Clamped BC without RBEs and with Fuselage using NAST, Freq. = 2.3061 Hz

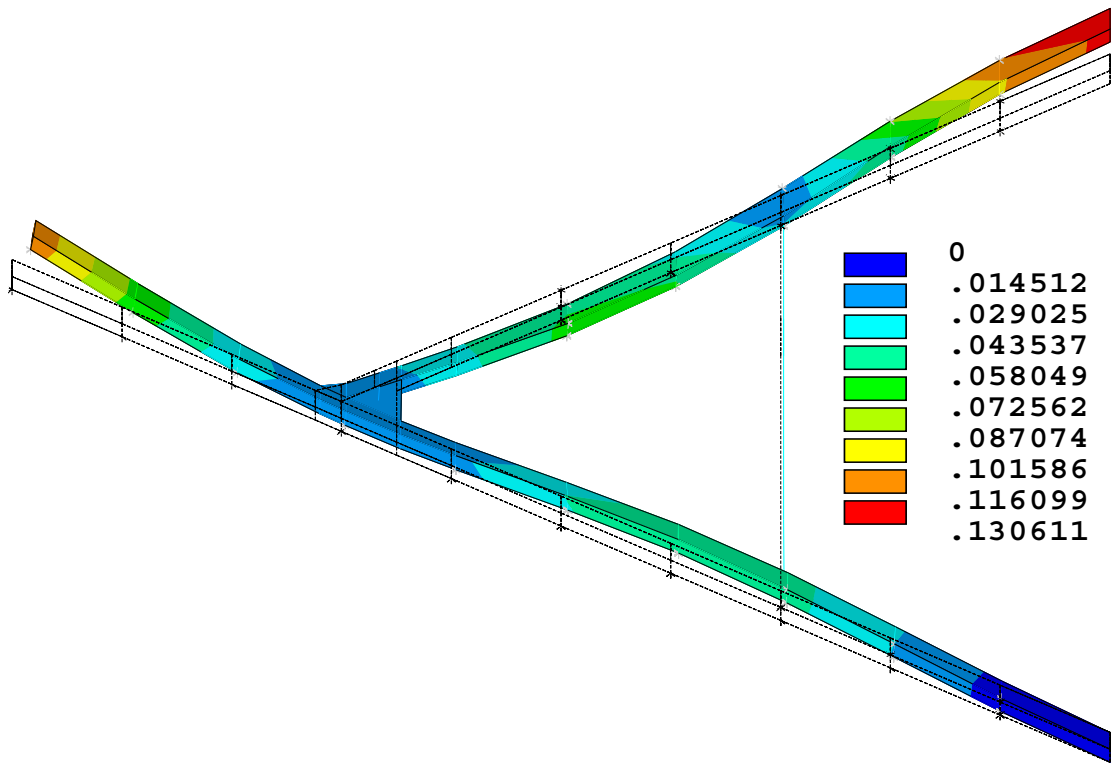


Fig. 80. Mode 5 for Clamped BC without RBEs and with Fuselage using ANSYS, Freq. = 3.2199 Hz

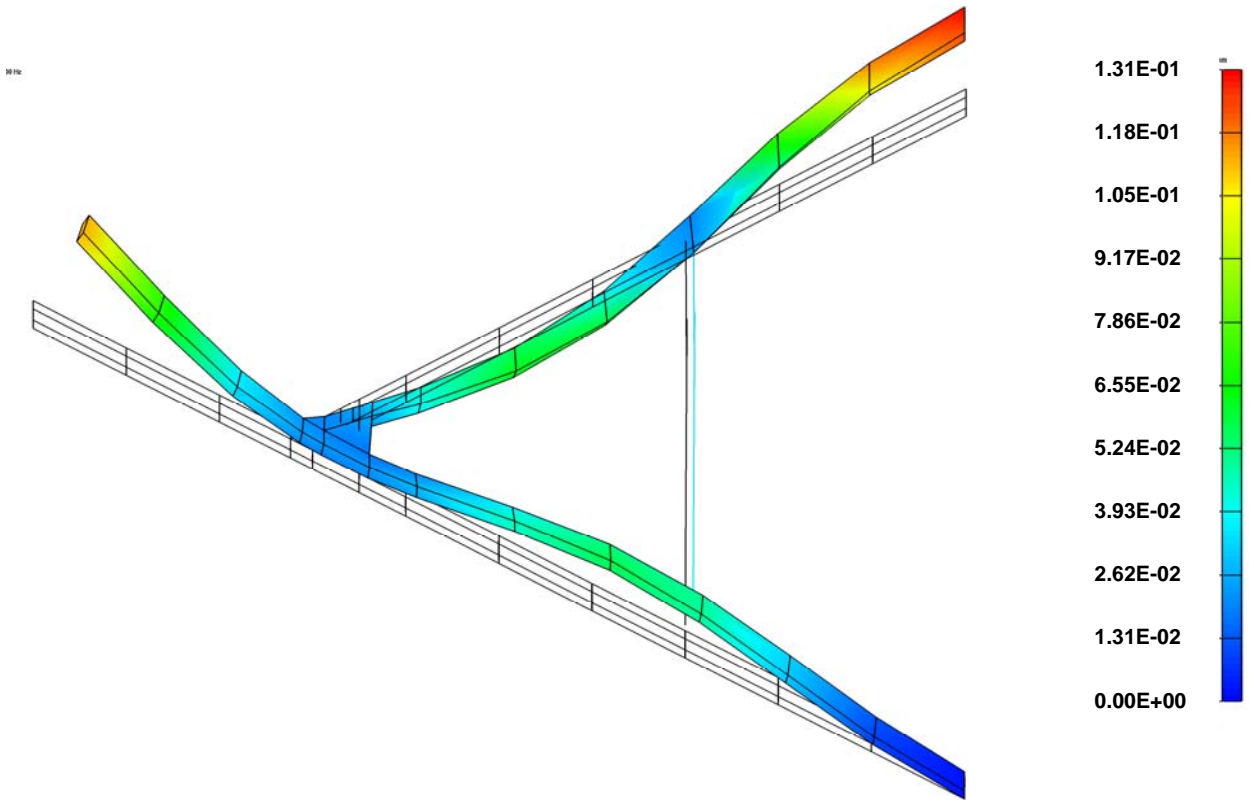
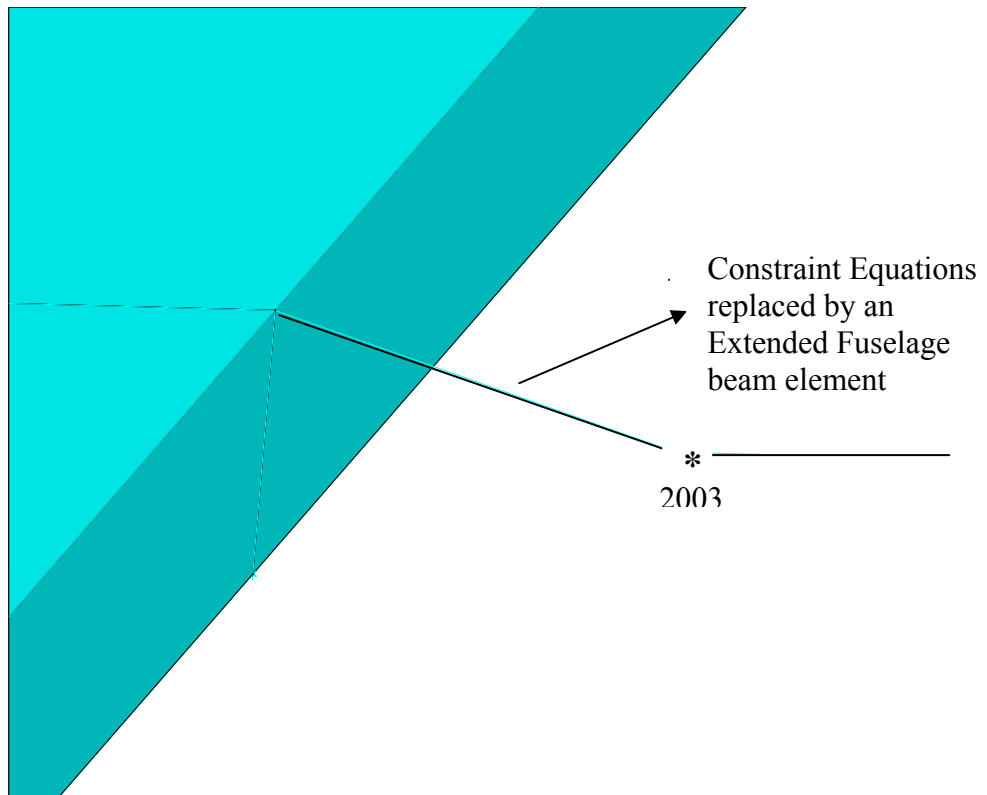


Fig. 81. Mode 5 for Clamped BC without RBEs and with Fuselage using NAST., Freq. = 3.2159 Hz



**Fig. 82. Extended Fuselage Model with CEs and RBEs at Node 2003 Replaced by Beam Element**

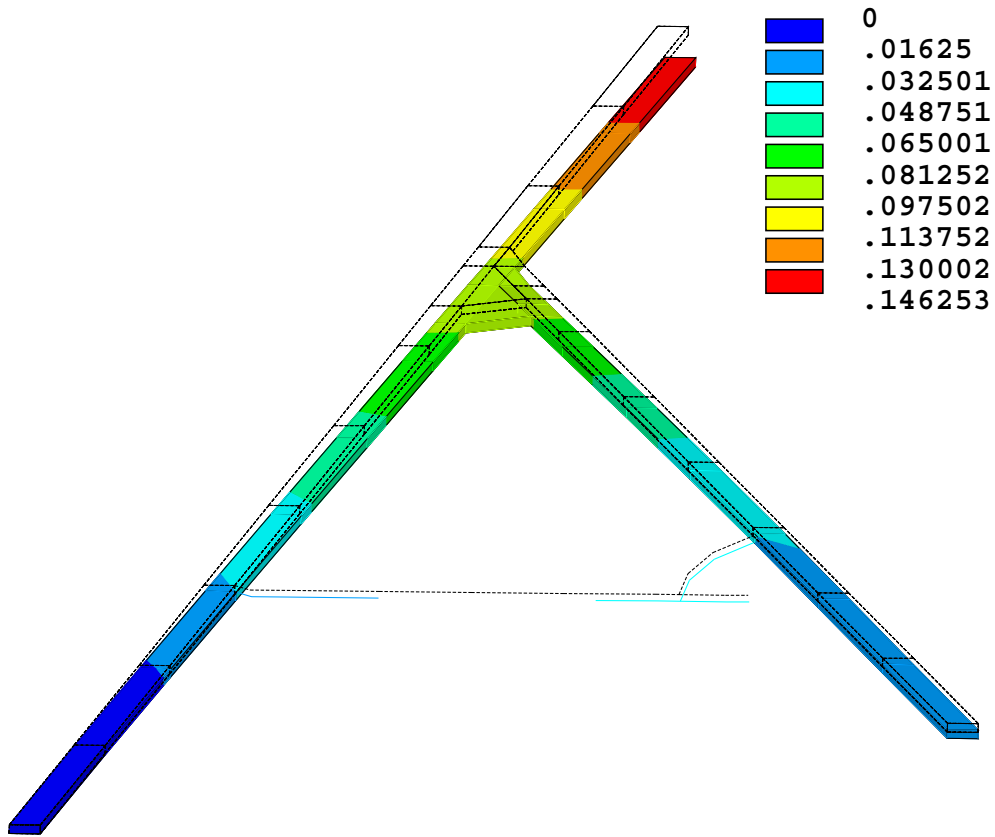


Fig. 83. Mode 1 for Clamped BC with RBEs and Extended Fuselage using ANSYS, Freq. = 0.6447 Hz

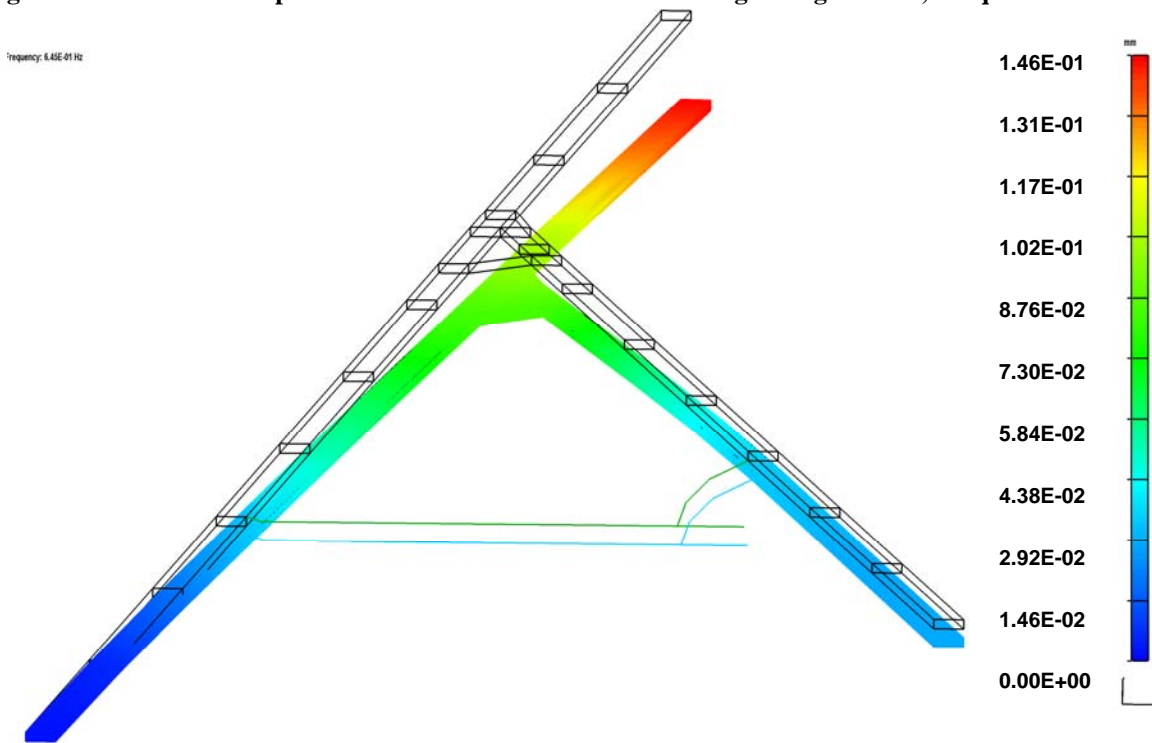


Fig. 84. Mode 1 for Clamped BC with RBEs and Extended Fuselage using NAST., Freq. = 0.6447 Hz

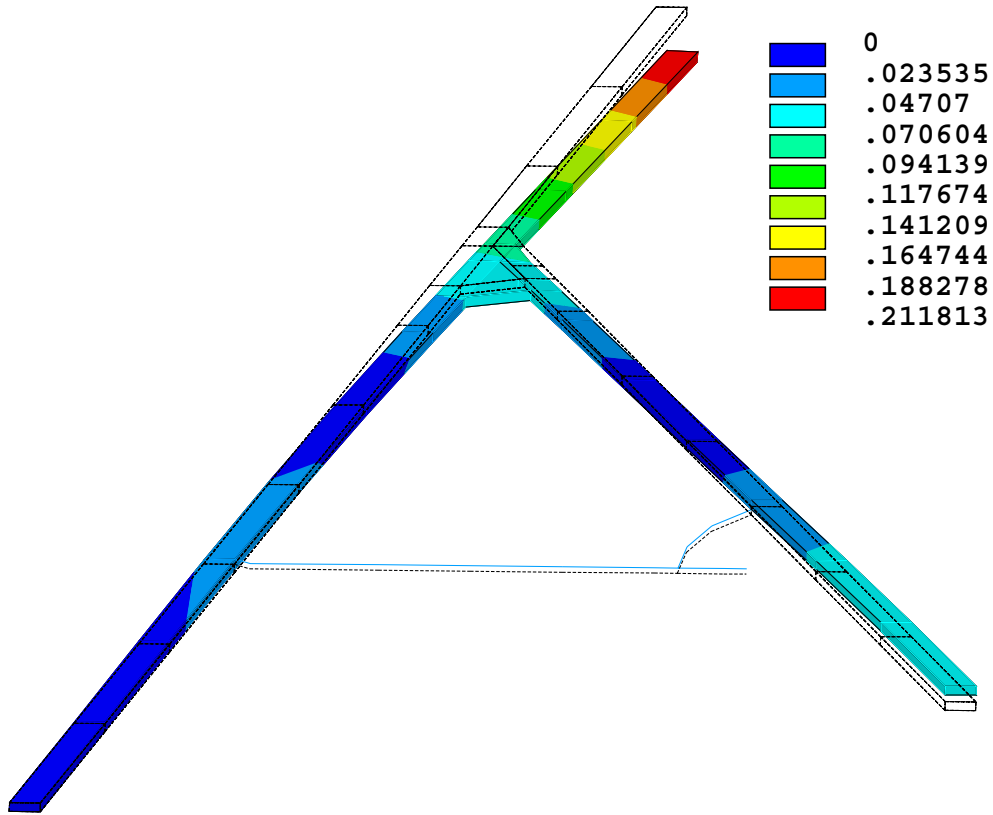


Fig. 85. Mode 2 for Clamped BC with RBEs and Extended Fuselage using ANSYS, Freq. = 1.2383 Hz

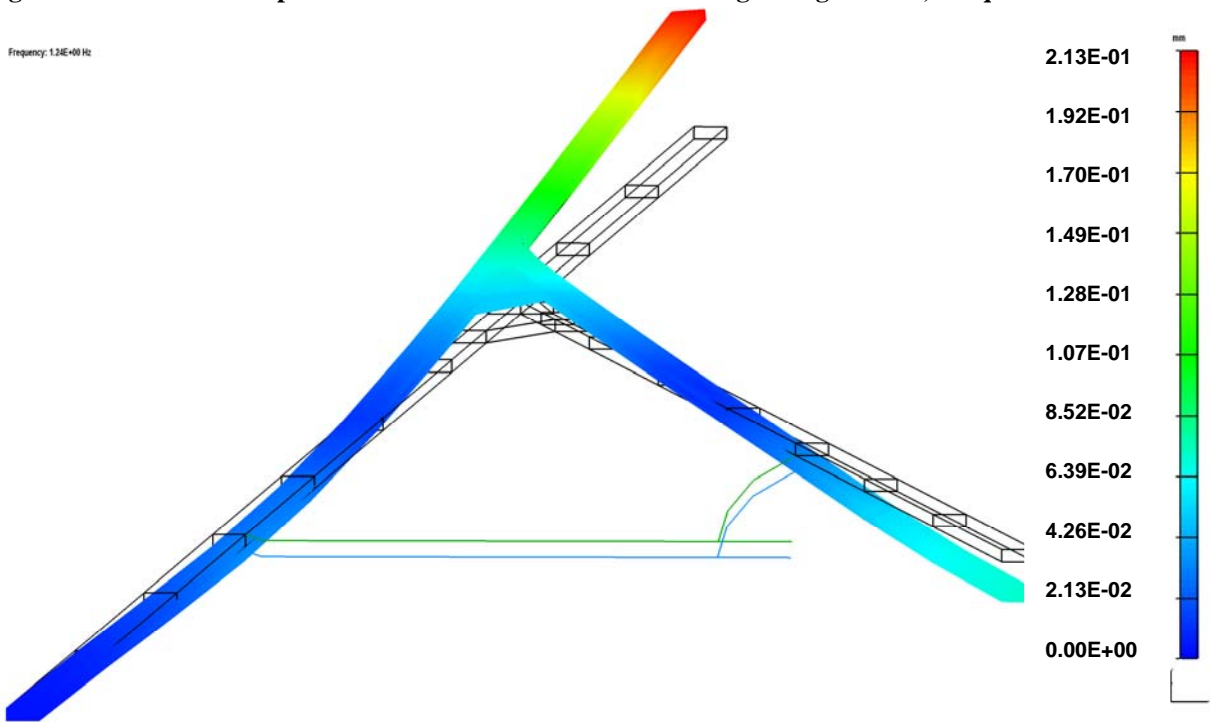


Fig. 86. Mode 2 for Clamped BC with RBEs and Extended Fuselage using NAST., Freq. = 1.2386 Hz

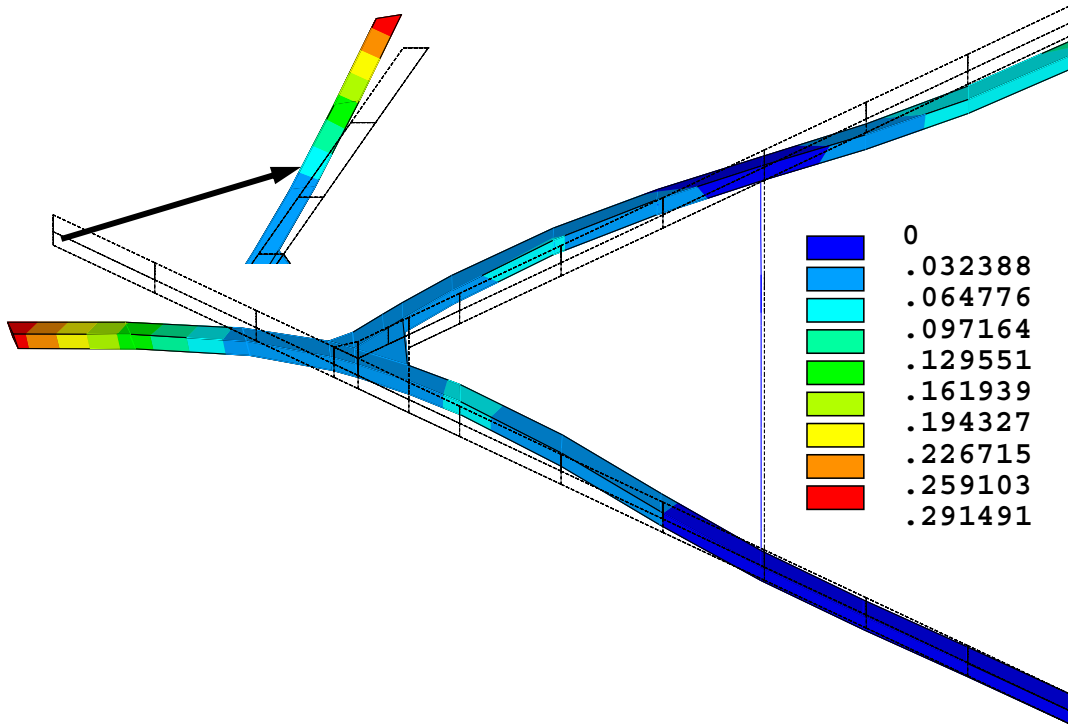


Fig. 87. Mode 3 for Clamped BC with RBEs and Extended Fuselage using ANSYS, Freq. = 2.8848 Hz

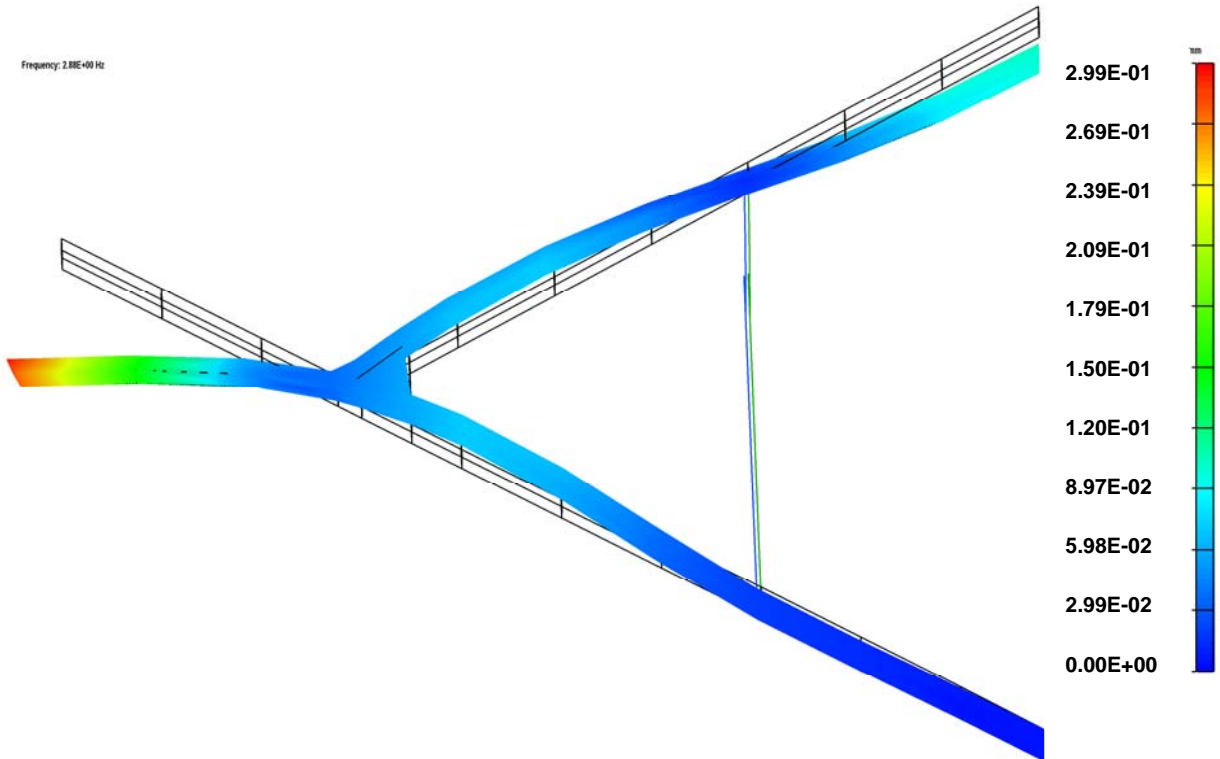


Fig. 88. Mode 3 for Clamped BC with RBEs and Extended Fuselage using NAST., Freq. = 2.8835 Hz

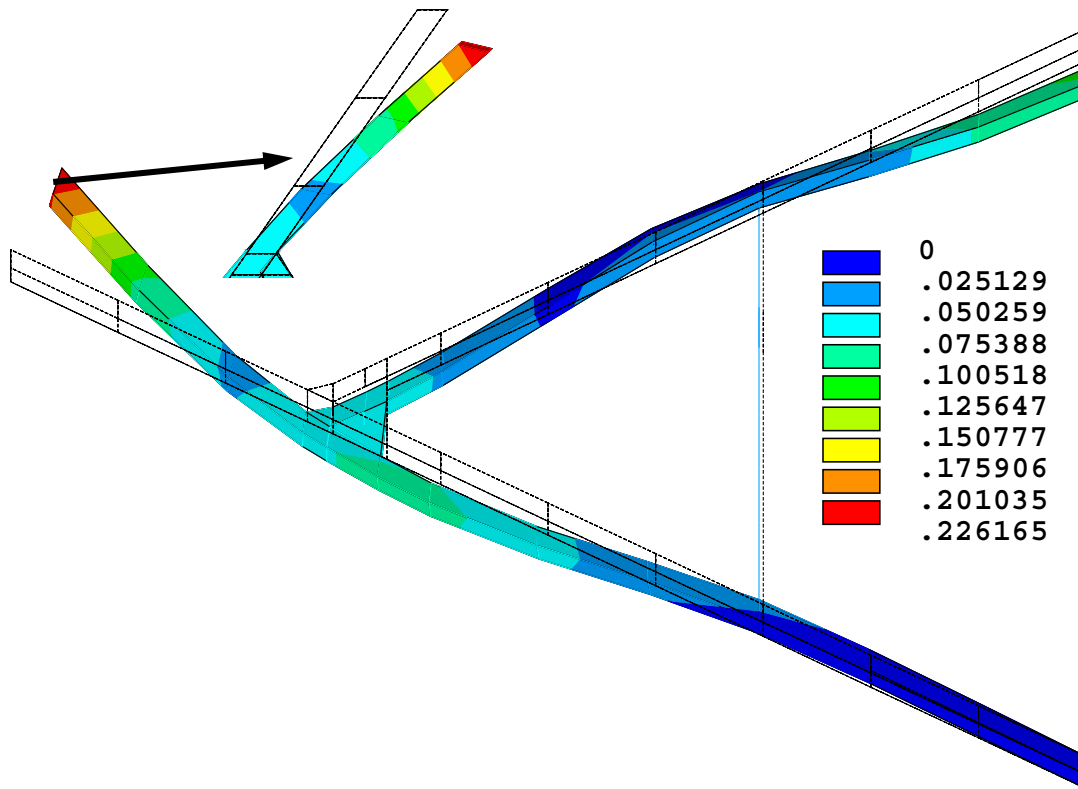


Fig. 89. Mode 4 for Clamped BC with RBEs and Extended Fuselage using ANSYS, Freq. = 3.8373 Hz

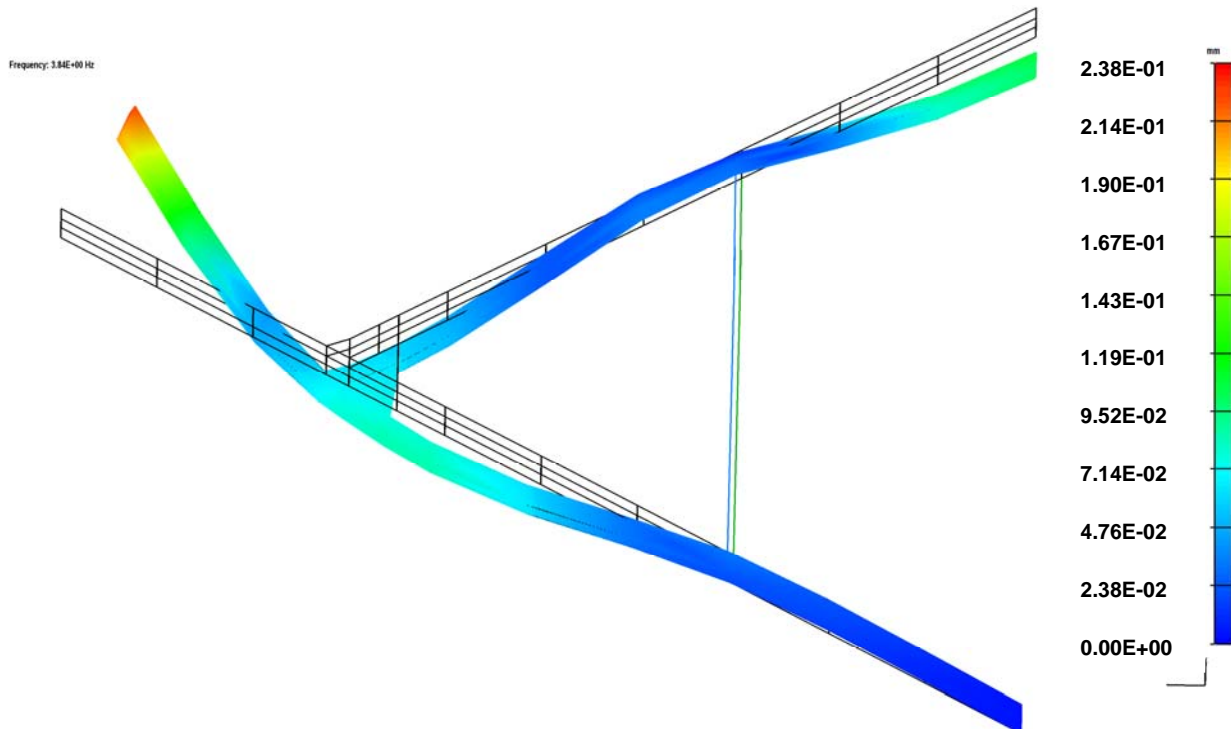


Fig. 90. Mode 4 for Clamped BC with RBEs and Extended Fuselage using NAST., Freq. = 3.8352 Hz

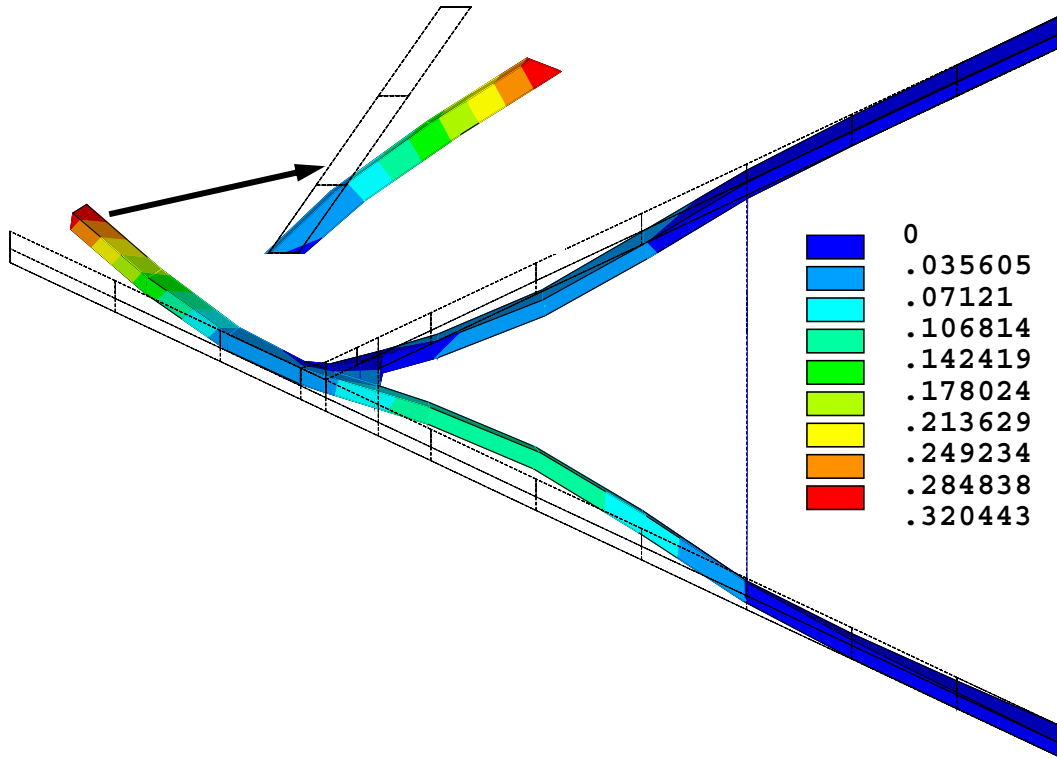


Fig. 91. Mode 5 for Clamped BC with RBEs and Extended Fuselage using ANSYS, Freq. = 5.7605 Hz

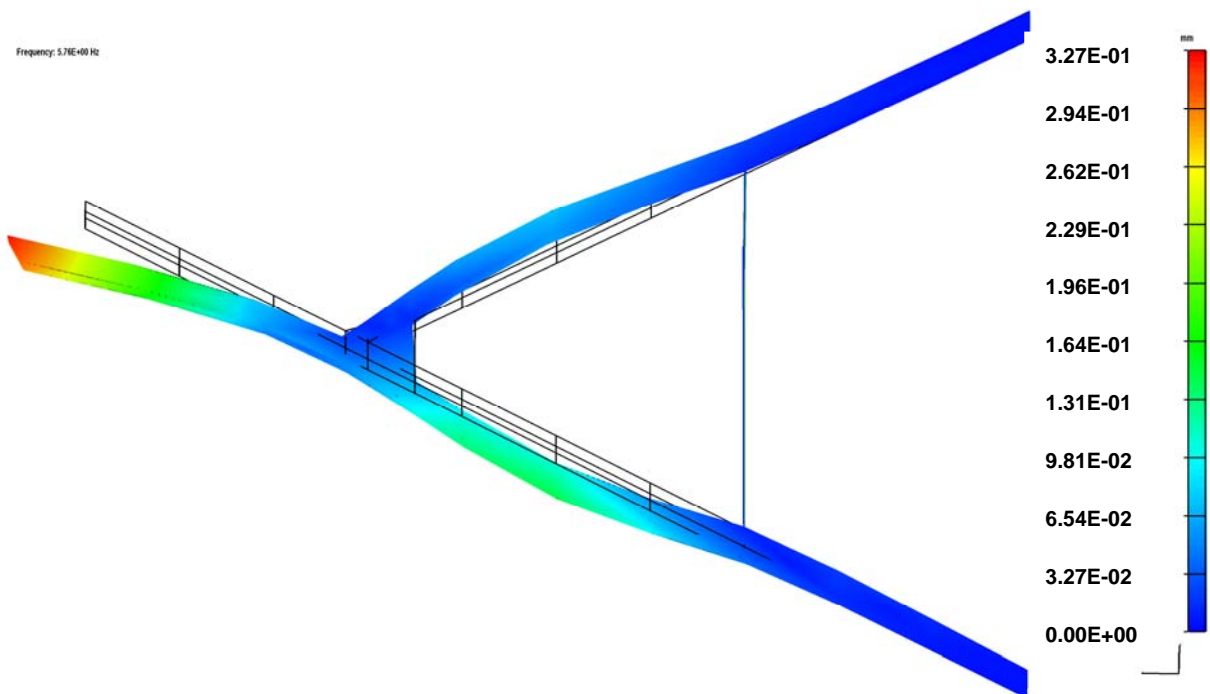


Fig. 92. Mode 5 for Clamped BC with RBEs and Extended Fuselage using NAST., Freq. = 5.7621 Hz

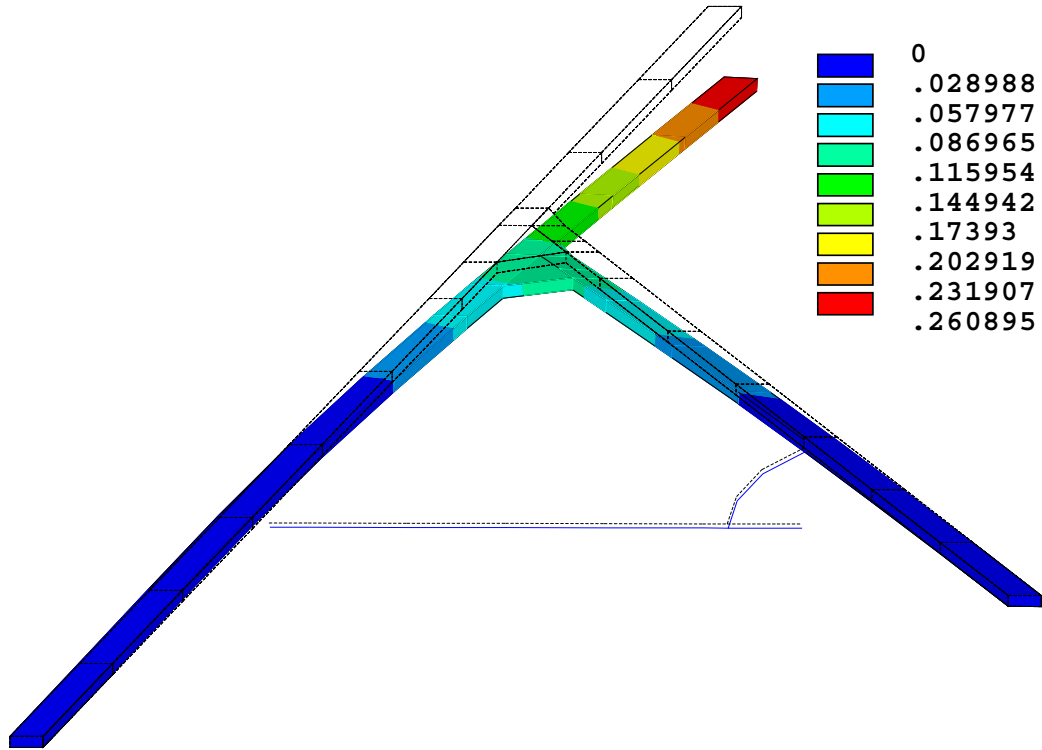


Fig. 93. Mode 1 for Rigid BC with RBEs and Fuselage using ANSYS, Freq. = 1.0784 Hz

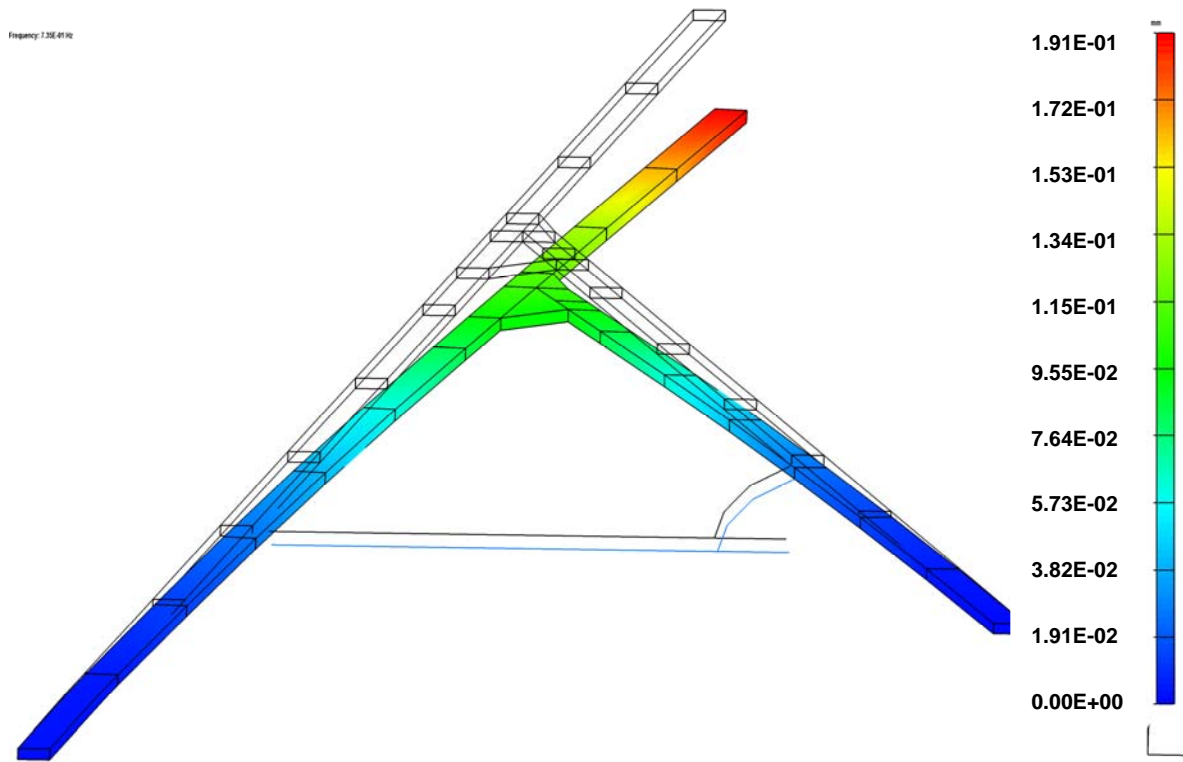


Fig. 94. Mode 1 for Rigid BC with RBEs and Fuselage using NASTRAN, Freq. = 0.7353 Hz

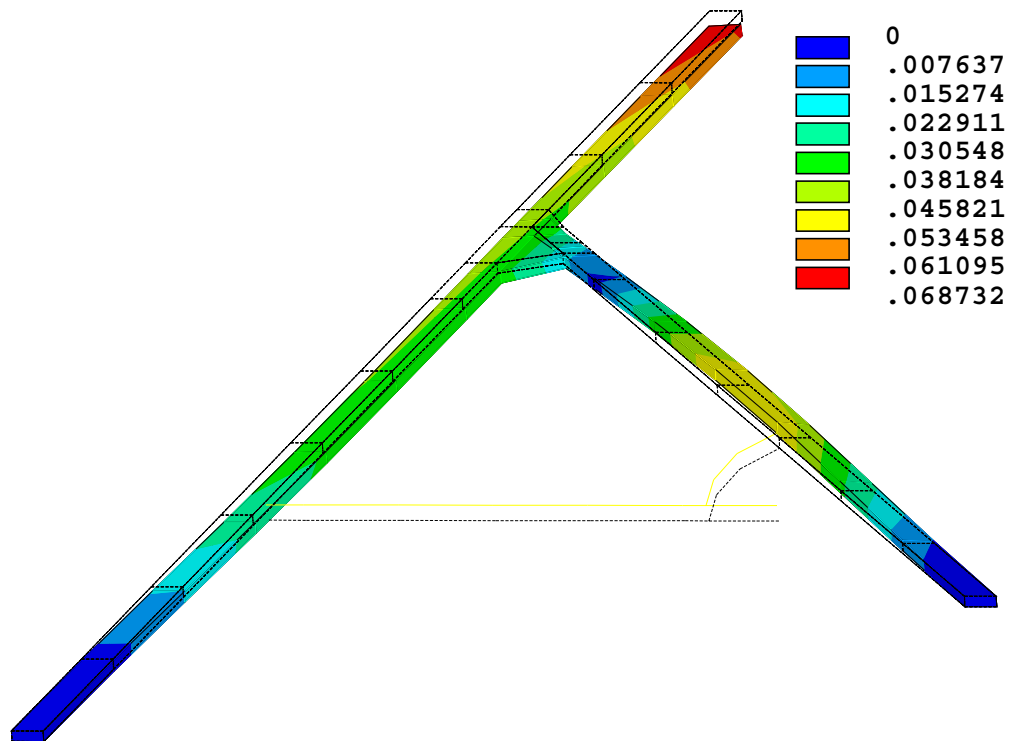


Fig. 95. Mode 2 for Rigid BC with RBEs and Fuselage using ANSYS, Freq. = 1.5358 Hz

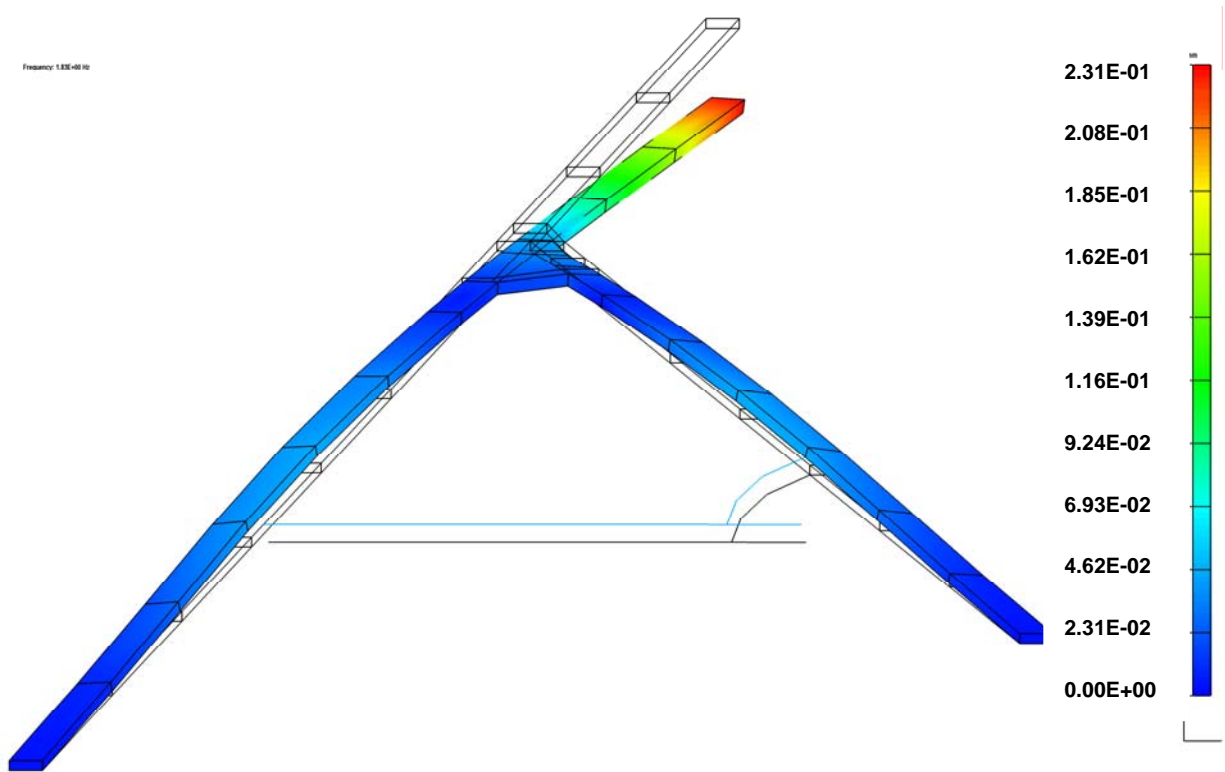


Fig. 96. Mode 2 for Rigid BC with RBEs and Fuselage using NASTRAN, Freq. = 1.8320 Hz

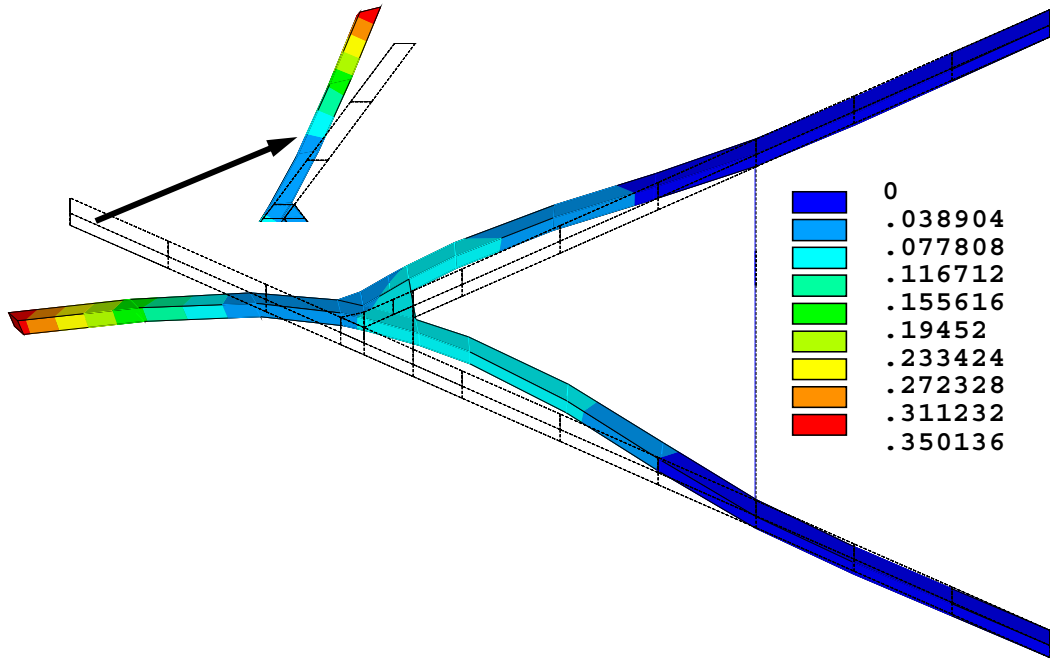


Fig. 97. Mode 3 for Rigid BC with RBEs and Fuselage using ANSYS, Freq. = 3.1998 Hz

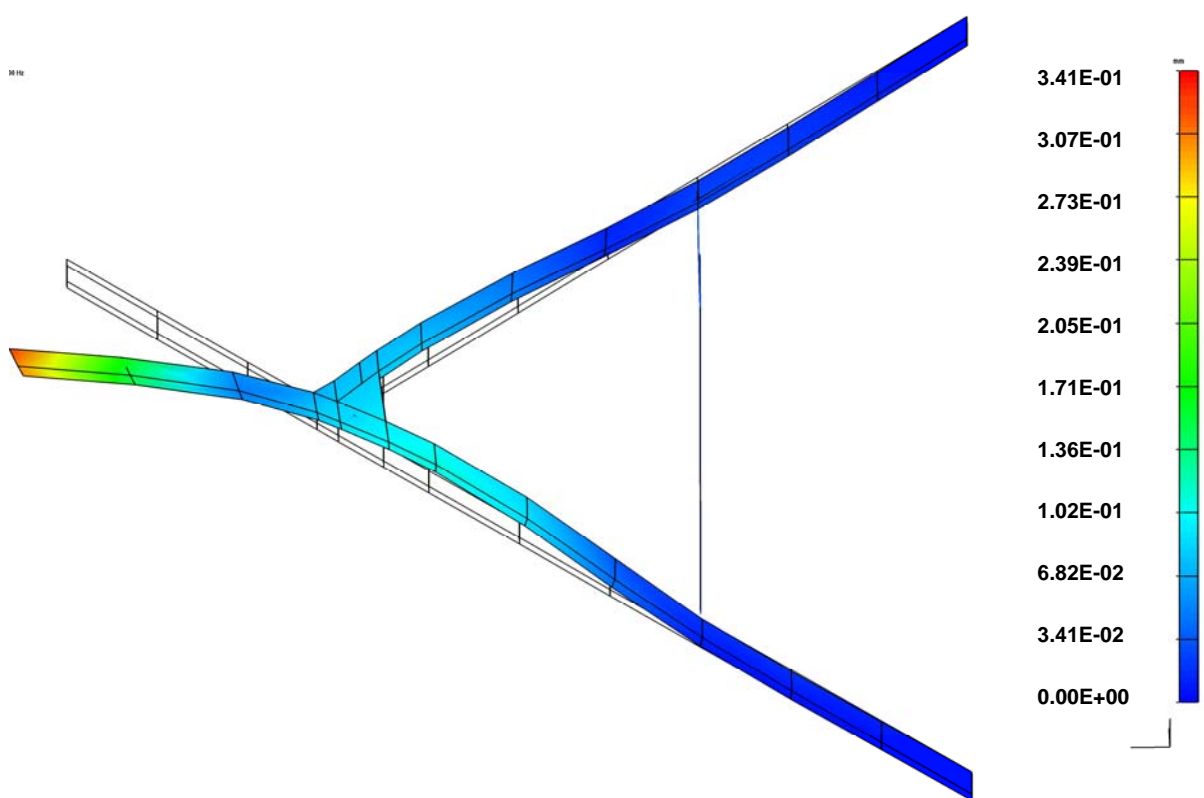
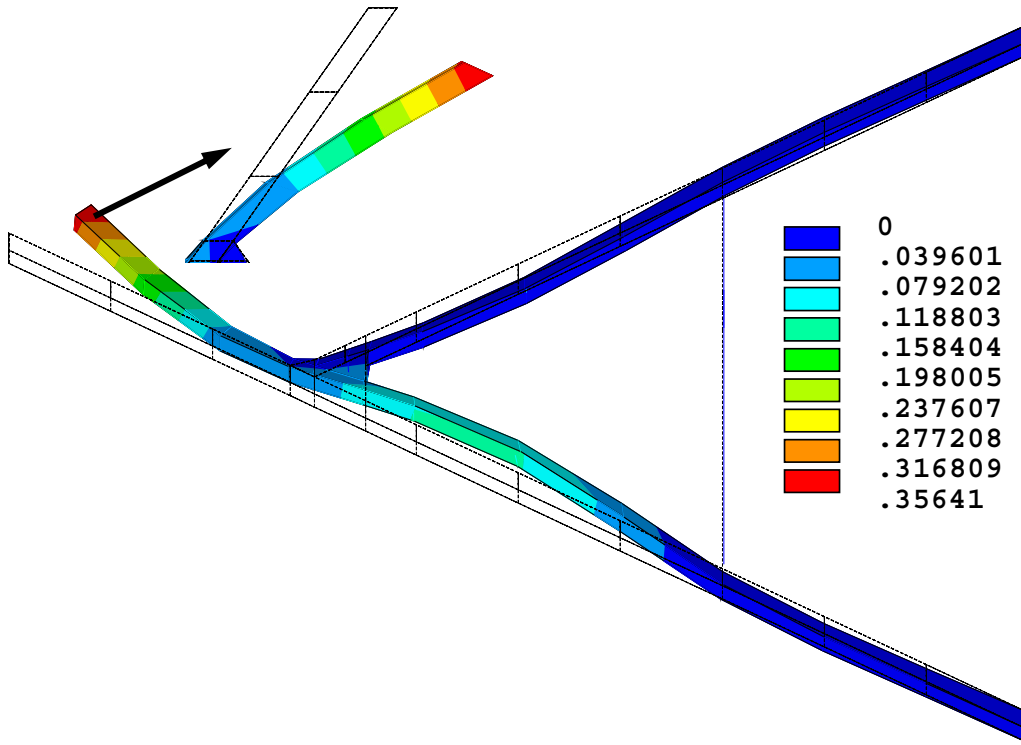
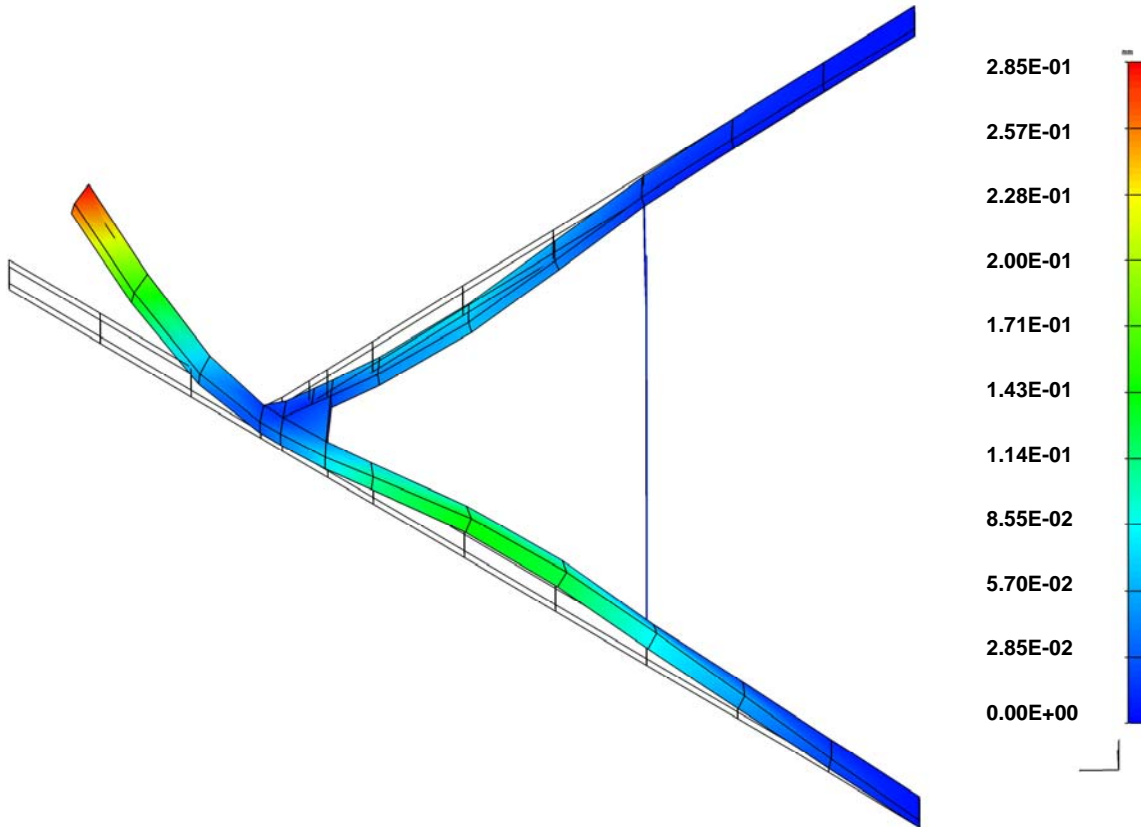


Fig. 98. Mode 3 for Rigid BC with RBEs and Fuselage using NASTRAN, Freq. = 3.3299 Hz



**Fig. 99. Mode 4 for Rigid BC with RBEs and Fuselage using ANSYS, Freq. = 5.9837 Hz**



**Fig. 100. Mode 4 for Rigid BC with RBEs and Fuselage using NASTRAN, Freq. = 5.4719 Hz**

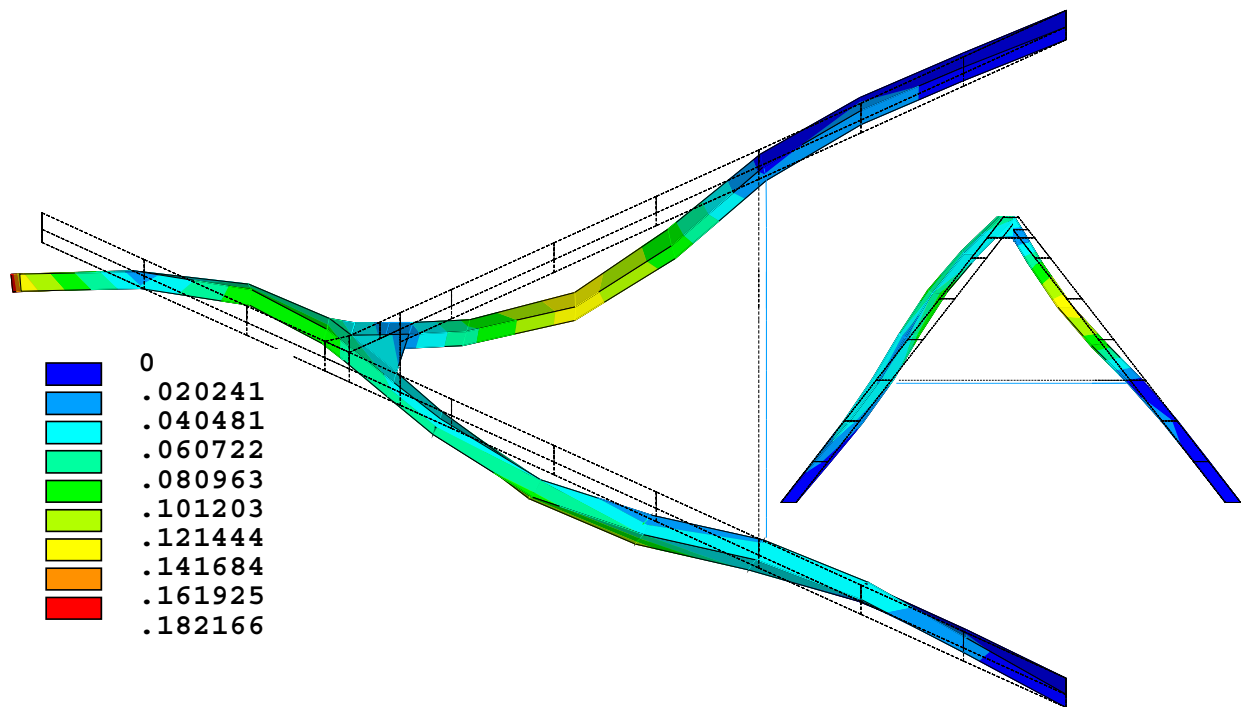


Fig. 101. Mode 5 for Rigid BC with RBEs and Fuselage using ANSYS, Freq. = 7.3316 Hz

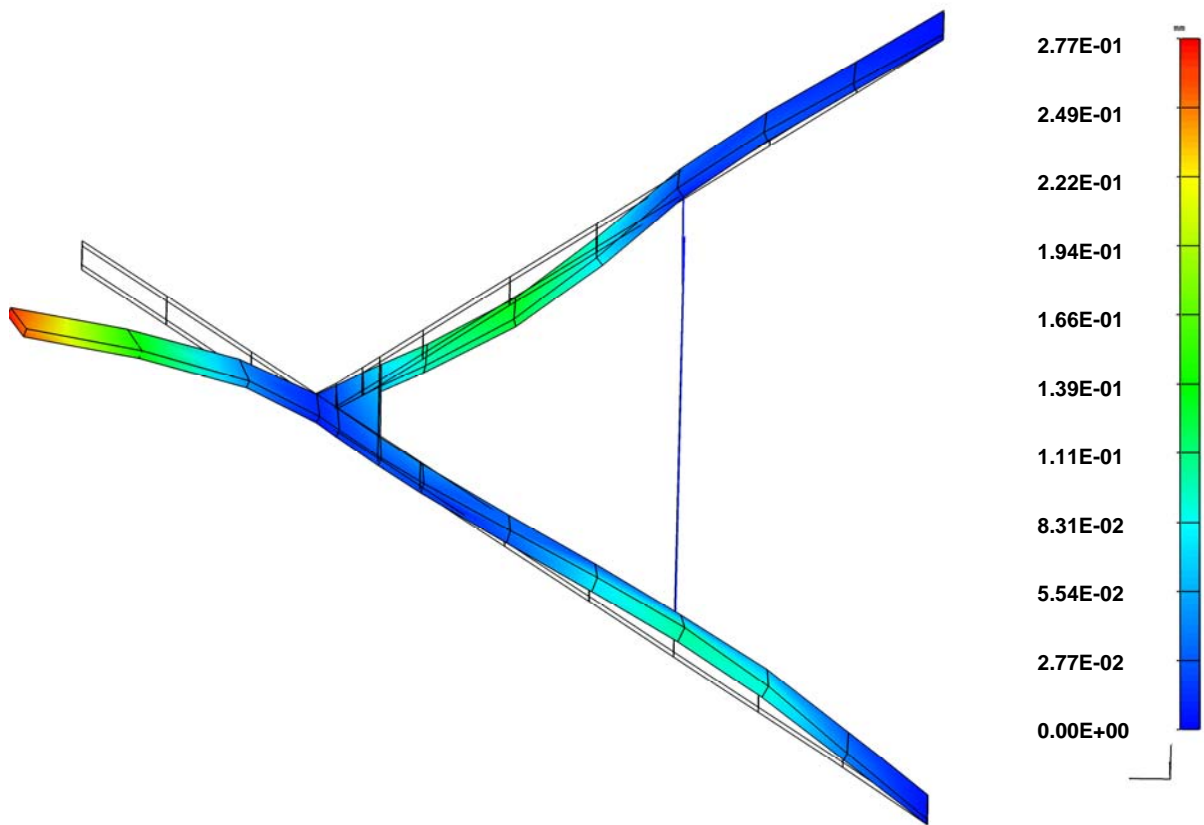


Fig. 102. Mode 5 for Rigid BC with RBEs and Fuselage using NASTRAN, Freq. = 7.1573 Hz

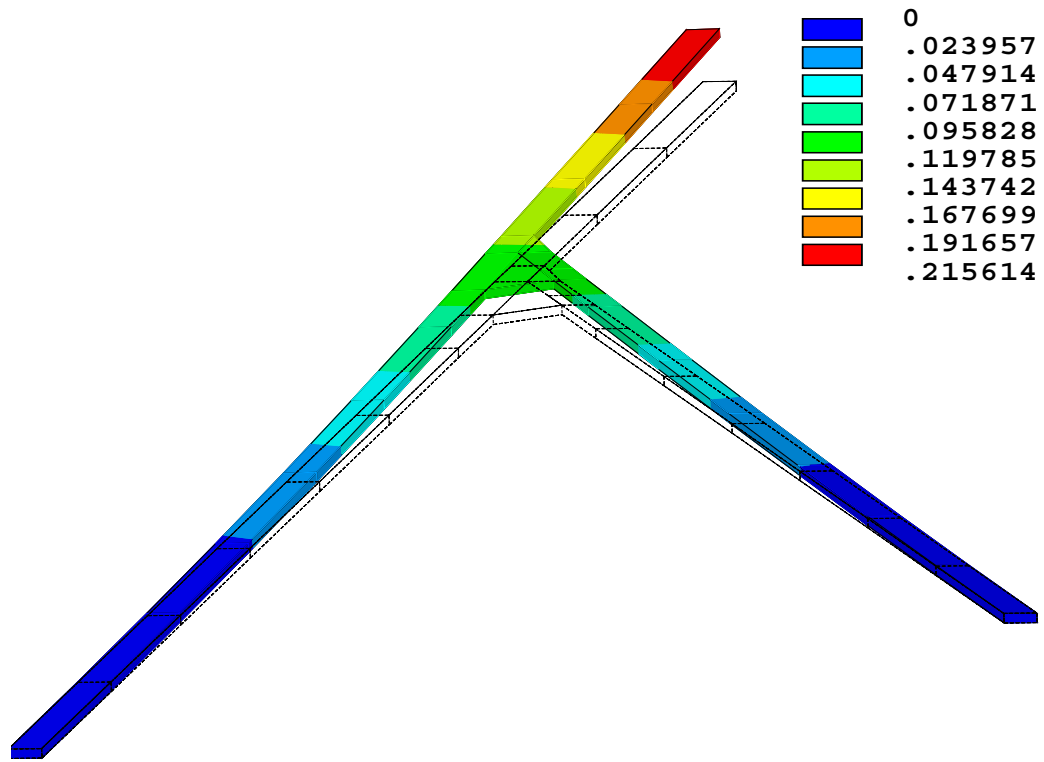


Fig. 103. Mode 1 for Rigid BC without RBEs and without Fuselage using ANSYS, Freq. = 0.7972 Hz

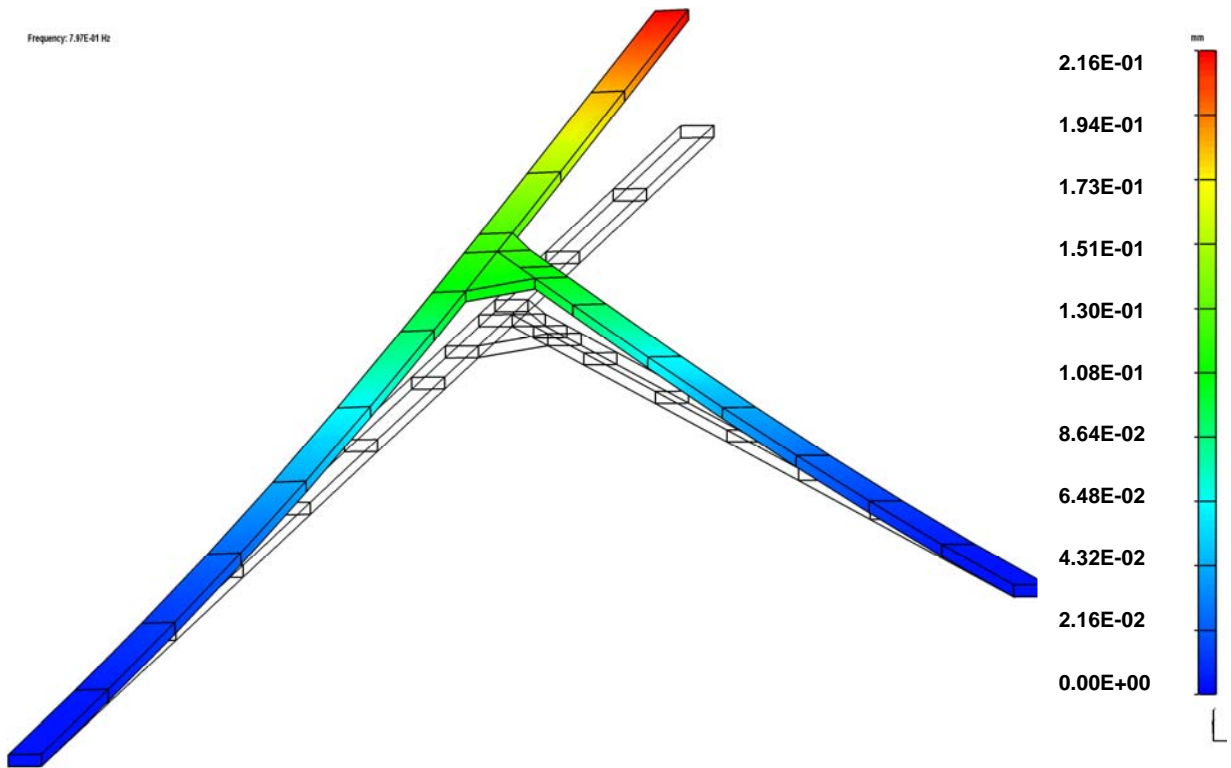


Fig. 104. Mode 1 for Rigid BC without RBEs and without Fuselage using NAST., Freq. = 0.7972 Hz

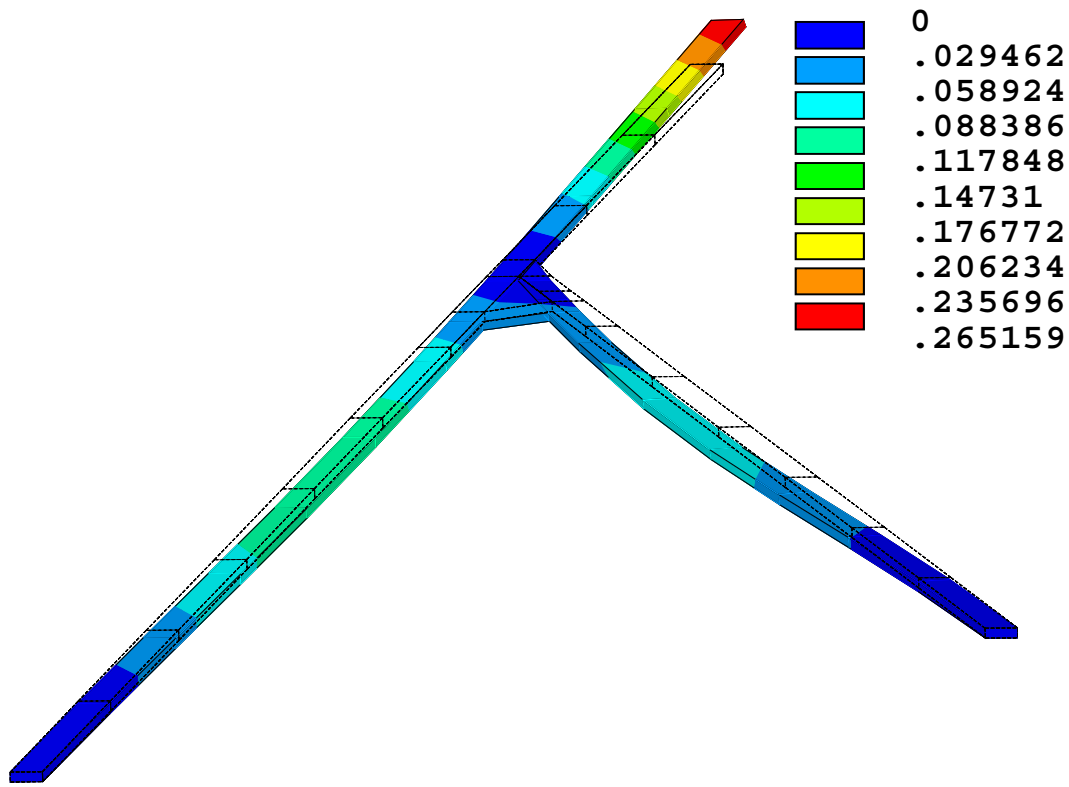


Fig. 105. Mode 2 for Rigid BC without RBEs and without Fuselage using ANSYS, Freq. = 2.0433 Hz

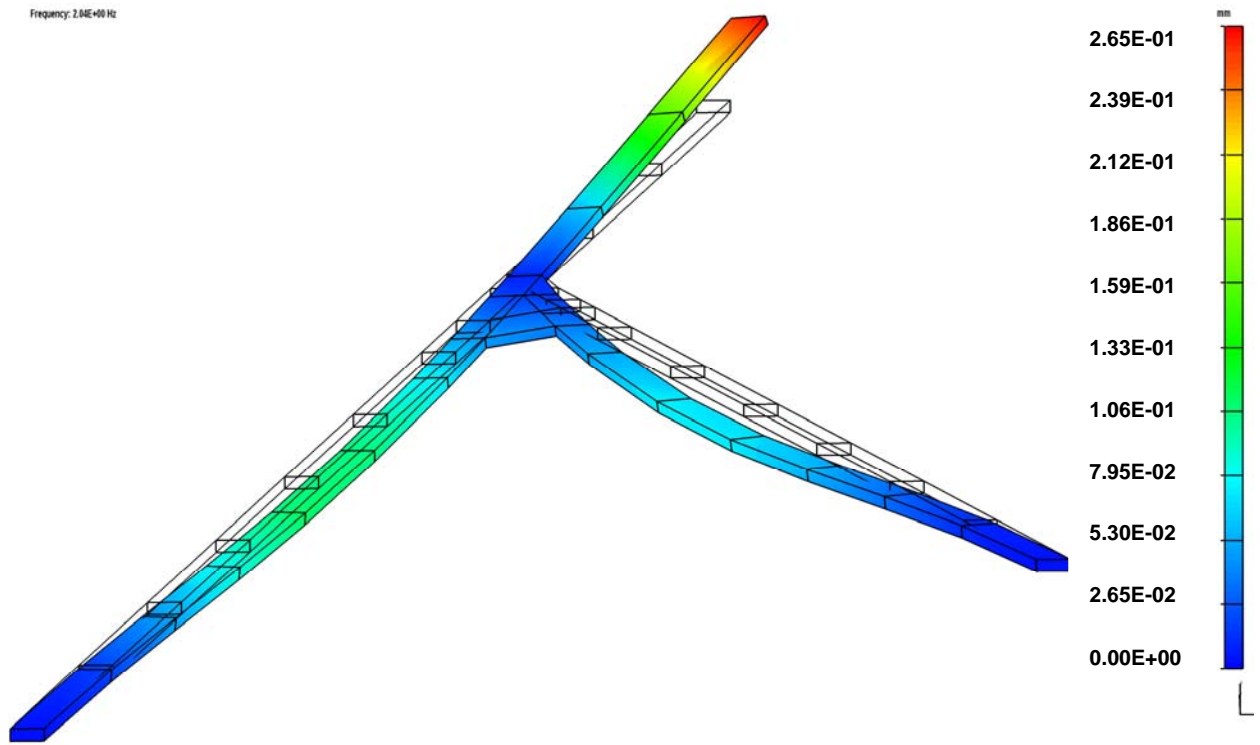


Fig. 106. Mode 2 for Rigid BC without RBEs and without Fuselage using NAST., Freq. = 2.0433 Hz

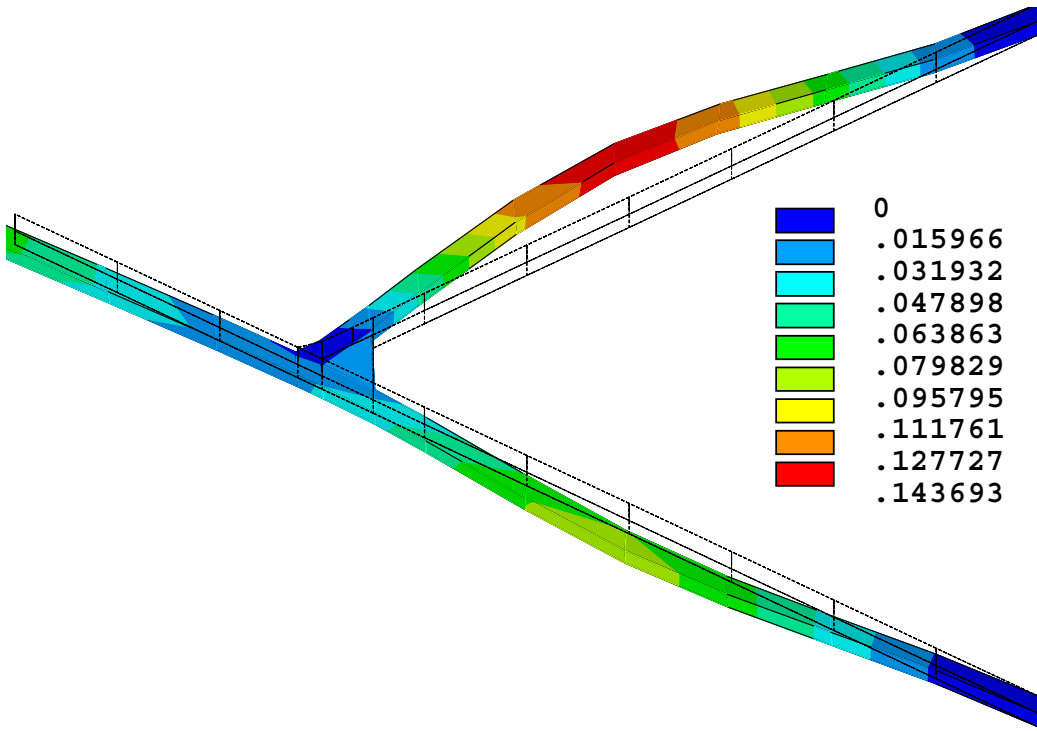


Fig. 107. Mode 3 for Rigid BC without RBEs and without Fuselage using ANSYS, Freq. = 3.0499 Hz

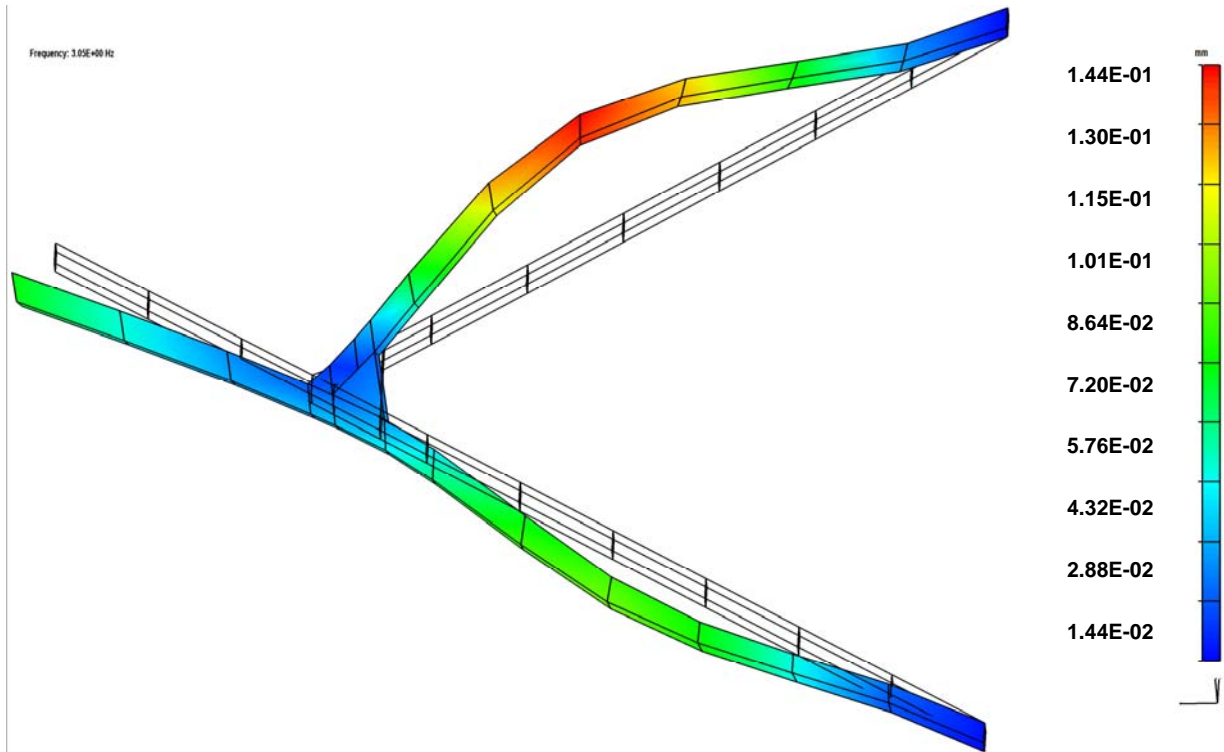


Fig. 108. Mode 3 for Rigid BC without RBEs and without Fuselage using NAST., Freq. = 3.0499 Hz

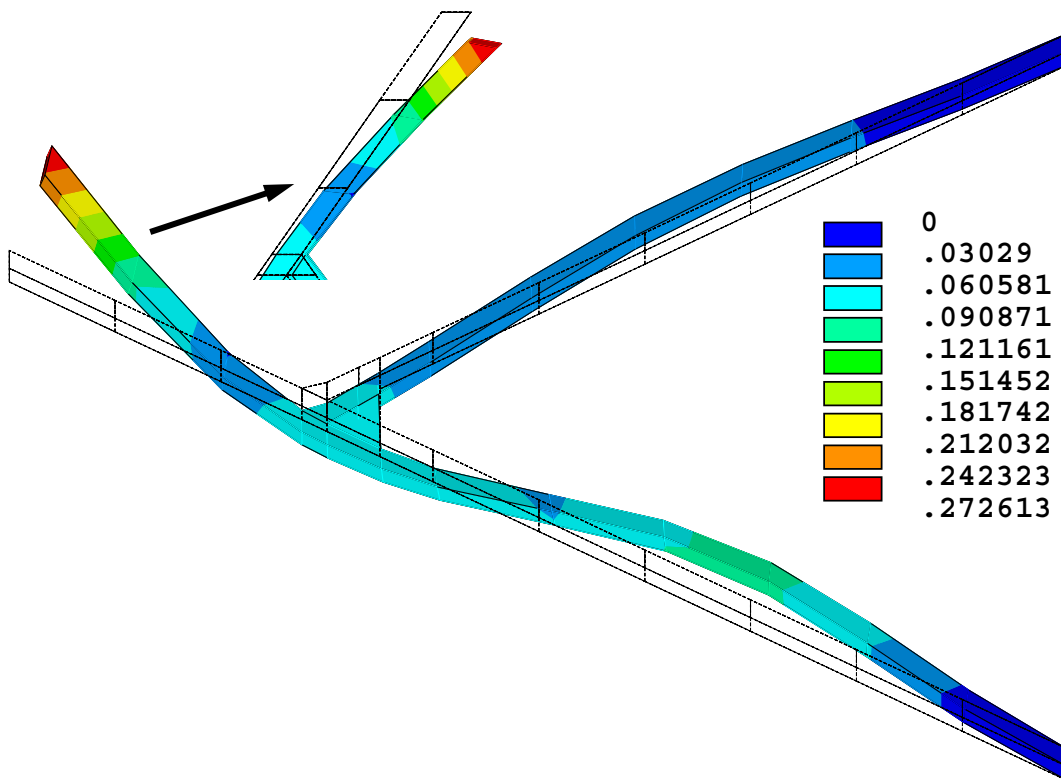


Fig. 109. Mode 4 for Rigid BC without RBEs and without Fuselage using ANSYS, Freq. = 4.1510 Hz

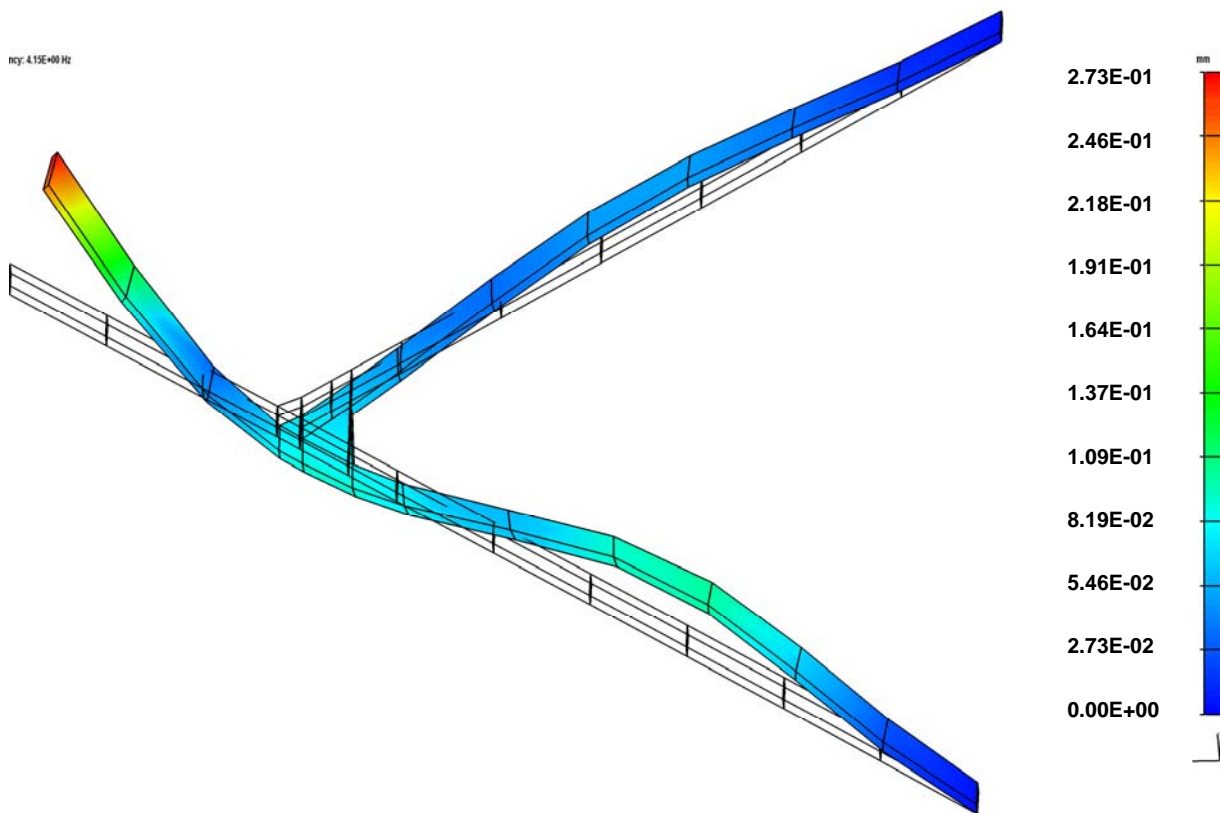


Fig. 110. Mode 4 for Rigid BC without RBEs and without Fuselage using NAST., Freq. = 4.1510 Hz

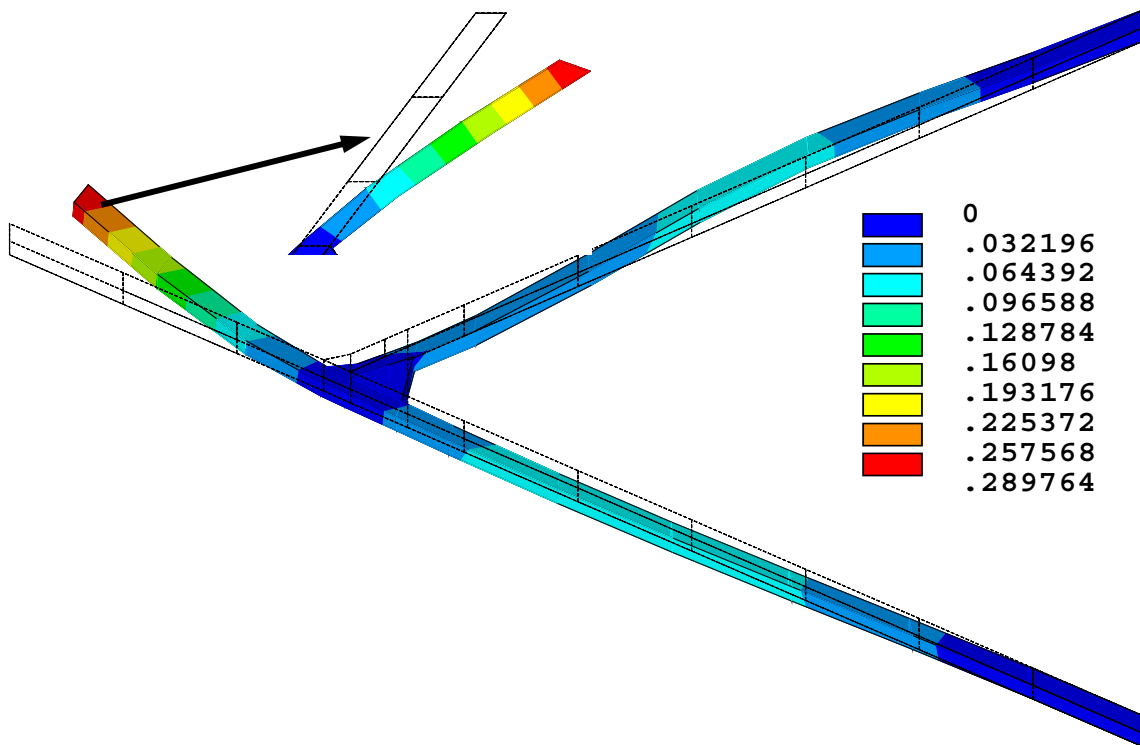


Fig. 111. Mode 5 for Rigid BC without RBEs and without Fuselage using ANSYS, Freq. = 4.6480 Hz

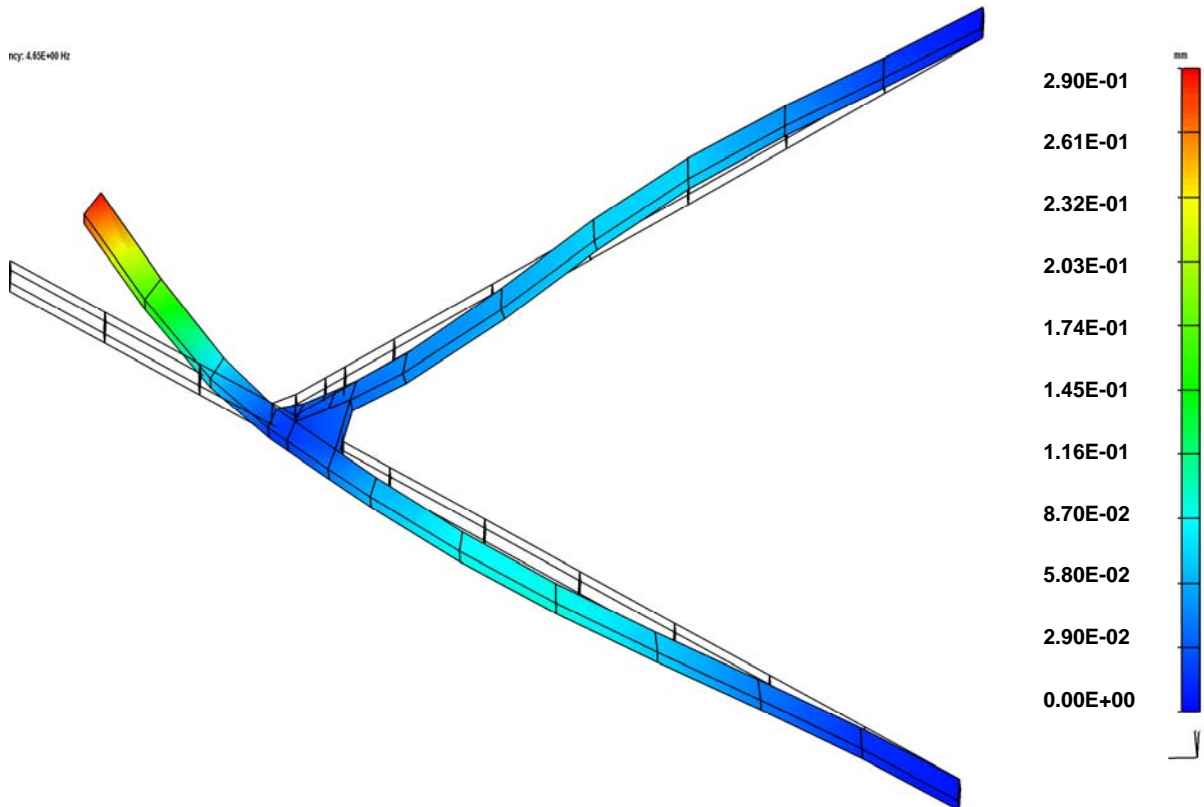


Fig. 112. Mode 5 for Rigid BC without RBEs and without Fuselage using NAST., Freq. = 4.6480 Hz

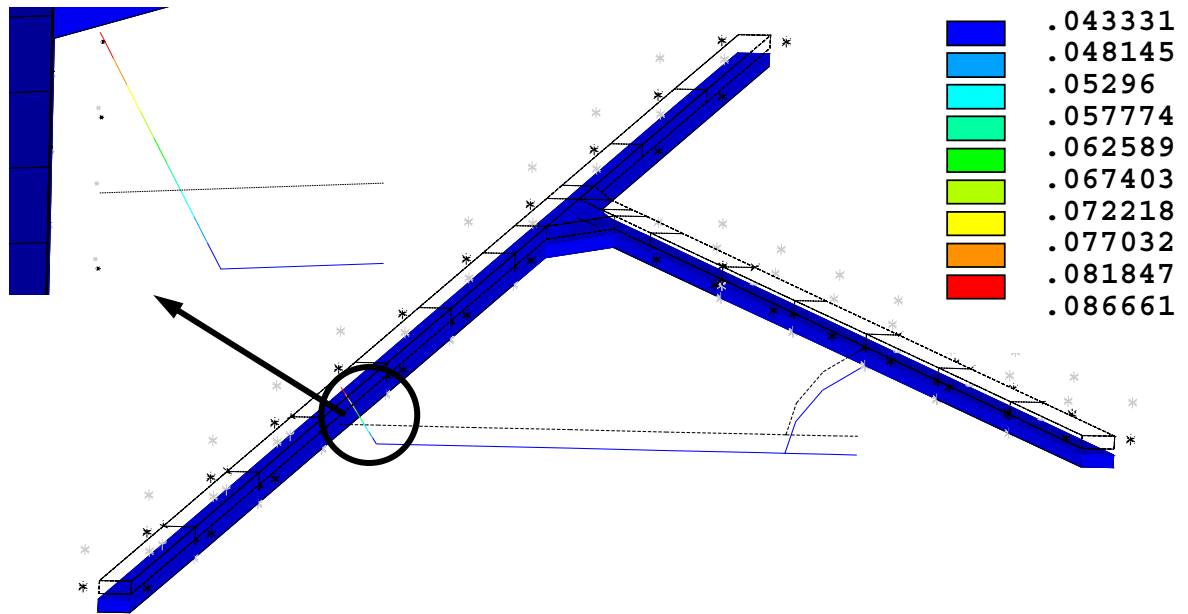


Fig. 113. Mode 1 for SUPORT BC with RBEs and Fuselage using ANSYS, Freq. = 0.0000 Hz

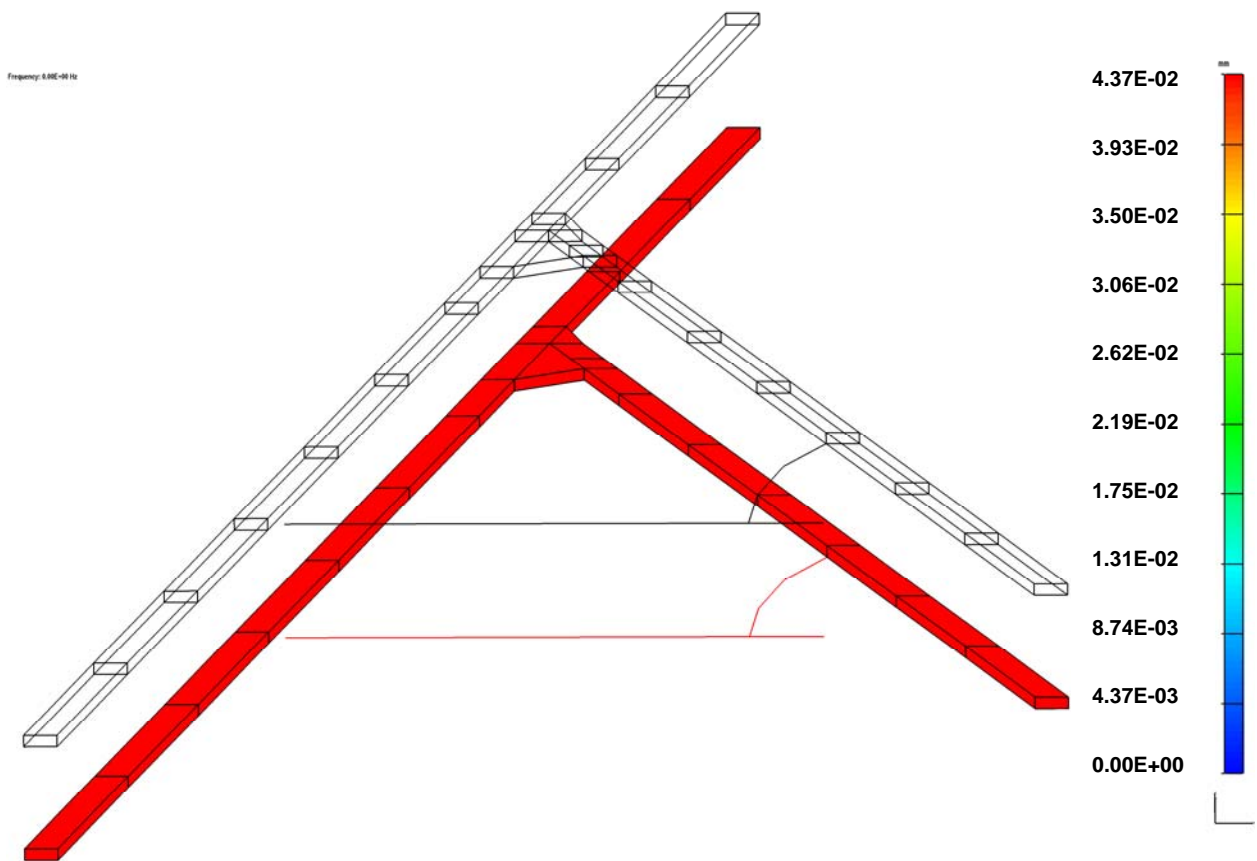


Fig. 114. Mode 1 for SUPORT BC with RBEs and Fuselage using NASTRAN, Freq. = 0.0000 Hz

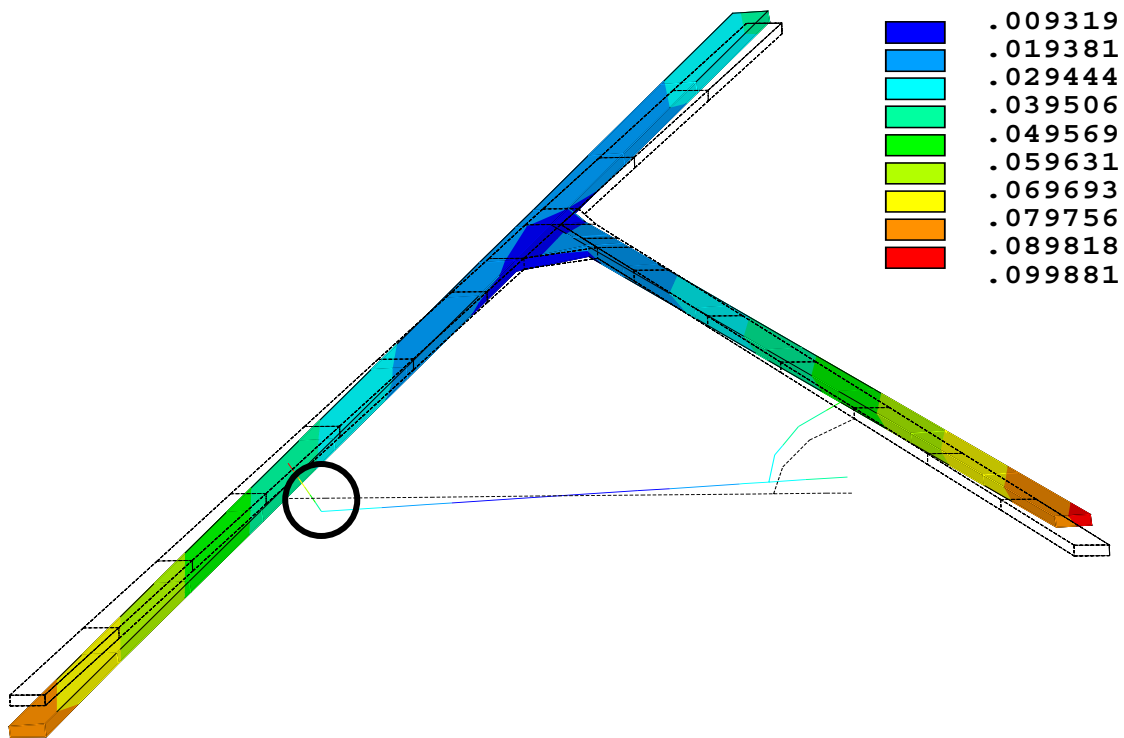


Fig. 115. Mode 2 for SUPORT BC with RBEs and Fuselage using ANSYS, Freq. = 0.0000 Hz

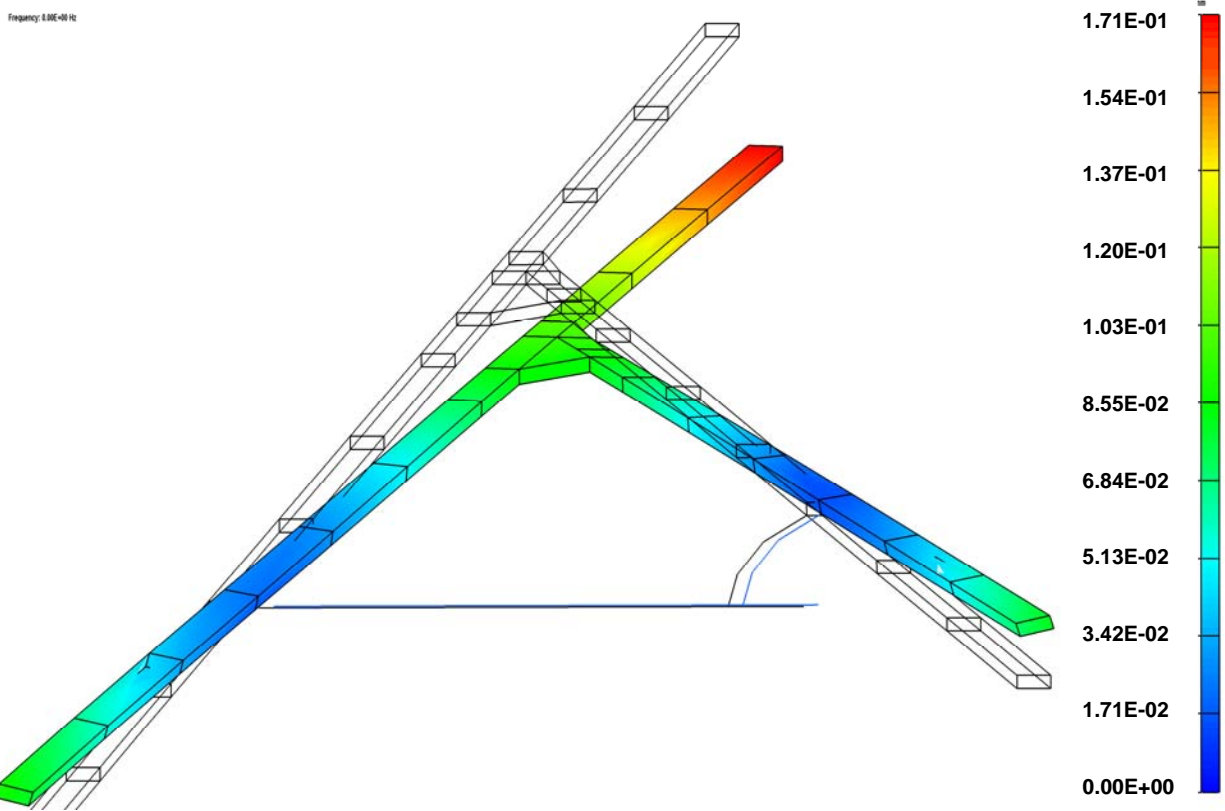


Fig. 116. Mode 2 for SUPORT BC with RBEs and Fuselage using NASTRAN, Freq. = 0.0000 Hz

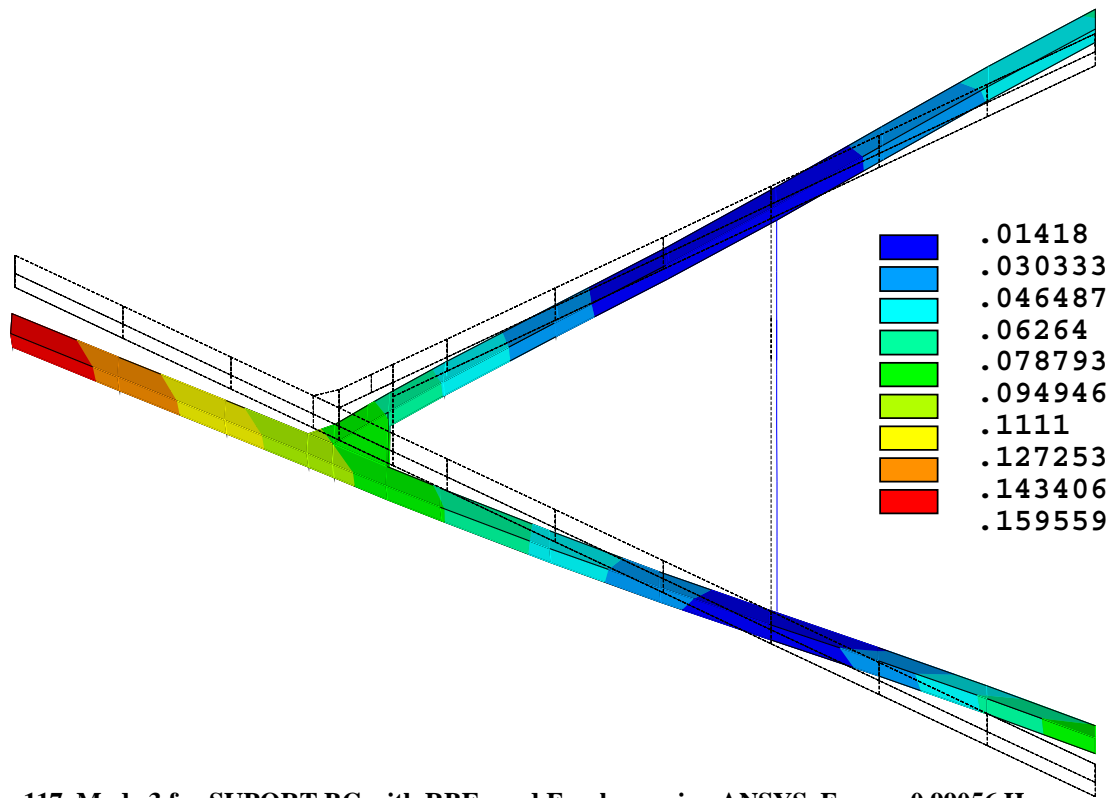


Fig. 117. Mode 3 for SUPORT BC with RBEs and Fuselage using ANSYS, Freq. = 0.99056 Hz

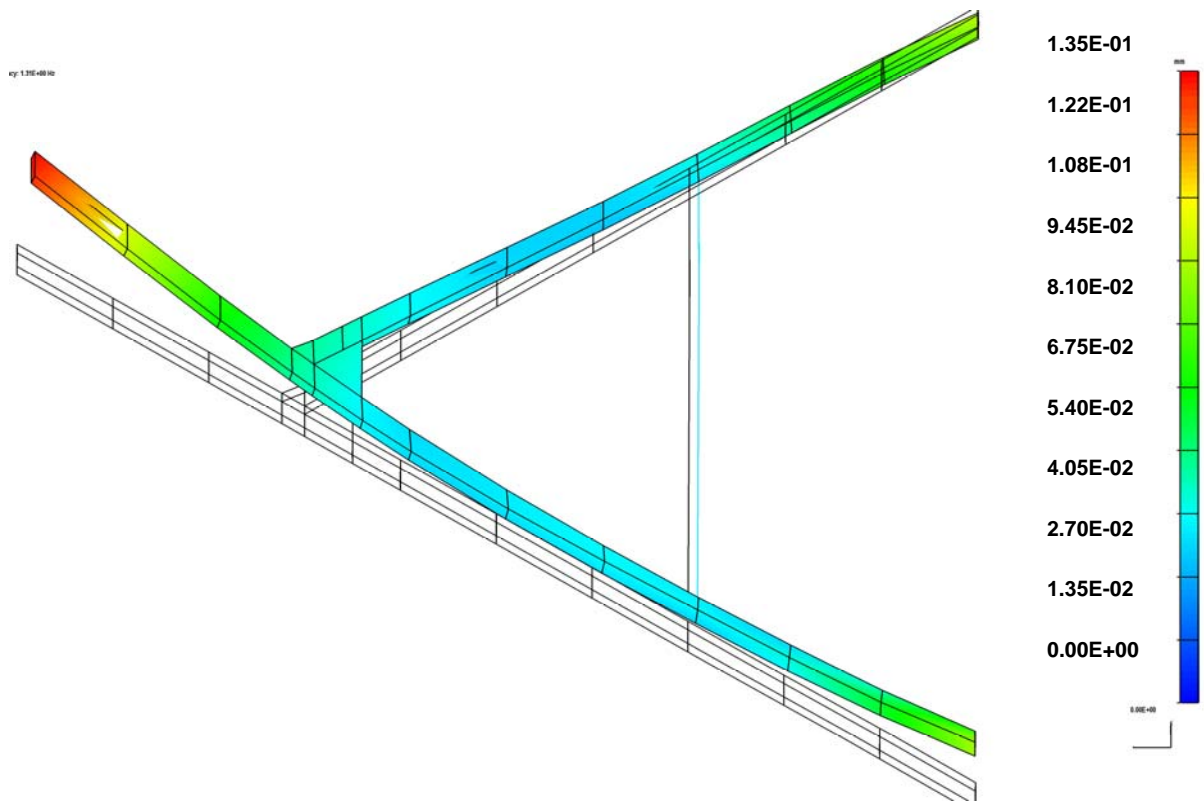


Fig. 118. Mode 3 for SUPORT BC with RBEs and Fuselage using NASTRAN, Freq. = 1.3134 Hz

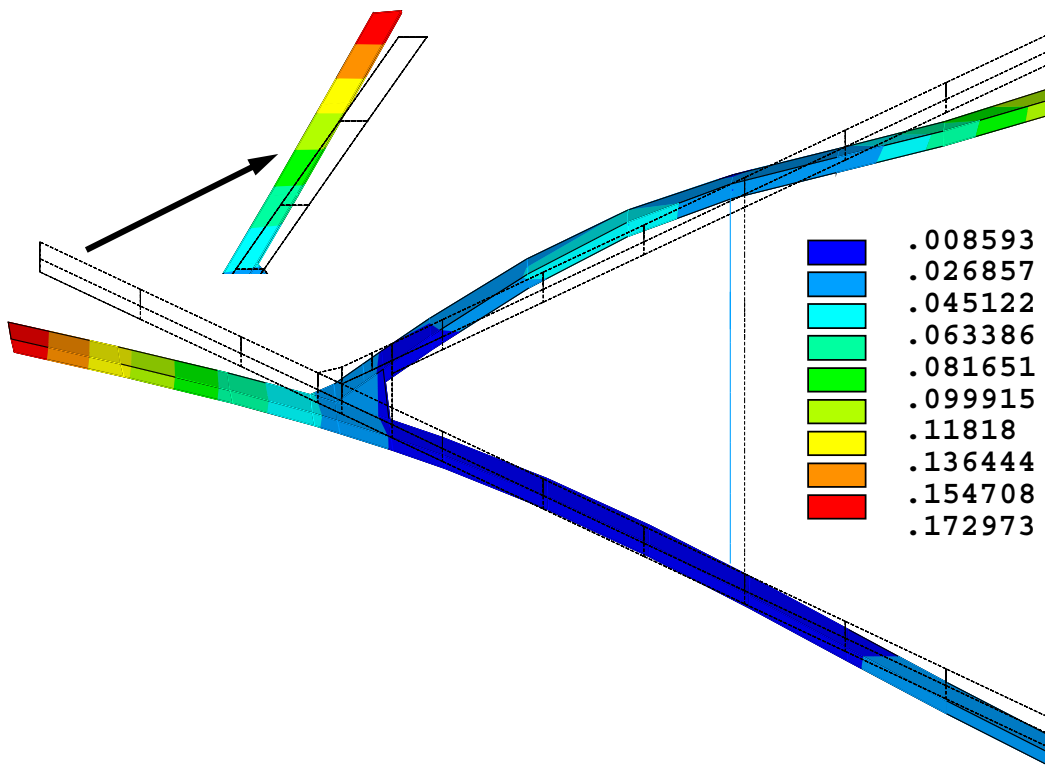


Fig. 119. Mode 4 for SUPORT BC with RBEs and Fuselage using ANSYS, Freq. = 1.6238 Hz

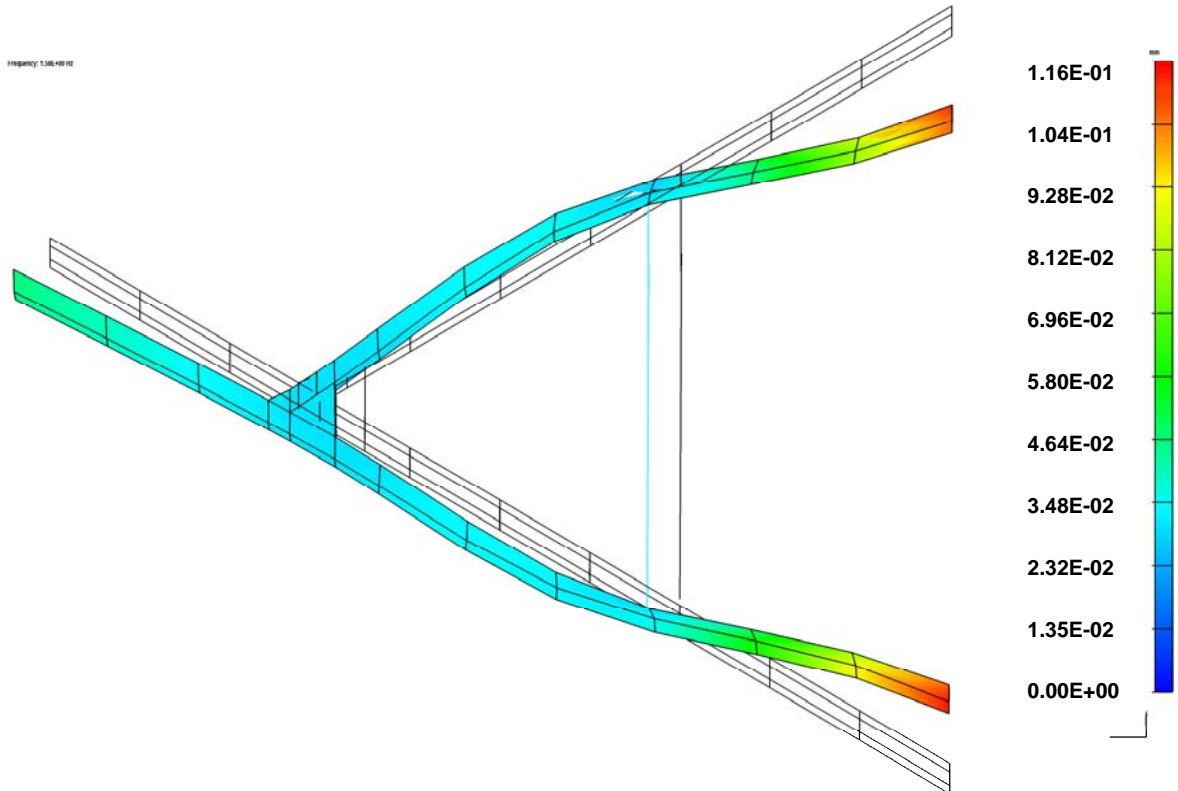


Fig. 120. Mode 4 for SUPORT BC with RBEs and Fuselage using NASTRAN, Freq. = 1.5751 Hz

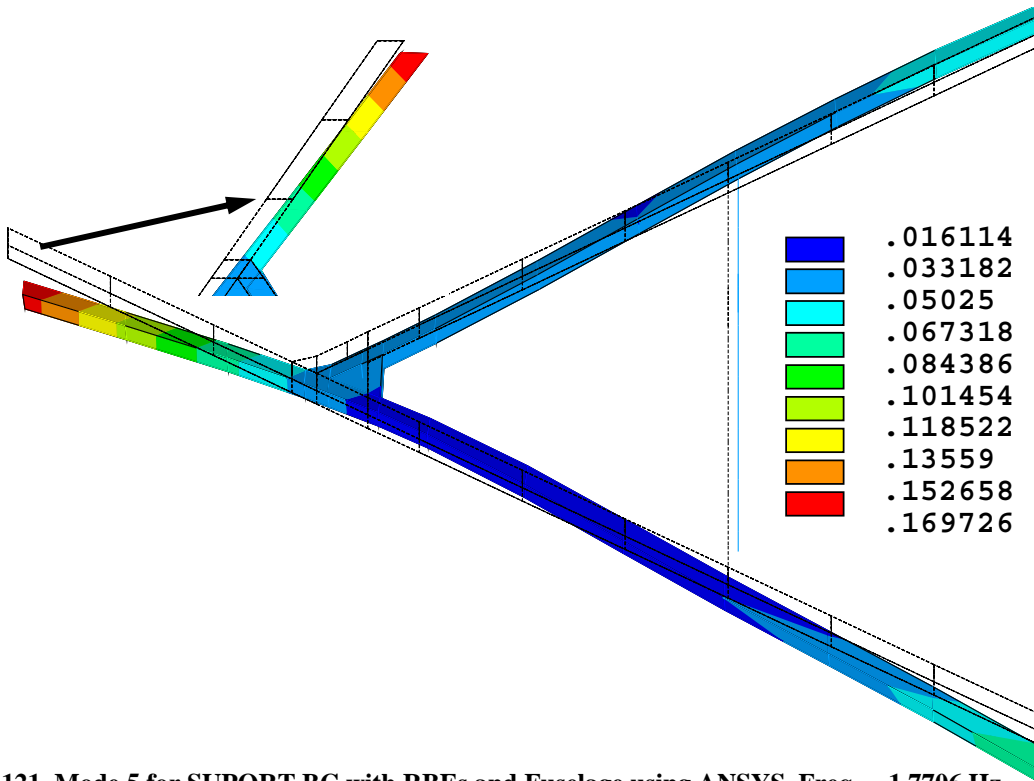


Fig. 121. Mode 5 for SUPORT BC with RBEs and Fuselage using ANSYS, Freq. = 1.7706 Hz

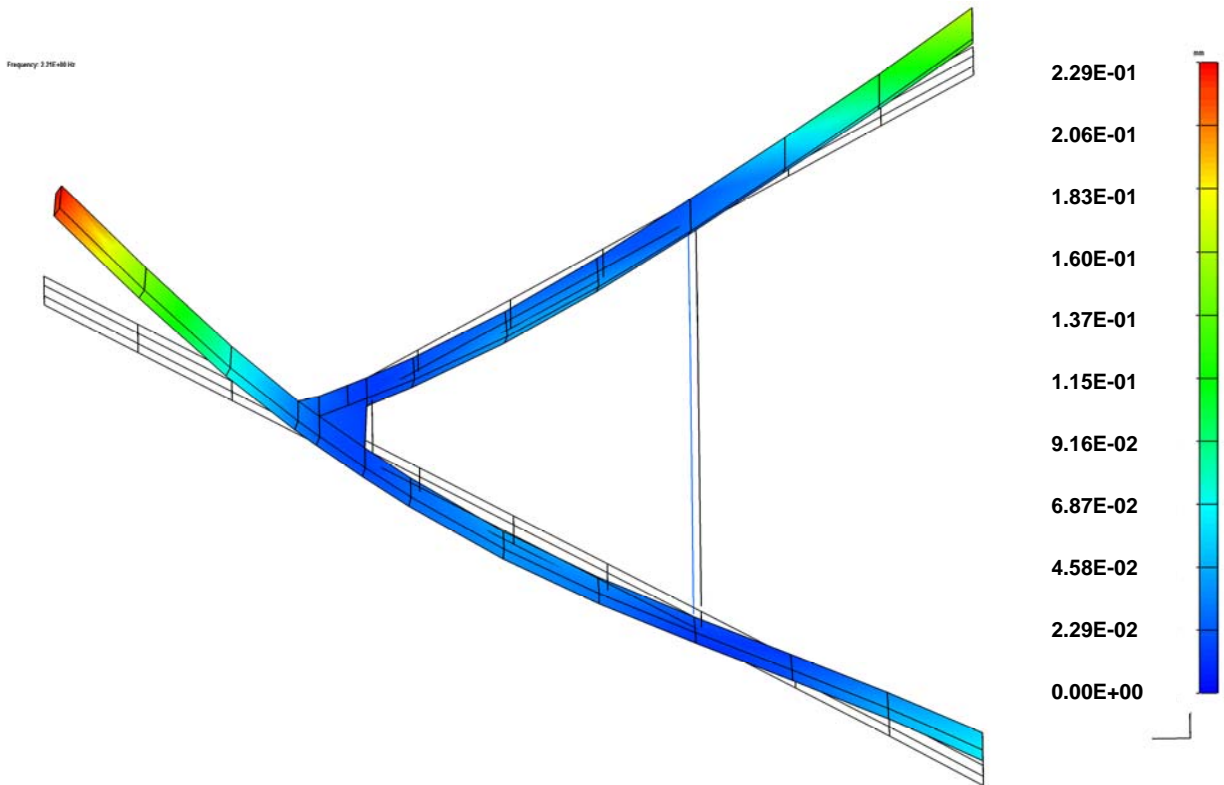


Fig. 122. Mode 5 for SUPORT BC with RBEs and Fuselage using NASTRAN, Freq. = 2.2107 Hz

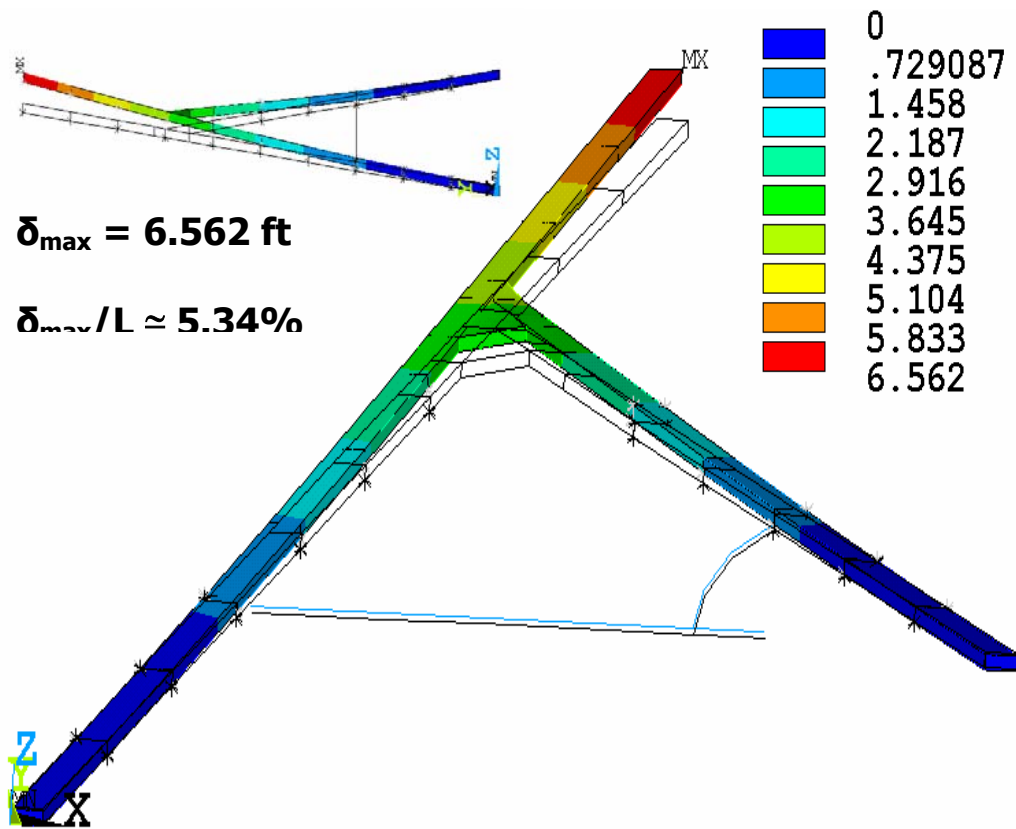


Fig. 123. Linear Static Analysis, with CEs and Fuselage - Deflection Contours

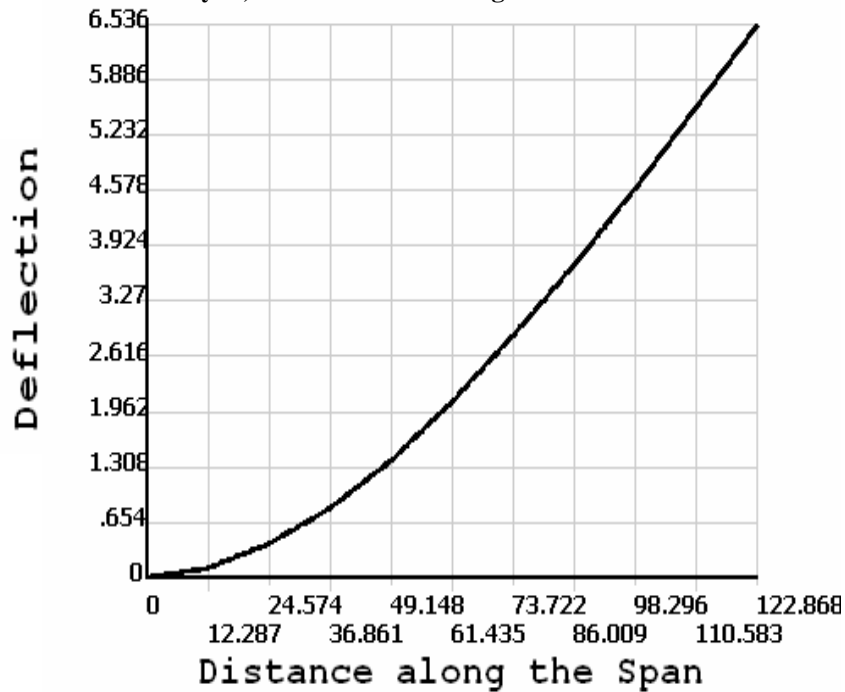


Fig. 124. Linear Static Analysis, with CEs and Fuselage - Deflection vs Distance Along Span of Main Wing

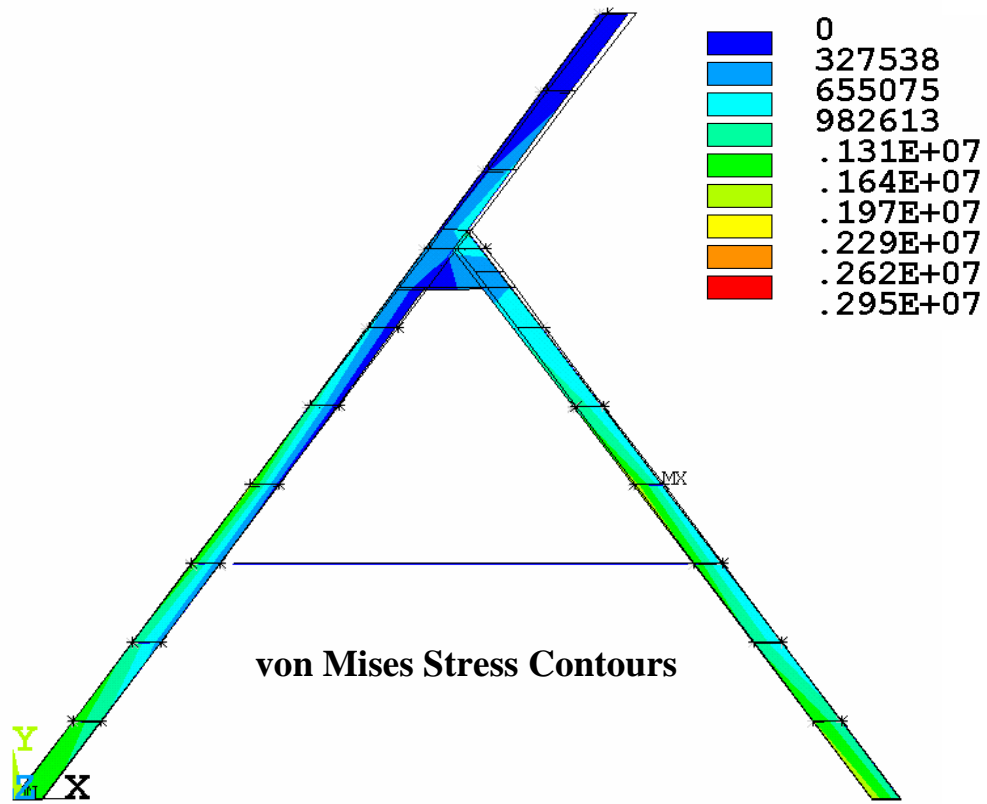


Fig. 125. Linear Static Analysis, with CEs and Fuselage – Stress Contours

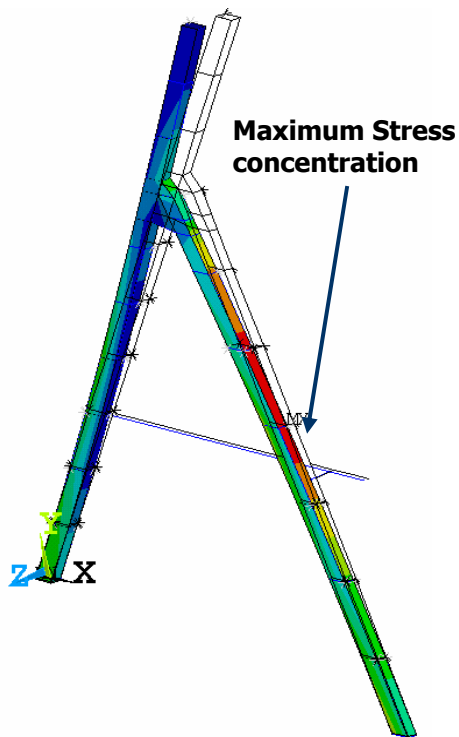


Fig. 126. Linear Static Analysis, with CEs and Fuselage – Left View of Stress Contours

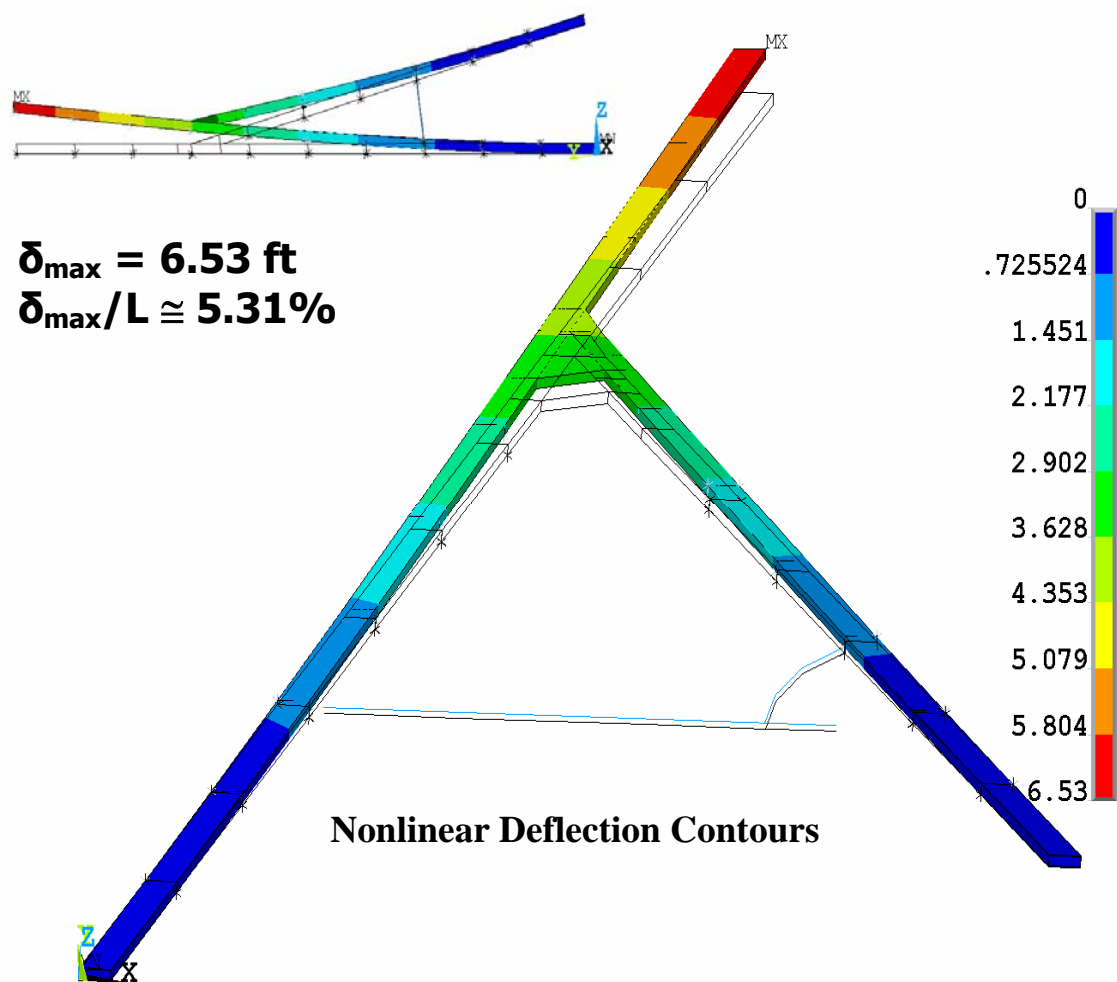


Fig. 127. Nonlinear Static Analysis, with CEs and Fuselage – Deflection Contours

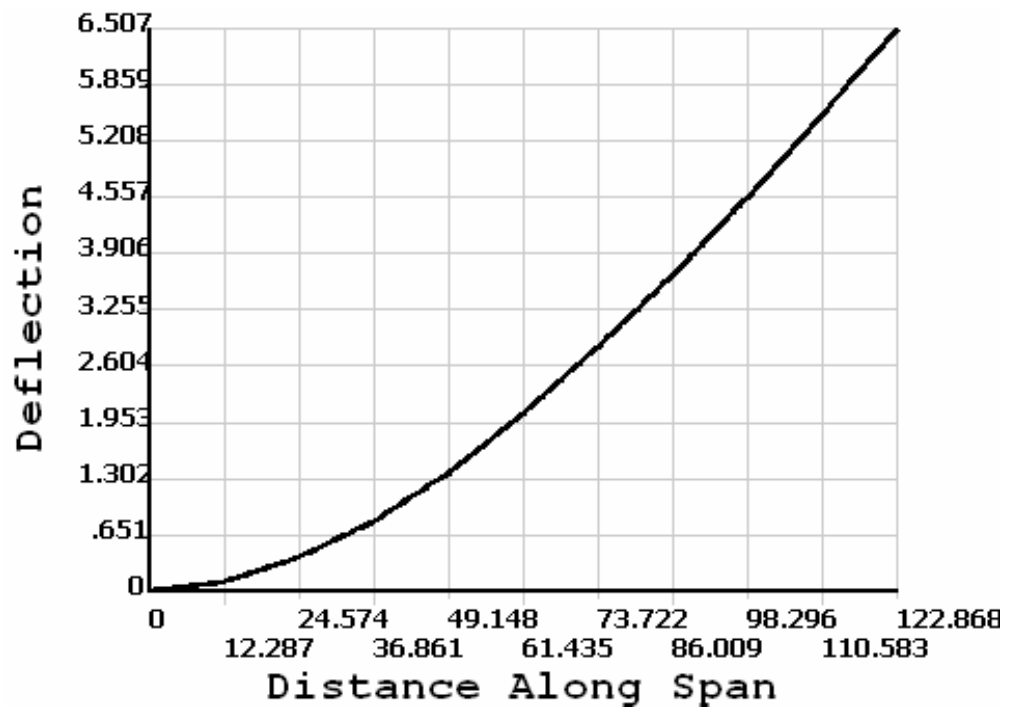


Fig. 128. Nonlinear Static Analysis, with CEs and Fuselage – Deflection vs Distance Along Span of Main Wing

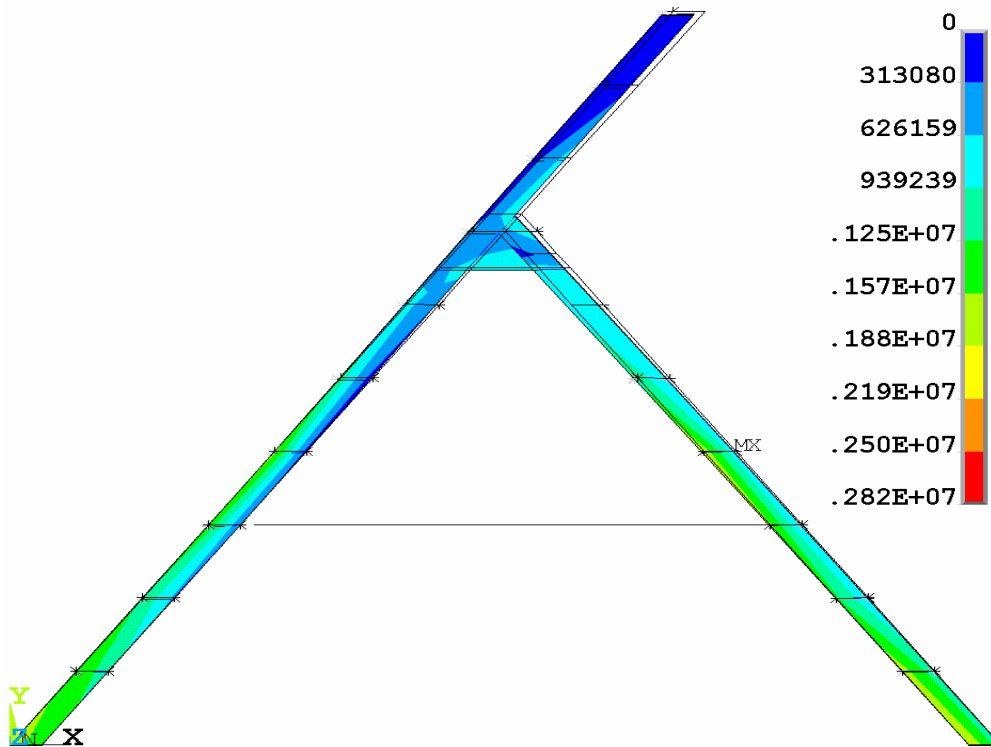


Fig. 129. Nonlinear Static Analysis, with CEs and Fuselage – Stress Contours

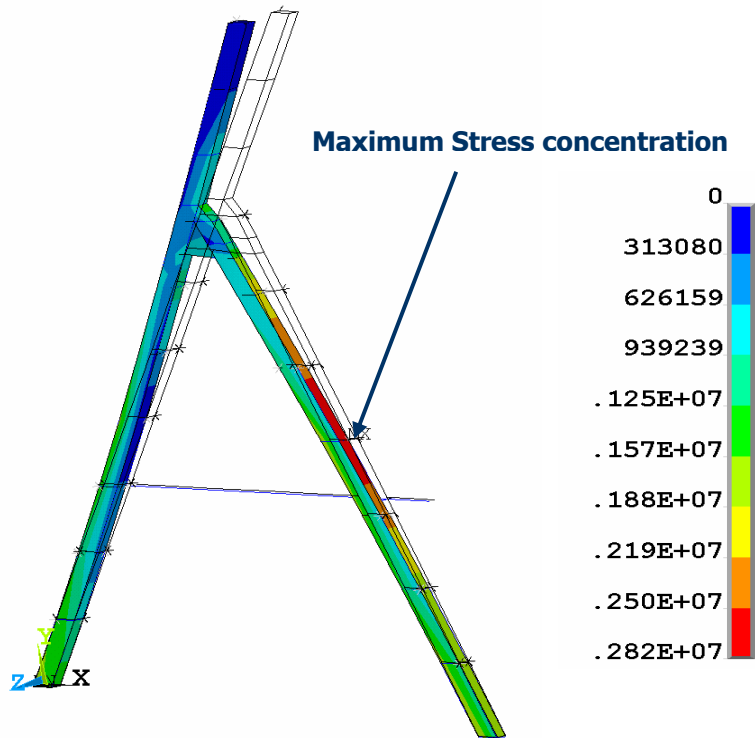


Fig. 130. Nonlinear Static Analysis, with CEs and Fuselage – Left View of Stress Contours

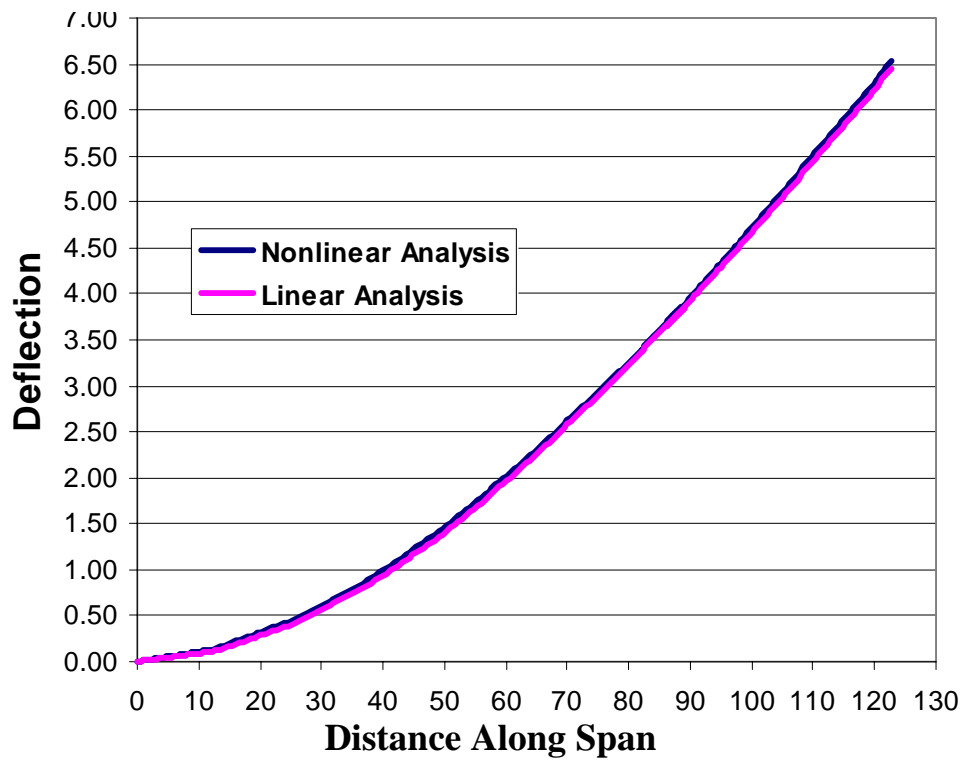
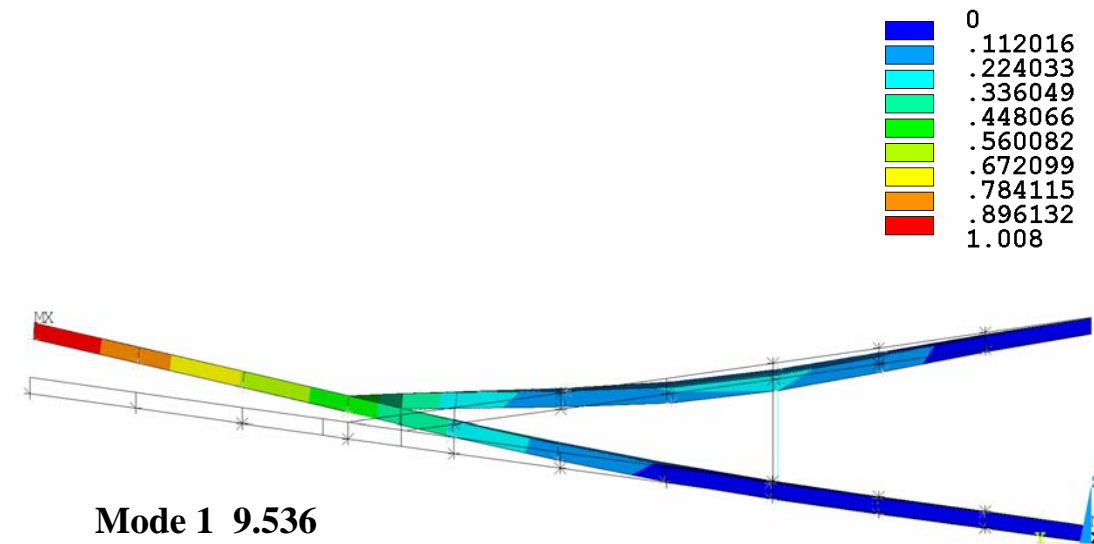
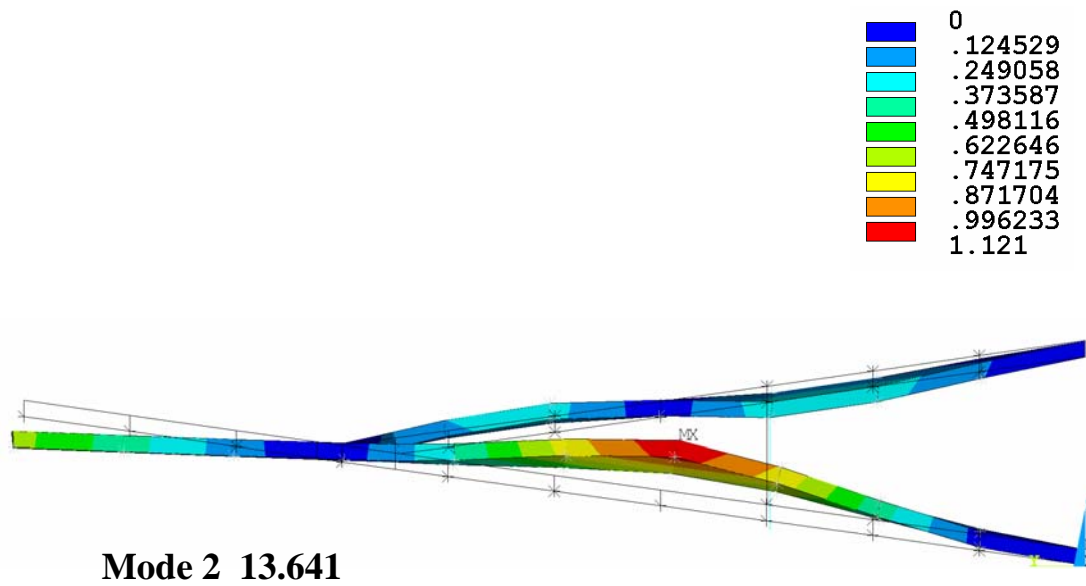


Fig. 131. Linear Vs Nonlinear – Deflection Vs Distance Along Span of Main wing



**Fig. 132. Eigenvalue Buckling Analysis – Mode 1, Eigenvalue = 9.436**



**Fig. 133. Eigenvalue Buckling Analysis – Mode 2 Eigenvalue = 13.641**

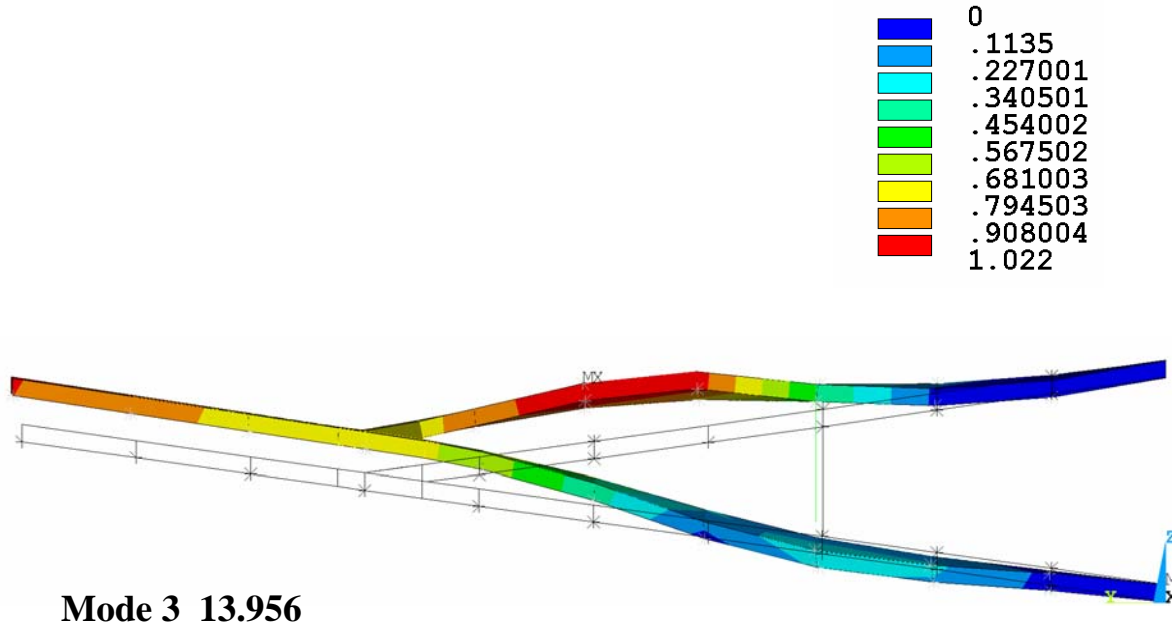


Fig. 134. Eigenvalue Buckling Analysis – Mode 3 Eigenvalue = 13.956

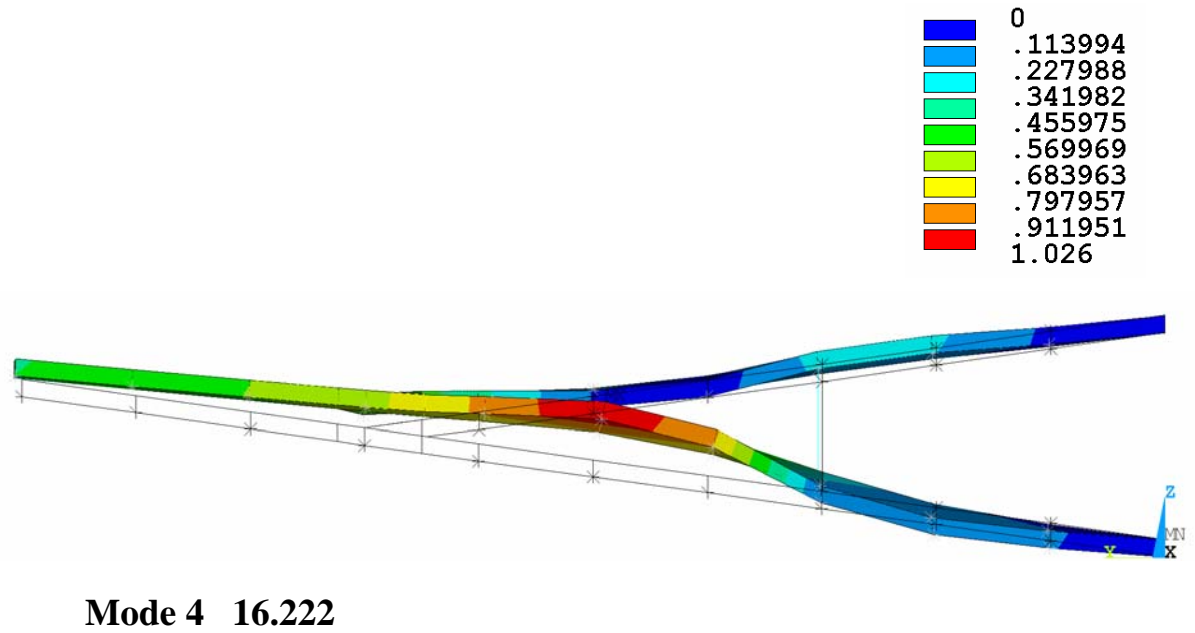
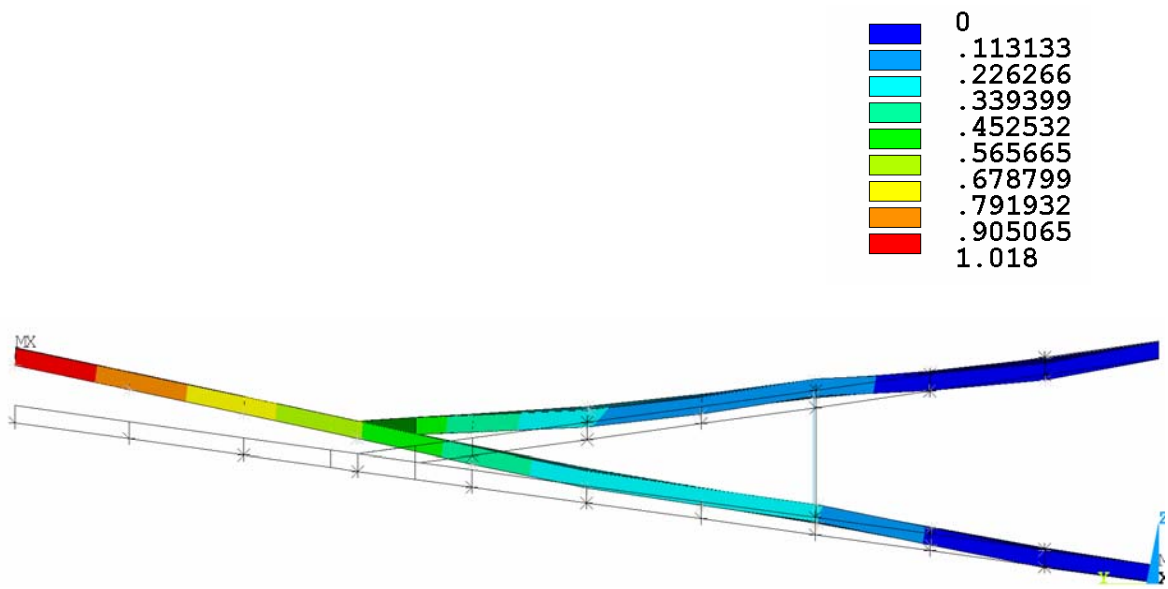


Fig. 135. Eigenvalue Buckling Analysis – Mode 4 Eigenvalue = 16.222



**Mode 5 20.821**

**Fig. 136. Eigenvalue Buckling Analysis – Mode 5 Eigenvalue = 20.821**

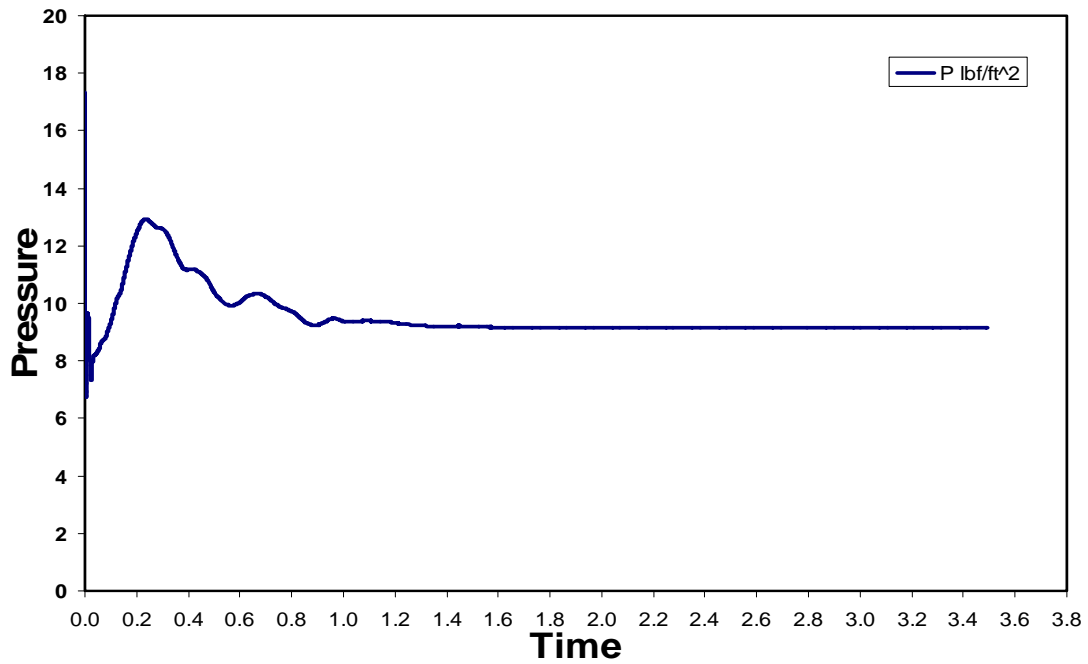


Fig. 137. Dynamic Analysis – Time History of Applied Pressure Loads

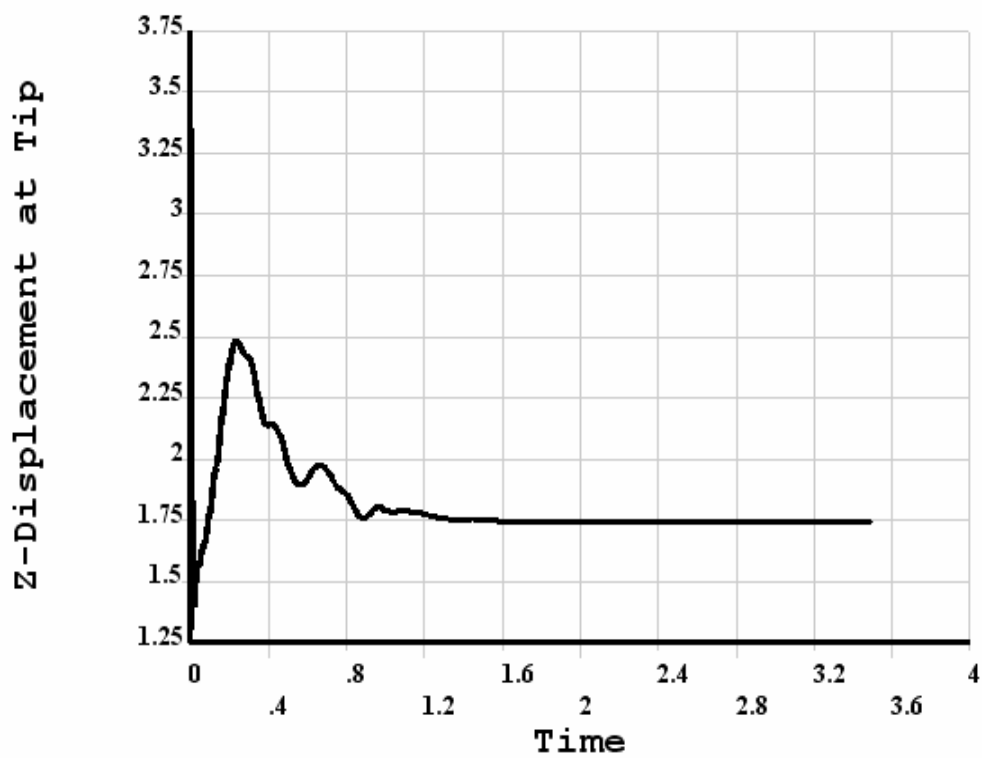


Fig. 138. Dynamic Analysis – Time History of z-Displacement at Tip

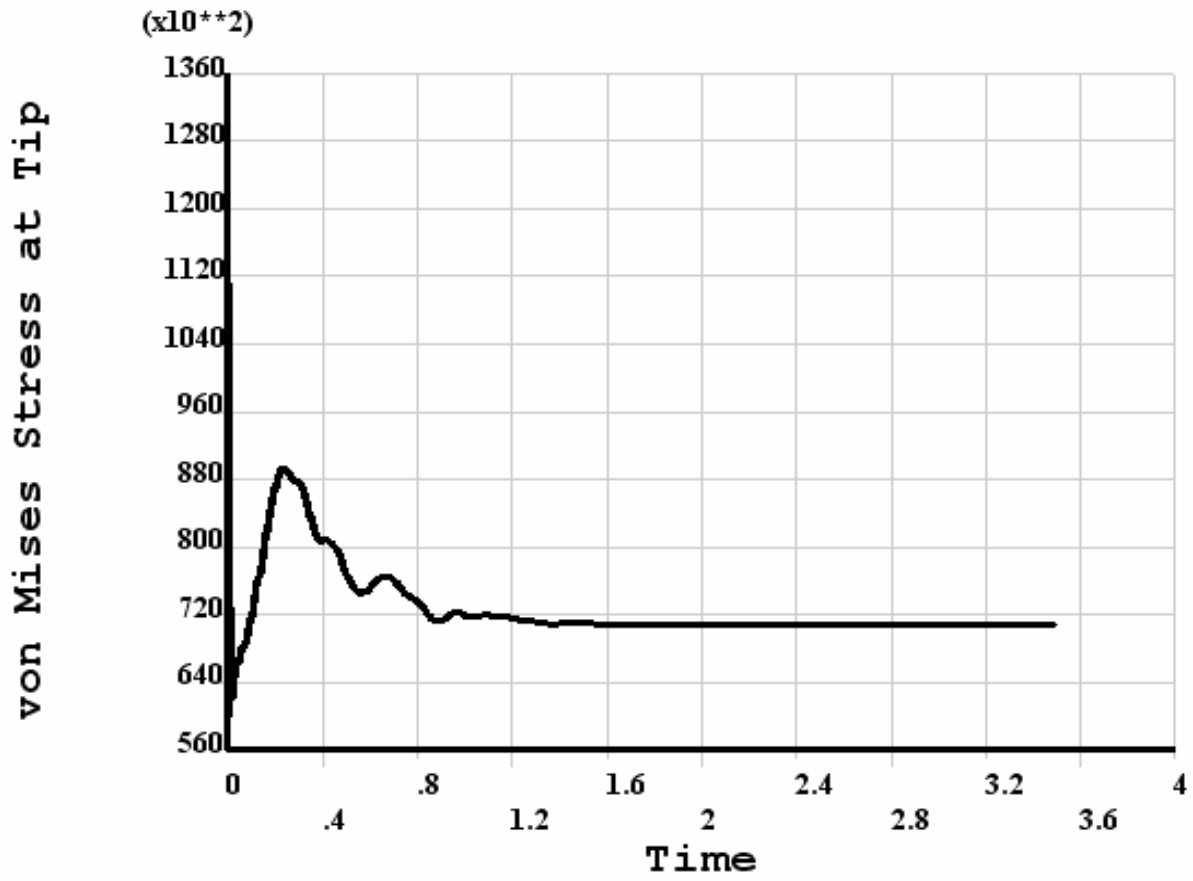


Fig. 139. Dynamic Analysis – Time History of von Mises stress at Tip